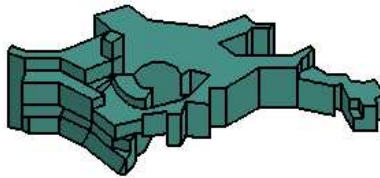
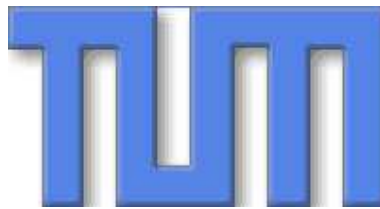


Max-Planck-Institut für Astrophysik

Black hole formation from non-axisymmetric instabilities in quasi-toroidal stars

Burkhard Sebastian Zink



Dissertation an der Fakultät für Physik der
Technischen Universität München

Technische Universität München

Max-Planck-Institut für Astrophysik

Black hole formation from non-axisymmetric instabilities in quasi-toroidal stars

Burkhard Sebastian Zink

Vollständiger Abdruck der von der Fakultät für Physik der Technischen Universität München zur Erlangung des akademischen Grades eines

Doktors der Naturwissenschaften

genehmigten Dissertation.

Vorsitzender: Univ.-Prof. Dr. Lothar Oberauer

Prüfer der Dissertation:

1. Priv.-Doz. Dr. Ewald Müller
2. Univ.-Prof. Dr. Andrzej Jerzy Buras

Die Dissertation wurde am 11.04.2006 bei der Technischen Universität München eingereicht

und durch die Fakultät für Physik am 08.06.2006 angenommen.

Erklärung

Ich erkläre, dass ich die vorliegende Dissertation eigenständig verfasst und keine anderen als die angegebenen Hilfsmittel verwendet habe. Weiterhin erkläre ich, dass ich alleine die Stilsetzung meiner Arbeit vorgenommen habe.

München, am

Contents

1. Foreword	3
2. Preface	5
3. Theory and Tools	7
3.1. Notations and conventions	7
3.2. The physical system	7
3.2.1. The NOK-BSSN form of the initial-value problem	8
3.2.2. The Einstein-Christoffel form of the initial-value problem	9
3.2.3. The massless Klein-Gordon field	11
3.2.4. The perfect fluid	12
3.2.5. Excision and constraint-preserving boundary conditions	13
3.3. Well-posedness, hyperbolicity, and the summation-by-parts property	15
3.3.1. Well-posedness	15
3.3.2. Hyperbolicity	16
3.3.3. Strict stability	16
3.3.4. The summation-by-parts property	17
3.3.5. The penalty method	18
3.4. Cactus, Carpet and Whisky	19
3.4.1. The Cactus Computational Toolkit	20
3.4.2. The PUGH driver	20
3.4.3. The Carpet driver	20
3.4.4. Thorns for numerical relativity	22
3.4.5. The Whisky code	23
3.4.6. Mode extraction	23
3.4.7. Solution-adaptive mesh refinement	23
4. Code tests	25
4.1. Rotating neutron stars on a uniform grid	25
4.2. Rotating neutron star collapse on a uniform grid	29
4.3. A failed experiment: Core collapse with adaptive shift	37
4.4. Carpet tests	38
4.4.1. Shock propagation across mesh refinement boundaries	38
4.4.2. TOV solution	47
4.4.3. Rotating star solution	49
5. Fragmentation and black hole formation in quasi-toroidal polytropes	51
5.1. Previous work	53
5.2. Initial data	54
5.2.1. Quasi-toroidal polytropes	54
5.2.2. The reference polytrope and associated sequences	56

5.2.3.	Quasi-toroidal and spheroidal models of constant central rest-mass density . . .	62
5.2.4.	A sequence of central rest-mass densities containing the model <i>A0.2R0.40</i> . . .	72
5.3.	Results	73
5.3.1.	Evolution of the reference model	73
5.3.2.	Evolution of the sequence of axes ratios	97
5.3.3.	Evolution of the sequence of stiffnesses	97
5.3.4.	Evolution of the sequence of compactnesses	97
5.3.5.	Evolution of quasi-toroidal models of constant central rest-mass density	105
5.3.6.	The location of the instability in the corotation band	111
5.3.7.	Evolution of a model with a slow growth of the $m = 1$ instability	113
5.3.8.	Evolution of a sequence of models with different compactness starting from the boundary between the regions “I” and “(I)”	113
5.4.	Summary	114
6.	Spherically symmetric dynamical black holes modeled with high-order summation-by- parts techniques	117
6.1.	Numerical setup	118
6.1.1.	Cauchy–perturbative matching	118
6.1.2.	Numerical code	118
6.2.	Results	120
6.2.1.	Schwarzschild black hole in Painlevé–Gullstrand coordinates	120
6.2.2.	Gauge wave on a Schwarzschild background	123
6.2.3.	Accretion of a scalar field pulse	123
6.2.4.	Robust stability test with gauge noise	125
6.2.5.	Cauchy–perturbative matching: robust stability test with scalar field noise	127
6.2.6.	Cauchy–perturbative matching: Accretion of a “gravitational wave” and long- term evolution	131
6.3.	Summary	137
7.	Summary	139
	Bibliography	141

Abstract

Black hole formation from non-axisymmetric instabilities in quasi-toroidal stars

The stability of general relativistic, quasi-toroidal equilibrium polytropes with respect to non-axisymmetric perturbations is studied with non-linear numerical simulations. It is found that in many cases a fragmentation of the polytrope occurs, the number of fragments being determined by the discrete symmetry of the perturbation function. A systematic study of this feature is performed with the objective to relate the fragmentation process to gravitational collapse and black hole formation. In one case, adaptive mesh refinement techniques are applied to connect the “collapse of the lapse” in a representative example to the formation of an apparent horizon centered on a fragment, and, together with the parameter space study, a preliminary identification of certain limit surfaces in parameter space signalling the onset of unstable modes and black hole formation from fragmentation is performed. Finally, some evidence for motion of the corotation point of the $m = 1$ mode towards the pole is found, which supports recent arguments by Watts et al. on the development of spiral arm and low- $T/|W|$ instabilities in differentially rotating polytropes.

Furthermore, the performance of finite-difference and dissipation operators with the summation-by-parts property is tested in the context of spherically symmetric black hole evolutions with excision, multiple coordinate patches, constraint-preserving boundary conditions and a first order symmetric hyperbolic formulation of the Einstein-Klein-Gordon system. It is found that the discrete system, which should be considered a test case for efforts to evolve black hole spacetimes in three spatial dimensions with multiple coordinate patches and Cauchy-perturbative matching, is stable in equilibrium and dynamical settings, including the inflow of strong scalar field pulses through the outer boundary. A particular example, a black hole accreting a spherically symmetric scalar pulse, is demonstrated to be stable for a coordinate time of 1,000,000 M.

Erzeugung Schwarzer Löcher durch nicht-axialsymmetrische Instabilitäten in quasi-toroidalen Sternen

Die Stabilität allgemein-relativistischer, quasi-toroidaler Gleichgewichts-Polytropen gegen nicht-axialsymmetrische Störungen wird mit nichtlinearen numerischen Simulationen untersucht. In vielen Fällen wird eine Fragmentation der Polytrope gefunden, wobei die Anzahl der Fragmente durch die diskrete Symmetrie der Störungsfunktion bestimmt ist. Eine systematische Studie dieses Prozesses wird mit dem Ziel durchgeführt, den Fragmentationsprozess mit der Produktion Schwarzer Löcher in Verbindung zu setzen. In einem Fall werden "adaptive mesh refinement"-Techniken eingesetzt, um den Kollaps der Lapse-Funktion mit der Ausbildung eines "apparent horizon" an dem Fragment zu verbinden, und, zusammen mit der Parameterraumstudie, eine vorläufige Identifikation gewisser Grenzflächen im Parameterraum mit dem Auftreten instabiler Moden und der Formation Schwarzer Löcher aufzustellen. Schliesslich werden einige Hinweise für die Bewegung des Kororationspunktes der $m = 1$ -Mode in Richtung des Pols gefunden, was Argumente, die kürzlich von Watts et al. zu dem Auftreten von Spiralarminstabilitäten und solchen, die mit niedrigem $T/|W|$ verbunden sind, unterstützt.

Weiterhin wird die Leistungsfähigkeit von diskreten Differential- und Dissipationsoperatoren mit der sog. "summation by parts"-Eigenschaft im Kontext der Evolution von sphärisch symmetrischen Schwarzen Löchern mit "excision", mehreren Karten, Randbedingungen mit der "constrain preservation"-Eigenschaft, und einer symmetrisch hyperbolischen Formulierung erster Ordnung des Einstein-Klein-Gordon-Systems getestet. Es stellt sich heraus, dass das diskrete System, welches als Testfall für Versuche, Schwarzlöcherzeiten in drei Raumdimensionen mit mehreren Karten und "Cauchy-perturbative matching" zu entwickeln, angesehen werden kann, stabil in Gleichgewichts- und dynamischen Situationen ist, einschliesslich dem Einfluss von starken Skalarfeldpulsen über den äusseren Rand. In einem speziellen Beispiel, in dem ein Schwarzes Loch einen sphärisch symmetrischen Skalarfeldpuls akkretiert, wird demonstriert, dass das System über eine Koordinatenzeit von 1.000.000 M stabil entwickelt wird.

1. Foreword

What happens when a black hole forms? Under which conditions is black hole formation possible? And: How can we model black holes with discrete techniques? Since the development of the general theory of relativity and Schwarzschild's first non-trivial exact solution, black holes have evolved from a curious mathematical artefact of the field equations to an object of considerable astrophysical significance, not only because their existence has been shown to be no limitation to the predictive power of the theory (at least from the point of view of an observer exterior to the event horizon), but also, and specifically, after Chandrasekhar's monumental discovery that stars can achieve evolutionary states in which a collapse is unavoidable, and thus has connected the field of stellar astrophysics to the study of general relativity.

Since then, the investigation of black hole properties has initiated a number of rapid developments in the different fields of general relativity and astrophysics associated with them. On the side of gravitational physics, some of these are: global properties of black hole space-times, horizons and their dynamics, the hoop and cosmic censorship conjectures, the "no hair" uniqueness theorems, connections between black holes and thermodynamics, critical collapse, the structure of singularities, the stability of black holes and their Cauchy horizons, and their treatment with discrete techniques. On the side of astrophysics, black holes have appeared in models to explain violent phenomena like active galactic nuclei and their associated jet outflows, microquasars and X-ray binaries, collapsars, and gamma-ray bursts. One of the most important developments in general relativistic astrophysics, however, is clearly the advent of *gravitational wave astronomy*, which opens a new window of observation to processes involving relativistic sources, of which, again, black holes of all kinds are a prominent example due to their extreme compactness. While there are a number of dynamical scenarios associated with black holes, the most promising gravitational wave sources would likely include *binary black hole mergers* and *black hole formation*. And although it is usually expected that these processes are unrelated, we will here collect evidence that they might indeed be connected in some cases.

Effectively starting with the study of spherically symmetric gravitational collapse by Oppenheimer and Snyder in 1939, and incorrectly rejected by Einstein in the very same year, the study of the properties of black hole formation processes has spawned a large variety of publications illuminating issues ranging from the mathematical consistency of the theory to observational signatures. One limitation, however, is shared by many works on this subject: the assumption of approximate spherical symmetry or axisymmetry. This is to be explained not only by the fact that both analytical and numerical models increase significantly in complexity when relaxing this assumption, but also by stability considerations for equilibrium system and the implications of the no-hair theorems. During the formation process however, the system is not in an equilibrium state, and it is in precisely these phases where a breaking of approximate symmetry can occur.

The agent to induce such large deviations from symmetry are non-axisymmetric unstable modes, and indeed, black hole formation is closely connected to the investigation of stellar stability, as the phase of dynamical collapse is usually preceded by an evolution on secular timescales. If we think of the secular state to be approximated by an equilibrium system of similar structure, the question which systems might form black holes directly connects to the theory of the stability of relativistic stars. It is from this point of reference where we will conduct a study of fragmentation processes in toroidal stars, which will, as compared to the canonical axisymmetric collapse scenario, lead us to a new channel of black hole production.

Given that black holes and their production are such a rich area of phenomenology, it is rather unfortunate that they have also proven to bring forth a number of technical difficulties in their mathematical treatment. This is already true for the analysis of the continuum system and perturbations thereof: the very notion of a black hole as a physical system has brought about, or is accompanied by, an increased understanding of the geometrical properties of Einstein's field equations. However, it has been even more elusive to model black holes with discrete methods. Numerical simulations have been plagued by instabilities and generally quite undesirable behaviour, and only recently methods introduced by the application of theorems from discrete analysis, combined with considerations of the hyperbolic nature of the field equations and their non-constrained extended system as an initial value problem, have brought about the development of highly accurate, stable techniques to investigate black holes. We will try to give partial answers to the third question posed above by considering the performance of these methods in black hole evolutions.

The history of the black hole phenomenon should teach us one important lesson about the scientific endeavour: A single thing can offer a multitude of facets not previously expected by any limited mind (and whose is not?), but a collective effort involving different paths of approach, while seemingly chaotic and uncoordinated at times, may bring forth more than any individual could achieve. But: if prejudice and narrow-mindedness are dominating our minds at any time, such communal achievement of significance could be made unnecessarily arduous. Therefore, the study of black holes is not one of either astrophysics or rather general relativity, not an issue of observation versus mathematics, and not a decision between fundamental generality and detailed particularity. It is all of this.

Burkhard Zink, Garching bei München, March 2006

2. Preface

This thesis is concerned with two related problems: Firstly, the formation of black holes from non-axisymmetric instabilities, and secondly, the numerical representation of black holes with techniques from discrete analysis.

The first problem is discussed in Chapter 5, where we will be concerned with the development of non-axisymmetric instabilities in quasi-toroidal polytropes, that is, stars whose stratification satisfies a fixed two-parametric relation $P = K\rho^\Gamma$ between pressure P and rest-mass density ρ , and which additionally have at least one isodensity surface with toroidal shape. To investigate this system, the Cactus computational toolkit [1] has been applied with several modules (not developed by the author) to construct differentially rotating, quasi-toroidal stars, and evolve them in general relativity. Details of the physical setup and the numerical tools can be found in Chapters 3 and 5. We will find that many of the quasi-toroidal polytropes are unstable to low-order non-axisymmetric perturbations, even, in contrast to classical stability considerations from idealized homogeneous models [2], those models with low ratios of rotational kinetic over gravitational binding energy $T/|W|$, and that these instabilities subsequently evolve into fragments, one or several, depending on the discrete symmetry of the perturbation function, and the degree of instability of the initial polytrope. Cases with one, two or three fragments have been found, and, given a sufficient compactness of the initial model, a collapse of the fragments can proceed, apparently without bound. In a specific case of one fragment, an *apparent horizon*, which may be considered a local definition of a black hole surface in replacement of the unknown location of the globally defined event horizon [3], is identified.

The results from a parameter space study of quasi-toroidal polytropes and the development of their instabilities together enable us to identify the approximate location of several surfaces of interest in this space, namely those separating systems exhibiting fragmentation with a certain number of azimuthal nodes (and thus fragments) from those which collapse by axisymmetric modes, and those forming black holes from others which do not.

All these studies are performed in three-dimensional general relativity, use high-resolution shock-capturing techniques, and mesh refinement for the computational grids. Still, with the present impressive range of tools, it has proven impossible to evolve the physical system much *beyond* the formation of a black hole.

The issues with obtaining discrete models of black hole spacetimes are well-known in the field. They are connected to the non-linear nature of the continuum system, and the fact that black holes contain singularities. While the introduction of *excision*, that is, the placement of a spherical boundary of the computational domain inside the black hole to avoid singular boundaries [4], has been able to stabilize the discrete evolution of black holes in certain cases, the question how to *generically* treat these systems must still be considered open. Many problems can be attributed to possibly ill-posed initial-boundary-value problems [5], while others, and specifically those related to discretization errors and extraction of gravitational waves from the computational domain, could be improved upon by more accurate methods.

Two approaches are being pursued nowadays: the application of pseudo-spectral methods [6], and finite-difference and dissipation operators with the so-called *summation-by-parts* property [7], a discrete version of integration by parts, which, given a well-posed initial-boundary-value problem, satisfy linear stability requirements and admit the use of quasi-spherical grids with multiple coordinate patches. The resulting improvements in stability and accuracy directly relate to the astrophysical question of gravitational wave signatures from black hole spacetimes, since only a stable evolution beyond black hole formation allows

the gravitational waves to propagate far enough from the source to extract the signal by projection of the dynamical metric onto some static background geometry (typically Schwarzschild) [8]. While in a very compact source like neutron star collapse, a short extension of the simulation time can be sufficient to extract the signals, the more demanding collapse of, say, supermassive stars (radiation-pressure dominated stars with masses beyond $10^4 M_\odot$), requires advanced techniques.

During a collaboration with the Center for Computation and Technology and the Horace Hearne Jr. Institute for Theoretical Physics, both at Louisiana State University in Baton Rouge, the author has started to work on methods based on recent theorems from discrete analysis. These methods, which are all obtained from notions of “energy” (squared norms) in systems of partial differential equations, can be used to construct well-posed initial-boundary-value problems for numerical relativity [9], and to define constraints for the construction of discrete representations of these well-posed systems by enforcing *stability* properties, to find bounds on the discrete energy associated with a certain metric. One of these properties is called *summation by parts*, and, combined with a technique for interface boundaries called *penalization*, the discrete operators satisfying these properties admit highly accurate and stable (in the linear sense) representations of the continuum system, even when the domain is covered by several coordinate patches [10]. This is also crucial for the evolution of general-relativistic stars, since the coordinate lines can be adapted to Killing fields (generators of spacetime symmetries), and the treatment of excision and outer boundaries is then much more natural.

In Chapter 6, an application of all these techniques, and an additional one, *constraint-preserving boundary conditions*, is applied to the case of the spherically symmetric Einstein-Klein-Gordon system, which can be considered a test case for a three-dimensional case with an interface between a full non-linear interior and a perturbative outer computational domain (*Cauchy-perturbative matching*). Multiple coordinate patches, penalties and the same summation-by-parts derivative and dissipation operators as in the three-dimensional case are applied to evolve Schwarzschild black holes in a certain coordinate system, *Painlevé-Gullstrand coordinates*, which cover the event horizon smoothly, and black holes with inflow of scalar and gauge pulses through the outer boundary. The resulting system is remarkably stable, even when high-order operators are used.

Some additional notes on the organization of the thesis: Since the results in Chapters 5 and 6 are concerned with different questions, each of them contains a separate introduction to the physical and technical issues connected with them. Also, the numerical code used in Chapter 6 is not the Cactus code, but has been implemented to large parts, up to the summation-by-parts operators, by the author.

The thesis is structured as follows: Chapter 3 covers some relevant equations and tools, Chapter 4 contains results from code tests with the Cactus/Carpet/Whisky code, Chapter 5 deals with fragmentation and black hole formation in differentially rotating, quasi-toroidal, general relativistic polytropes, and Chapter 6 presents results from the application of SBP operators, penalty techniques, symmetric hyperbolic systems, and constraint-preserving boundary conditions to spherically symmetric, accreting black holes.

3. Theory and Tools

In this chapter the physical evolution systems, Einstein-Klein-Gordon and Einstein-Euler, in several formulations as used in the numerical codes, are introduced in Section 3.2. The basic notions of well-posedness, stability, the summation-by-parts property and the penalty methods are introduced in Section 3.3. Finally, the set of tools used in Chapter 5 is introduced in Section 3.4.

3.1. Notations and conventions

We use the standard notations introduced e.g. in [11]. Greek tensor indices denote spacetime components and run from 0 to 3, while Latin indices run from 1 to 3 and denote components on a spacelike hypersurface. The signature of the spacetime metric is $(-, +, +, +)$, as conventional in numerical relativity. Tensors are written in bold face, e.g. \mathbf{G} for the Einstein tensor, while the normal face letter associated with a tensor, and without component indices, denotes the determinant or trace of the tensor, depending on the context.

A system of units is fixed by setting $G = c = 1$. In addition, in situations where polytropes are used as initial data, the constant K in the polytropic pressure-density relation $P = K\rho^\Gamma$ is set to unity. The resulting system can then be rescaled to SI or cgs units by insertion of appropriate factors of unity [11], and, in the case of stellar evolution, by setting a length scale through the mass of the star or black hole.

3.2. The physical system

The physical model system we will attempt to describe here is a spacetime coupled to either a perfect fluid, for the investigations of stellar stability and black hole formation in Chapters 4 and 5, or a Klein-Gordon field, for studies of the stability and accuracy properties of summation-by-parts operators in dynamical black hole spacetimes in Chapter 6.

In general relativity, the content of the field equations can be quickly summarized in covariant form by [11]

$$\mathbf{G} = 8\pi\mathbf{T} \tag{3.1}$$

$$\nabla \cdot \mathbf{T} = 0, \tag{3.2}$$

where \mathbf{G} is the Einstein tensor, \mathbf{T} the energy-momentum tensor, and ∇ the covariant derivative. For hydrodynamics, the vector $\mathbf{J} = \rho\mathbf{u}$ built from the rest-frame mass density ρ and the fluid four-velocity \mathbf{u} is conserved as well:

$$\nabla \cdot \mathbf{J} = 0 \tag{3.3}$$

These equations are not directly solvable, even when expressing them in terms of tensor components with respect to a certain coordinate chart. For any physical situation, we are interested in finding solutions to an *initial-boundary value problem*, i.e. given initial and boundary data, we are looking for the time development of the model. A common way to recast the equations of general relativity into such an evolutionary form is by performing a *3+1 split*, that is, by selecting a time function which foliates the

spacetime manifold into spacelike 3-surfaces, introducing coordinates on these surfaces, and expressing Einstein's field equations by projection onto the tetrad obtained from the time function and the triads [11, 12]. The *Arnowitt-Deser-Misner formalism* [13] is such a split, and introduces canonical variables g_{ij} and π_{ij} , which now represent the local geometrical properties of the manifold at each point. g_{ij} are components of the induced 3-metric on the hypersurface, while π_{ij} is closely related to the second fundamental form, also *extrinsic curvature*, K_{ij} of the embedding of the hypersurfaces into the spacetime, which measures the convergence and divergence of the surface normals over the time sequence.

In fact, it is nowadays customary to express the ADM system in terms of g_{ij} and K_{ij} [14]:

$$\partial_t g_{ij} = -2\alpha K_{ij} + \mathcal{L}_\beta g_{ij} \quad (3.4)$$

$$\partial_t K_{ij} = \alpha(R_{ij} - 2K_{ik}K^k_j + KK_{ij}) - D_i D_j \alpha + \mathcal{L}_\beta K_{ij} - 8\pi\alpha(S_{ij} - \frac{1}{2}g_{ij}(S - \tilde{\rho})) \quad (3.5)$$

Here, \mathbf{D} is the 3-covariant derivative, \mathcal{L} the 3-Lie derivative, \mathbf{R} is the 3-Ricci tensor, α and β are the lapse function and the shift 3-vector, which comprise the four gauge fields in the system, and $\tilde{\rho}$ and \mathbf{S} are source tensors built from the energy-momentum tensor by the surface normal vector \mathbf{n} and the tangential projection tensor $\mathbf{h} = \mathbf{n} \otimes \mathbf{n} + \mathbf{g}$:

$$\tilde{\rho} \equiv n^\mu n^\nu T_{\mu\nu} \quad (3.6)$$

$$S_{ij} \equiv h_i^\mu h_j^\nu T_{\mu\nu} \quad (3.7)$$

$$T \equiv g^{\mu\nu} T_{\mu\nu} \quad (3.8)$$

The line element can then be written in the form

$$ds^2 = -\alpha^2 dt^2 + g_{ij}(dx^i + \beta^i dt)(dx^j + \beta^j dt). \quad (3.9)$$

In addition, the initial data (and each subsequent 3-surface) is subject to the Hamiltonian and momentum constraint equations

$$H \equiv R + K^2 + K_{ij}K^{ij} - 16\pi\tilde{\rho} = 0 \quad (3.10)$$

$$P^i \equiv D_j(K^{ij} - g^{ij}K) - 8\pi S^i = 0, \quad (3.11)$$

where S^i is again built from \mathbf{T} by projection ($S_i = -n^\mu h_i^\nu T_{\mu\nu}$).

3.2.1. The NOK-BSSN form of the initial-value problem

While the ADM equations can be implemented in a straightforward manner into a numerical system, e.g. by replacing the spatial first and second derivatives by polynomial approximants and using a standard ODE integrator on the semi-discrete problem, it has been demonstrated that a reformulation of the system can improve discrete stability significantly [15]. One such system is the NOK-BSSN scheme [16, 17, 15], in which the 3-metric and extrinsic curvature are conformally split to yield new variables:

$$\phi \equiv \frac{1}{12} \ln(\det g_{ij}) \quad (3.12)$$

$$\tilde{g}_{ij} \equiv e^{-4\phi} g_{ij} \quad (3.13)$$

$$A_{ij} \equiv K_{ij} - \frac{1}{3} g_{ij} K \quad (3.14)$$

$$\tilde{A}_{ij} \equiv e^{-4\phi} A_{ij} \quad (3.15)$$

In addition, a set of *conformal connection coefficients* is introduced by contracting the Christoffel symbols $\tilde{\Gamma}^i_{jk}$ from the metric connection of the conformal metric \tilde{g}_{ij} :

$$\tilde{\Gamma}^i \equiv \tilde{g}^{jk} \tilde{\Gamma}^i_{jk} \quad (3.16)$$

which results in the following evolution equations for the variables ϕ , K , \tilde{g}_{ij} , \tilde{A}_{ij} and $\tilde{\Gamma}^i$:

$$\partial_t \phi = -\frac{1}{6} \alpha K + \mathcal{L}_\beta \phi \quad (3.17)$$

$$\partial_t K = -g^{ij} D_j D_i \alpha + \alpha (\tilde{A}_{ij} \tilde{A}^{ij} + \frac{1}{3} K^2) + \frac{1}{2} \alpha (\tilde{\rho} + S) + \mathcal{L}_\beta K \quad (3.18)$$

$$\partial_t \tilde{g}_{ij} = -2\alpha \tilde{A}_{ij} + \mathcal{L}_\beta \tilde{g}_{ij} \quad (3.19)$$

$$\begin{aligned} \partial_t \tilde{A}_{ij} = & e^{-4\phi} [-(D_i D_j \alpha)^{TF} + \alpha (R_{ij}^{TF} - S_{ij}^{TF})] \\ & + \alpha (K \tilde{A}_{ij} - 2\tilde{A}_{il} \tilde{A}^l_j) + \mathcal{L}_\beta \tilde{A}_{ij} \end{aligned} \quad (3.20)$$

$$\begin{aligned} \partial_t \tilde{\Gamma}^i = & -2\tilde{A}^{ij} \partial_j \alpha + 2\alpha (\tilde{\Gamma}^i_{jk} \tilde{A}^{kj} - \frac{2}{3} \tilde{g}^{ij} \partial_j K - \tilde{g}^{ij} S_j + 6\tilde{A}^{ij} \partial_j \phi) \\ & + \partial_j (\beta^l \partial_l \tilde{g}^{ij} - 2\tilde{g}^{m(j} \partial_m \beta^{i)}) + \frac{2}{3} \tilde{g}^{ij} \partial_l \beta^l \end{aligned} \quad (3.21)$$

Here the symbol TF stands for the trace-free part of 3-tensors, i.e. $A_{ij}^{TF} \equiv A_{ij} - \frac{1}{3} g_{ij} A$.

3.2.2. The Einstein-Christoffel form of the initial-value problem

In addition to the NOK-BSSN form, which is first order in time and second order in space, a number of entirely first order formulations have been obtained in the past, specifically to enable a direct analysis of the level of hyperbolicity of the system of PDEs (cf. Section 3.3). One of these first order systems is the *Einstein-Christoffel* form [18], which is symmetric hyperbolic and admits only physical propagation speeds of evolutionary and constraint variables, and is therefore especially interesting in the context of *excision*, a method to evolve the exterior spacetime of a black hole by placing a physical outflow boundary on or interior to the event horizon [19, 20, 4], thus avoiding physical singularities on the grid. A convenient property is that the Einstein-Christoffel (EC) system also admits the full set of Bona-Massó slicings [21].

The system consists of the 3-metric g_{ij} , the extrinsic curvature K_{ij} , and the quantities f_{kij} , which are built from the 3-Christoffel symbols Γ^i_{jk} via symmetrization and anti-symmetrization¹ by

$$f_{kij} \equiv \Gamma_{(ij)k} + g_{ki} g^{lm} \Gamma_{[lj]m} + g_{kj} g^{lm} \Gamma_{[li]m}. \quad (3.22)$$

Using the conventions in [6], we now write the lapse function as N , and define a *densitized lapse* α by

$$\alpha \equiv \frac{N}{\sqrt{g}}. \quad (3.23)$$

¹The symmetric part of a tensor is defined by $A_{(ij)} \equiv \frac{1}{2}(A_{ij} + A_{ji})$, and its antisymmetric part correspondingly by $A_{[ij]} \equiv \frac{1}{2}(A_{ij} - A_{ji})$

The EC evolution system then reads [6]:

$$\partial_t g_{ij} = -2NK_{ij} + \mathcal{L}_\beta g_{ij} \quad (3.24)$$

$$\begin{aligned} \partial_t K_{ij} = & -Ng^{kl}\partial_l f_{kij} + N\{g^{kl}(K_{kl}K_{ij} - 2K_{ki}K_{lj}) + g^{kl}g^{mn}(4f_{kmi}f_{lnj} + 4f_{km[n}f_{l]ij} - f_{ikm}f_{jlm}) \\ & + 8f_{(ij)k}f_{[ln]m} + 4f_{km(i}f_{j)ln} - 8f_{kli}f_{mnj} + 20f_{kl(i}f_{j)mn} - 13f_{ikj}f_{jmn}) \\ & - \partial_i \partial_j \ln \alpha - (\partial_i \ln \alpha)(\partial_j \ln \alpha) + 2g_{ij}g^{kl}g^{mn}(f_{kmn}\partial_l \ln \alpha - f_{kml}\partial_n \ln \alpha) \\ & + g^{kl}[(2f_{(ij)k} - f_{kij})\partial_l \ln \alpha + 4f_{kl(i}\partial_{j)} \ln \alpha \\ & - 3(f_{ikl}\partial_j \ln \alpha + f_{jkl}\partial_i \ln \alpha)]\} + \mathcal{L}_\beta K_{ij} - 8\pi NS_{ij} + 4\pi N g_{ij} T \end{aligned} \quad (3.25)$$

$$\begin{aligned} \partial_t f_{kij} = & -N\partial_k K_{ij} + N\{g^{mn}[4K_{k(i}f_{j)mn} - 4f_{mn(i}K_{j)k} + K_{ij}(2f_{mnk} - 3f_{kmn})] \\ & + 2g^{mn}g^{pq}[K_{mp}(g_{k(i}f_{j)qn} - 2f_{qn(i}g_{j)k}) + g_{k(i}K_{j)m}(8f_{npq} - 6f_{pqn}) \\ & + K_{mn}(4f_{pq(i}g_{j)k} - 5g_{k(i}f_{j)pq})] - K_{ij}\partial_k \ln \alpha \\ & + 2g^{mn}(K_{m(i}g_{j)k}\partial_n \ln \alpha - K_{mn}g_{k(i}\partial_{j)} \ln \alpha)\} \\ & + \mathcal{L}_\beta f_{kij} + 16\pi N g_{k(i}S_{j)}. \end{aligned} \quad (3.26)$$

If we restrict consideration to spherically symmetric spacetimes, and define polar coordinates (t, r, θ, ϕ) and the additional variables

$$g_T \equiv \frac{g_{\theta\theta}}{r^2} \quad (3.27)$$

$$K_T \equiv \frac{K_{\theta\theta}}{r^2} \quad (3.28)$$

$$f_{rT} \equiv \frac{f_{r\theta\theta}}{r^2} \quad (3.29)$$

$$\tilde{\alpha} \equiv \alpha r^2 \sin \theta, \quad (3.30)$$

the evolution system eqns. (3.24-3.26) simplifies significantly [6], and the resulting dynamical spacetime variables are $g_{rr}, g_T, K_{rr}, K_T, f_{rrr}$, and f_{rT} :

$$\partial_t g_{rr} = -2NK_{rr} + 2g_{rr}\partial_r \beta^r + \beta^r \partial_r g_{rr} \quad (3.31)$$

$$\partial_t g_T = -2NK_T + 2\frac{\beta^r}{r}g_T + \beta^r \partial_r g_T \quad (3.32)$$

$$\begin{aligned} \partial_t K_{rr} = & \beta^r \partial_r K_{rr} - \frac{N}{g_{rr}}\partial_r f_{rrr} + N\left[2f^r{}_{rr}(f^r{}_{rr} + \frac{1}{r} - \frac{4f_{rT}}{g_T}) - \frac{6}{r^2} + K_{rr}\left(2\frac{K_T}{g_T} - K^r{}_{rr}\right) \right. \\ & \left. - 6\left(\frac{f_{rT}}{g_T}\right)^2 - \partial_r^2 \ln \tilde{\alpha} - (\partial_r \ln \tilde{\alpha})^2 + \left(\frac{4}{r} - f^r{}_{rr}\right)\partial_r \ln \tilde{\alpha}\right] + 2K_{rr}\partial_r \beta^r \\ & + 4\pi N(Tg_{rr} - 2S_{rr}) \end{aligned} \quad (3.33)$$

$$\partial_t K_T = \beta^r \partial_r K_T - \frac{N}{g_{rr}}\partial_r f_{rT} + N\left(K_T K^r{}_{rr} + \frac{1}{r^2} - \frac{2f_{rT}^2}{g_{rr}g_T} - \frac{f_{rT}}{g_{rr}}\partial_r \ln \tilde{\alpha}\right) + 2\frac{\beta^r}{r}K_T \quad (3.34)$$

$$\begin{aligned} \partial_t f_{rrr} = & \beta^r \partial_r f_{rrr} - N\partial_r K_{rr} + N\left[4g_{rr}\frac{K_T}{g_T}\left(3\frac{f_{rT}}{g_T} - f^r{}_{rr} + \frac{2}{r} - \partial_r \ln \tilde{\alpha}\right) \right. \\ & \left. - K_{rr}\left(10\frac{f_{rT}}{g_T} + f^r{}_{rr} - \frac{2}{r} + \partial_r \ln \tilde{\alpha}\right)\right] + 3f_{rrr}\partial_r \beta^r + g_{rr}\partial_r^2 \beta^r \\ & + 16\pi NS_r g_{rr} \end{aligned} \quad (3.35)$$

$$\partial_t f_{rT} = \beta^r \partial_r f_{rT} - N\partial_r K_T + N\left[K_T\left(2\frac{f_{rT}}{g_T} - f^r{}_{rr} - \partial_r \ln \tilde{\alpha}\right)\right] + \left(\partial_r \beta^r + \frac{2\beta^r}{r}\right)f_{rT}. \quad (3.36)$$

A characteristic decomposition² of the principal part of eqns. (3.31-3.36) can be obtained by introducing the variables $u_1 \dots u_6$ as defined in [22]:

$$u_1 = g_{rr} \quad (3.37)$$

$$u_2 = g_T \quad (3.38)$$

$$u_3 = K_{rr} - \frac{f_{rrr}}{\sqrt{g_{rr}}} \quad (3.39)$$

$$u_4 = K_T - \frac{f_{rT}}{\sqrt{g_{rr}}} \quad (3.40)$$

$$u_5 = K_{rr} + \frac{f_{rrr}}{\sqrt{g_{rr}}} \quad (3.41)$$

$$u_6 = K_T + \frac{f_{rT}}{\sqrt{g_{rr}}} \quad (3.42)$$

Additional variables are required when matter sources are part of the system. The variables $u_1 \dots u_6$ are associated with speeds β for u_1 and u_2 (*surface modes*), $\beta + \tilde{\alpha}g_T$ for u_3 and u_4 , and $\beta - \tilde{\alpha}g_T$ for u_5 and u_6 (*light-cone modes*), making the physical nature of the characteristics explicit. Note that the subsidiary system of constraint propagation equations, discussed in Section 3.2.5, can be decomposed into surface and light-cone modes, too.

3.2.3. The massless Klein-Gordon field

One of the two sources of interest here is the minimally coupled generalization of the massless, real Klein-Gordon field:

$$\nabla^2 \Psi = 0 \quad (3.43)$$

This field equation is associated with the energy-momentum tensor [6]

$$T_{\mu\nu} = \frac{1}{4\pi} [(\partial_\mu \Psi)(\partial_\nu \Psi) - \frac{1}{2}g_{\mu\nu}(\partial_\kappa \Psi)(\partial^\kappa \Psi)] \quad (3.44)$$

and can be reduced to first-order form via introduction of the variables

$$\Pi \equiv \frac{\partial_t \Psi - \mathcal{L}_\beta \Psi}{N} \quad (3.45)$$

$$\Phi_i \equiv \partial_i \Psi, \quad (3.46)$$

where N denotes the lapse function. With these variables, the matter sources and additional dynamical equations of the first order system read [6]

$$4\pi\rho = \frac{1}{2}(\Pi^2 + \Phi^i \Phi_i) \quad (3.47)$$

$$4\pi S_i = \Pi \Phi_i \quad (3.48)$$

$$4\pi T = \Pi^2 - \Phi^i \Phi_i \quad (3.49)$$

$$4\pi S_{ij} = \Phi_i \Phi_j + \frac{1}{2}g_{ij}(\Pi^2 - \Phi^k \Phi_k) \quad (3.50)$$

$$\partial_t \Pi = Ng^{ij}[-\partial_i \Phi_j + \Pi K_{ij} - \Phi_i \partial_j \ln \tilde{\alpha} + 4\Phi^k f_{[ki]j}] + \mathcal{L}_\beta \Pi \quad (3.51)$$

$$\partial_t \Phi_i = -N[\partial_i \Pi + \Pi \partial_i \ln \tilde{\alpha} + \Pi g^{jk}(3f_{ijk} - 2f_{kij})] + \mathcal{L}_\beta \Phi_i \quad (3.52)$$

²The set of first-order linear equations $\partial_t u = A \partial_x u$, where u is a vector-valued function and A is a matrix, admits a *characteristic decomposition* into a set of uncoupled advection equations $\partial_t v_i = \lambda_i v_i$ with $v_i \in \mathbb{R}$ and $\lambda_i \in \mathbb{R}$, provided that A is diagonalizable. Each of the v_i is called a *characteristic mode*, and it is advected with the *characteristic speed* λ_i independently of the remaining modes. If the boundary of a computational domain is under consideration, the set of modes can be divided into incoming ($\lambda_i > 0$ on the right boundary, $\lambda_i < 0$ on the left boundary), outgoing (vice versa), and boundary modes ($\lambda_i = 0$).

Again, restriction to spherical symmetry greatly simplifies the equations. When introducing the variable $\Phi \equiv \Phi_r$ in spherical polar coordinates, the evolution equations are [6, 22]:

$$\partial_t \Pi = \beta^r \partial_r \Pi + N \left[-\frac{1}{g_{rr}} \partial_r \Phi + \Pi \left(\frac{K_{rr}}{g_{rr}} + \frac{2K_T}{g_T} \right) - \frac{\Phi}{g_{rr}} \left(\frac{4f_{rT}}{g_T} - \frac{2}{r} + \partial_r \ln \tilde{\alpha} \right) \right] \quad (3.53)$$

$$\partial_t \Phi = \beta^r \partial_r \Phi - N \left[\partial_r \Pi + \Pi \left(\frac{f_{rrr}}{g_{rr}} - \frac{f_{rT}}{g_T} - \frac{2}{r} + \partial_r \ln \tilde{\alpha} \right) \right] + \Phi \partial_r \beta^r \quad (3.54)$$

In the same manner as for the EC system, characteristic variables can be introduced by [22]

$$u_7 = \Pi + \frac{\Phi}{\sqrt{g_{rr}}} \quad (3.55)$$

$$u_8 = \Pi - \frac{\Phi}{\sqrt{g_{rr}}} \quad (3.56)$$

with speeds $\beta - \tilde{\alpha} g_T$ and $\beta + \tilde{\alpha} g_T$, which are again light-cone modes, as expected.

3.2.4. The perfect fluid

A special relativistic perfect fluid, that is, a fluid without any heat transport or shear stresses, has the energy-momentum tensor [11]

$$\mathbf{T} = \rho h \mathbf{u} \otimes \mathbf{u} + P \mathbf{g}, \quad (3.57)$$

where ρ is the density given in a *rest frame* (an orthonormal tetrad where ∂_t is parallel to the four-velocity \mathbf{u}), P the isotropic pressure, \mathbf{g} the flat spacetime metric, and, given the specific internal energy ϵ , $h = 1 + \epsilon + P/\rho$ denotes the specific enthalpy. Its generalization to general relativity is straightforward.

To solve the initial-value problem, a 3+1 split is performed. It is convenient in numerical relativity to define an *Eulerian observer*, that is, an observer normal to the spacelike 3-surfaces, by introduction of the tetrad (\mathbf{n}, ∂_i) and projection of the conservation laws $\nabla \cdot \mathbf{J} = 0$ and $\nabla \cdot \mathbf{T} = 0$ onto this tetrad.

The resulting system of equations can then be brought into *flux-conservative form*: A differential system with this property admits to be cast into the form

$$\partial_t w + \partial_i f^i(w) = s(w), \quad (3.58)$$

where the state vector w is associated with *fluxes* f^i and *sources* s . This form makes it explicit that a change in the state can only occur through inflow and outflow over a differential cell boundary, or through external forces embodied in the terms s .

For general relativistic hydrodynamics, a typical choice of conservative variables, which are the components of the state vector w , is [23]³:

$$D \equiv \sqrt{g} W \rho \quad (3.59)$$

$$S_j \equiv \sqrt{g} \rho h W^2 v_j \quad (3.60)$$

$$\tau \equiv \sqrt{g} (\rho h W^2 - P) - D \quad (3.61)$$

Here, g is the determinant of the 3-metric, $W = (1 - g_{ij} v^i v^j)^{-1/2}$ is the Lorentz factor, and the velocity components v^i are defined by [23]

$$v_i = \frac{\mathbf{u} \cdot \partial_i}{-\mathbf{u} \cdot \mathbf{n}}. \quad (3.62)$$

³This is the set of variables used in the Whisky code, which slightly differ from the variables in [23].

With the set of variables defined by eqns. (3.59-3.61), one obtains the fluxes and sources [23]

$$f^i = \alpha \begin{pmatrix} D(v^i - \beta^i/\alpha) \\ S_j(v^i - \beta^i/\alpha) + \delta_j^i \sqrt{g} P \\ \tau(v^i - \beta^i/\alpha) + \sqrt{g} P v^i \end{pmatrix} \quad (3.63)$$

$$s = \alpha \sqrt{g} \begin{pmatrix} 0 \\ T^{\mu\nu} g_{\nu\sigma} \Gamma_{\mu j}^\sigma \\ T^{\mu 0} \partial_\mu \alpha - \alpha T^{\mu\nu} \Gamma_{\mu\nu}^0 \end{pmatrix}. \quad (3.64)$$

The system of equations needs to be closed by defining an *equation of state* $P(\rho, \epsilon)$. Throughout this thesis, we will use the ideal fluid *gamma law* $P = (\Gamma - 1)\rho\epsilon$, which neglects chemical (and nuclear) reactions and surface effects in the perfect fluid. In specific cases, the *polytropic constraint* $P = K\rho^\Gamma$ is imposed in addition to this, which yields the structure equations of homentropic stars if used on the initial data, and of isentropic flows if used during evolution.

A serious complication arises when representing the system of equations (3.58) by finite differences or spectral methods: this is due to the fact that the continuum perfect fluid model might develop shocks after a finite time interval, even from smooth initial data [24]. Therefore, one must either extend the model to avoid the crossing of characteristics, or one extends the solutions space to include *weak solutions*, i.e. those which are consistent with an integral representation of the differential system subject to some set of trial functions. It is clear that physically the first option is preferable, since the limitation in predictive power from smooth initial data is a failure of our model. Indeed, the classical generalization of the Euler equation in Newtonian gravity to include viscosity, the Navier-Stokes equation, extends the principal part by second derivatives and transforms the Euler system, which is hyperbolic, into a mixed hyperbolic-parabolic type, and avoids discontinuous solutions from smooth data by dissipating high-frequency modes. However, the generalization of the Navier-Stokes equation to general relativity is anything but obvious, since we expect any physical transport to be limited by the speed of light. Secondly, and more importantly, fluids with low viscosity, commonly encountered in astrophysical problems, can exhibit very steep gradients, which, to a typical discrete representation, indeed appear like a discontinuity. These phenomena, *shocks* and *contact discontinuities*, are actually better represented when looking for weak solutions to the Euler equations.

However, standard polynomial or spectral approximations are not sufficient to represent the partial derivative terms in the equations if discontinuities are present, which is why *high-resolution shock capturing techniques* are used: for a review of these methods in special or general relativistic hydrodynamics, see [25, 26]. In short, the integral system is split into cells, and the values of the conservative variables are represented by their cell averages. Then, the fluxes on the cell boundary are determined, direction-wise, by considering the local *Riemann problem*, a solution to the idealized shock tube problem, where a fluid in two different states, separated by a boundary layer, is observed after the layer is suddenly removed. This Riemann problem is of an algebraic nature, in form of the *Rankine-Hugoniot conditions*, since the conservation laws represent the conservation of mass, momentum and energy across each wave (shocks, contact discontinuities, and rarefaction waves, cf. [25]), and can be solved either directly or by iterative techniques. To improve the accuracy of the evolution in smooth parts of the solution, high-order extrapolation techniques, e.g. *PPM* or *ENO*, are often used to determine the initial data for the local Riemann problem.

3.2.5. Excision and constraint-preserving boundary conditions

The initial-boundary-value problem for general relativistic evolutions is often formulated as a *free evolution* problem. This refers to the fact that the Hamiltonian and momentum constraints are only considered

when constructing initial data, but not when setting boundary data. In addition, free evolution schemes often do not actively use the constraints to solve for a part of the state vector on each time step. In these cases, the values of the constraints can be used as rough indicators of the solution error.

If one decides to not only enforce the constraint equations on the initial data surface, but also on the spatial domain boundaries, one requires a specific subclass of free boundary data, namely *constraint-preserving boundary conditions*. We will only discuss this class in the case of the spherically symmetric Einstein-Christoffel-Klein-Gordon system described above; for more general cases, see [27].

In the following exposition, we will follow [22]. Assume that the inner and outer boundary of a spherically symmetric domain are given by the shells $r = r_{inner}$ and $r = r_{outer}$. If we model Schwarzschild black holes with horizon-penetrating coordinate systems⁴, e.g. the Eddington-Finkelstein [11] or Painlevé-Gullstrand [28, 29, 30] coordinates, the inner boundary can be positioned inside the event horizon, where the Killing field⁵ ∂_t is spacelike. Then, since the outgoing shell $r = r_{inner}$ is also spacelike in consequence, we need to impose no boundary data on the inner boundary provided we describe the boundary in terms of its normal characteristic decomposition. This kind of boundary is called an *excision boundary* [19, 20].

If the outer boundary is external to the event horizon, it is clearly timelike, and we need to impose boundary data on the incoming modes, or on their time derivatives. However, this data is also subject to the requirement that the inflow of Hamiltonian and momentum constraint modes is zero. In fact, there are additional constraints in the Einstein-Christoffel system due to the first order reduction [18], such that, in spherical symmetry, the constraints read [6]

$$C = \frac{\partial_r f_{rT}}{g_{rr}g_T} - \frac{1}{2r^2g_T} + \frac{f_{rT}}{g_{rr}g_T} \left(\frac{2}{r} + \frac{7f_{rT}}{2g_T} - f^r{}_{rr} \right) - \frac{K_T}{g_T} \left(K^r{}_r + \frac{K_T}{2g_T} \right) + 4\pi\tilde{\rho} \quad (3.65)$$

$$C_r = \frac{\partial_r K_T}{g_T} + \frac{2K_T}{rg_T} - \frac{f_{rT}}{g_T} \left(K^r{}_r + \frac{K_T}{g_T} \right) + 4\pi S_r \quad (3.66)$$

$$C_{rrr} = \partial_r g_{rr} + \frac{8g_{rr}f_{rT}}{g_T} - 2f_{rrr} \quad (3.67)$$

$$C_{rT} = \partial_r g_T + \frac{2g_T}{r} - 2f_{rT}, \quad (3.68)$$

where C is the Hamiltonian constraint, C_r the radial momentum constraint, and C_{rrr} and C_{rT} are additional constraints from the definition of the first-order system. By use of the evolution equations for the g_{rr} , g_T , K_{rT} , and f_{rT} , eqns. (3.31-3.36), the constraints can be written as a subsidiary evolution system, which admits a decomposition into the characteristic variables [22]

$$C_1 = C + \frac{C_r}{\sqrt{g_{rr}}} \quad (3.69)$$

$$C_2 = C - \frac{C_r}{\sqrt{g_{rr}}} \quad (3.70)$$

$$C_3 = C_{rrr} \quad (3.71)$$

$$C_4 = C_{rT}, \quad (3.72)$$

where the modes C_1 and C_2 are light-cone modes with speeds $\beta \pm \tilde{\alpha}g_T$, and the modes C_3 and C_4 are surface modes with speed β .

⁴A coordinate system of a black hole spacetime is *horizon-penetrating* if it covers the event horizon in a smooth manner.

⁵A *Killing vector field* \mathbf{k} satisfies $\mathcal{L}_{\mathbf{k}}\mathbf{g} = 0$, i.e. it is compatible with a spacetime symmetry.

From this decomposition it follows that, in a black hole setting, we have three incoming subsidiary constraint modes C_2 , C_3 and C_4 on the outer boundary, which is generated by the Killing field ∂_t . For the boundary data data, represented by the four incoming modes u_1 , u_2 , u_3 , and u_4 (eqns.3.31-3.36), to be on the constraint hypersurface, we therefore require $C_2(u_1, \dots, u_4) = C_3(u_1, \dots, u_4) = C_4(u_1, \dots, u_4) = 0$. which leaves us with one freely specifiable incoming mode. This is easy to see from a physical point of view as well: since spherically symmetric vacuum spacetimes are static exterior to an event horizon, we are only left with the gauge freedom of the equation: therefore, the remaining free incoming mode is called a *gauge mode*. We note that in the spherically symmetric Einstein-Klein-Gordon system, the scalar field has an additional incoming *physical mode*, in our notation u_8 .

3.3. Well-posedness, hyperbolicity, and the summation-by-parts property

3.3.1. Well-posedness

This short exposition is based on the textbook by Gustafsson, Kreiss, and Olinger [31]. See also [24].

The concept of well-posedness is necessary to determine the limits of predictability in a certain physical model, and it is crucial in constructing stable numerical algorithms. Given a system of PDEs, the basic idea is to require that solutions must be unique and depend continuously on the data. This appears a reasonable constraint on physical models based on classical field equations, and it is an important property if we expect discretizations of the problem to have diminishing distance (in some sense) to the exact solution.

The definition of well-posedness, which we will only discuss for the simplest case of a one-dimensional periodic linear problem, involves a norm on the solution space, which might be the L_2 norm or something more sophisticated involving additional weight functions. Also, the solution and data considered here will be assumed to be C^∞ , but this requirement can be relaxed as well. Keeping this in mind, well-posed systems have these properties:

Definition. Consider a system of partial differential equations on the compact interval $I \subset \mathbb{R}$ given by

$$\begin{aligned} \partial_t u &= P(x, t, \partial_x)u \\ u(x, t_0) &= f(x) \end{aligned} \tag{3.73}$$

where P denotes the principal symbol, t_0 is the initial time, and f the initial data. This problem is called *well-posed* if, for every t_0 and every $f \in C^\infty(x)$:

1. There exists a unique solution $u(x, t) \in C^\infty(x, t)$, which is 2π -periodic in every space dimension and
2. there are constants α and K , independent of f and t_0 , such that

$$\|u(\cdot, t)\| \leq K e^{\alpha(t-t_0)} \|f(\cdot)\|. \tag{3.74}$$

Thus, a well-posed problem admits only solutions which are bounded by exponential growth, and which are determined uniquely by the data. Note that the use of the exponential function is arbitrary, and another function class could be used as well. However, the exponential function is necessary to exclude simple low-order terms of the form $\partial_t u = u$ from consideration in proofs of well-posedness.

3.3.2. Hyperbolicity

A hyperbolic system of PDEs is, roughly speaking, one in which only real speeds of propagation exist. Therefore, hyperbolic PDEs admit the formulation of *initial-boundary-value problems* (IBVPs) by setting data at some time t_0 and determining the future development of the data, as is often required in physics.

It is convenient to define different classes of hyperbolicity in the first order form of a system of PDEs. For the simplest case of a linear, constant coefficient problem, the classes are defined by:

Definition. Consider the linear system of partial differential equations given by

$$\begin{aligned}\partial_t u &= A \partial_x u \\ u(x, 0) &= f(x)\end{aligned}\tag{3.75}$$

where $u \in \mathbb{R}^n$ and $A \in \mathbb{R}^n \times \mathbb{R}^n$. The system is called

- weakly hyperbolic, if all eigenvalues of A are real,
- strongly hyperbolic, if it is weakly hyperbolic, and if there exists a complete system of eigenvectors,
- strictly hyperbolic, if it is strongly hyperbolic, and if all eigenvalues are distinct, and finally
- symmetric hyperbolic, if it is strongly hyperbolic, and if A is Hermitian.

Note that sometimes the term *symmetrizable hyperbolic* is used to refer to systems where symmetric hyperbolicity can be achieved by a change of base, using an appropriate *symmetrizer* H , i.e. such that HA is Hermitian. In such a case, and also when $H = 1$, the quantity $E = \langle u, Hu \rangle$ built from some scalar product $\langle \cdot, \cdot \rangle$ is called the *energy* of the solution.

The most important property of strongly hyperbolic systems is its relation to well-posedness:

Theorem. The initial value problem for the system (3.75) is well-posed if, and only if, the system is strongly hyperbolic.

Thus, we can reduce the analytical problem of determining well-posedness to the much simpler algebraical problem of performing an eigendecomposition on the principal part. This also holds if we add a low-order term $B \in \mathbb{R}^n$ to the PDEs in the form $\partial_t u = A \partial_x u + B$.

For non-constant coefficient and multi-dimensional system, the requirement “strongly hyperbolic” needs to be restricted to “symmetric hyperbolic”. The Einstein-Christoffel-Klein-Gordon system applied in this thesis has this property [18], and thus admits a well-posed continuum problem.

Finally, note that, while non-linear systems clearly cannot satisfy such a theorem, they at least do so on some finite time interval. This is to be expected, since not even the existence of solutions can be guaranteed for all times in many problems.

3.3.3. Strict stability

In a discrete approximation, there is no direct representation of the well-posedness property in the continuum problem. However, another property of *discrete* systems can be formulated which ensures a bounded solution in a similar manner as for the continuum problem, and, in addition, guarantees that a series of such discrete solutions will converge to the solution of the well-posed problem for diminishing grid spacing.

First, consider the discrete representation of the system (3.75)

$$\begin{aligned}\mathbf{v}^{n+1} &= Q(t_n) \mathbf{v}^n \\ \mathbf{v}^0 &= \mathbf{f}.\end{aligned}\tag{3.76}$$

We can write the solution \mathbf{v}^{n+1} using the *solution operator* $S_h(t, t_0)$ as $\mathbf{v}^{n+1} = S_h(t_n, 0)\mathbf{f}$, where h denotes the grid spacing. Next, we need a *discrete norm*, which can quite generally be constructed from a bilinear form by

$$\|v\|_h^2 = \langle v, v \rangle_h \equiv h \sum_{i,j=1}^N \sigma_{ij} v^i v^j, \quad (3.77)$$

where N is the number of grid points. The form σ is called the *discrete metric*, and different forms of this metric may be used depending on the problem. For the construction of the SBP operators used in Chapter 6, diagonal and non-diagonal metrics were used.

With these notions, the *strict stability* property of a discrete representation of well-posed systems is defined by:

Definition. Assume that the solution operator $S(t, t_0)$ of the continuum problem satisfies the estimate

$$\|S(t, t_0)\| \leq K e^{\alpha(t-t_0)}. \quad (3.78)$$

We call the difference approximation strictly stable for $0 < h \leq h_0$, if there exist K_S and α_S such that

$$\begin{aligned} \|S_h(t, t_0)\|_h &\leq K_S e^{\alpha_S(t-t_0)}, \\ \alpha_S &\leq \alpha + O(h). \end{aligned} \quad (3.79)$$

That is, for each discrete solution, there is an exponential bound in the same way as for the continuum system, up to $O(h)$.

3.3.4. The summation-by-parts property

Given an interval $I \subset \mathbb{R}$, real-valued differentiable functions $u, v : I \rightarrow \mathbb{R}$, and the scalar product

$$\langle u, v \rangle \equiv \int_I u v dx \quad (3.80)$$

we have the well-known *integration-by-parts* property of the differential operator ∂_x :

$$\langle u, \partial_x v \rangle + \langle v, \partial_x u \rangle = [uv]_{\partial I} \quad (3.81)$$

To illustrate why this is important in the context of well-posedness, consider the symmetric hyperbolic advection equation on the interval $[0, 1]$

$$\begin{aligned} \partial_t u &= \partial_x u \\ u(0, \cdot) &= f \\ u(t, x=1) &= u(t, x=0) \end{aligned} \quad (3.82)$$

with arbitrary smooth initial data. Since the symmetrizer is trivial, we have the energy $E = \langle u, u \rangle = u^2$, and can calculate its time derivative:

$$\begin{aligned} \partial_t E &= \partial_t \langle u, u \rangle \\ &= 2 \langle u, \partial_t u \rangle \\ &= 2 \langle u, \partial_x u \rangle \\ &= 2[u^2]_0^1 \\ &= 0 \end{aligned} \quad (3.83)$$

In the second last step, we have made use of the integration-by-parts property of ∂_x , and in the last one we have used the periodicity of the solution. Since the time derivative of the squared norm is zero, the periodic advection equation is *energy-conserving*.

Consider, next, a semi-discrete representation of (3.82) on the grid $x_i \in I, i = \{1, \dots, N\}$ with corresponding values $u^i(t)$:

$$\begin{aligned}\partial_t u &= Du \\ u(0, \cdot) &= f \\ u_N(t) &= u_1(t).\end{aligned}\tag{3.84}$$

Here, $D \in \mathbb{R}^N \times \mathbb{R}^N$ is a discrete representation of the differential operators ∂_x . The discrete version of the energy, given some metric σ and the grid spacing h , is defined as

$$E_h = \langle u, u \rangle_h = h \sum_{i,j=1}^N \sigma_{ij} u^i u^j.\tag{3.85}$$

This energy will *not* be conserved even for this simple problem, since the proof (3.83) has no discrete equivalent for the integration-by-parts property. However, if the operator D is additionally constrained by the requirement

$$\langle u, Dv \rangle_h + \langle v, Du \rangle_h = [uv]_0^1,\tag{3.86}$$

the proof can be directly transferred to the discrete system, and thus it is energy-conserving as the continuum one. Such a discrete operator D is said to have the *summation-by-parts* (SBP) property.

Operators of this kind can be constructed by first assuming a certain metric σ , and then solving the algebraic system (3.86). The most simple types of metrics are diagonal, and SBP operators constructed from these metrics have, on the boundary (where they are one-sided by definition!) half the order of accuracy as in the interior. Therefore, an operator which is, say, 8th order accurate in the interior would only be 4th order accurate at the boundary points, and it is then denoted by D_{8-4} . The global order of convergence is then 4th order. In the same manner, certain non-diagonal metrics admit construction of SBP operators which have only one order less accuracy on the boundary, say e.g. D_{6-5} . Finally, it should be noted that operators of higher orders are highly non-unique, and sophisticated optimization algorithms are required to find operators with suitable properties.

3.3.5. The penalty method

If a solution is covered by several separate domains with common boundaries, e.g. in the multi-patch approach, its discrete representation needs a *stable* prescription for setting boundary condition at inter-patch boundaries. The simple advection example, again, demonstrates how this is achieved [10].

W.l.o.g. we assume the computational domain to be \mathbb{R} , and divide it into the two semi-bounded intervals $(-\infty, 0]$ and $[0, \infty)$. We slightly generalize the advection equation to $\partial_t u = \Lambda \partial_x u$, and denote the solutions on the left and right domains by u^l and u^r , respectively. To ensure that the boundary data from incoming modes is set correctly, we add to the semi-discrete system two *penalty terms* (we assume the inter-patch boundary point $x = 0$ to have the same index zero on both discrete patch representations):

$$\begin{aligned}\partial_t u_i^l &= \Lambda D^l u_i^l + \frac{\delta_{i,0} S^l}{h^l \sigma_{00}^l} (u_0^r - u_0^l) \\ \partial_t u_i^r &= \Lambda D^r u_i^r + \frac{\delta_{i,0} S^r}{h^r \sigma_{00}^r} (u_0^l - u_0^r)\end{aligned}\tag{3.87}$$

The numbers S^l and S^r are parameters, which can now be constrained by the requirement that the entire system satisfies a certain inequality for the total energy $E \equiv E^l + E^r$. This leads to certain inequalities for S^l and S^r [10], which also involve the characteristic speed Λ , if one requires the penalty boundary to be symmetric and either energy-conserving or dissipative (i.e. $\partial_t E \leq 0$), and the amount of dissipation can then be controlled by one free parameter.

3.4. Cactus, Carpet and Whisky

The Cactus Computational Toolkit [1] is a computational infrastructure originally developed by members of the Albert Einstein Institute in Golm, Germany, of Washington University in St. Louis, Missouri, and of the National Center for Supercomputing Applications at the University of Illinois at Urbana-Champaign, for simulations of the merger of black hole binaries. The infrastructure itself, however, is based on general concepts of code interoperability, scheduling and common interfaces, and can thus, in principle, be used for a diverse range of applications in scientific computing.

The basic components of Cactus are a central set of services called the *flesh*, providing interoperability, basic communication and profiling, and a number of user-provided modules, here named *thorns*. Thorns need to adhere to a set of interface standards imposed by the flesh, and the interfaces themselves are realized as text files in each thorns' home directory.

A set of thorns of specific significance, denoted by the term *driver*, is responsible for providing services like discrete grid structures, memory allocation, parallelization, input/output, hyperslab extraction and interpolation. The internal administration of grid variables is thus a function provided by the driver, and application thorns only need to take care of set-local operations. The currently implemented drivers for finite differencing and finite volume applications are PUGH (unigrid), Carpet (domain-based adaptive mesh refinement, multi-patch) [32] and recently also TAKA (block-structured adaptive mesh refinement, based on SAMRAI) [33].

The flesh and driver together, in turn, provide an additional abstraction service called *scheduling*. Each thorn consists of a set of functions which are read into a database of scheduling relations. A Perl-based parser in the flesh produces an effective calling sequence of all thorn functions, and the driver then calls the functions appropriately.

All services described so far are not restricted to a specific physical system, and in fact, the intention is to provide with Cactus a generic set of interfaces for *all* types of scientific computing applications. However, the applications realized so far are mostly in the field of numerical relativity, and as such a number of well-tested user thorns exist for this field. The most important one is an implementation of the BSSN system for binary black hole mergers in the thorns ADM_BSSN and BSSN_MoL, the latter being an adaptation of ADM_BSSN to the method of lines. A number of support thorns provide important functionality, like modules for finding apparent and event horizons (see below), modules for calculating the constraints and setting physical boundary conditions, extracting gravitational waves and so on.

The Whisky code [34] is an implementation of general relativistic hydrodynamics for the Cactus infrastructure, and was planned and developed in the context of the EU network program on *Sources of Gravitational Waves* mostly by Luca Baiotti, Ian Hawke, Pedro Montero and Luciano Rezzolla. Whisky uses high-resolution shock-capturing methods to handle the development and propagation of shocks accurately. In addition, Nikolaos Stergioulas has implemented an interface for his initial data solver for rotating neutron stars (SF, here also called RNS) into Whisky. Together with an interface between Whisky and BSSN_MoL it is then possible to evolve the full system of general relativistic hydrodynamics, and investigate e.g. the collapse of rotating neutron stars, including horizon dynamics and gravitational wave emission.

Recent efforts to improve the numerical stability of single and binary black hole evolutions have led to

the development of an infrastructure to implement a *multi-patch* or *multi-block* grid setup. This includes an appropriate driver, here Carpet, and a number of additional thorns which represent the SBP derivative and dissipation operators, the penalty boundary conditions and the characteristic structure associated with the hyperbolic evolution system.⁶

In this chapter, we will shortly describe the functionality provided by each of these components.

3.4.1. The Cactus Computational Toolkit

Cactus has been developed and maintained by a large number of people: the Cactus code server [1] has an incomplete list of contributors. As a core system for scientific applications, Cactus is intended as a community effort, not exclusively for numerical relativity, but in practice still mainly so.

From the perspective of a user of this toolkit, which will be our preferred one here, Cactus and some driver provide a computational grid, together with parallelization and input/output of data. The user then, in turn, provides a number of modules which specify the grid variables, initial data, evolution system, physical boundary conditions and runtime data analysis functionality. Each such thorn module has an interface to the core system, realized in text files written in the Cactus configuration language, or CCL. The file *interface.ccl* specifies variable declarations needed by the thorn, and function interfaces between different thorns. The file *schedule.ccl* attaches to functions a scheduling relationship, which is evaluated later in the flesh to generate global relationships between the code's functions. Finally, the file *param.ccl* declares parameters to steer the thorn's functionality during runtime by the parameter text file, or even by other thorns or web interfaces.

Thorns may be written in C, C++, Fortran 77 and Fortran 90, and the actual configuration of thorns used in practical application is indeed a mixture of the different programming languages. Cactus has a standard interface for passing data and aliasing functions between the source files in different programming languages.

3.4.2. The PUGH driver

The first, and at the time the author started his PhD work only, available driver for Cactus was PUGH, a *unigrid*⁷ driver written entirely in C by Gabrielle Allen, Tom Goodale, Thomas Radke, Matei Ripeanu and Paul Walker. PUGH provides a single, three-dimensional grid with a simple domain-based parallelization and ghost zones⁸. The driver is, after a number of optimizations, rather efficient and has been shown to scale to over 1000 processes [35]. PUGH has been used in numerical relativity applications like single [4, 36, 37] and binary black evolutions [38], and the collapse of rotating neutron stars [39]. Today, this driver is mostly superseded by Carpet.

3.4.3. The Carpet driver

Carpet, written by Erik Schnetter and Thomas Radke, is an implementation of domain-based adaptive mesh refinement for Cactus, based on an earlier C++ library by Erik Schnetter. The total coordinate domain, which is assumed to be of rectangular shape, is represented by several levels of increasing resolution called *refinement levels*, and each such level contains a number of Cartesian grids (*patches* or

⁶There is also another multi-patch implementation for Cactus: it has been developed by Jonathan Thornburg and uses the standard BSSN_MoL thorn and its regular derivative operators. The grid patches are overlapping, and interpolation is used to obtain the ghost zone values.

⁷We will denote with the term *unigrid* a discrete grid setup based on a sampling with constant distances.

⁸*Ghost zones* are additional computational cells extending beyond the proper domain of computation to provide finite-difference operators with centered stencils with the required data. The data is either filled by synchronization with other processes (for domain-based parallelization), or by physical boundary conditions.

components) which, together, form the computational domain on the sub-levels. Consistency between the data representation on the levels is achieved by the standard techniques of prolongation and restriction [40], which are interpolation operations in time and space. Details of the implementation can be found in [41].

The driver uses *non-global time stepping*, that is, finer resolved grid components are evolved more often, subject to the same Courant factor, than coarser ones. In all application cases presented here the relative factor of resolution between refinement levels is 2, so that the refinement level $n + 1$ is evolved twice as often as the level n .

The hierarchical sequence of time evolution steps in Carpet first involves the coarsest refinement level, and then successively the finer levels, which obtain boundary conditions from the evolution of the coarser ones by prolongation. If a solution value has been set at the same coordinate location, but on different refinement levels, each coarser level's value is replaced by restriction from the finer levels. In this way the grid hierarchy is traversed down, including prolongation, and up, including restriction.

The currently available restriction operation is a simple copy operation, which proves to be sufficient in practice. Prolongation is a more delicate issue, especially when possibly non-continuous grid functions are involved, as is the case with shocks in hydrodynamics. Therefore, Carpet provides a number of high-order ENO interpolators implemented into Carpet by Ian Hawke. These operators work equally well with the spacetime variables, since they reduce to standard high-order polynomial interpolations in smooth parts of the solution⁹.

Carpet makes use of the concept of *buffer zones* to evolve hyperbolic systems. Since each point has a certain past domain of dependence, which, for numerical stability, is contained in the past Courant cone, the stencil of an evolution method will determine the size of the discrete future domain of determinacy of some time slice. For any time integrator using sub-time steps, like e.g. the Runge-Kutta class of integrators, the points outside the domain of determinacy are not filled by prolongation, but are understood as buffer zones, which are then obtained by prolongation after the whole time step is calculated. This method has been found to perform well [41]. As a consequence of this, a typical evolution stencil for general relativistic hydrodynamics with the PPM method (seven points) will need six buffer zones with a three-step time integrator. This has to be considered when determining the effective size of grid components.

Like every Cactus driver, Carpet has parallelization services. It makes use of the MPI standard, which often also provides a shared memory implementation on appropriate machines. Each refinement level is distributed via standard domain decomposition, which makes it necessary to communicate the prolongation results between processes. The performance of Carpet with a single refinement level was significantly inferior to PUGH beyond 16 processes for a long time, until a more efficient MPI communication scheme by collecting packages was implemented recently. Now Carpet scales well beyond 64 processes. However, with a mesh-refined grid, it is always preferable to make use of machines with fewer, faster processors.

From the perspective of a thorn using Carpet, all grid components appear as unigrids with ghost zones. Therefore, code written to run with PUGH will often without effort work with Carpet as well, at least as long as it performs local operations. Global code, like e.g. elliptic solvers, is more difficult to port to Carpet, and indeed there is no elliptic solver right now for Carpet, although there is one for PUGH.

Recently, Carpet has been extended to support *multi-patch grids*, i.e. grids where each refinement level is logically composed of several independent components, but their topological relationship is determined by application thorns. These extensions were done in the general efforts to achieve stable and accurate evolutions of black holes, and are only a part of the multi-patch infrastructure.

Output is available in two variants: either as explicit ASCII tables, including global reductions like norms and extrema, and data sections along the coordinate axes, or as three-dimensional binary data in

⁹The geometric quantities will typically be smooth functions of the coordinates, but inappropriate choices of gauge can introduce non-differentiability or discontinuity.

the HDF5 format. Visualization tools such as OpenDX or Amira have custom import modules for Carpet data. OpenDX also contains a module to import multi-patch output from Carpet.

3.4.4. Thorns for numerical relativity

These set of thorns include the NOK-BSSN system module BSSN_MoL, tools for finding apparent and event horizons (see below), setting gauge conditions, calculating the constraints and performing simple versions of black-hole excision. We will describe four thorns of this set which are most relevant to black hole formation.

The most important module is BSSN_MoL: the stable evolution of black holes has, over years of experience, turned out to be a challenging task, and it must still be considered an unsolved problem. However, significant advances in evolution time for single and binary black holes have been achieved by the use of the BSSN formulation and a set of specific gauge conditions [15, 37]. These are implemented in BSSN_MoL, and also a number of modifications which improve numerical stability in several situations. The module has been tested over many years in diverse applications in numerical relativity. It might be replaced at some point by the HyperGR code, which uses a first order formulation of Einstein's equations and supports the multi-patch infrastructure of Carpet, but right now all practical applications use BSSN_MoL.

When dealing with gravitational collapse, horizons are clearly the most important geometrical quantity, since they are used for defining black holes. The most important practical difference between the *event horizon* of a black hole and an *apparent horizon* is that an event horizon is a null surface only defined in the context of the global structure of space-time, while apparent horizons, which approximate event horizons after a newly formed black hole has settled down, are defined locally, by the expansion or contraction of null rays crossing the surface under consideration. Strictly speaking, the Cactus module AHFinderDirect written by Jonathan Thornburg [42], which, starting from an initial guess, evaluates the total expansion of outgoing null geodesics of surfaces, and thus defines an iterative process to obtain surfaces of vanishing outgoing expansion, can only identify *marginally trapped surfaces*, a superset of apparent horizons, but if one assumes to cover all such surfaces by this process, the outermost surface found is also an apparent horizon. This assumption is often made in practice. These surfaces can define a foliation of a *marginally trapped tube*, and depending on whether this tube is timelike, null, or spacelike, timelike membranes, isolated and dynamical horizons can be identified as well. For details on the different definitions of horizons and their relation see [3, 43].

The classical definition of black holes is by the event horizon, and since it is global, it can be obtained only after evolving a system long enough that it reaches a state near stationarity. If that is achieved, the EHFinder by Peter Diener [44] is able to use three-dimensional output from the computational domain to find approximations of event horizons, assuming that the exterior spacetime is asymptotically flat and close to Schwarzschild. The method proceeds by injecting null surfaces into the domain, starting from some guess in the future and propagating back in time. At least 30 to 50 M of near-stationary evolutions is needed to recognize an event horizon with some certainty. Given the numerical stability problems with evolving black holes, this is barely enough for neutron star collapse simulations, but not enough for binary black hole mergers, collapsars or more complicated channels of collapse like the fragmentation described in this thesis, at least with the numerical techniques currently implemented in Cactus.

Simple versions of excision are also implemented in a set of thorns [4]. A global mask can be set to define the excised region; this would typically be done by an apparent horizon finder. The evolution thorns then have to be aware of this mask, and approximate outgoing boundary conditions are set by the excision thorns, under the assumption that the boundary is indeed outflow. It turns out in practice that this approach only performs well in very controlled situations, like in the case of a single, non-rotating, stationary black hole, but tends to fail in more complicated scenarios.

3.4.5. The Whisky code

To simulate astrophysical scenarios beyond black hole dynamics, the EU network program on *Sources of Gravitational Waves* has supported a project to develop an implementation of general relativistic hydrodynamics for the Cactus infrastructure. The resulting set of Fortran 90 thorns, called the Whisky code [34], was planned and developed mostly by Luca Baiotti, Ian Hawke, Pedro Montero and Luciano Rezzolla.

Whisky is based exclusively on the finite volume model, and uses high-resolution shock-capturing techniques, specifically also the PPM and ENO reconstruction methods and the Marquina approximate Riemann solver. This allows to investigate astrophysical systems involving shocks (core collapse, jets), but it is also easily applicable if the solution is mostly smooth (neutron star collapse, supermassive star collapse, stellar oscillations). Since all methods are grid-local, Whisky directly ports to Carpet as well.

Because axisymmetric, rotating stars are a typical system under consideration, Nikolaos Stergioulas has implemented a version of his SF/RNS code in Whisky. This code [45, 46] generates models of uniformly rotating barotropes¹⁰ in general relativistic equilibrium by means of the KEH (Komatsu, Eriguchi, Hachisu) iterative scheme [47, 47], including the compactification of the radial domain suggested by Cook, Shapiro, Teukolsky [48] and some additional modifications (see [46]). The Whisky version of SF/RNS can also generate differentially rotating equilibrium polytropes.

One of the first and most significant application of Cactus/Carpet/Whisky is the simulation of the collapse of unstable rotating neutron stars to black holes, including analyzing the dynamics of dynamical and event horizons [39] and the extraction of gravitational wave signatures from this process [49]. A first set of code tests has been published in [50]. Recent efforts also aim to apply this code to core collapse, stellar oscillations, and, in this thesis, black hole formation by fragmentation.

3.4.6. Mode extraction

If a star develops non-axisymmetric instabilities, one convenient way to analyze the mode growth is by Fourier decomposition of the density function on certain coordinate radii [51]. This allows to find growth times, frequencies and pattern speeds of a mode while its development is almost linear. An implementation in Cactus has been provided by Ian Hawke, which makes use of the interpolator interface provided by Carpet to obtain the appropriate density projections, and their Fourier components, at a set of coordinate radii in the equatorial plane defined by the user.

3.4.7. Solution-adaptive mesh refinement

While Carpet has the internal capabilities to generate and move grid components on refinement levels, it is the user's task to define grid hierarchies in a manner well-suited to the solution. For a central collapse problem, like core collapse or supermassive star collapse, one option is to use *progressive* mesh refinement, where the maximum of the density is used to switch on additional refinement levels in the center.

An extension of this method to the fragmentation problem presented in Chapter 5 has been implemented by the author. Here, the location of the global maximum of the rest-mass density is obtained from Whisky by reduction operations, and the refinement steering module then instructs Carpet to center a hierarchy of components, with a number of refinement levels determined by the maximum value of density as in progressive mesh refinement, on the location of the maximum. For a fragmentation, this means that, as the fragment collapses and moves across the grid, it is tracked by an increasingly better resolved number of additional grid components.

¹⁰A *barotrope* is a star which satisfies a relation $P = P(\rho)$, where P is the pressure and ρ is the rest-mass density.

4. Code tests

Cactus, BSSN_MoL, Whisky and Carpet are a well-tested set of tools, and have been used for publication-quality results for several years now (see references in Section 3.4). In this section, a number of additional tests of the non-linear evolution of selected systems is presented to highlight certain aspects and limitations of the code’s performance.

First, results from unigrid evolutions with the PUGH driver are presented, specifically focusing on the evolutions of uniformly rotating neutron stars¹, in Section 4.1. The collapse of these stars to black holes is studied in Section 4.2, with a specific focus on the typical phenomenology (“collapse of the lapse”) and the numerical difficulties associated with the development of NaNs².

In Section 4.3, we shortly discuss the outcome of a failed experiment by the author to follow the collapse of iron cores or supermassive stars by using the gauge freedom in the shift vector on a uniform grid, at a time when Carpet was not yet available. And finally, in Section 4.4, Carpet is tested in several settings, namely a special relativistic shock tube, the evolution of a TOV solution, and the evolution of uniformly rotating neutron stars provided by SF/RNS.

4.1. Rotating neutron stars on a uniform grid

The term *unigrid* was already introduced in the description of the PUGH driver for Cactus in 3.4.2. For our purposes, it is a uniform Cartesian grid in coordinate space, and our typical choices of gauge are asymptotically flat in the naïve sense: that is, the spacetime metric reduces to $ds^2 = dt^2 + dx^2 + dy^2 + dz^2$ at spacelike infinity. This provides a good amount of flexibility for describing a large number of systems, including single and binary stars, but has also the disadvantage that the coordinate lines are hard to adapt to certain spacelike Killing vectors, if present, in the initial data. Specifically, a neutron star will be approximately spherically symmetric or axisymmetric, and a typical excision surface of a black hole is also spherical.

The *uniformity* property of the grid means fixed distances between grid points. While this clearly applies only to coordinate space, adaptivity by choice of gauge turns out to be difficult in practice. A specific example of this will be provided in 4.3, but most generally it is clear that a unigrid, by its very nature, does not support the operation of smoothly *inserting* points between existing ones, which is exactly what mesh refinement will admit. Some simple systems are not greatly troubled by this, but most are: this is specifically true in general relativistic simulations, where the outer boundary conditions are often wave-like conditions assuming a background close to Schwarzschild. A mesh refinement technique, even when not applied to the support³ of the density function, can greatly reduce computational cost by extending the location of the matching hypersurface between the computational domain and the external Schwarzschild background.

However, while grid adaptivity is essential for the three-dimensional representation of systems like core

¹We will sometimes use the terms polytropes and neutron stars interchangeably, as it is customary in numerical relativity. It should be obvious that in both cases we refer to *models*, not to an actual physical object.

²The term *NaN* or *not a number* specifies an undefined state of the finite representation of real numbers. Typically, NaNs are produced by either division by zero, or by trying to construct numbers beyond the domain of the finite representation.

³The *support* of a real function is the set closure of arguments not mapped to zero.

collapse, at least with present-day computational resources, this is not necessarily so for systems like neutron stars and black holes, where the dynamical processes have a limited range of scales. Specifically, the proper areal radius of a collapsing neutron star only reduces by a factor of ≈ 10 when it collapses to a black hole, at least from the point of view of a distant observer, so there is reasonable hope to handle this process with unigrids. There is ample use of three-dimensional unigrids in the literature, for systems like single black holes (e.g. [52] and references therein), neutron stars ([53] and references) and gravitational collapse ([39] and references).

Before one turns to black hole formation, however, one would like to gain experience with the numerical tools at hand by consideration of *stationary* systems. The most natural choice are neutron stars and black holes, since they are compact, relativistic objects. Since black holes must be treated with excision or singularity-avoiding coordinates, neutron stars are, in a numerical sense, simpler systems. Here and in all what follows, our model of a neutron star will be a polytrope. The perturbative stability of these equilibria has been investigated with linear methods in spherical symmetry and in uniform rotation [54, 55, 56], so that one has reasonable hope to use them as a numerical test-bed. If an equilibrium configuration is expected to be stable, the numerical scheme should converge to a stable solution, where each discrete representation exhibits oscillations around some equilibrium state, and possibly an additional linear drift.

In this section we will turn to the performance of Whisky in evolving stationary, rotating neutron stars. Some equivalent results were published in [39], but the author would like to take the opportunity to enlighten some aspects of this comparatively simple system which are not elaborated on in detail in that publication.

Let us first fix the parameters of the polytrope. A commonly used model for a testbed calculation is obtained from the choice $K = 100[P]/[\rho]^\Gamma$ and $\Gamma = 2$. We will not argue for its proximity to realistic neutron star models here, although the stiffness of the equation of state and resulting masses are more or less in the expected range. We will only need its stability properties: For non-rotating and uniformly rotating sequences, the graphs $M(e_0)$ relating the gravitational mass to the central energy density can be found e.g. in [39], and the graphs clearly indicate a turning point around $e_0 \approx 4 \cdot 10^{-3}$. From the turning point method [57] it follows that the non-rotating model has a neutral radial fundamental mode for dynamical stability at the turning point. Perturbative studies [58, 59, 60] indicate that the low-density branch is stable, while the high-density branch is not. For the rotating models we note that the convenient criterion provided by the Friedman-Ipser-Sorkin theorem [61] only applies to secular stability, but numerical evidence [62] indicates that the neutral point for the quasi-radial fundamental mode is not far from the turning point. Finally, the stability of *non-axisymmetric* modes is unclear, but since the equation of state is quite stiff, there is hope that some indication can be gained from properties of the Maclaurin spheroids, which are dynamically stable for any $T/|W|$ below some critical value, which is not attained below the mass-shedding sequence. Numerical evidence, again, [63, 64] shows that general relativity and inhomogeneity do not greatly affect this conclusion, and it is therefore that we expect the uniformly rotating polytropes used here to be stable.

A typical initial model constructed in this way is shown in figures 4.1 and 4.2, and the corresponding parameters and integral quantities can be found in table 4.1. This specific model is not near the mass-shedding sequence, as the quantity Ω/Ω_K , which is the ratio of angular velocity over the limit angular velocity defined by Keplerian motion on the equator, is only ≈ 0.4 . However, even this moderate amount of rotation can lead to numerical problems, as is indicated in figure 4.3. In this plot, the maximum of the density is displayed over time. While the choice of gauge is of course arbitrary, the choice $\beta^i = 0$ quickly leads to a numerical instability⁴ by a coordinate distortion phenomenon commonly called *grid stretching*,

⁴We note here that in the context of evolutions with BSSN_MoL the term *numerical instability* is used in opposition to *physical instability*, and as such also includes instabilities caused by motions from the constraint surface, or by an ill-posed continuum formulation.

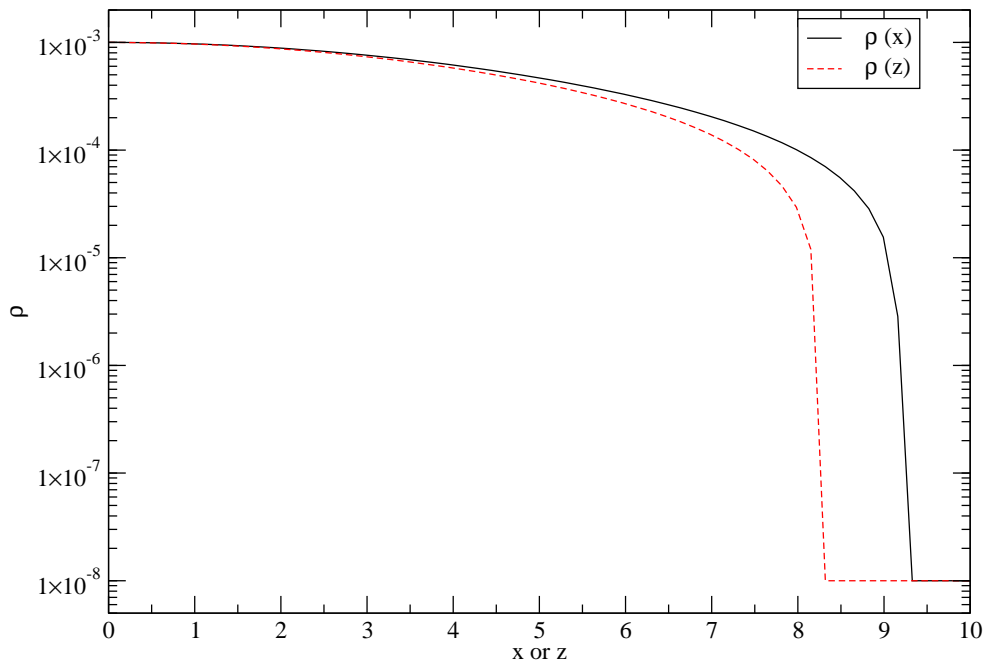


Figure 4.1.: Density profiles in x and z direction of a moderately fast rotating neutron star (see Table 4.1) constructed by the equilibrium solver RNS. In the mapping from RNS to Cactus, the z axis generally coincides with the axis of symmetry, while the x and y axes are located in the equatorial plane.

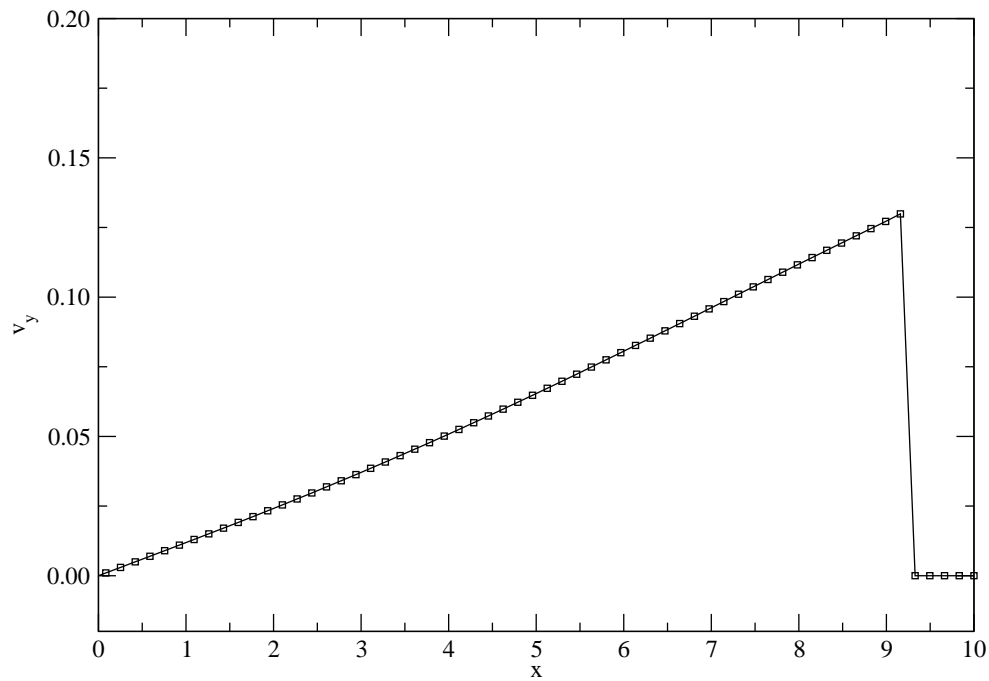


Figure 4.2.: ∂_y velocity profile in x direction of a rotating neutron star constructed by RNS.

Polytropic K	K	100
Polytropic Γ	Γ	2
Central rest-mass density	ρ_c	10^{-3}
Central rest-frame energy density	e_c	$1.100 \cdot 10^{-3}$
ADM mass	M	1.3331
Rest mass	M_0	1.4222
Equatorial proper radius	R_e	10.611
Axes ratio	r_p/r_e	0.9
Equatorial compactness	R_e/M	7.9595
Total angular momentum	J	0.58908
Normalized angular momentum	J/M^2	0.33148
Kinetic over potential energy	$T/ W $	$2.4366 \cdot 10^{-2}$
Equatorial surface angular velocity	Ω	$1.3257 \cdot 10^{-2}$
Equatorial surface Keplerian angular velocity	Ω_K	$3.3426 \cdot 10^{-2}$
Mass shedding factor	Ω/Ω_K	0.3966

Table 4.1.: Parameters and integral quantities of a stable rotating neutron star. The quantities are all measured in units of $K = 100$ and $G = c = 1$. Note that K , Γ , ρ_c and r_p/r_e are parameters, and as such exact.

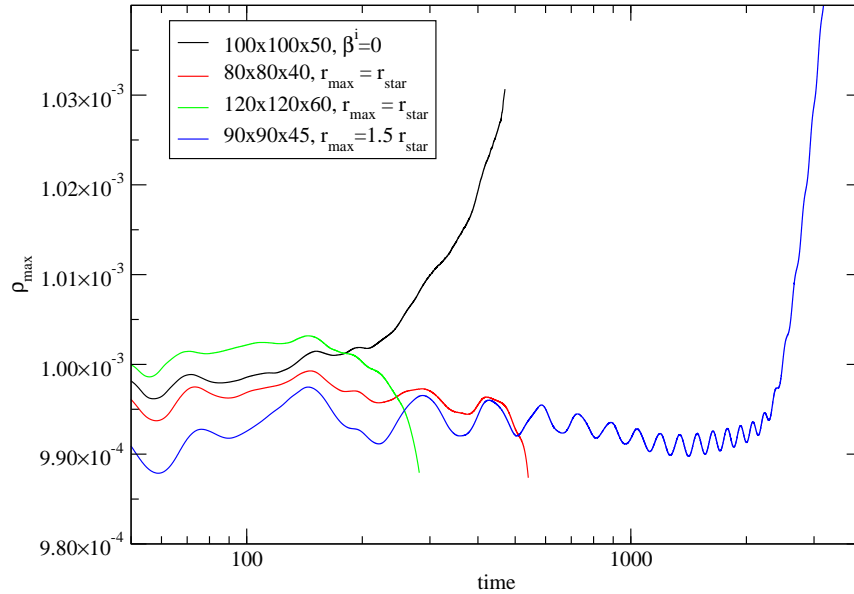


Figure 4.3.: Evolution of the maximum of the density of the rotating neutron star model defined in table 4.1 with different numerical setups. The figure caption denotes the number of grid points used, and the location of the outer boundary r_{max} with respect to the stellar surface r_{star} . The first graph uses a zero shift function, while the second and third one make use of a outer boundary close to the stellar surface. Both quickly encounter numerical instabilities, which can be partially avoided by shifting the outer boundary to about 1.5 times the stellar radius. The unit of time can be converted to seconds by a choice $M = M_\odot \approx 5\mu s$.

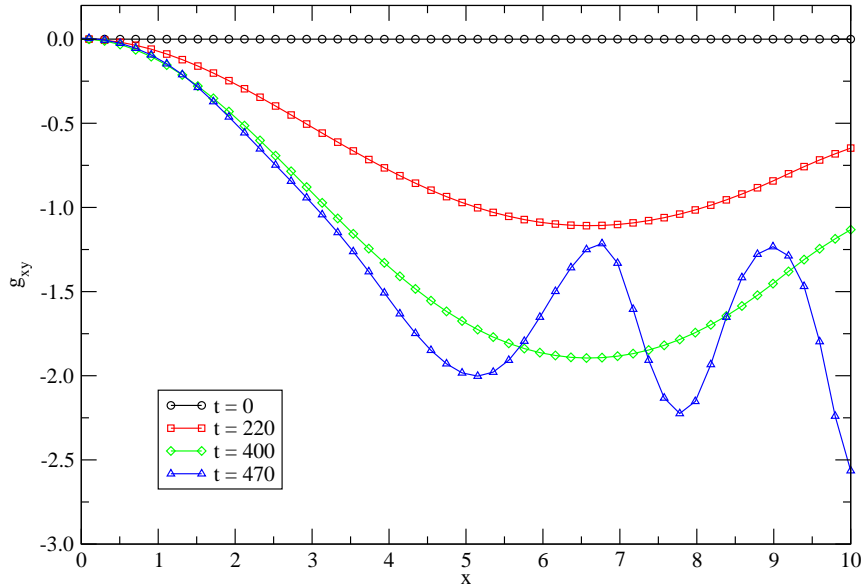


Figure 4.4.: Evolution of the 3-metric component g_{xy} along the x axis with time, for a rotating neutron star with the gauge choice $\beta^i = 0$. The dragging of inertial frames caused by the rotating, relativistic star introduces *grid stretching* and, finally, a numerical instability. Note that the outer boundary of the computational domain is slightly beyond the diagram abscissa, at $x_{outer} = 12$.

which is apparent in the temporal evolution of the metric function g_{xy} in figure 4.4. The function is initially zero as a consequence of the gauge choice in RNS, but since the gauge $\beta^i = 0$ is not adopted to the Killing field ∂_ϕ , the metric function changes over time. At late times, the interaction with the outer boundary introduces oscillations and a numerical instability. The plots in Figure 4.3 make it clear that the location of the outer grid boundary suppresses a numerical instability in the system, which is possibly introduced by the use of ill-posed boundary conditions on the surface of the computational domain.

Since $M_\odot \approx 5\mu s$ [11], the coordinate time $\approx 2000M$ relates to an asymptotic observer time of $\approx 14ms$ for a neutron star of mass $1.4 M_\odot$. It may be possible to improve on this by shifting the outer boundary and increasing resolution, but if long-term stability, as opposed to dynamical processes, is under consideration, methods involving solution-adapted grid geometries, higher accuracy, and stable discrete representations have clear advantages.

4.2. Rotating neutron star collapse on a uniform grid

A primary objective of this thesis is to study gravitational collapse and black hole formation. A comparatively simple test system for this is the collapse of an axisymmetric equilibrium polytrope in a unigrid evolution using BSSN_MoL and Whisky. This system is specifically interesting since it shows a number of typical features and problems encountered also in the more complex collapse situations discussed later. We note that a more extensive study of this system with the same set of evolutionary tools is presented in [39, 49].

To initiate collapse, an unstable stellar model needs to be set up. The Friedman-Ipser-Sorkin turning point theorem [61] states that in axisymmetric, general relativistic equilibrium polytropes, an extremum of the function $M(\lambda)$, for a sequence constrained to $J = \text{const}$ and parameterized by λ , indicates a change

		Stable model	Unstable model
Polytropic K	K	100	100
Polytropic Γ	Γ	2	2
Central rest-mass density	ρ_c	10^{-3}	$8 \cdot 10^{-3}$
Central rest-frame energy density	e_c	$1.100 \cdot 10^{-3}$	$1.440 \cdot 10^{-2}$
ADM mass	M	1.3331	1.4858
Rest mass	M_0	1.4222	1.5741
Equatorial proper radius	R_e	10.611	6.0976
Axes ratio	R_p/R_e	0.9	0.9
Equatorial compactness	R_e/M	7.9595	4.1039
Total angular momentum	J	0.58908	0.616469
Normalized angular momentum	J/M^2	0.33148	0.27924
Kinetic over potential energy	$T/ W $	$2.4366 \cdot 10^{-2}$	$1.9424 \cdot 10^{-2}$
Equatorial surface angular velocity	Ω	$1.3257 \cdot 10^{-2}$	$3.4482 \cdot 10^{-2}$
Equatorial surface Keplerian angular velocity	Ω_K	$3.3426 \cdot 10^{-2}$	$7.9344 \cdot 10^{-2}$
Mass shedding factor	Ω/Ω_K	0.3966	0.4346

Table 4.2.: Parameters and integral quantities of a rotating neutron star on the unstable branch (last column). The quantities are all measured in units of $K = 100$ and $G = c = 1$. Note that K , Γ , ρ_c and R_p/R_e are parameters, and as such exact. For comparison, the third column shows the parameters of the stable model in Table 4.1.

in secular stability.

A few qualifications are appropriate here: (a) the Friedman–Ipser–Sorkin theorem is only valid in some open interval containing the extremum λ_0 , (b) the neutral mode of dynamical stability may be different from λ_0 for rotating models, and (c) the unstable model has evolutionary channels to stable models, which is typically not the case for accretion-induced collapse. (a) and (b) are limitations of the applicability of the theorem, which will make numerical experiments necessary in practice. Results of such experiments, e.g. in [39], have shown that for uniformly rotating, stiff ($\Gamma = 2$) configurations, the turning point criterion is reasonably applicable to the stability of the fundamental p mode⁵ as well. The limitation (c) refers to the fact that the evolution of the system can proceed to another model with the same mass on the stable branch (e.g. [57]); however, in accretion-induced collapse, the star will evolve close to a stable equilibrium branch, until it obtains its maximum equilibrium mass and encounters a dynamical instability which leads inevitably to black hole formation. Since a sequence of numerical models can approach the sequence maximum arbitrarily with sufficient resolution, such a sequence of simulations would converge to the neutral model applicable to accretion-induced collapse situations.

The equilibrium quantities of the model constructed for this series of tests are displayed in table 4.2, and it has been checked that the model is on the unstable branch. There are now two distinct possibilities to perturb the model out of its continuum equilibrium limit: (i) We make use of the fact that the sequence of discrete models limiting in the continuous equilibrium fails to be in *discrete equilibrium*, or (ii) we impose a certain perturbation function to the model. Possibility (i) has the advantage that — assuming momentarily that the system is stable and well-posed — the set of discrete evolutions naturally converges

⁵The classification of oscillations of spherical stars into *f*, *p* and *g* modes has been introduced by Cowling [65]. The p modes are dominated by pressure perturbations, and their fundamental has a spherical harmonic index $\ell = 0$, i.e. it is purely radial. On a sequence of slowly rotating stars smoothly limiting in a non-rotating model, the associated modes of oscillations limiting in the p mode of the non-rotating member are then often also called p modes.

to a solution satisfying the geometric constraints. However, there are two disadvantages of (i): Firstly, since there is almost no control over the perturbation function, which has to be considered a numerical artefact, the system might as well expand to another stable equilibrium, a process sometimes called migration (e.g. [50]). Secondly, again assuming well-posedness, the system does not converge to a collapsing or migrating neutron star, but rather to a stationary star without further dynamics. Possibility (ii) has the advantage that we can control the perturbation function, but the disadvantage that the perturbation might be constraint-violating. As long as it is kept small, however, there is no significant concern related to this, since any discrete representation of free evolution will bring about a certain level of constraint violation. It is possible to project the set of perturbations to the constraint surface, or, alternatively, to reduce the perturbation amplitude with resolution. In the latter case, the limit system is again stationary, while in the former case the limit is a collapsing or migrating continuum star. In both cases, however, the induced perturbation permits control over the numerical artefact of discrete symmetry violation, and therefore the author suggests that possibility (ii) is preferable.

Here, a density perturbation function of the form

$$\rho(P) \rightarrow \rho(P) + A\rho_c \frac{\sin(\pi r(P)/r_e)}{r_e} \quad (4.1)$$

is applied, where A denotes the amplitude of the perturbation (in our case $A = 10^{-2}$), ρ_c the central density, $r(P)$ the coordinate radius of the event P and r_e the coordinate equatorial radius of the star. The perturbed initial model thus specified is evolved using different grid resolutions, with a common outer boundary location at $6M$. Since the outer boundary is close to the star due to unigrid constraints, it has to be expected that improper boundary conditions will affect the evolution to some extent.

The resolutions chosen for these tests are $\Delta x = \Delta y = \Delta z = 0.3M, 0.2M, 0.15M, 0.1M$, and $0.075M$. No grid symmetry is assumed. Excision has not been applied in these early set of tests. As a choice of gauge, the initial values of lapse and shift are given by RNS, while subsequently the shift is kept fixed and the lapse function is given by the “1+log” approximation to maximal slicing [66]. The time evolution of the central density and lapse is shown in Figure 4.5, and it is clear from these plots that the star evolves to high central density and vanishing central lapse. The simulations all terminate around $t \approx 50$ with the appearance of NaNs, which is first and foremost a resolution issue (more details below). From these graphs it is found that, while a very low resolution of $0.3M$ yields qualitatively correct results, reasonable relative accuracy of better than 10% is only achieved for $\Delta x < 0.15M$.

The *collapse of the lapse* is associated with regions of high curvature; this observation comes from the well-known property of maximal slices, i.e. those spacelike hypersurface with vanishing trace of the extrinsic curvature, that singular spacelike boundaries of the spacetime manifold are approached asymptotically. While this is no proof that a black hole has formed, it is indeed a good indicator, unless we expect the spacetime to obtain non-singular regions of extreme curvature not covered by an event horizon. There is, however, another tool available: The singularity theorem by Penrose [3] states that a spacetime cannot be null geodesically complete if (i) the null projection of the Ricci tensor is positive semi-definite, (ii) there exists a non-compact Cauchy surface⁶ and (iii) there exists a closed trapped surface. Condition (i) is true for hydrodynamics with positive pressure, and condition (iii) can be tested by an “apparent horizon” finder, which actually solves for surfaces of vanishing momentary outgoing null expansion, i.e. marginally trapped surfaces. Condition (ii) is more involved since the initial spacelike slice containing the star, while certainly non-compact, may or may not be Cauchy. Starting from smooth initial data covering a spacelike hypersurface containing the entire star up to spacelike infinity, the spacetime may develop a

⁶A *Cauchy surface* is a spacelike hypersurface from which, given appropriate data, the entire spacetime can be constructed. A spacetime which admits a Cauchy surface is *globally hyperbolic*.

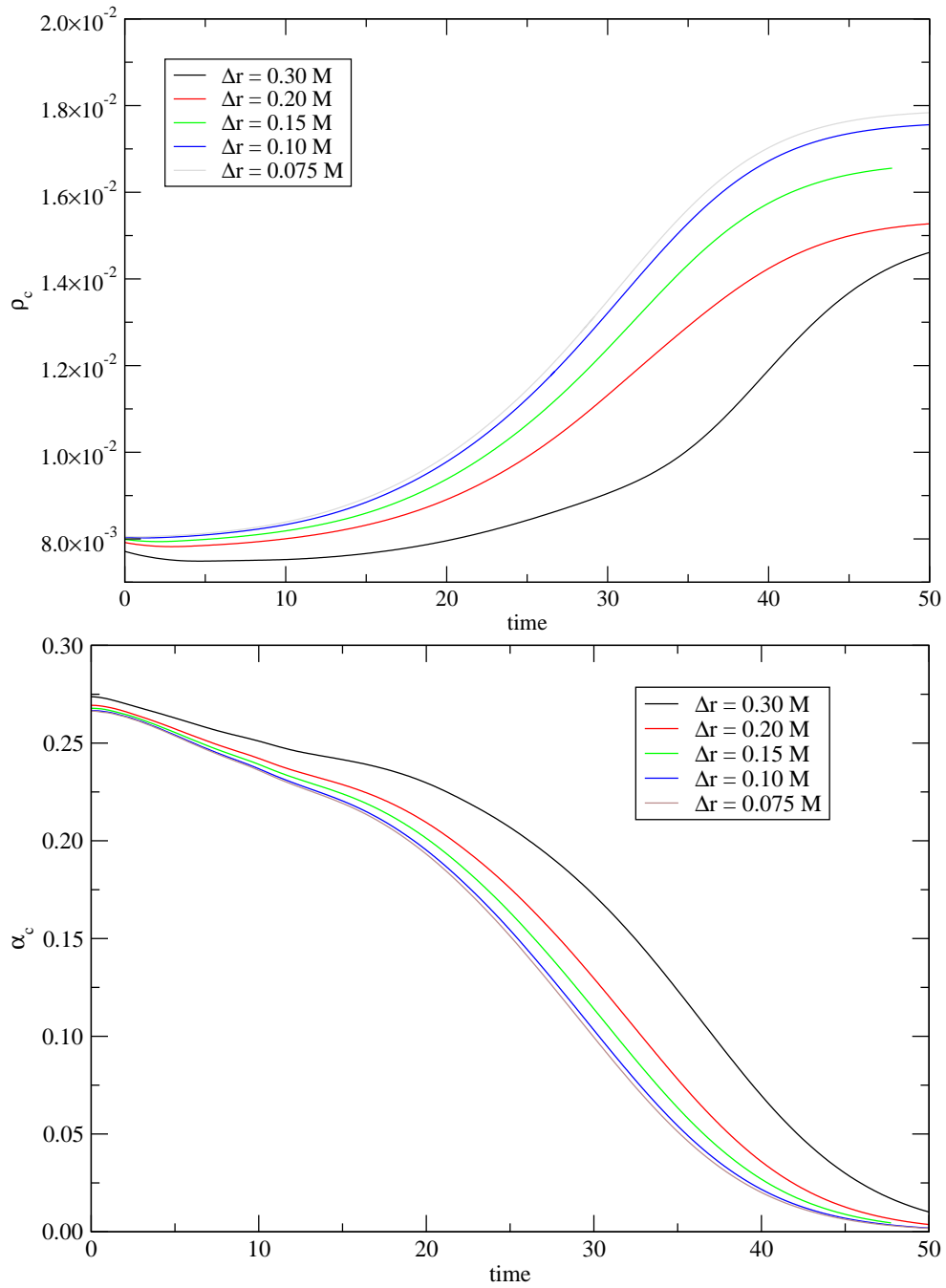


Figure 4.5.: Collapse of an unstable, uniformly rotating neutron star (see Table 4.2): Evolution of the central density ρ_c (top) and lapse function α_c (bottom) for different uniform ($\Delta x = \Delta y = \Delta z$) grid resolutions.

Cauchy horizon⁷. Recent studies of the stability of Cauchy horizons in Reissner-Nordstrom spacetimes⁸ ([68] and references therein) seem to indicate that it is indeed singular, but it also is apparent that observers passing the horizon will observe finite tidal forces [69]. The situation is completely unclear for Kerr or more general black hole spacetimes, and it is therefore that the implications of Penrose’s theorem have to be considered with some care.⁹ However, if we assume a singularity or a Cauchy horizon is always covered by an event horizon (the first part of this statement is the content of the *weak cosmic censorship conjecture* [3]) then we can make use of trapped surfaces to indicate black hole formation. To some extent, operational notions of black holes can even be built out of locally defined surfaces instead of event horizons, e.g. in the framework of *trapping* [70], *isolated* [71] and *dynamical* [72] horizons, or their generalization, the *marginally trapped tubes* [73].

In the spacetimes constructed in these tests, the Cactus module AHFinderDirect has been used to locate trapped surfaces, which, in the usual language of numerical relativity, we will assume to be apparent horizons. The angular average of the coordinate radius and areal mass of the horizon found here, for different grid resolutions, is shown in Figure 4.6. On a certain time surface the apparent horizon is found for the first time, and then subsequently accretes matter from the star. After the mass of the star is located almost entirely inside the horizon, the system settles down, under the assumptions stated above, to an isolated horizon of the expected mass.

The time evolution of a number of grid functions is shown in part in Figures 4.7 and 4.8. All profiles are taken from the highest resolution case with $\Delta x = 0.075M$, and are extracted along the x axis (which is contained in the initial equatorial symmetry plane and intersects the axis defined by the initial ∂_ϕ Killing field¹⁰ of the star). Shown are the rest-mass density ρ , the 3-metric component g_{xx} , the lapse function α and the Hamiltonian constraint H . The density profile exhibits a collapse behaviour. It is apparent in Figure 4.5, that at late times the collapse seems halted. The density profiles at $t = 50$ and $t = 55$ hardly differ. A look at the lapse function in Figure 4.8 explains this behaviour: At $t = 50$, the apparent horizon is located at approximately $x = 4$ (see Figure 4.6), and inside the black hole the lapse function is almost zero. This corresponds, for an infalling observer, to a reduction in the ratio of proper to coordinate time, and thus, while any comoving observer measures an exponentially growing unstable mode, the choice of coordinates entails an equally exponentially growing *collapse of the lapse*. In effect, the evolution inside the black hole is almost frozen. A look at the evolution of the metric in Figure 4.7, however, indicates the disadvantages of this choice of gauge. At late times, the region around the horizon expands in response to the “1+log” lapse. Immediately within the horizon, high-frequency noise in the Hamiltonian constraint violation in Figure 4.8 indicates an instability, and shortly afterwards NaNs terminate the simulation.

There are several ways imaginable to address this problem. One might immediately think of using more grid points in the region around and inside the event horizon. However, a practical difficulty with this suggestion is that the growth of the metric profile is super-linear, and thus the requirements in resources are likely too severe. Also, this depends crucially on the question whether the numerical system is ill-posed or not: if it is ill-posed, no simple strategy but changing the continuum system will alleviate the issues. One possible change is the introduction of an *excision boundary*. The basic idea behind excision has already been mentioned in Section 3.2. An excision surface must necessarily be *outflow*, since otherwise we are forced to impose boundary conditions on it — a failure to do so would lead to ill-posedness. The outflow property is only defined for sufficiently, i.e. strongly, strictly or symmetric, hyperbolic systems,

⁷A Cauchy horizon is a limit of predictability, see [67].

⁸The *Reissner-Nordstrom geometry* models black holes with charge. Its structure interior of the event horizon is vastly different from the Schwarzschild black hole, which also applies to the idealized rotating black hole (*Kerr geometry*).

⁹A variation has been provided by Hawking and Penrose [3] which avoids global hyperbolicity and replaces it with a number of causality assumptions.

¹⁰Note that the tangential vectors associated with coordinates are *derivatives*, i.e. ∂_ϕ is the basis vector associated with the angular coordinate ϕ .

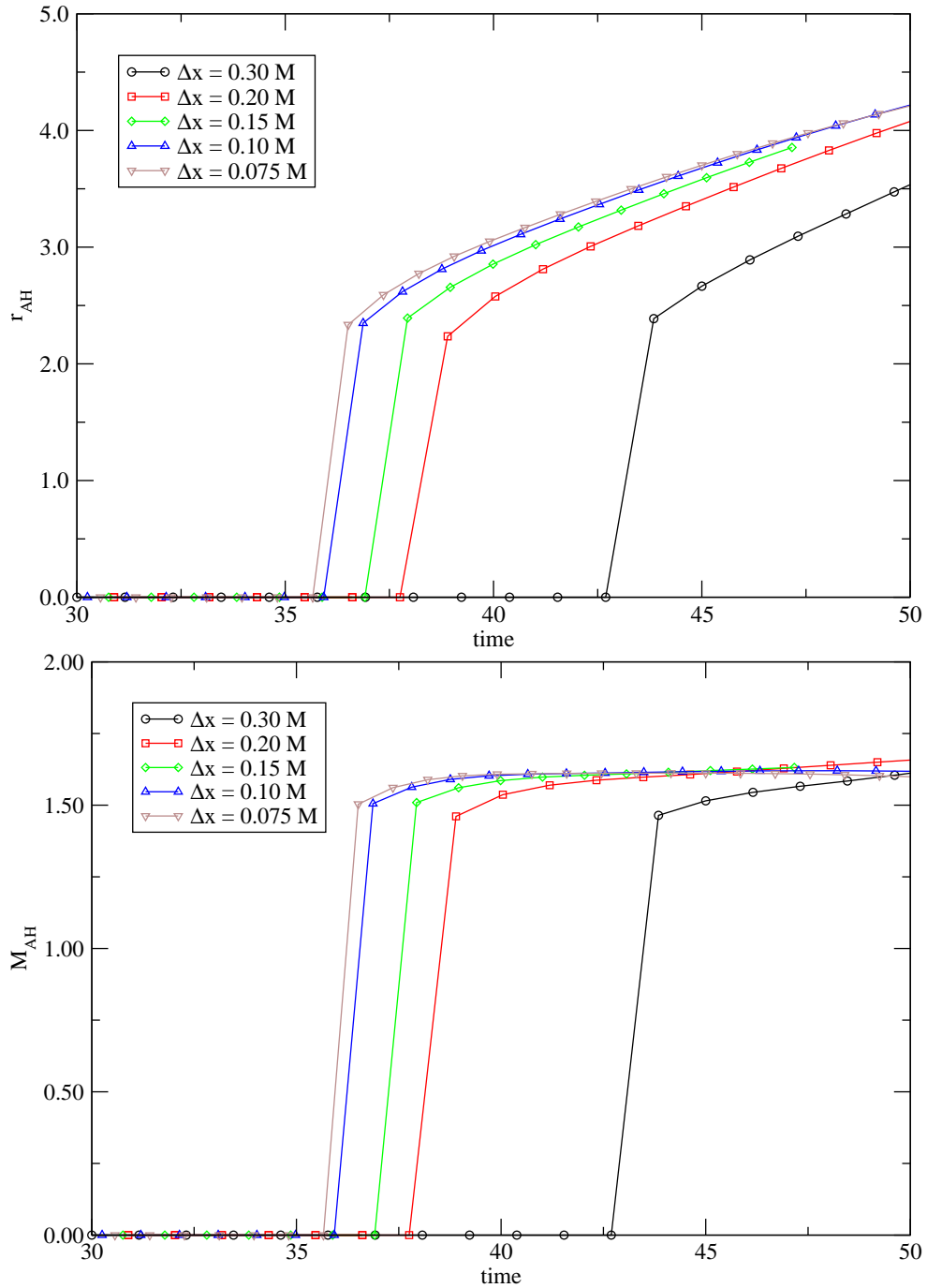


Figure 4.6.: Collapse of an unstable, uniformly rotating neutron star (see Table 4.2): Apparent horizon (angular average of the) coordinate radius (top) and areal mass (bottom) over coordinate time, for different grid resolutions.

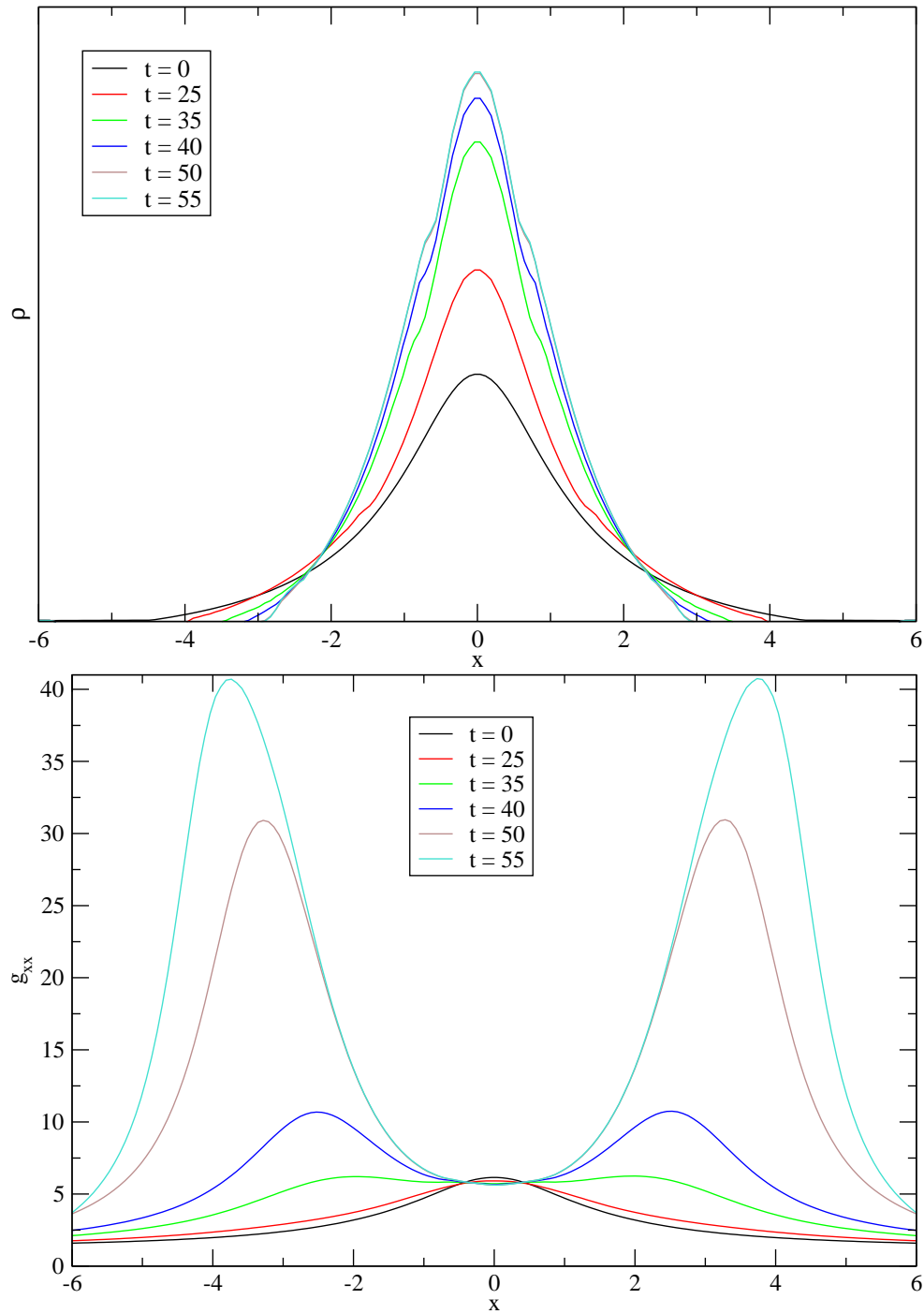


Figure 4.7.: Collapse of an unstable, uniformly rotating neutron star (see Table 4.2): Time evolution of the x axis profiles of the density ρ (top) and g_{xx} (bottom) for the highest resolution case $\Delta x = 0.075M$.

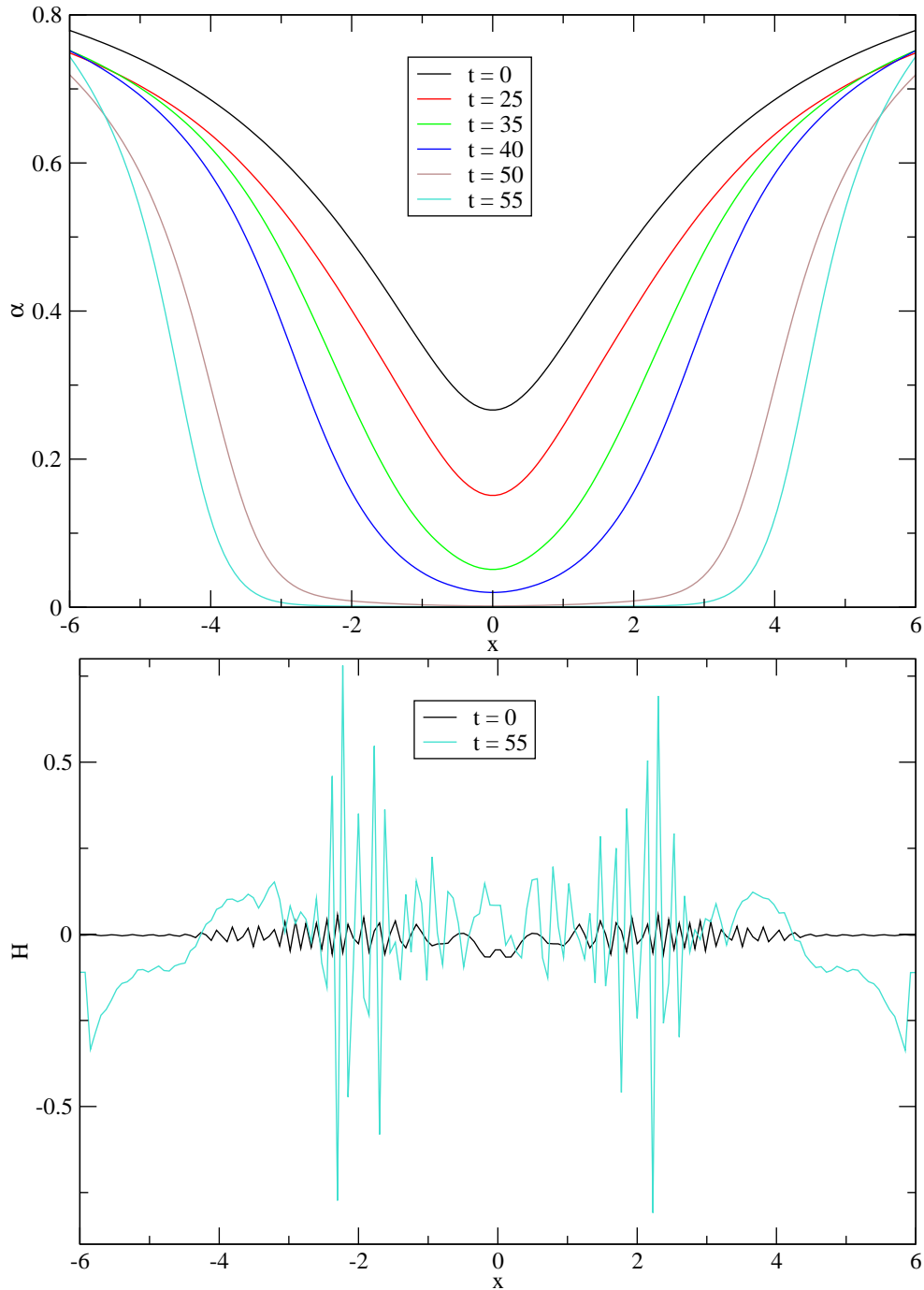


Figure 4.8.: Collapse of an unstable, uniformly rotating neutron star (see Table 4.2): Time evolution of the x axis profiles of the lapse function α (top) and the Hamiltonian constraint H (bottom), for the highest resolution case $\Delta x = 0.075M$.

preferably with “physical” speeds of propagation limited by the speed of light. The simple kind of excision boundaries available in Cactus are insufficient to render the evolution in the example presented here stable.

It is worthwhile to take a moment and stress the difficulties this type of problem presents for evolutions of gravitational wave sources. One of the main applications of GRHD simulations is certainly the prediction of gravitational wave signatures from certain astrophysical models. It is in the nature of gravitational waves that they are only well defined far from a dynamical source (as perturbations of a background spacetime), which requires the domain of simulation to extent far enough into the *local wave zone* [8] of the source. This can, in principle, be achieved by mesh refinement or more advanced techniques like Cauchy–perturbative [74, 75, 76, 77] or Cauchy–characteristic [78, 79, 80] matching. However, if the simulation can not evolve a black hole stably, part of the domain of dependency of the signal may not intersect the world-sheet of the detector. To some extent, different prescriptions of excision boundaries have helped to increase the lifetime of stationary [4] black holes and those forming by collapse [81]. The author is uncertain whether the method in [81] can be considered a solution to this problem; with Cactus/Whisky, no stable evolution of neutron star collapse appears to be possible beyond a certain time interval [82]. This interval may appear sufficient for the specific scenario of neutron star collapse, but is insufficient for more complex scenarios, like, say, collapsars, or the fragmentation discussed later.

4.3. A failed experiment: Core collapse with adaptive shift

It is, in principle, possible to use uniform grids for systems with a large range of scales like core collapse or supermassive star collapse, where an initial object of typical compactness $R/M \approx 1000$ collapses to a neutron star or black hole with $R/M \approx 1 \dots 10$. In Newtonian physics, a well-known and simple technique is to re-write the equations of motions in *Lagrangian* form, in which each fluid element is marked by its initial location, and the subsequent trajectory in phase space is a function of the marker and time. Equivalently, this can be viewed as a coordinate transformation from the Eulerian form, where the fluid is a set of fields depending on location and time, to the comoving Lagrangian system. In spherical symmetry, this allows to produce simple unigrid algorithms to calculate discrete models of collapse [83]. Without the restriction to spherical symmetry the comoving system can be disadvantageous due to grid deformations which may be difficult to control, but a simple radial prescription analogous to the spherical case may be sufficient for certain collapse situations [84].

In any Newtonian spacetime, the equations of motions, which are canonically given in inertial frames of reference, need to be explicitly transformed to allow for a Lagrangian or partially Lagrangian treatment with unigrids. This is not necessary in general relativity, since the physical meaning of coordinate distances is part of the solution, and the associated gauge freedom is manifestly contained in the theory. Specifically, the gauge functions lapse (α) and shift (β^i) can be chosen freely¹¹. A possible way to emulate the advantages of Lagrangian variables in a general relativistic, unigrid simulation is thus to choose a radial shift vector component which moves coordinate shells towards the center while the collapse proceeds. This is not a comoving system, since the set of observers in typical formulations of GRHD is in the *Eulerian frame* [23] given by the normals of the spacelike hypersurfaces. Still, the central idea of mesh refinement, to enhance resolution where necessary, appears achievable in the specific case of stellar collapse.

To implement a radial shift vector of this kind, a matching between two functions has been used to obtain a function which is C^2 . For core collapse, a natural choice is

$$\beta^r(r) = \begin{cases} ar & r < r_m \\ b \exp(-c(r - r_0)^2) & r \geq r_m \end{cases} \quad (4.2)$$

¹¹But not every choice yields a well-posed system.

where the parameters are chosen appropriately to satisfy smoothness at the matching radius r_m . This choice is natural insofar as the discussion of Newtonian collapse by Goldreich and Weber [85] and numerical experiments (e.g. [86, 87, 88, 89]) suggest that some central part of a collapsing polytrope with soft equation of state will collapse in a self-similar way, while the outer parts, which are sonically decoupled, are in free fall. If one selects a reasonable initial matching radius r_m and time dependence of the maximal shift amplitude, one can follow the collapse of the self-similar core with monotonously decreasing physical distance between grid shells, while the outer, low density part of the star is covered by less shells. The dynamical steering of the parameters can be performed in different ways; the examples discussed below have used a simplified prescription which, under the assumption of approximately self-similar collapse in the center, fixes the location of the minimum of the radial velocity profile on the grid.

The first test of this kind has been performed with the collapse of a spherically symmetric $N = 3$ polytrope in the so-called *octant* symmetry, which is a reflection symmetry about all three axis planes and allows to reduce the computational domain — and computational resource requirements — to an eighth. The equation of state used, however, was not polytropic, but, in expectation of applying the code to a core collapse scenario, a *hybrid* equation of state modelling a transition to a hard supranuclear phase at a certain transition density [90]. To simplify the first test of the adaptive shift vector, the transition density has been lowered significantly to about four times the initial central density of the iron core. As it is expected that the hybrid equation of state results in either a black hole or an almost stationary central core of high pressure (a neutron star in the core collapse analogy), the radial shift modification is set to zero again a certain time after the transition density has been exceeded.

This test resulted in the profiles shown in Figure 4.9. The radial component of the shift vector has the form described in eqn. (4.2), and this leads to the evolution of the metric depicted in the third graph. The physical resolution in the inner part is increasing with time, while the resolution decreases in the outer regions of the star. The outer boundary remains almost unchanged, which requires that the metric must have a maximum between the homogeneously contracting region and the outer boundary. This maximum can lead to problems as will be apparent in a simulation where the transition density is set to nuclear density in the iron core analogue: Figure 4.11 demonstrates that the metric function can develop significant curvature, and is not represented well by the discrete grid, which quickly leads to the termination of the simulation. On the other hand, the coordinate location of the minimum of the radial velocity profile (cf. Figure 4.10) is kept almost fixed, as expected, and in this manner approximately retains the resolution in the self-similar part of the collapse.

These experiments do not imply that this approach is entirely hopeless: A more careful adjustment of the coordinate shells, more grid resolution, and most importantly, a different treatment of the outer boundary might yield a metric profile with a less pronounced peak, or even none at all. However, at the time these results were obtained, the Carpet mesh refinement driver became available, which admitted a more natural, and more flexible, solution to the refinement problem. Therefore, the shift vector approach was abandoned by the author.

4.4. Carpet tests

4.4.1. Shock propagation across mesh refinement boundaries

The *shock tube* is one of the most basic test cases for hydrodynamics. It consists of a hydrodynamical system with one fluid in distinct states of constant density, velocity and temperature separated by an interface at the initial time. Physically, such a setup can be imagined to model a fluid inside a tube with a separating membrane, which is removed; the subsequent evolution can then be described algebraically using the conservation laws across the fronts of elementary waves in form of the Rankine-Hugoniot conditions

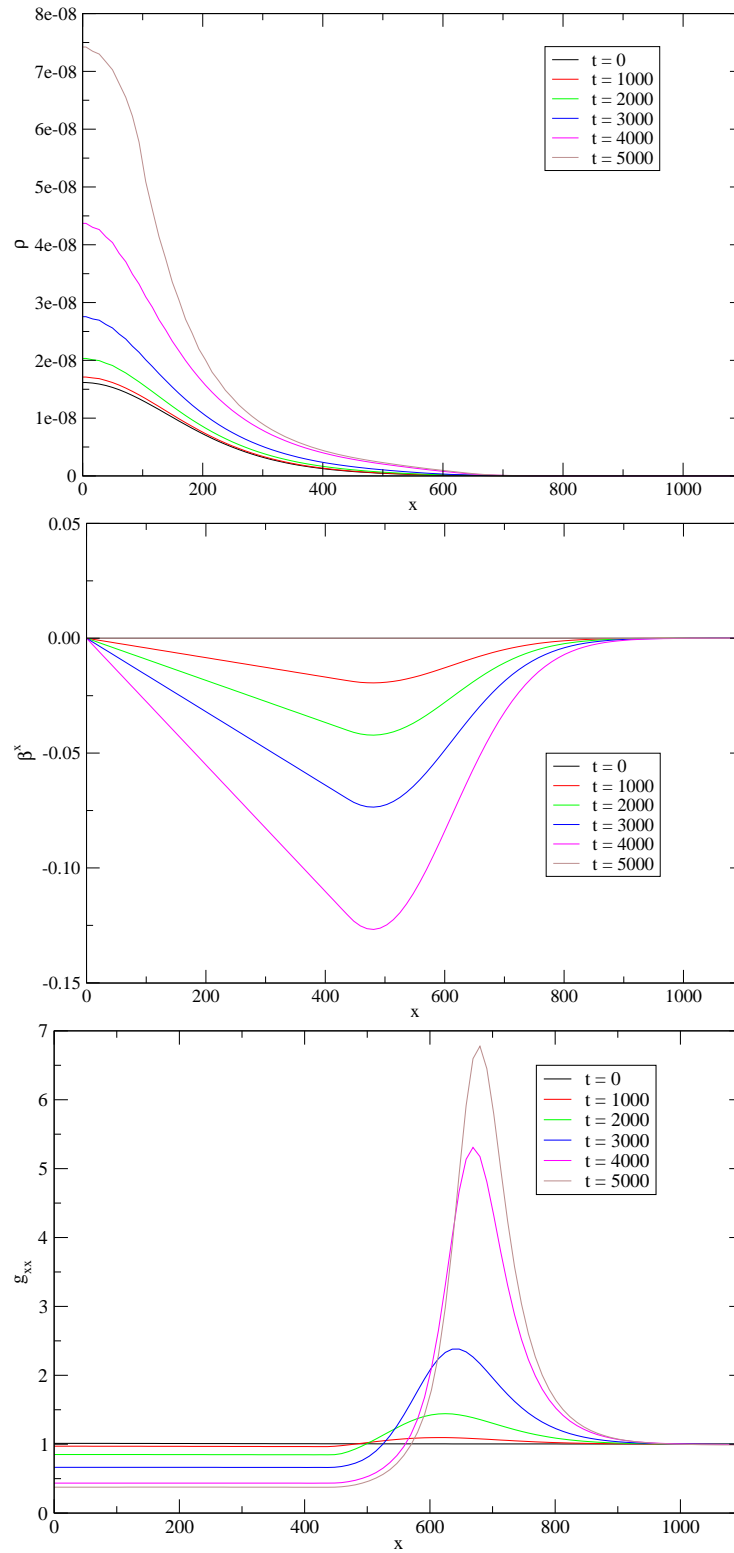


Figure 4.9.: Collapse of a soft polytrope with the hybrid equation of state of Janka et al. [90], and a low transition density $\rho_T = 5 \cdot 10^{-8}$. The panels show the x axis profiles at different times, for the rest-mass density ρ (top), x component of the shift vector (β^x , middle) and the metric component g_{xx} (bottom), respectively.

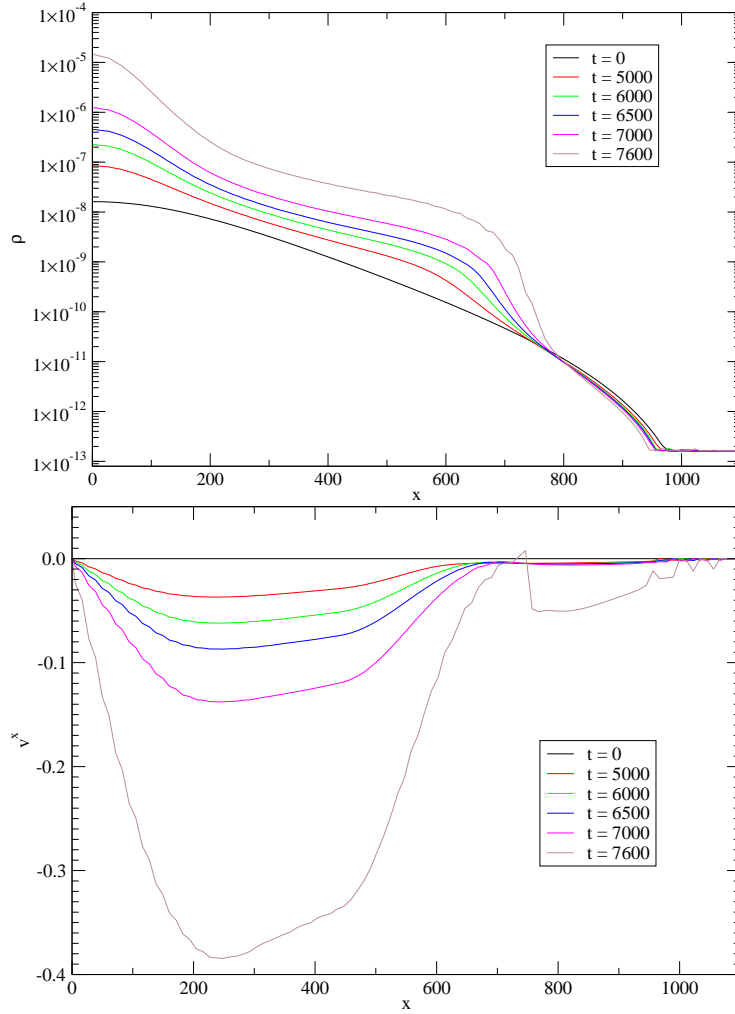


Figure 4.10.: Collapse of a soft polytrope with the hybrid equation of state of Janka et al. [90], and a transition density $\rho_T = 3.2 \cdot 10^{-4}$. The panels show the rest-mass density ρ (top) and the x component of the 3-velocity vector (v^x , bottom), respectively. Note that the coordinate location of the minimum of the velocity profile is kept almost fixed by the adaptive shift condition.

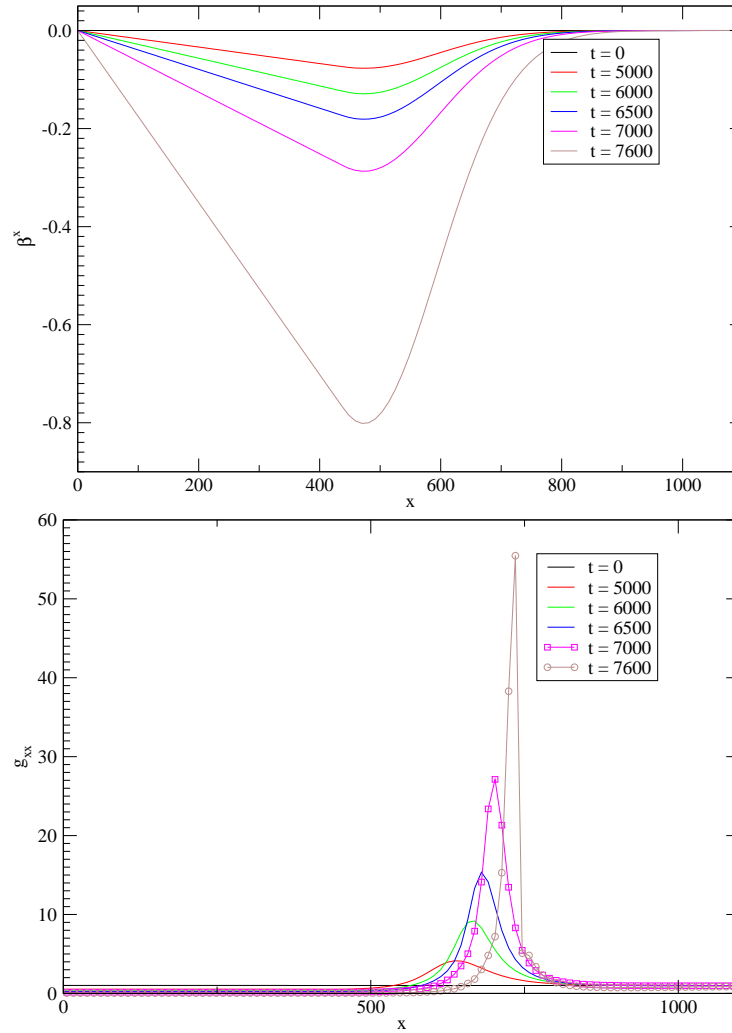


Figure 4.11.: Collapse of a soft polytrope with the hybrid equation of state of Janka et al. [90], and a transition density $\rho_T = 3.2 \cdot 10^{-4}$. The panels show the x axis profiles at different times, for the x component of the shift vector (β^x , top) and the metric component g_{xx} (bottom), respectively. The explicit locations of grid points is indicated here to exhibit the lack of resolution. The simulation terminated with NaNs shortly after $t = 7600$.

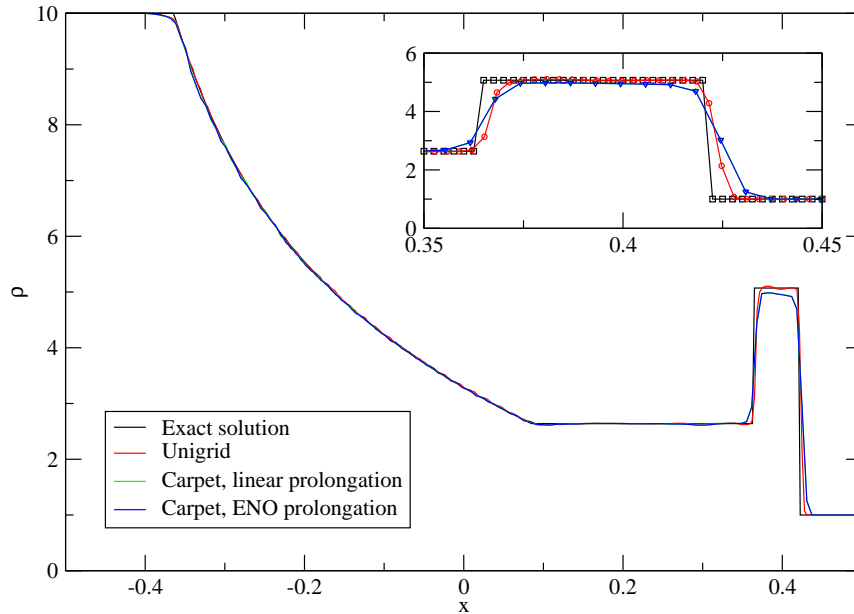


Figure 4.12.: Shock tube test with and without mesh refinement. The graphs show the density profile $\rho(x)$ after a certain coordinate time, and compare the solutions obtained by using a uniform grid to Carpet evolutions with linear and ENO interpolation operators, with a mesh refinement interface at $|x| = 0.25$. The “exact” solution is obtained by solving the algebraic system with iterative methods [25]. Note that the results for different prolongation operators are almost identical.

[25]. These waves are *shock waves*, *contact discontinuities* and *rarefaction waves*, and their fronts separate fluid states of constant density, velocity and temperature. A closed solution of the algebraic system is not available, but iterative methods can provide reference solutions with arbitrary levels of accuracy.

To use the special relativistic shock tube solution as a test case for a general relativistic code, it is necessary to assume a flat spacetime and a test fluid approximation, which will be provided in the present case by fixing the metric quantities to their initial values. We are then interested in how the introduction of mesh refinement boundaries affect the propagation of shock and rarefaction waves.

In Figure 4.12, we compare the evolution of a shock tube model, with initial values $\rho_l = 10$, $\rho_r = 1$, $v_l = v_r = 0$, $P_l \approx 13.3$, and $P_r \approx 6.66 \cdot 10^{-7}$, between a uniform grid and a nested grid with a central patch from $x = -0.25$ to $x = 0.25$, and a coarser patch from $x = -0.5$ to $x = 0.5$. The uniform grid has the same resolution as the central Carpet patch. In addition, the effects of using a linear or ENO¹² interpolation operator are compared. The “exact” results were obtained using the program *riemann* from [25]. We can see that the Carpet results naturally suffer from the lower grid resolution near the fronts, but the shock is represented reasonably well, even after passing a refinement boundary. Since the solution region near the shock wave and contact discontinuity only needs first order accurate discrete representation, the nature of the interpolation operators has no significant effect here.

A related, but numerically more demanding example is the *diagonal shock tube*, which is simply obtained by a coordinate rotation by $\pi/4$ in every direction. On a Cartesian grid, and keeping in mind that all fluxes are split by direction, this can exhibit more artefacts than the one-dimensional example above. Figures 4.13 and 4.14 show the evolution of the function $\rho(x, y)$ with two nested grids. The refinement

¹²*Essentially non-oscillatory*; an special high-order interpolation operator used in numerical hydrodynamics.

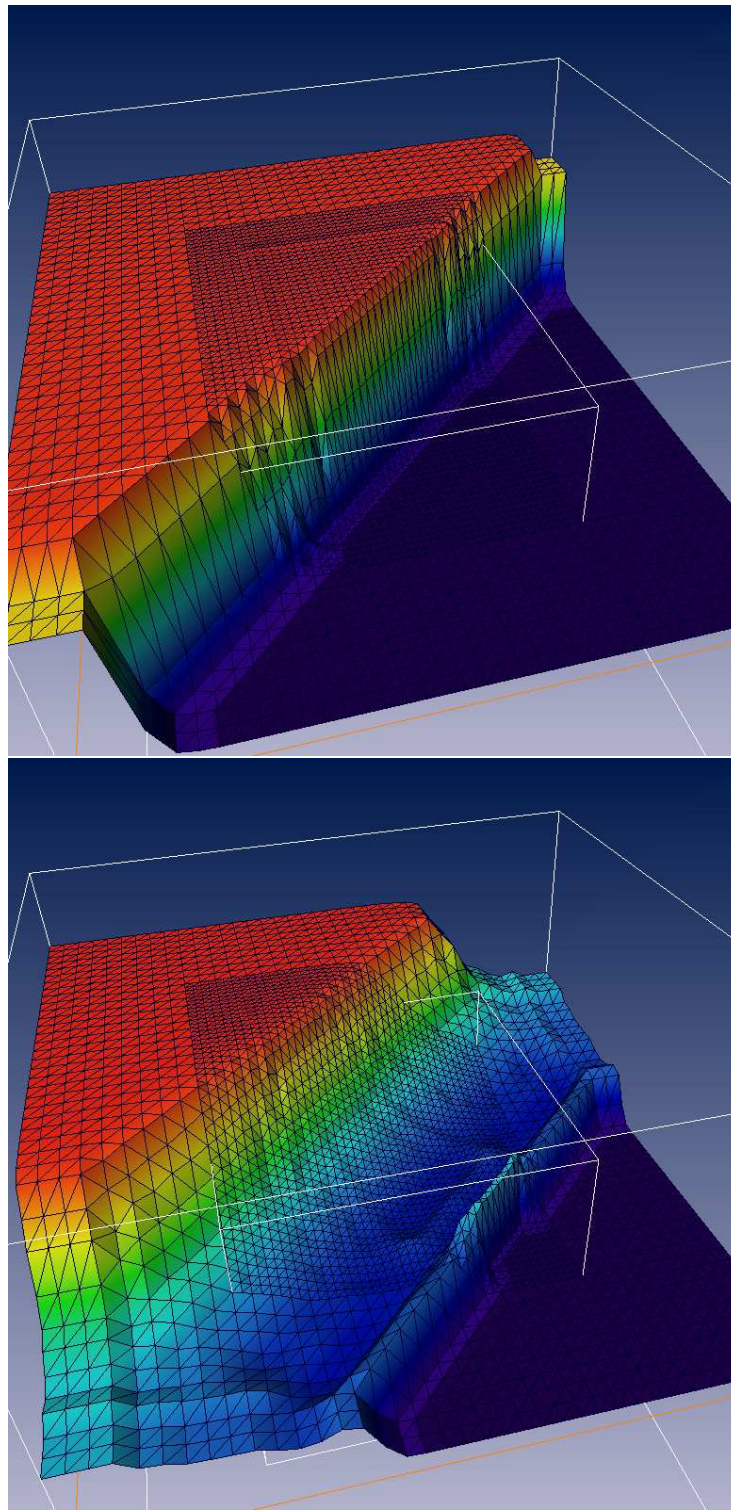


Figure 4.13.: Evolution of a diagonal shock tube with states $\rho_l = 10$, $\rho_r = 1$, $v_l = v_r = 0$, $P_l \approx 13.3$ and $P_r \approx 6.66 \cdot 10^{-7}$, with a nested grid setup in Carpet. The plot shows the function $\rho(x, y)$ at different times.

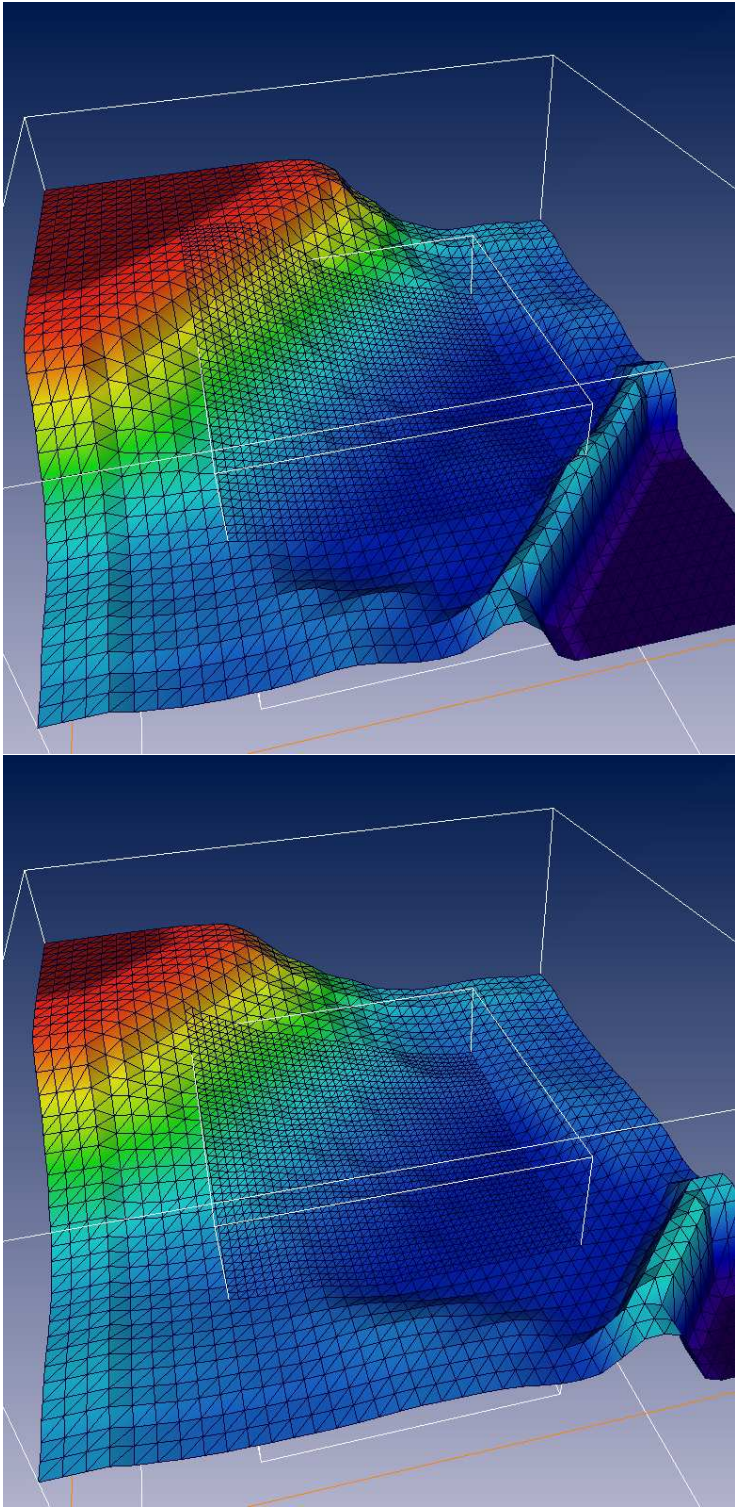


Figure 4.14.: Continuation of Figure 4.13.

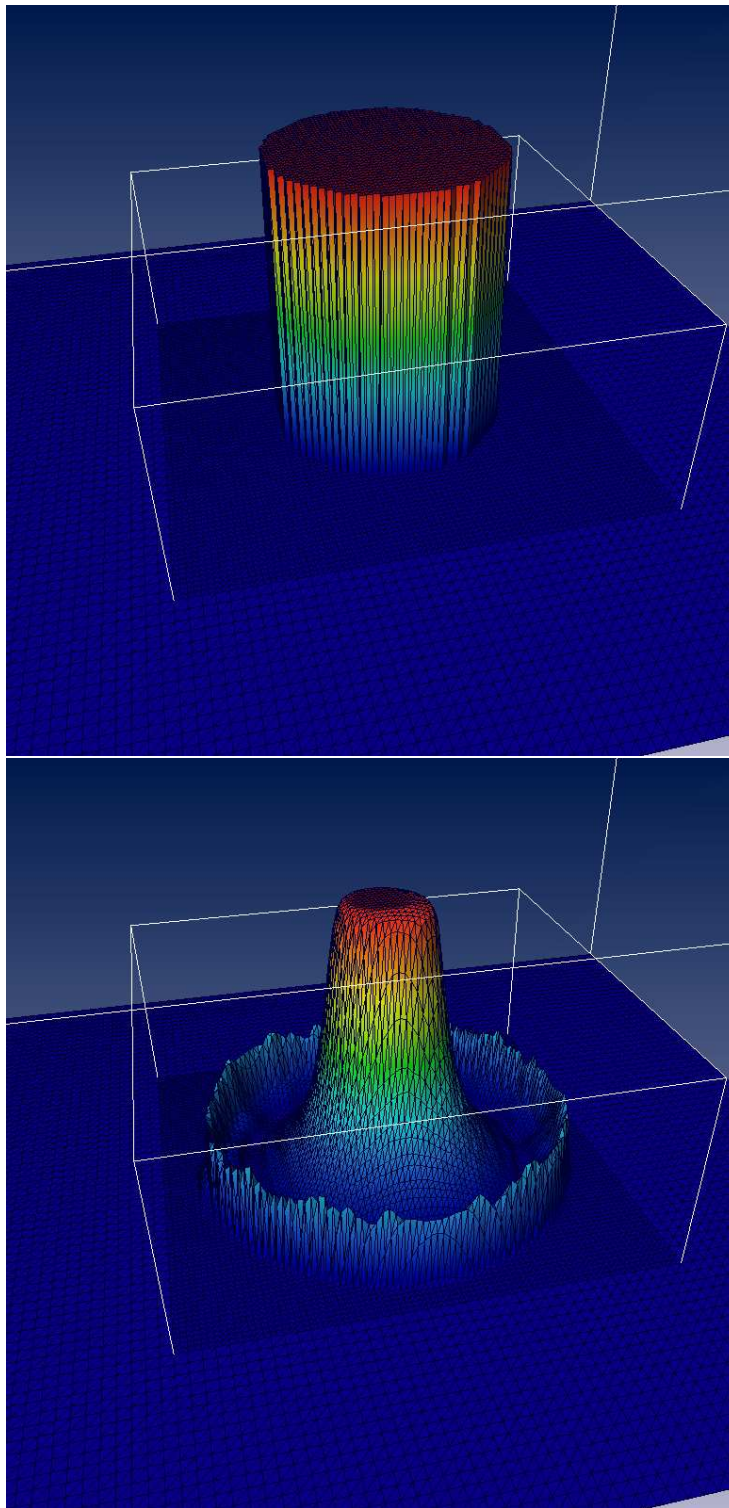


Figure 4.15.: Evolution of a spherical shock tube in Carpet, with central state $\rho_c = 10$, $v_c = 0$ and $P_c \approx 13.3$, and outer state $\rho_o = 1$, $v_o = 0$ and $P_o \approx 6.66 \cdot 10^{-7}$. The plot shows the function $\rho(x, y)$.

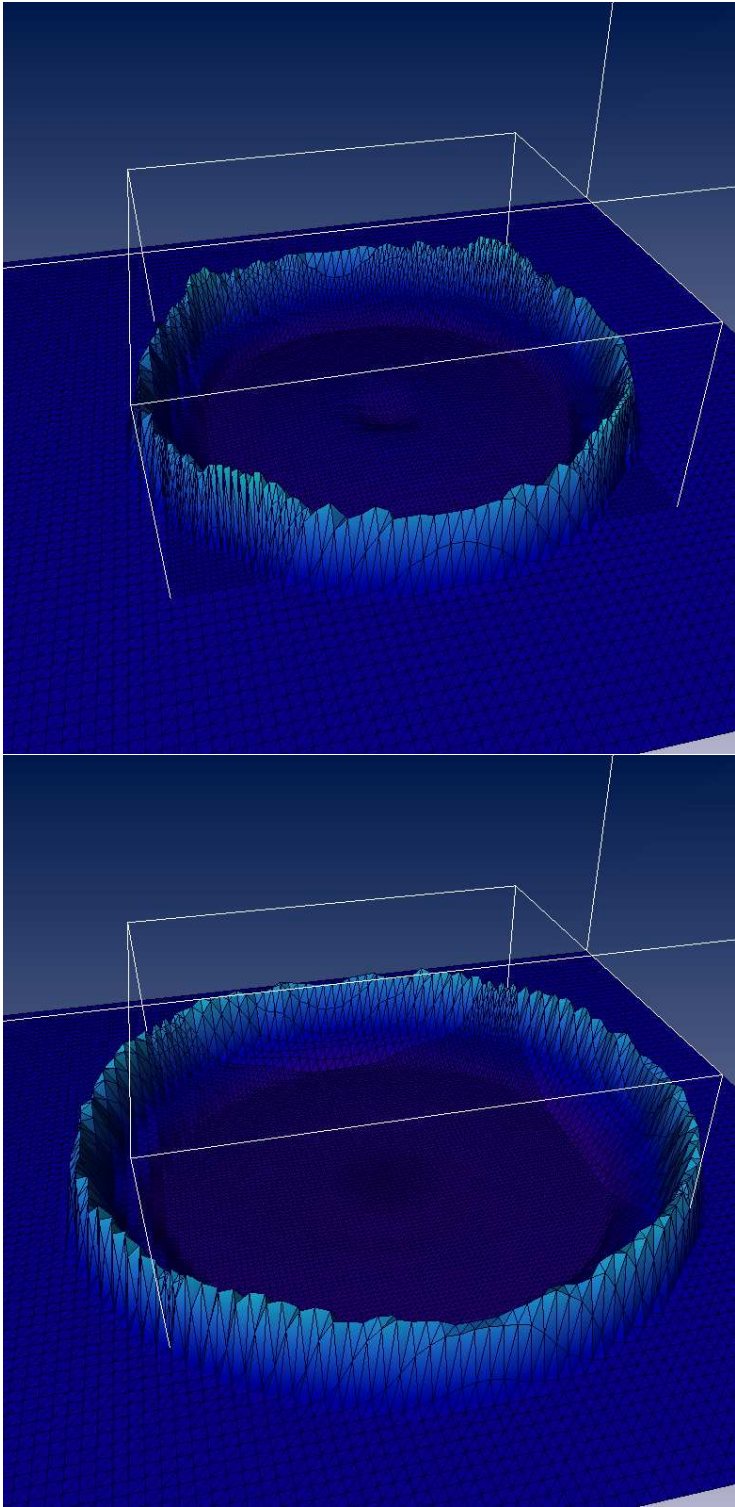


Figure 4.16.: Continuation of Figure 4.15.

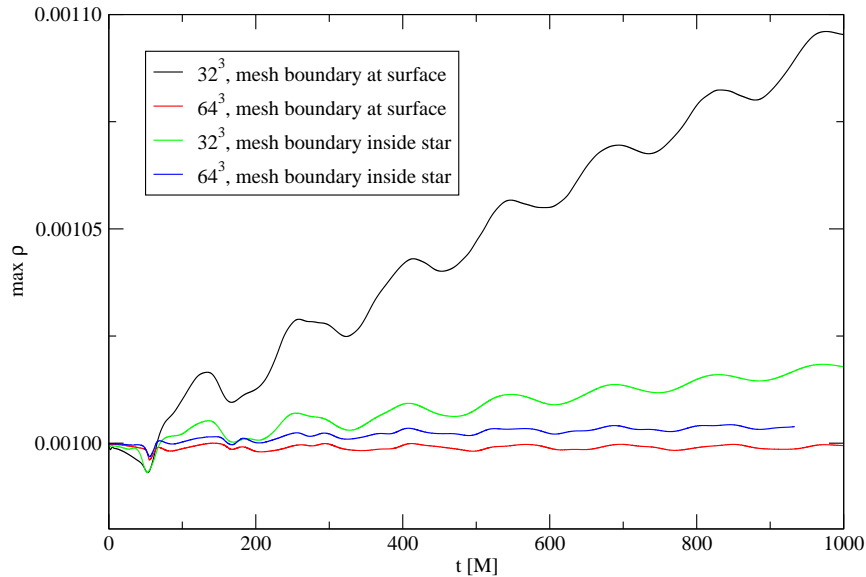


Figure 4.17.: Maximal density in a TOV solution evolved with Carpet. The exact solution is $\max\rho = 10^{-3}$. In the first two plots, the mesh refinement boundary is located at the stellar surface, while it is located inside the star in the next two. Note that, for a neutron star with $M = 1.4M_{\odot}$, we have $1000 M \approx 7$ ms.

interface does not produce any apparent artefacts. Note that the outer boundary is stationary, i.e. the waves introduce reflections. The final example is a *spherical shock tube*, where two constant fluid states are separated by a coordinate sphere. The evolution of this system is shown in Figures 4.15 and 4.16: again, the mesh refinement boundary does not introduce any significant artefacts.

4.4.2. TOV solution

As we have already discussed, the evolution of TOV solutions is one of the simplest test cases for general relativistic hydrodynamics. To test TOV evolutions with Carpet, the next test models a TOV solution with a central density $\rho_c = 10^{-3}$, and $\Gamma = 2$ on two patches of 32^3 (low resolution) or 64^3 (high resolution) zones, in an octant symmetry. In one case, the mesh refinement boundary is near the star's surface, for our particular setup at $10 M$, and in a related case it is inside the star at $7.5 M$. The evolution of the maximum density is displayed in Figure 4.17. It is apparent that the code converges to the exact solution of $\max\rho = 10^{-3}$ with increasing resolution. The stellar surface with its large density gradient is particularly difficult for the interpolation operators. Therefore, a stronger growth in the maximal density is introduced as opposed to cases with a mesh refinement boundary inside the star. Note that these problems are less severe for soft polytropes.

The long-term behaviour of the code, displayed in Figure 4.18, demonstrates the evolution of the same TOV solution on a grid using four refinement levels and a resolution of 50^3 zones per patch. If the TOV solution is understood as an approximate model of a neutron star with mass $M = 1.4M_{\odot}$, then the evolution is stable for ≈ 50 ms, and does not show any sign of computational instability. However, the oscillations in the maximum density obtain some high-frequency components at later times.

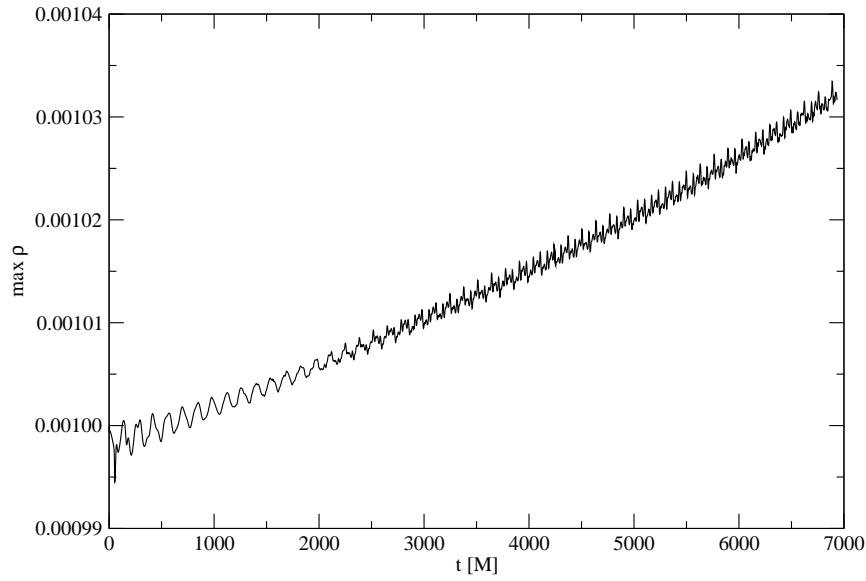


Figure 4.18.: Long-term evolution of a TOV star with Carpet and four refinement levels with a resolution of 50^3 in octant symmetry.

		(From Table 4.1)	
Polytropic K	K	100	100
Polytropic Γ	Γ	2	2
Central rest-mass density	ρ_c	10^{-3}	10^{-3}
Central rest-frame energy density	e_c	$1.100 \cdot 10^{-3}$	$1.100 \cdot 10^{-3}$
ADM mass	M	1.3331	1.5612
Rest mass	M_0	1.4222	1.6702
Equatorial proper radius	R_e	10.611	14.319
Axes ratio	r_p/r_e	0.9	0.574
Equatorial compactness	R_e/M	7.9595	9.1721
Total angular momentum	J	0.58908	1.6387
Normalized angular momentum	J/M^2	0.33148	0.6724
Kinetic over potential energy	$T/ W $	$2.4366 \cdot 10^{-2}$	$9.3956 \cdot 10^{-2}$
Equatorial surface angular velocity	Ω	$1.3257 \cdot 10^{-2}$	$2.3343 \cdot 10^{-2}$
Equatorial surface Keplerian angular velocity	$3.3426 \cdot 10^{-2} \Omega_K$	Ω_K	$2.3378 \cdot 10^{-2}$
Mass shedding factor	Ω/Ω_K	0.3966	0.9985

Table 4.3.: Parameters and integral quantities of a rapidly rotating neutron star (last column). The quantities are all measured in units of $K = 100$ and $G = c = 1$. Note that K , Γ , ρ_c and r_p/r_e are parameters, and as such exact. The third column shows the parameters of the model in Table 4.1 for comparison.

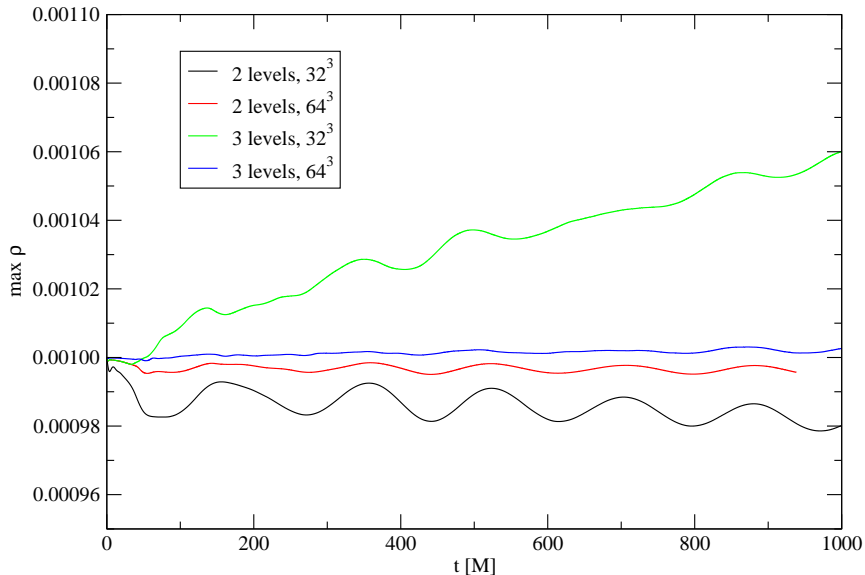


Figure 4.19.: Evolution of the maximum density of the rapidly rotating neutron star in Table 4.3 with Carpet. Either two or three refinement levels are used, where the innermost one or two cover the star.

4.4.3. Rotating star solution

To test Carpet with rapidly rotating equilibrium solutions, a star with $\rho_c = 10^{-3}$ and an axes ratio $r_p/r_e = 0.574$, which is near the mass-shedding limit, has been constructed. The parameters and integral quantities of the model are summarized in Table 4.3. In this case, the grid consists of either two or three refinement levels, where the innermost one (or two) cover the star itself. No grid patch boundary is located near the stellar surface to achieve higher accuracy (see preceding section). Resolutions used are 32^3 and 64^3 zones, using an octant of the domain like in the previous section, but applying an $\pi/2$ symmetry to the meridional boundary planes for consistency with the ∂_ϕ Killing field.

The results from evolving this system are shown in Figure 4.19. We note immediately that the discrete system is convergent to the exact solution. Also, adding refinement levels inside the star does not necessarily decrease the solution error, in accordance with what we have found before. Therefore, mesh refinement will be mostly useful in *soft* polytropes with their core-halo structure, or in collapse situations.

5. Fragmentation and black hole formation in quasi-toroidal polytropes

The study of oscillations and stability of stars has a long history (see e.g. [91]), and, while its classical results tried to address the limits of possible models for main-sequence stars, and the question of binary star formation from protostellar clouds, it has been extended in the last century to examine the properties of relativistic fluid equilibria, and their connection to the formation of black holes by axisymmetric instabilities.

Due to the recent prospect of detecting gravitational radiation directly, the connection between the local dynamics of collapse and gravitational wave emission receives increased attention nowadays (e.g. [92, 49]). In this context, a non-axisymmetric instability in a star is expected to change the nature of the signal, and to enhance the chances of detecting it [93]. We shall discuss a number of scenarios for gravitational collapse and black hole formation to illustrate this point.

1. *Stars retaining spherical symmetry:* If the initial matter distribution has spherical symmetry, no gravitational waves are emitted as a consequence of Birkhoff's theorem. The famous exact solution by Oppenheimer and Snyder [94] already exhibits many features of the local dynamics, while the connection to dynamical stability in general relativity has been made explicit by Chandrasekhar [60]. The assumption of spherical symmetry admits already a simple model of phenomena like mass limits for compact stars, the bulk properties of black hole formation from supermassive stars, neutron stars and iron cores (or proto-neutron stars, if the center of the iron core stabilizes temporarily after a first dynamical collapse phase) (e.g. [83, 95, 96]), and the dynamics of apparent and event horizons (ibido).
2. *Stars retaining (approximate) axisymmetry:* If the symmetry assumption is relaxed to axisymmetry, models of gravitational collapse admit to represent a number of additional features: most importantly, the emission of gravitational radiation. Stars in axisymmetry can be rotating, which changes the radial modes of the non-rotating member of a sequence into a "quasi-radial" mode. If that is unstable, the star may collapse to a black hole in a manner which is similar to the spherical symmetric case in its bulk properties, and it proceeds by (i) contraction due to a quasi-radial instability, (ii) formation of an event horizon centered on the axis, and (iii) ring-down to a Kerr black hole with a disk. We will call this process the *canonical scenario* to represent that it provides the expected properties of the collapse of slowly rotating stars. It has been studied extensively in numerical investigations [97, 98, 99, 100, 101, 102, 103, 84, 104, 105, 106, 107, 81, 49, 62, 39], and seems even appropriate to describe the quality of collapse of some rapidly and differentially neutron stars [81]. It should not be considered implicit here that the canonical scenario is generic for axisymmetric collapse: see e.g. [108, 109] for systems involving toroidal black holes.
3. *Stars not retaining (approximate) axisymmetry:* As already mentioned, even in many numerical models with three spatial dimensions, the collapse to a black hole proceeds in an almost axisymmetric manner, although the initial data is represented on discrete Cartesian grids. One has found that, even when non-axisymmetric perturbations are applied to the collapsing material, no large deviations from axisymmetry obtain during the collapse [62], which, at least judging from the perturbative theory of Newtonian polytropes [91], indicates that either the amount of rotational over

gravitational binding energy $T/|W|$ is insufficient, or that the growth time of an unstable, non-axisymmetric mode is in the order of, or larger than, the collapse timescale.

The situation can be quite different when the system is not unstable to axisymmetric modes, or if the collapse stabilizes around a new equilibrium with higher $T/|W|$. The classical limit of $T/|W| \approx 0.27$ for Maclaurin spheroids [2] indicates the onset of a dynamical instability to transition to the $x = +1$ Riemann S-type sequence [2, 110]. To which extent this idealized behaviour is also realized in general relativistic compressible polytropes, and, more specifically, how it is connected to the formation of black holes, is the issue we would like to address in part here.

If a general relativistic star encounters a non-axisymmetric instability, the nature of its subsequent evolution may be characterizable by certain properties of the equilibrium model, like the rotation law, $T/|W|$, compactness, and equation of state. For the limit of uniformly rotating, almost homogeneous models of low compactness, we expect, if $T/|W| > 0.27$, a dynamical transition to an ellipsoid by a principle of correspondence with Newtonian gravity. For this very reason, the system would also fail to form a black hole.

By relaxing all but the assumption of low compactness, we can make use of the rich body of knowledge about the stability and evolution of stars in Newtonian gravity. Two classical applications of stability theory are the oscillations of disks and the fission problem, which most prominently appears in the context of iron core collapse, and the question how binary stellar systems are formed. These matters have been investigated extensively over the last decades [111, 112, 51, 113, 114, 115, 116, 117, 118, 119, 120, 121, 122, 123, 124, 125], and a number of possible scenarios have emerged for the non-linear evolution of non-axisymmetric dynamical instabilities in rotating polytropes:

1. The polytrope develops a bar-mode instability similar to the Maclaurin case, and possibly retains this shape over many rotational periods (e.g. [119]).
2. Two spiral arms and an ellipsoidal core region develop, where the latter transports angular momentum to the spiral arms by gravitational torques, is spun down, and collapses (e.g. [112]). This scenario is interesting for black hole formation, since the rotational support of the initial model can be partially removed by such a mechanism. If this transport is efficient enough, the core ellipsoid might collapse, resulting in a Kerr black hole with a disk of material around it. One might conjecture that, if the equation of state is soft enough, the disk itself may be subject to fragmentation, and form several smaller black holes which are subsequently accreted.
3. One spiral arm develops, and the mode saturates at some amplitude [116, 126], leaving a central condensation. This might also lead to central black hole formation. Note that the onset for this dynamical instability in terms of $T/|W|$ is significantly lower than the Maclaurin limit.
4. For polytropes with strong differential rotation, the initial model may be *quasi-toroidal*, i.e. it has at least one isodensity surface which is homeomorphic to a torus. If models of this kind, or purely toroidal ones, are subject to the development of a non-axisymmetric instability, they may exhibit fragmentation [118, 121]. This is clearly the most interesting setting for the fission problem, but has been discussed also in the context of core collapse (“collapse, pursuit and plunge” scenario, Fig. 24.3 in [11], also [115, 123]).

It is this last kind of instability we will investigate here in the context of general relativity, and its relation to the formation of black holes.

Concerning the *nature* of the spiral-arm and low- $T/|W|$ instabilities, Watts et al. ([127], see also [128, 129]) have suggested a relation to the location of the corotation band¹ with respect to the frequency of f modes². That corotation has a bearing on the nature of oscillations in differentially rotating disk has been known for some time; the perturbation operator is singular at corotation points, which gives rise to a continuous spectrum of “modes.” While the initial-value problem of perturbations associated with the continuous spectrum of stars is not well understood even in Newtonian gravity, there is evidence [130, 131, 132, 128] that a mode entering corotation may be subject to a shear-type instability, or that it merges with another mode inside the corotation band, which appears to admit a certain class of solutions showing similar properties as the solutions in the discrete spectrum [129]. While three-dimensional Newtonian simulations would appear, at least as a first step, most appropriate to gain more intuition in these matters [133], we will collect some evidence on corotation points in the evolutions presented here as well.

Since the parameter space of possible initial models is large, and given that three-dimensional simulations of this kind are still quite expensive in terms of computational resources, we restrict attention to several isolated sequences, where just one initial model parameter is varied to gain evidence on its systematic effects, and to a plane in parameter space defined by a constant central rest-mass density and a fixed parameter $\Gamma = 4/3$ in the Γ -law equation of state $P = (\Gamma - 1)\rho\epsilon$; the latter choice will be motivated in a moment. We will find that, at least as long as we are concerned with the question when certain modes become dynamically unstable on a sequence, the restriction to constant central density is not severe, while the nature of the final remnant might be rather sensitive to it. This latter issue, namely whether a black hole forms or not, will not be answered in full here, since we will only determine whether the fragment stabilizes during collapse, and re-expands, or if it does not. We leave the location of the apparent horizon with adaptive mesh-refinement techniques and the subsequent evolution with excision, to future work, and concentrate here on the general structure of the parameter space and its relation to the non-axisymmetric instability.

The choice $\Gamma = 4/3$ is well-known to approximately correspond to the adiabatic coefficient of a degenerate, relativistic Fermi gas or a radiation pressure dominated gas [57], and is thus closely connected to iron cores and supermassive stars. The author would like to point out on this occasion that a collapsing iron core, even if its initial state is assumed to be determined mostly by electron pressure, is subject to a complex set of nuclear reactions, which involve the generation of neutrinos and transition to nuclear matter at high densities. It is for this complexity, which we do not take into account here to reduce the numbers of free parameters, that we do not suggest the use of the fragmentation and black hole formation investigated in [134] as a highly idealized model of core collapse. For supermassive stars, the situation is different, since an event horizon can form before thermonuclear reactions become important, depending on the metallicity and mass of the progenitor [135]. Because of this, it is not inconceivable that the type of evolution in [134] can be used as an approximate model of supermassive black hole formation. Finally, we would like to mention the possibility that gravitational wave detection may uncover so-far unexpected processes involving black hole formation, and in that case it is useful to have a general understanding of possible dynamical scenarios.

5.1. Previous work

The background for this study comes from three areas: the study of (i) fragmentation in Newtonian polytropes, (ii) non-axisymmetric instabilities in general relativistic polytropes, and (iii) black hole formation by gravitational collapse. The first area is represented by a large number of publications, as already

¹The *corotation band* in a differentially rotating star is the set of frequencies associated with modes having at least one *corotation point*, i.e. a point where the local pattern speed of the instability matches the local angular velocity.

²The term *f mode* is introduced in [65].

above, but we would like to mention specifically the recent work by Centrella, New et al. [136, 121], since the kind of initial model and subsequent evolution studied in these publications are similar to the ones presented by us in [134] and here, apart from the fact that Newtonian gravity and a softer equation of state ($\Gamma = 1.3$) was used. New and Shapiro [137] investigated equilibrium sequences of differentially rotating Newtonian polytropes with $\Gamma = 4/3$ to present an evolutionary scenario where supermassive stars develop a bar-mode instability instead of collapsing axisymmetrically. This kind of scenario (see also [138, 93]) would also be important when connecting the general relativistic fragmentation presented here to the evolution of supermassive stars.

Non-axisymmetric dynamical instabilities in general relativistic, self-gravitating fluid stars have been studied by several authors [63, 64, 139, 81, 140]. Some evidence of fragmentation has been found in [81] in a ring resulting from a “supra-Kerr” collapse with $J/M^2 > 1$, but no black hole was identified. Finally, black hole formation by gravitational collapse has been studied extensively, (see references in the introduction), and in recent years also in three spatial dimensions [103, 104, 107, 141, 81, 49, 39, 142]. The collapse of differentially rotating supermassive stars in the approximation of conformal flatness has been investigated by Saijo [62].

In addition, the work on low- $T/|W|$ instabilities by Watts et al. [128, 129, 127] has already been described in the introduction, and recent numerical studies of related interest can be found in [143, 144, 133].

5.2. Initial data

5.2.1. Quasi-toroidal polytropes

We will focus on relativistic, differentially rotating polytropes which are *quasi-toroidal*: Such a polytrope has at least one isopycnic (constant density) surface which is homeomorphic to a torus. To construct equilibrium polytropes of this kind, an extended version of the Stergioulas-Friedman (SF, also RNS) code is used [45, 145, 46], which applies a modification of the method developed by Komatsu, Hachisu and Eriguchi [47, 146]. The code assumes a certain gauge in a stationary, axisymmetric spacetime, such that we can write the line element in terms of potentials ν, ψ, ω and μ , and the Killing fields ∂_t and ∂_ϕ as [46]

$$ds^2 = -e^{2\nu} dt^2 + e^{2\psi} (d\phi - \omega dt)^2 + e^{2\mu} (dr^2 + r^2 d\theta^2). \quad (5.1)$$

Matter is modelled as a perfect fluid with

$$T^{ab} = \rho h(\rho, \epsilon) u^a u^b + P g^{ab}, \quad (5.2)$$

where ρ is the rest-mass density, ϵ is the specific internal energy, $h = 1 + \epsilon + P/\rho$ the specific enthalpy, and the four-velocity is parameterized by

$$u^a = \frac{e^{-\nu}}{\sqrt{1-v^2}} (\partial_t^a + \Omega \partial_\phi^a). \quad (5.3)$$

To compute an equilibrium polytrope, the central rest-mass density ρ_c , the coordinate axes ratio r_p/r_e and a barotropic equation of state $P(\rho)$ need to be specified³. In addition, the equations of structure [46] contain an additional freely specifiable function $F(\Omega)$. We will use the common choice

$$F(\Omega) = \tilde{A}^2 (\Omega(r=0) - \Omega) \quad (5.4)$$

which reduces to uniform rotation in the limit $\tilde{A} \rightarrow \infty$, and to the constant specific angular momentum case in the limit $\tilde{A} \rightarrow 0$. We will, however, often use the normalized parameter $A = \tilde{A}/r_e$, where r_e

³A purely toroidal model would have the constraint $r_p/r_e = 0$.

is the coordinate radius of the intersection of the stellar surface with the equatorial plane $\theta = \pi/2$. For construction of a polytrope, the barotropic equation of state is constrained to

$$P = K\rho^\Gamma \quad (5.5)$$

with the polytropic constant K and the coefficient Γ , which can also be expressed by the polytropic index $N = (\Gamma - 1)^{-1}$. Without loss of generality we set $K = 1$ in all cases.

The resulting set of equations is solved iteratively [46], where the initial trial fields are a suitable solution of the TOV system. To converge to the desired model, it may be necessary to select a number of intermediate attractors as trial fields. Some models are thus constructed by first obtaining a specific quasi-toroidal model, and then moving in parameter space in the quasi-toroidal branch to the target model. In this work, a *hook model* with parameters $A_{hook} = 0.3$ and $(r_p/r_e)_{hook} = 0.15$ is generated, which then is used as initial guess to construct the target model.

If we include the polytropic coefficient Γ , we have to consider a four-dimensional parameter space $(\Gamma, \rho_c, A, r_p/r_e)$. We will not study the whole parameter space here: Rather, we first use a reference model and explore sequences in ρ_c , Γ and r_p/r_e containing this model, and will subsequently concentrate on the important case $\Gamma = 4/3$, since it approximately represents a radiation-pressure dominated star.

Most polytropes have been constructed with a meridional grid resolution of $n_r = 601$ radial zones and $n_{\cos\theta} = 301$ angular zones, a maximal harmonic index $\ell_{max} = 10$ for the spectral grid and a solution accuracy of 10^{-7} . Selected models have been tested for convergence with resolutions up to $n_r = 2401$, $n_{\cos\theta} = 1201$, and $\ell_{max} = 20$.

To investigate the stability of the polytropes constructed with the SF code, two kinds of perturbations are applied: the pressure is reduced by 0.1%, and a cylindrical density perturbation of the form

$$\rho(x) \rightarrow \rho(x) \left[1 + \frac{1}{r_e} \sum_{m=1}^4 \lambda_m B f(\varpi) \sin(m\phi) \right] \quad (5.6)$$

is added to the equilibrium polytrope. Here, $m \in \{1, 2, 3, 4\}$, λ_m is either 0 or 1, ϖ is the cylindrical radius and $f(\varpi)$ is a radial trial function. Experiments have been made with $f(\varpi) = \varpi$ and $f(\varpi) = \varpi^m$, but the exact choice was found not to affect the results significantly. This is true quite generally, since we only require the trial function to have some reasonable overlap with a set of quasi-normal modes. It is beyond our scope to investigate the full spectrum of quasi-normal modes of general relativistic polytropes; therefore, we determine stability only with respect to specific trial functions. The choice made is not completely arbitrary, however: a quasi-toroidal polytrope has an off-center toroidal region of maximal density, and it is this region which will dominate the gravitational wave signal if a fragmentation instability sets in. A linear perturbation without nodes in this region can be expected to be compatible (have non-zero scalar product) with most low-frequency quasi-normal modes. The function $f(\varpi) = \varpi^m$ has the additional property of smoothness at the center, but, as already noted, numerical experiments have shown the difference to be negligible in practice. An additional note on the use of language: If we find that a perturbation with $\lambda_j = \delta_{ij}$, $j \in \{1, 2, 3, 4\}$ leads to an instability with the associated number of node lines in the equatorial plane, we will denote this instability with the term $m = j$ mode (and the corresponding perturbation $m = j$ perturbation). This is a simplification insofar as each m is expected to represent a (discrete) infinite spectrum of modes [147], from which we will observe only the fastest-growing unstable member. While we will attempt to discuss the nature of the global evolution to some extent, we will, for the reasons stated above, concentrate on the high-density torus, and mostly neglect the dynamics of its halo.

The perturbations applied are both constraint-violating. This is no significant issue, since the discrete evolution of the BSSN system will necessarily introduce constraint violations even if some minimization technique has been applied to the initial data. Fig. 5.1 shows the evolution of the L^2 norm of the

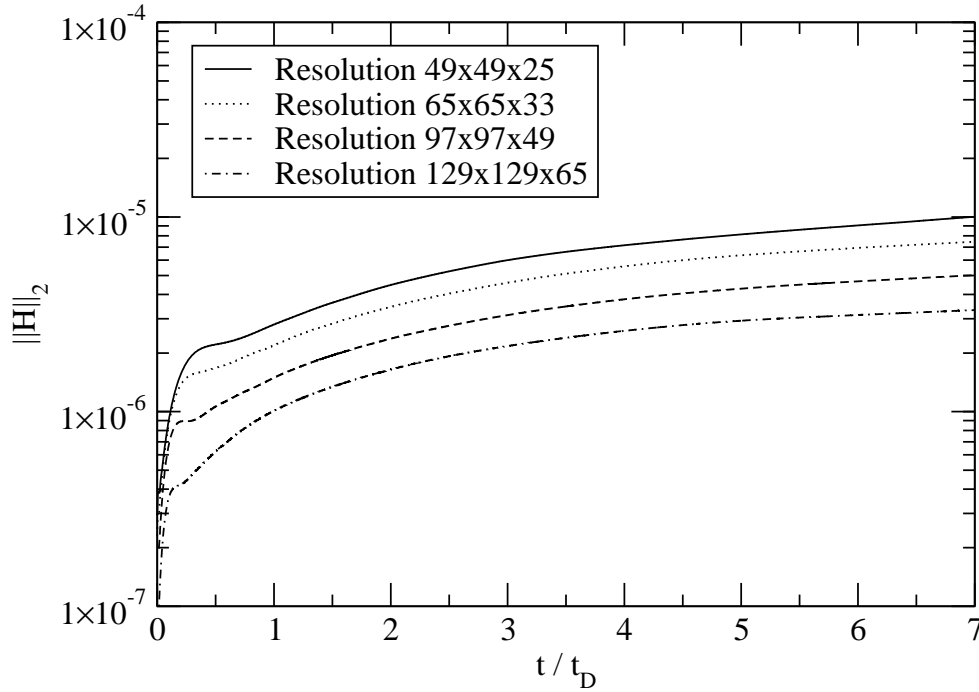


Figure 5.1: Time evolution of the L^2 norm of the Hamiltonian constraint for different resolutions. The time is normalized to the dynamical timescale $t_D = R_e \sqrt{R_e/M}$.

Hamiltonian constraint for different grid resolutions. Note that, for a typical perturbation amplitude of $\delta\rho/\rho \approx 10^{-3}$, the Hamiltonian constraint will be violated by $\delta H \approx 16\pi\rho \cdot 10^{-3} \approx 2.5 \cdot 10^{-7}$, which is sufficiently smaller than the violations during evolution in Fig. 5.1. Also, tests have been performed where the perturbation amplitude B (cf. eqn. 5.6) is reduced by a factor of 10, and found that this does not affect the growth rate of the perturbation, as one might expect from small perturbations. To conveniently compare different resolutions, the amplitude is kept constant; however, it is possible to reduce the perturbation amplitudes for resolutions significantly higher than the ones used here (specifically, in the regime where δH would become comparable to the constraint violations during evolutions) to obtain a system where convergence, now to the equilibrium system, does only depend on the well-posedness of the continuum IBVP and the stability of the discrete system⁴.

5.2.2. The reference polytrope and associated sequences

We start with a polytrope with the same central rest-mass density ($\rho_c = 3.38 \cdot 10^{-6}$) as Saijo's series of differentially rotating supermassive star models [62]. To obtain experience with the influence of certain parameters on the stability properties of the relativistic quasi-toroidal polytropes, some sequences containing this *reference model* have been constructed.

Polytropic index Γ	Γ	4/3
Central rest-mass density	ρ_c	$3.38 \cdot 10^{-6}$
Degree of differential rotation	A	1/3
Coordinate axes ratio	r_p/r_e	0.24
Density ratio	ρ_{max}/ρ_c	16.76
ADM mass	M	6.989
Rest mass	M_0	7.037
Equatorial inverse compactness	R_e/M	11.71
Angular momentum	J	52.00
Normalized angular momentum	J/M^2	1.065
Kinetic over binding energy	$T/ W $	0.227
(See caption)	Ω_e/Ω_K	0.467

Table 5.1.: Parameters and integral quantities of the reference quasi-toroidal polytrope [134]. The quantities Γ , ρ_c , A and r_p/r_e are parameters. The quantity Ω_e is the angular velocity on the equator, while Ω_K is the associated Keplerian velocity. Therefore, the mass-shedding sequence is located at $\Omega_e/\Omega_K = 1$.

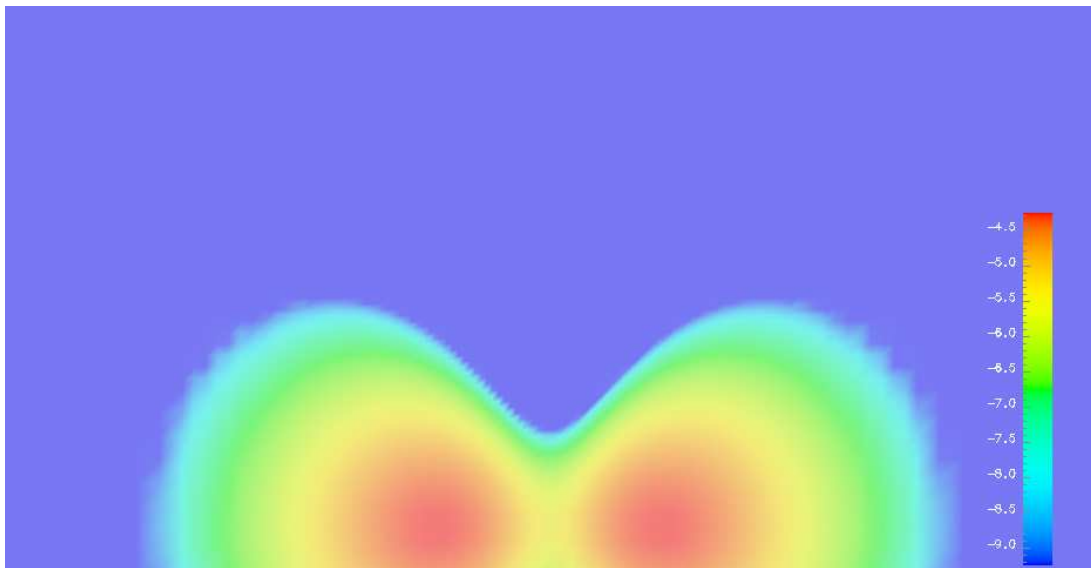


Figure 5.2.: Decadic logarithm of the density in a meridional plane of the model constructed with the parameters in Table 5.1. The model is of quasi-toroidal nature.

Model	ρ_c	r_p/r_e	ρ_{max}/ρ_c	M	M_0	R_e/M	J	J/M^2	$T/ W $	Ω_e/Ω_K
<i>R0.20</i>	$3.38 \cdot 10^{-6}$	0.20	38.12	6.181	6.200	9.660	38.59	1.010	0.235	0.487
<i>R0.22</i>	$3.38 \cdot 10^{-6}$	0.22	25.69	6.662	6.710	10.41	45.46	1.024	0.228	0.475
<i>R0.24</i>	$3.38 \cdot 10^{-6}$	0.24	16.76	6.989	7.037	11.71	52.00	1.065	0.227	0.467
<i>R0.26</i>	$3.38 \cdot 10^{-6}$	0.26	11.07	7.334	7.391	13.10	58.99	1.097	0.223	0.460
<i>R0.28</i>	$3.38 \cdot 10^{-6}$	0.28	7.312	7.585	7.646	14.83	65.19	1.133	0.219	0.455
<i>R0.30</i>	$3.38 \cdot 10^{-6}$	0.30	4.733	7.764	7.825	17.13	70.82	1.175	0.213	0.452
<i>R0.32</i>	$3.38 \cdot 10^{-6}$	0.32	2.934	7.847	7.905	20.46	75.48	1.226	0.207	0.452
<i>R0.34</i>	$3.38 \cdot 10^{-6}$	0.34	1.539	7.755	7.803	27.42	78.72	1.309	0.196	0.463

Table 5.2.: Parameters and integral quantities of the R sequence of axes ratios, which contains the reference model for $r_p/r_e = 0.24$. Each member of the sequence is denoted by the term $R\langle r_p/r_e \rangle$. All models have $\Gamma = 4/3$ and $A = 1/3$.

5.2.2.1. The reference model

The reference model is identical to the model used in [134]; its parameters and integral quantities are shown in Table 5.1. Fig. 5.2⁵ is a graph of the density in the meridional plane for this model. This model has been found to be unstable to perturbations with $m = 1$ and $m = 2$ (see below, and [134]), which lead to a fragmentation. In the case $m = 1$, black hole formation has been demonstrated by location of an apparent horizon centered on the fragment.

5.2.2.2. The sequence of axes ratios

A number of sequences containing this model have been constructed to study the stability properties when varying typical parameters. The first of these sequences is parameterized by the coordinate axes ratio r_p/r_e . Its members are denoted by $R\langle r_p/r_e \rangle$, and their properties can be found in Table 5.2. It is apparent that, with increasing axes ratios, the quantity $T/|W|$ and the ratio of maximal to central rest-mass density ρ_{max}/ρ_c both decrease monotonically. None of the sequence members is close to the mass-shedding limit. Below $r_p/r_e = 0.20$, no models could be constructed due to failure of convergence. We will also not consider models with larger r_p/r_e . The reason for this is indicated in Fig. 5.3: Beyond an axes ratio of $r_p/r_e \approx 0.3423$, quasi-toroidal models could not be constructed, and the discontinuity in $T/|W|$ indicates that the sequence terminates at this value.

5.2.2.3. The sequence of stiffnesses

This sequence is a variation of the parameter Γ in the polytropic relation $P = K\rho^\Gamma$, which also determines the stiffness of the ideal fluid equation of state $P = (\Gamma - 1)\rho\epsilon$ used for evolution. To obtain a sequence of comparable compactness, we adjust the central density ρ_c to yield approximately the same R_e/M . The parameters and integral quantities are shown in Table 5.3, and selected stratifications are depicted in Fig. 5.5. Along the sequence of increasing Γ , the value $T/|W|$ decreases from 0.227 to 0.159. Therefore, it would be also interesting to consider a sequence of models with varying Γ , but constant $T/|W|$ by adjusting the axes ratio r_p/r_e accordingly. Unfortunately, such a sequence could not be obtained, since the initial data solver did not converge to models with the required (low) axes ratios.

⁴In addition, this would, of course, require to reduce the density of the artificial atmosphere with resolution.

⁵Note that the contour plots are included to demonstrate the qualitative properties of representative solutions. Therefore, no detailed scale is provided.

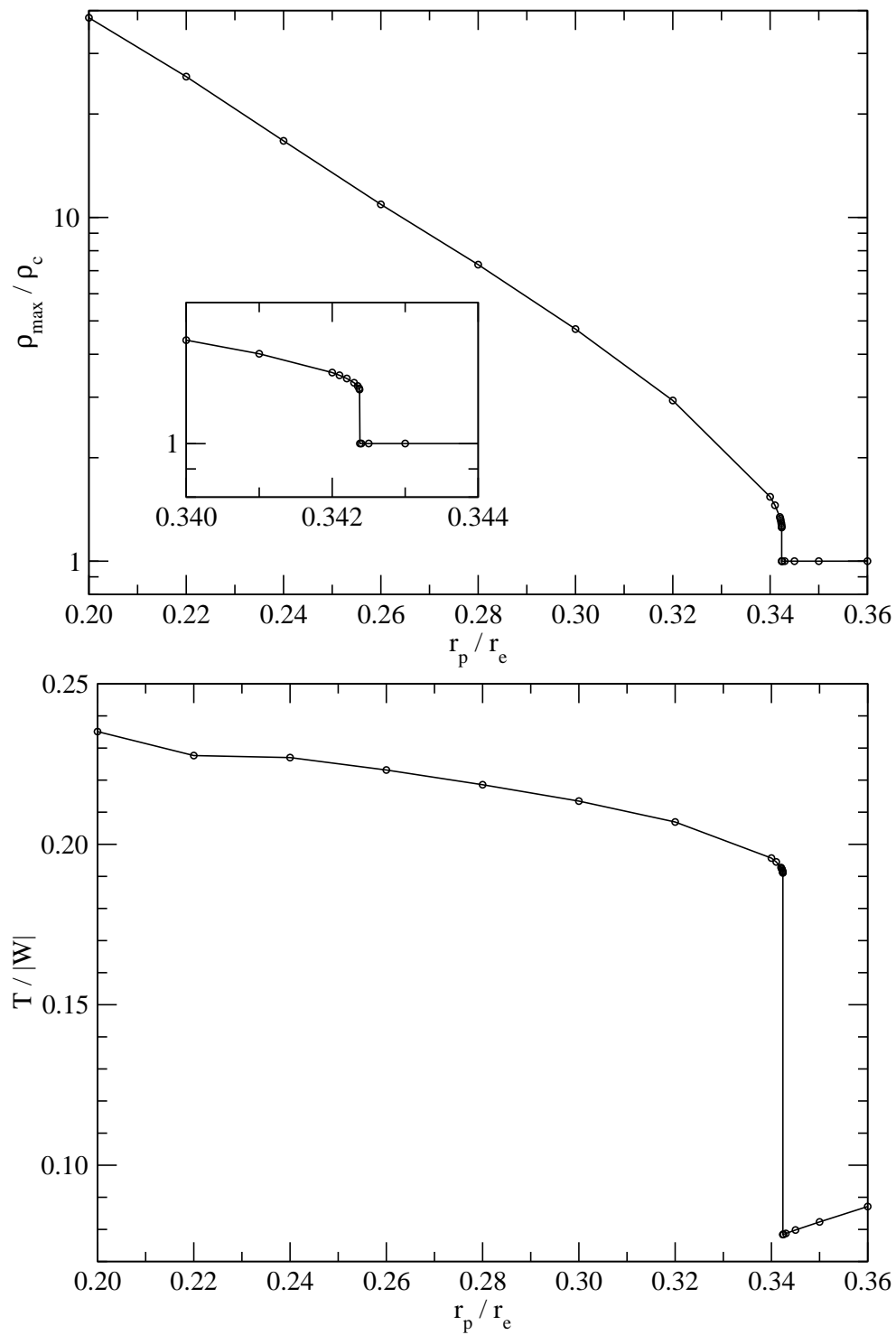


Figure 5.3.: ρ_{\max}/ρ_c (top) and $T/|W|$ (bottom) for the R sequence. Beyond an axes ratio of $r_p/r_e \approx 0.3423$, the initial data solver converges to spheroidal models. The discontinuity in $T/|W|$ indicates that the quasi-toroidal sequence terminates there.

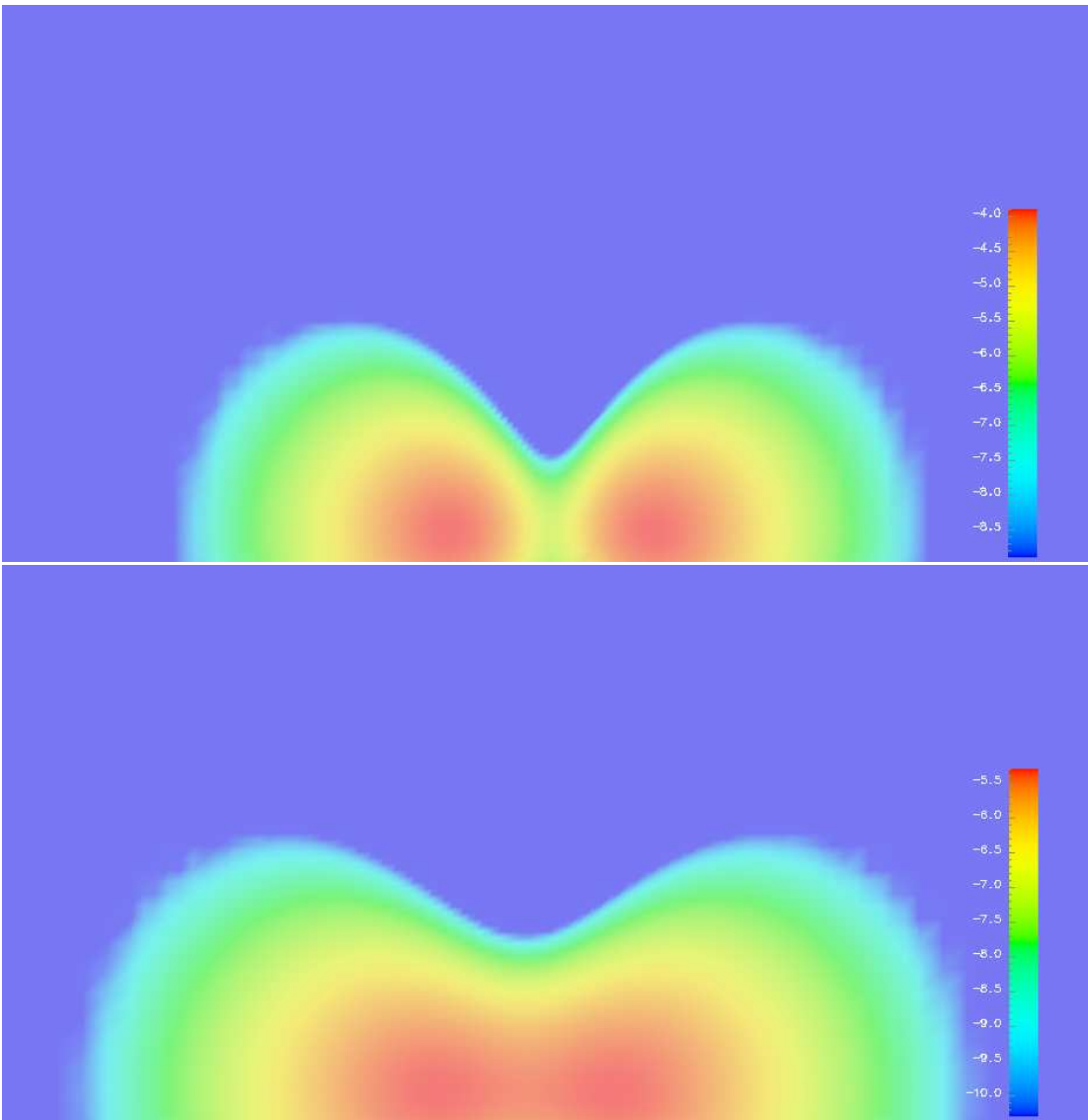


Figure 5.4.: Decadic logarithm of the density in a meridional plane of the R sequence members $R0.20$ (top) and $R0.34$ (bottom).

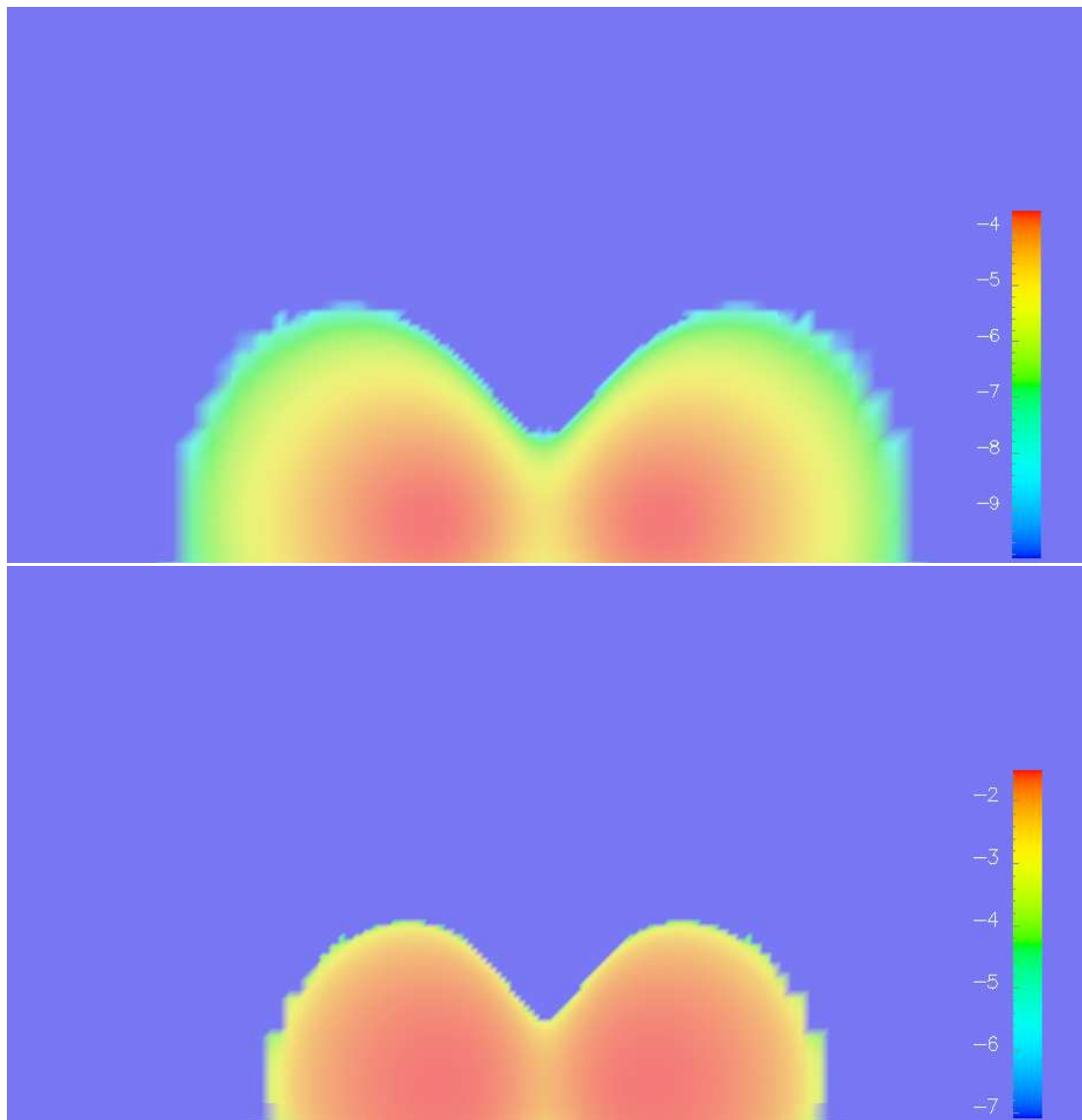


Figure 5.5.: Decadic logarithm of the density in a meridional plane of the G sequence members $G1.45$ (top) and $G2.0$ (bottom). The model $G1.333$, which is the reference polytrope, is shown in Fig. 5.2.

Model	Γ	ρ_c	ρ_{max}/ρ_c	M	M_0	R_e/M	J	J/M^2	$T/ W $	Ω_e/Ω_K
<i>G1.333</i>	4/3	$3.38 \cdot 10^{-6}$	16.76	6.989	7.037	11.71	52.00	1.065	0.227	0.467
<i>G1.4</i>	1.4	$1.32 \cdot 10^{-5}$	16.44	2.805	2.856	11.69	8.337	1.059	0.211	0.424
<i>G1.45</i>	1.45	$3.7 \cdot 10^{-5}$	13.83	1.624	1.662	11.70	2.767	1.049	0.202	0.404
<i>G1.5</i>	1.5	$9.2 \cdot 10^{-5}$	11.53	1.038	1.066	11.65	1.115	1.035	0.194	0.390
<i>G1.6</i>	1.6	$3.75 \cdot 10^{-4}$	8.349	0.5197	0.5363	11.80	0.2758	1.021	0.183	0.370
<i>G2.0</i>	2.0	$8.2 \cdot 10^{-3}$	3.880	0.1270	0.1323	11.69	0.0155	0.9633	0.159	0.331

Table 5.3.: Parameters and integral quantities of the G sequence of polytropic coefficient Γ , which contains the reference model for $\Gamma = 4/3$. Each member of the sequence is denoted by the term $G\langle\Gamma\rangle$. The central density is adjusted to yield approximately the same inverse equatorial compactness R_e/M as in the reference model. The models *G1.7* to *G1.9* have not been constructed, since the models *G1.6* and *G2.0* were found to be stable. All models have $A = 1/3$ and $r_p/r_e = 0.24$.

Model	ρ_c	r_p/r_e	ρ_{max}/ρ_c	M	M_0	R_e/M	J	J/M^2	$T/ W $	Ω_e/Ω_K
<i>C1</i>	$3.38 \cdot 10^{-6}$	0.24	16.76	6.989	7.037	11.71	52.00	1.065	0.227	0.467
<i>C2</i>	$1 \cdot 10^{-7}$	0.24	31.06	10.65	10.74	22.72	167.0	1.474	0.225	0.434
<i>C4</i>	$7.5 \cdot 10^{-9}$	0.24	37.01	12.54	12.60	45.65	326.0	2.073	0.225	0.423
<i>C8</i>	$8 \cdot 10^{-10}$	0.24	39.64	13.47	13.51	89.91	525.6	2.897	0.225	0.419

Table 5.4.: Parameters and integral quantities of the C sequence of compactnesses, which contains the reference model for $\rho_c = 3.38 \cdot 10^{-6}$. Each member of the sequence is denoted by the term $C\langle a \rangle$, where a denotes the approximate ratio of R_e/M to $(R_e/M)_{ref}$ of the reference model *C1*. The sequence is obtained by varying the central rest-mass density. All models have $\gamma = 4/3$ and $A = 1/3$.

5.2.2.4. The sequence of compactnesses

The next sequence is a variation of the central rest-mass density ρ_c while leaving all other parameters fixed. The resulting sequence, as is apparent from Table 5.4, is also a sequence of *inverse equatorial compactnesses* R_e/M . The members have been selected to represent models which are half to one eighth as compact as the reference polytrope. The sequence shows that $T/|W|$ is only slightly affected by the choice of ρ_c , but R_e/M and J/M^2 change significantly. The density structure of selected models is shown in Fig. 5.6.

5.2.3. Quasi-toroidal and spheroidal models of constant central rest-mass density

In addition to sequences containing the reference model, we explore a more extended part of the parameter space of models. We use $\Gamma = 4/3$ and $\rho_c = 10^{-7}$ to define a surface in the parameter space spanned by the axes ratio r_p/r_e and the degree of differential rotation A . While an ideal fluid with $\Gamma = 4/3$ is an approximation for the material properties of radiation-pressure dominated stars, the restriction to $\rho_c = 10^{-7}$ is arbitrary. However, as discussed in Section 5.3, the non-axisymmetric stability of the quasi-toroidal models is probably less sensitive to ρ_c than to r_p/r_e or A . The restriction to a plane is necessary since three-dimensional simulations of quasi-toroidal relativistic stars are still expensive; however, selected models will also be studied with different ρ_c in Section 5.3.

The general structure of the polytropes obtained with the SF code is shown for central rest-mass densities $\rho_c = 10^{-7}$ and 10^{-10} in Fig. 5.7 to 5.11. The first plot shows the function Ω_e/Ω_K , where Ω_e is the

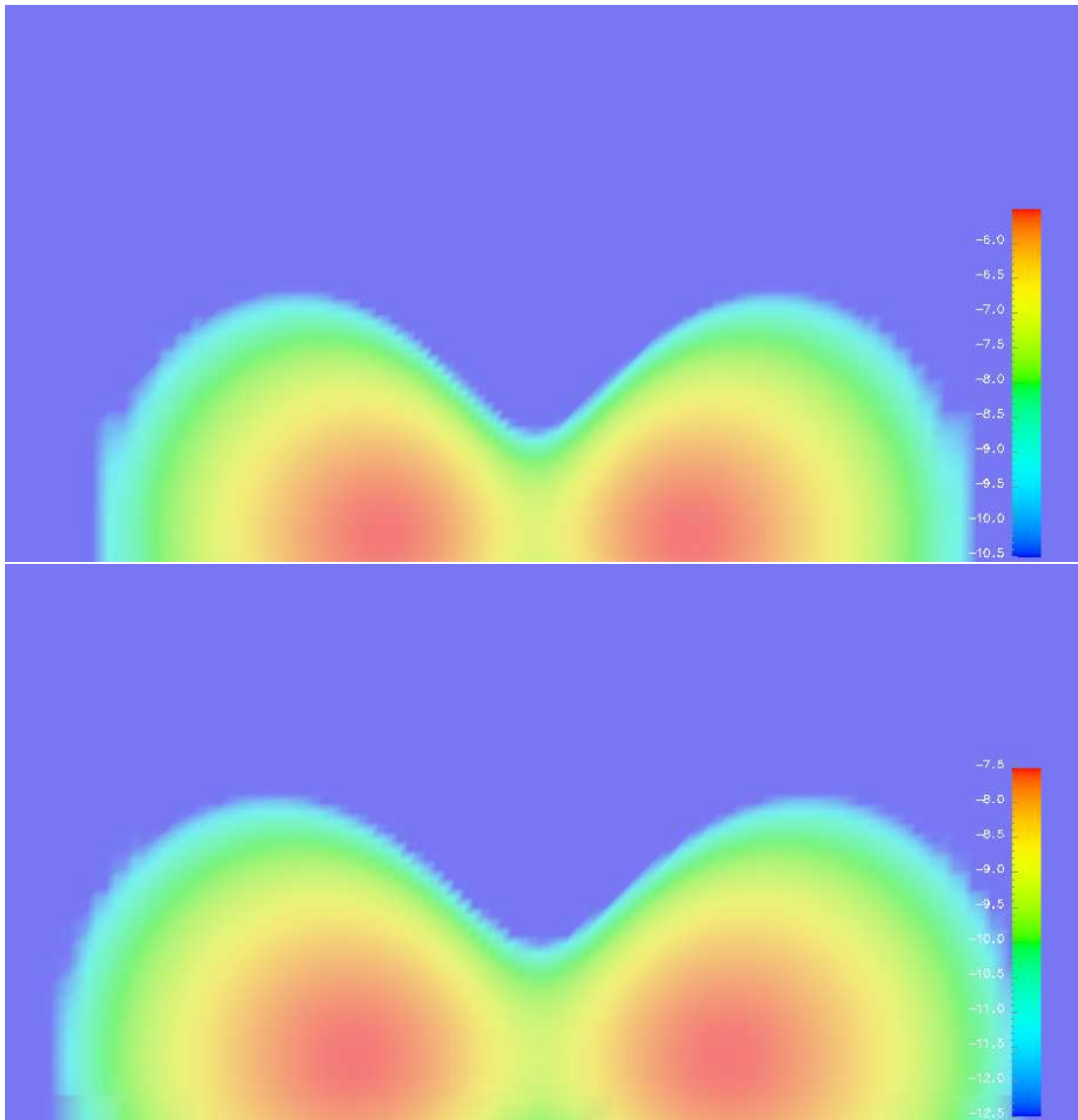


Figure 5.6.: Decadic logarithm of the density in a meridional plane of the C sequence members $C2$ (top) and $C8$ (bottom). The model $C1$, which is the reference polytrope, is shown in Fig. 5.2.

Model	ρ_c	A	r_p/r_e	ρ_{max}/ρ_c	M	M_0	R_e/M	J	J/M^2	$T/ W $	Ω_e/Ω_K
$A0.1R0.15$	10^{-7}	0.1	0.15	246.8	4.896	4.893	20.82	18.62	0.777	0.124	0.195
$A0.1R0.50$	10^{-7}	0.1	0.5	1.881	5.387	5.390	106.2	31.69	1.092	0.0706	0.126
$A0.3R0.15$	10^{-7}	0.3	0.15	356.9	7.964	8.034	12.04	70.66	1.114	0.228	0.434
$A0.3R0.50$	10^{-7}	0.3	0.5	1.00005	6.291	6.300	151.4	77.10	1.948	0.108	0.360
$A0.6R0.15$	10^{-7}	0.6	0.15	541.2	21.29	21.39	61.62	1360	3.000	0.276	0.650

Table 5.5.: Parameters and integral quantities of selected quasi-toroidal models in the parameter space plane defined by $\rho_c = 10^{-7}$ and $\Gamma = 4/3$. The models are labelled by $A\langle A \rangle R\langle r_p/r_e \rangle$. All models have $\Gamma = 4/3$.

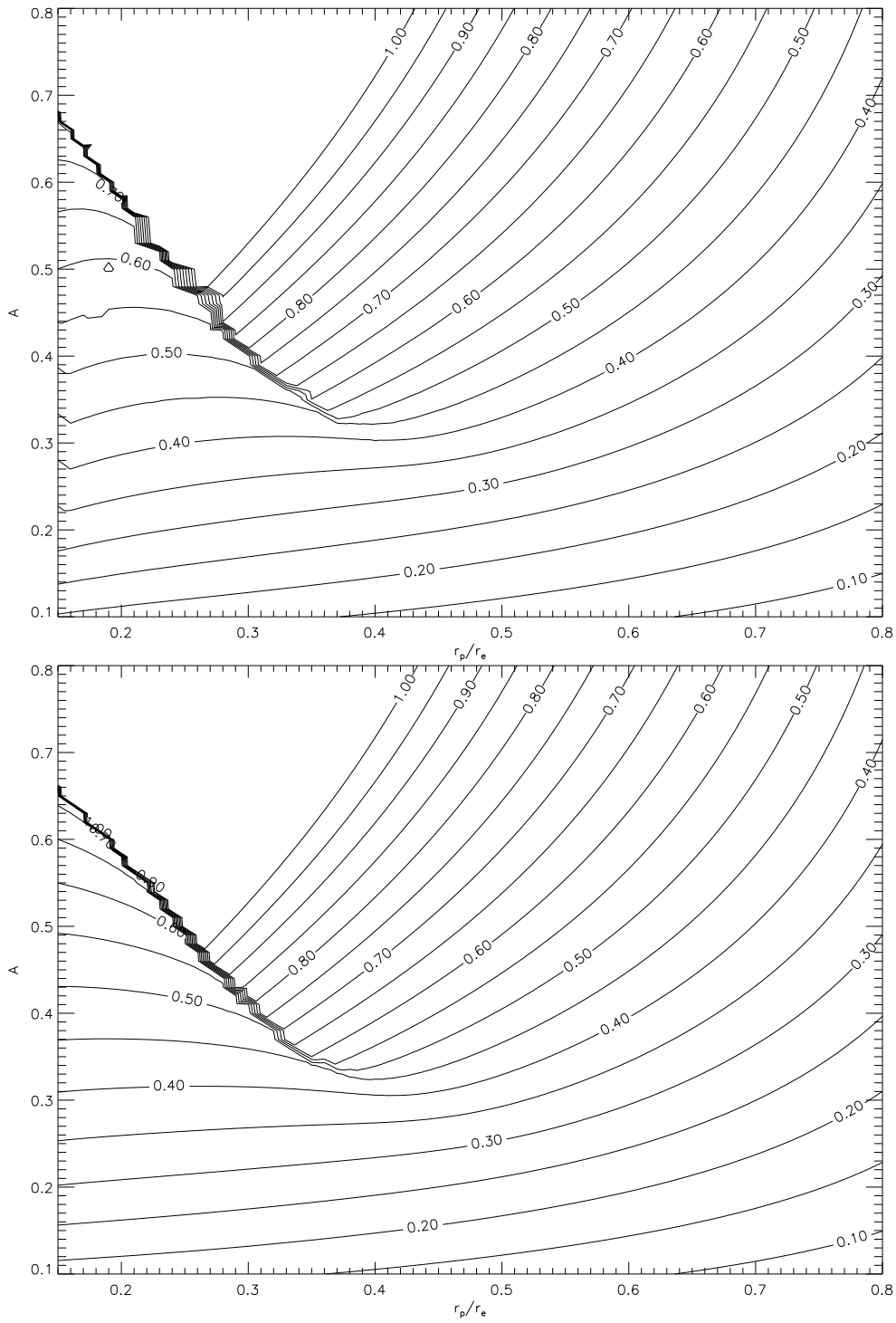


Figure 5.7.: Polytropic models constructed with the SF code. Shown are contours of the function Ω_e/Ω_K (equatorial stellar angular over Keplerian angular velocity) over the axes ratio r_p/r_e and the differential rotation parameter A , for $\rho_c = 10^{-7}$ (top) and $\rho_c = 10^{-10}$ (bottom). The mass-shedding sequence corresponds to the function value 1. The plot has been obtained by construction of 6400 (80×80) models in the $(r_p/r_e, A)$ plane.

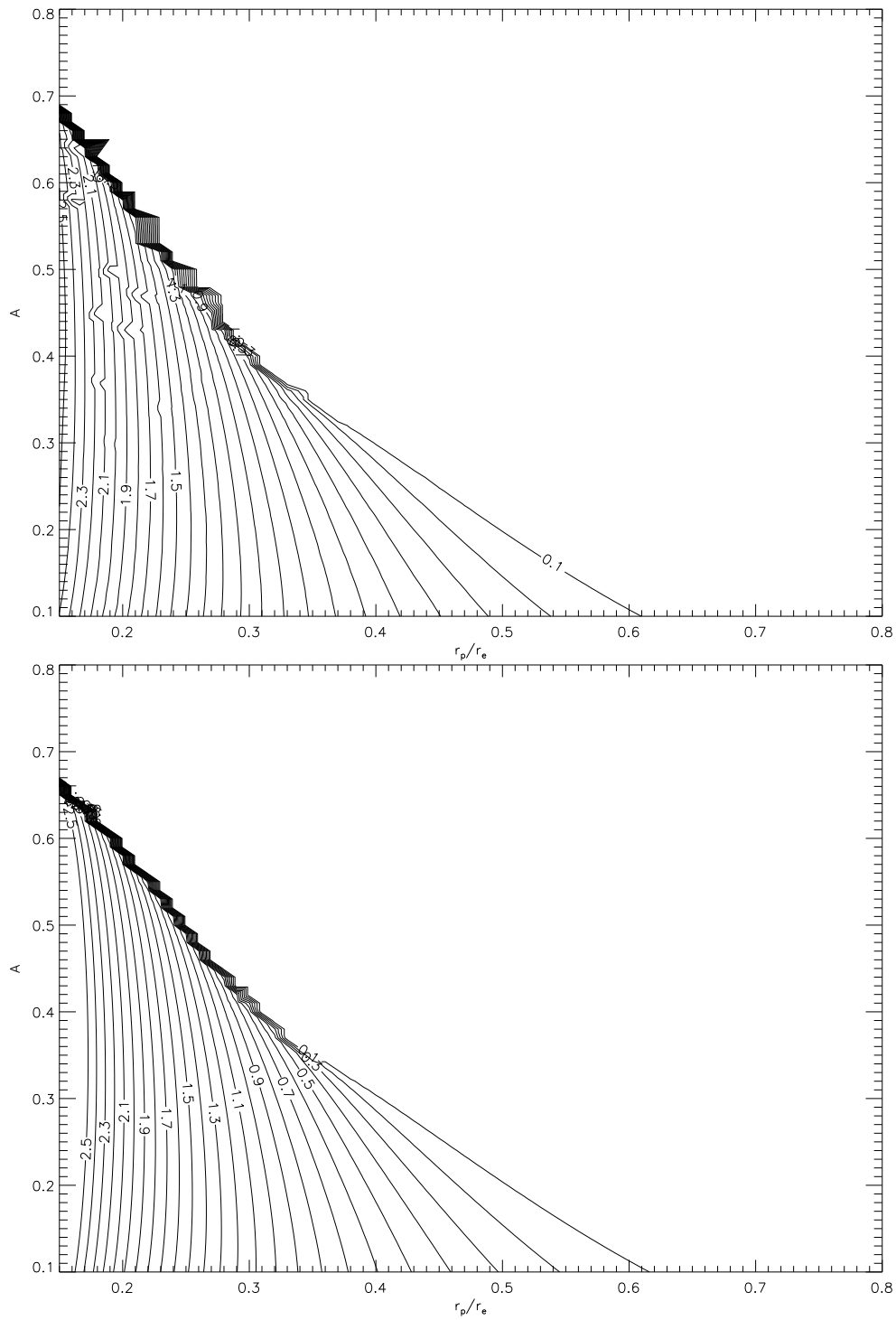


Figure 5.8.: As Fig. 5.7, but showing the contours of the decadic logarithm of the ratio of maximal to central density $\log_{10}(\rho_{max}/\rho_c)$. Models in the region without contours have $\rho_{max}/\rho_c \approx 1$, and are thus spheroidal.

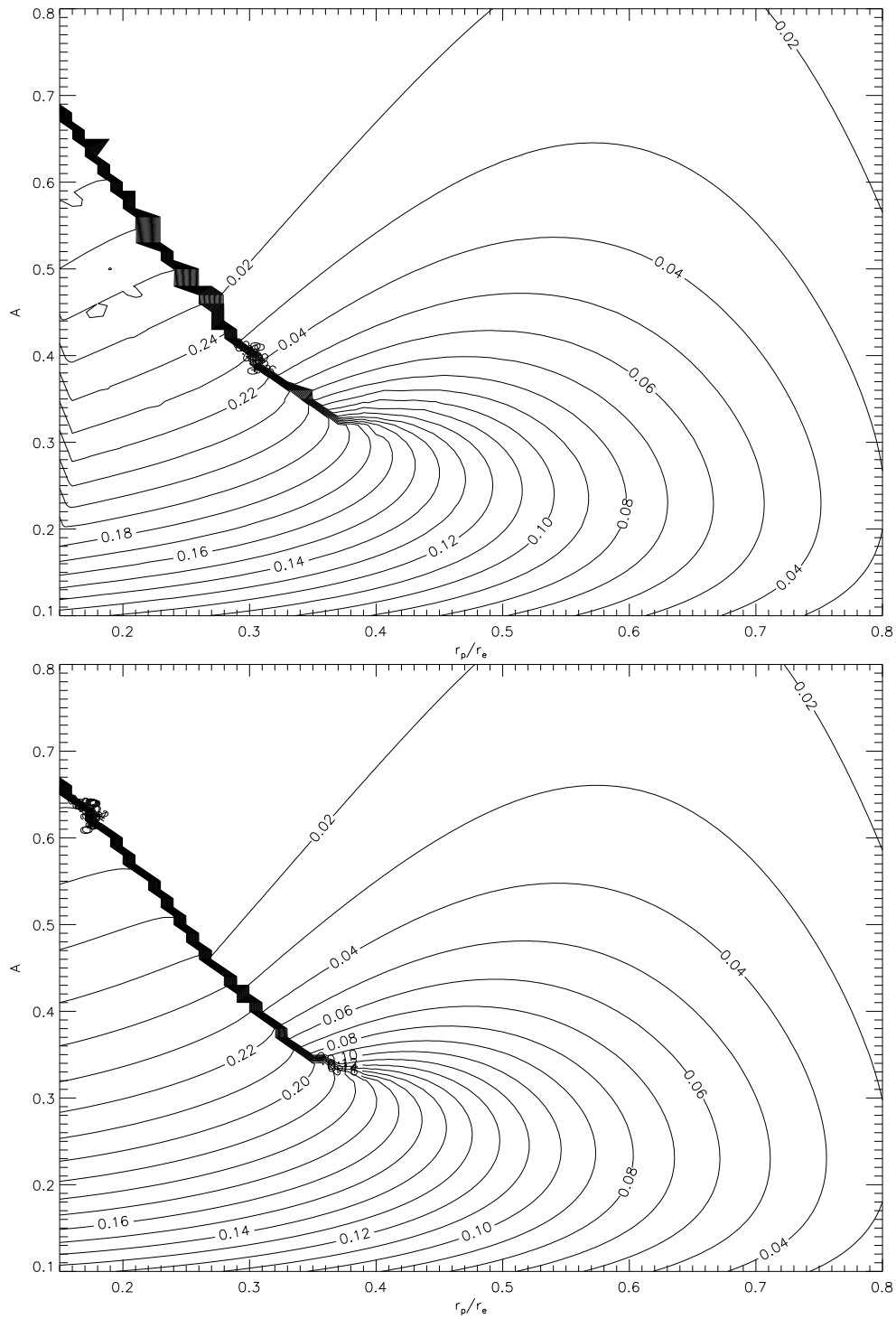


Figure 5.9.: Same as Fig. 5.7, but showing the contours of the rotation parameter $T/|W|$.

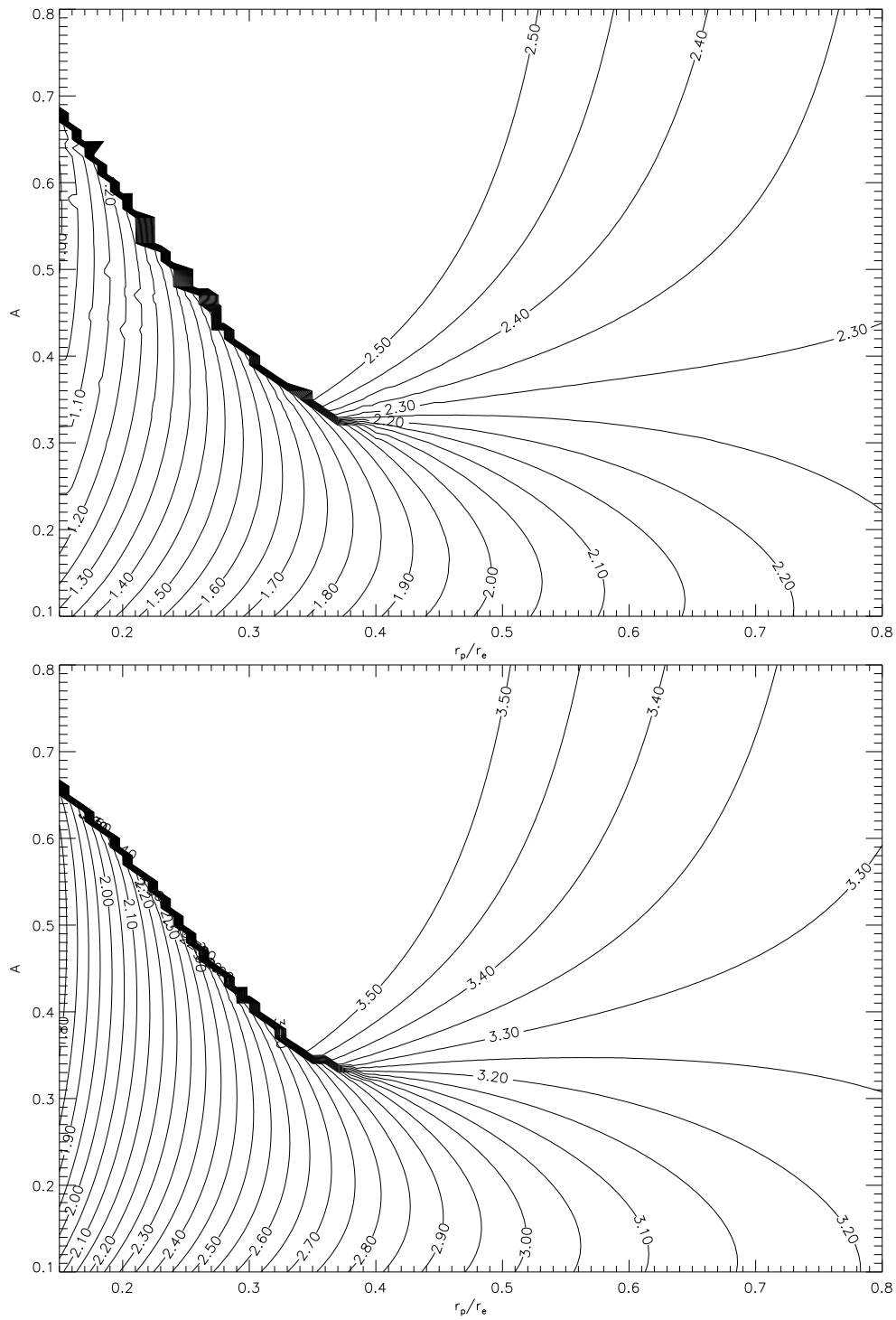


Figure 5.10.: Same as Fig. 5.7, but showing the contours of the decadic logarithm of the inverse equatorial compactness R_e/M .

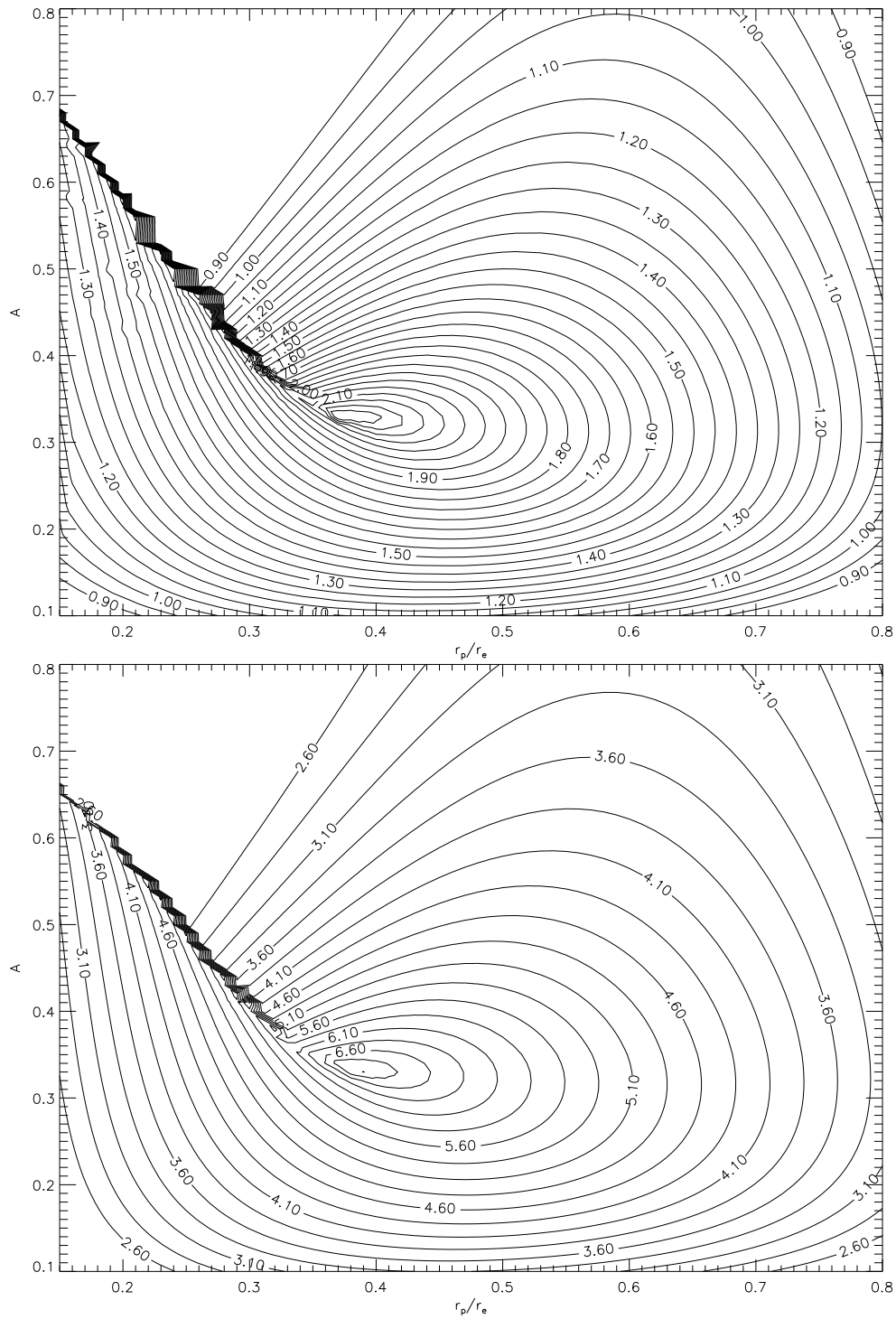


Figure 5.11.: Same as Fig. 5.7, but showing the contours of the function J/M^2 .

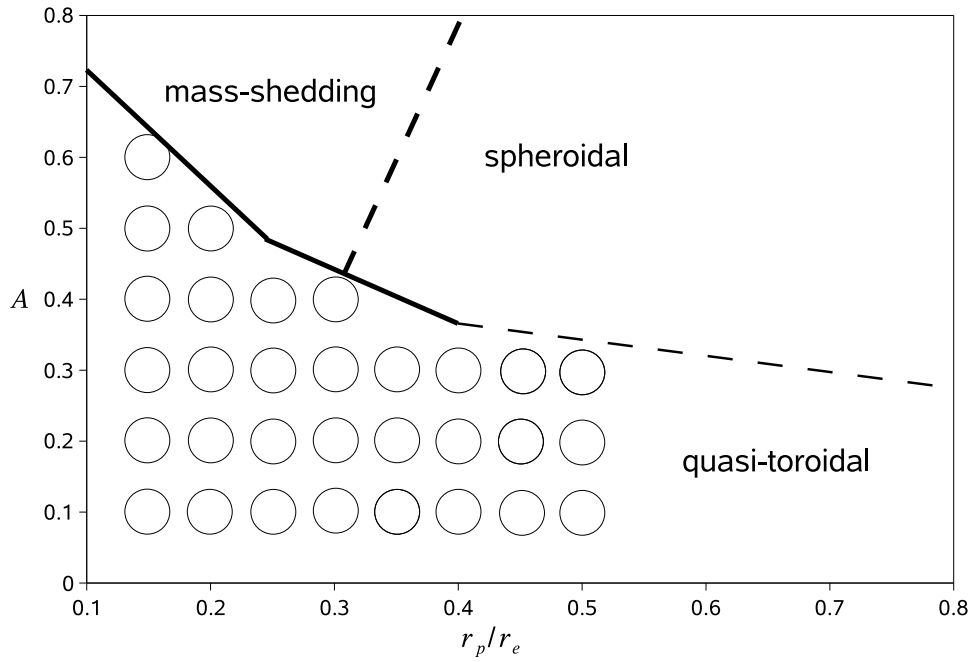


Figure 5.12.: Parameters space constrained by $\rho_c = 10^{-7}$ and $\Gamma = 4/3$. The thick continuous line marks the discontinuity apparent in Fig. 5.7 to 5.11, the thick dashed line is the mass-shedding limit, and the thin dashed line indicates an approximate division between spheroidal and quasi-toroidal models. The models selected for numerical evolution are marked by circles.

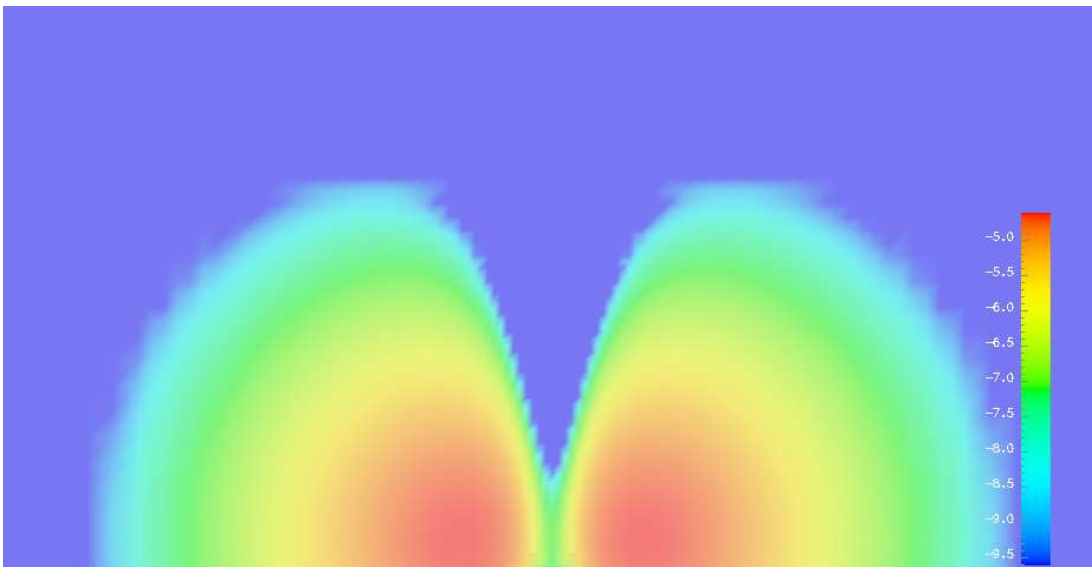


Figure 5.13.: Decadic logarithm of the density in a meridional plane of the model *A0.1R0.15*.

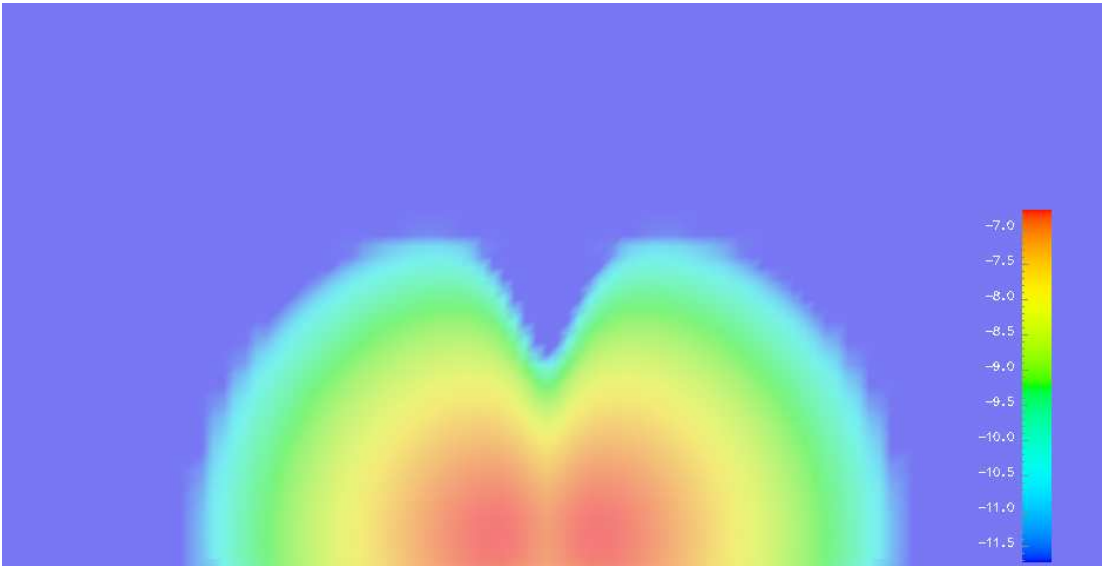


Figure 5.14.: Decadic logarithm of the density in a meridional plane of the model A0.1R0.50.

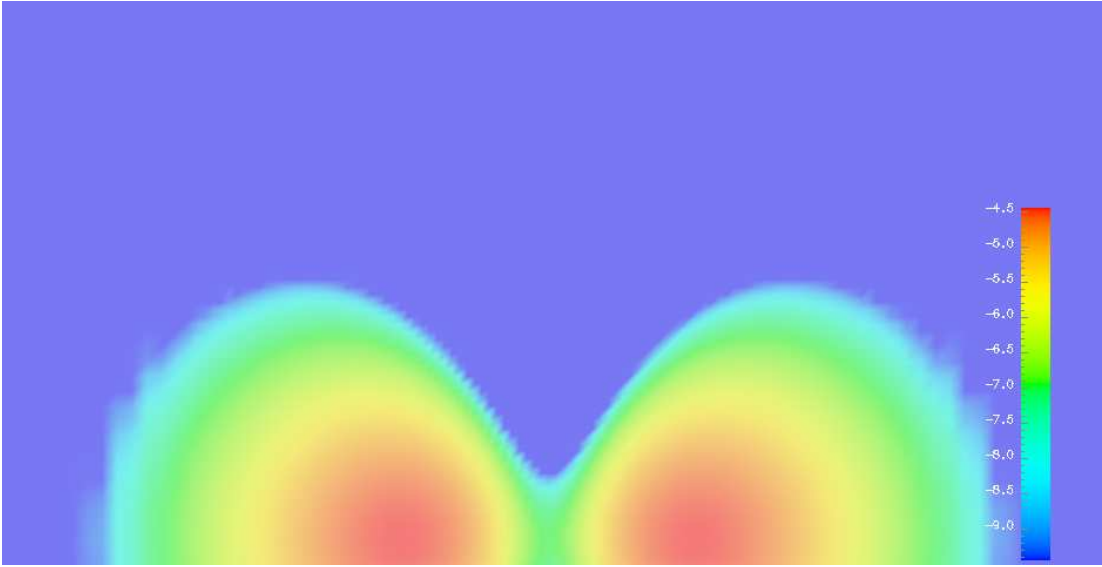


Figure 5.15.: Decadic logarithm of the density in a meridional plane of the model A0.3R0.15.

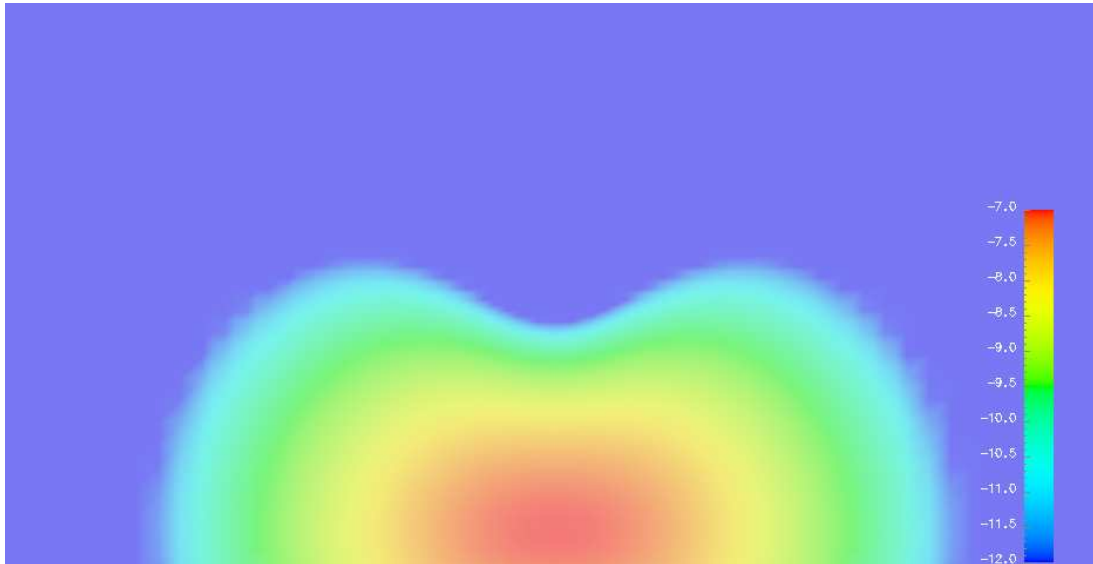


Figure 5.16.: Decadic logarithm of the density in a meridional plane of the model *A0.3R0.50*.

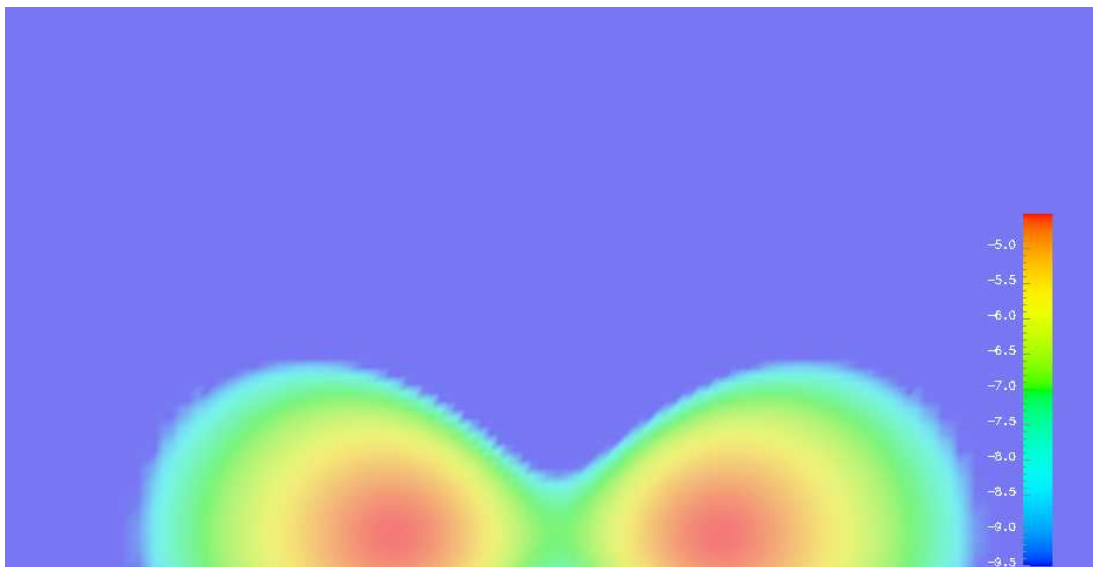


Figure 5.17.: Decadic logarithm of the density in a meridional plane of the model *A0.6R0.15*.

Model	Γ	ρ_c	A	r_p/r_e	ρ_{max}/ρ_c	M	M_0	R_e/M	J	J/M^2	$T/ W $	Ω_e/Ω_K
<i>L1</i>	4/3	10^{-4}	0.2	0.354	1.874	3.621	3.578	14.85	9.952	0.760	0.144	0.301
<i>L2</i>	4/3	10^{-5}	0.2	0.378	2.434	5.173	5.177	20.67	24.06	0.900	0.144	0.280
<i>L3</i>	4/3	10^{-6}	0.2	0.392	2.644	6.505	6.524	35.69	49.51	1.170	0.144	0.269
<i>L4</i>	4/3	10^{-7}	0.2	0.4	2.689	7.348	7.362	69.41	87.33	1.617	0.144	0.264

Table 5.6.: Parameters and integral quantities of the *L* sequence. This sequence is constructed by starting from the model *A0.2R0.40* (cf. Section 5.2.3), which is identical to the model *L4*, and keeping $T/|W|$ fixed while reducing the central density.

equatorial stellar angular velocity, and Ω_K is the corresponding Keplerian angular velocity. The discontinuity in the equilibrium model surface has already been found in the *R* sequence, see Fig. 5.3.

The topological nature of the polytropes is shown in Fig. 5.8, which plots the ratio of maximal to central rest-mass density ρ_{max}/ρ_c . This value measures the degree of toroidal deformation of the model, with the limiting cases $\rho_{max}/\rho_c = 1$ (purely spheroidal polytrope) and $\rho_{max}/\rho_c = \infty$ (purely toroidal polytrope). Since we are interested in the properties of quasi-toroidal models, we will concentrate our study on the part of this plot covered by contour lines.

Judging from the study of Newtonian polytropes, one would expect that the function $T/|W|$ is related to non-axisymmetric stability. For the sequence of Maclaurin spheroids, the dynamically unstable subset can be described by the simple inequality $T/|W| \geq (T/|W|)_{dyn}$ [2], suggesting to use $T/|W|$ to parameterize the sequence. While the situation is clearly more complicated with differentially rotating models, Fig. 5.9 suggests that the quasi-toroidal models near the axis $r_p/r_e = 0.15$ are more likely to be unstable to non-axisymmetric perturbations. We will study this in Section 5.3.

Comparing the results for both choices of central rest-mass density, the structure of the space of equilibrium models appears quite similar. The inverse equatorial compactness R_e/M and the specific angular momentum J/M^2 are sensitive to the choice of ρ_c , while $T/|W|$ is almost unchanged. We will discuss the relevance of this observation in Section 5.4.

Fig. 5.12 is an illustration of the initial model parameter space. The polytropes which have been evolved numerically are marked by circles. The equilibrium parameters and associated quantities of a selected set of these polytropes are listed in Table 5.5. In Fig. 5.13 to 5.17, the density stratifications of these models are plotted.

5.2.4. A sequence of central rest-mass densities containing the model *A0.2R0.40*

The *L* sequence (see Table 5.6) is a variation of the *C* sequence in Section 5.2.2.4. It starts from the model *A0.2R0.40* instead of the reference model. In contrast to the *C* sequence, we do not keep the axes ratio r_p/r_e fixed while varying the central rest-mass density, but rather the quantity $T/|W|$. This sequence is constructed to study the influence of the compactness on a model near the boundary to the region denoted by “I” in Fig. 5.50 (see also Section 5.3.8).

5.3. Results

The models constructed in Section 5.2 have been evolved numerically to study their stability properties. We will start with discussing the reference model, and show that it is unstable to a non-axisymmetric perturbation which leads to black hole formation. Then, the sequences of axes ratios, compactness and stiffness from Section 5.2 are studied. Finally, the parameter plane for $\Gamma = 4/3$ and $\rho_c = 10^{-7}$ is sampled, and the coordinate location of the corotation point on a sequence in this plane is investigated.

5.3.1. Evolution of the reference model

The main results from evolving the reference polytrope defined in Section 5.2.2.2 have already been discussed in [134]. When subject to a perturbation of the form given in eqn. 5.6, the torus transforms into one ($m = 1$) or two ($m = 2$) fragments. The dominant mode is $m = 1$, and in this case, it has been shown that the fragment is partially covered by an apparent horizon, indicating black hole formation.

In this section, we will take a more detailed look at this model, and discuss some technical issues of importance for the parameter space study below.

5.3.1.1. Development of the instability

Fig. 5.18 shows the development of the non-axisymmetric instability in the equatorial plane when using a perturbation of the form given by eqn. 5.6 and $\lambda_m = 1$ for $m = 1, \dots, 4$. The density perturbation is not apparent in the initial model, but, after a few dynamical timescales, an instability has developed which entirely destroys the structure of the star. In this case, one collapsing off-center fragment forms in the system. Judging from Fig. 5.19 and 5.20, there is a “collapse of the lapse”, which is a well-known effect when using singularity-avoiding slicings, and which indicates the development of a black hole.

To investigate the instability more closely, the Fourier mode extraction discussed in Section 3.4 has been applied to the coordinate radius of highest density in the initial model, which is at $r = 0.25R_c$ (note that part of the low-density halo of the star is covered by the atmosphere, which makes the star to appear slightly smaller in Fig. 5.18). We concentrate on this radius for reasons already discussed: different extraction radii will be considered in Section 5.3.1.3. Fig. 5.21 displays the evolution of the amplitude of the first four Fourier modes A_m , $m = 1, \dots, 4$. Although all four modes have been injected with the same amplitude ($\approx 10^{-4}$), the $m = 4$ mode displays a significant initial growth of about an order of magnitude, and then oscillates around this level until $t/t_{dyn} \approx 6$, where non-linear effects become important. The high level of $m = 4$ noise is very likely an artefact of the Cartesian grids used for the simulation. Support for this argument can be obtained by considering that the equatorial section of the grid has a discrete C_4 symmetry, and by comparing Fig. 3 and 4 in [121], where results from the development of a similar non-axisymmetric instability, though in Newtonian gravity, were achieved on cylindrical and Cartesian grids. We note that the model appears to be stable against this mode, and also against the $m = 3$ mode. The remaining modes $m = 1$ and $m = 2$ are unstable, and the growth times of both modes are almost the same. In this specific case the $m = 1$ mode is dominant, and leads to the spiral arm structure and fragmentation visible in Fig. 5.18.

The structure of the numerical noise depends on the grid geometry, resolution, finite difference operators and discrete methods for treating hydrodynamics, the outer boundary conditions and the artificial atmosphere. Therefore, it is important to know to which degree the four Fourier modes are coupled during the evolution. Since the initial perturbation is considered to be “small”, which holds when compared to the $m = 4$ noise level discussed above, we expect that coupling becomes important as soon as the amplitudes A_m get close to unity. To determine this in the reference model, a number of simulations have been performed with perturbations of the form given by eqn. 5.6, but with $\lambda_m = \delta_{mj}$ for different $j \in \{1, \dots, 4\}$

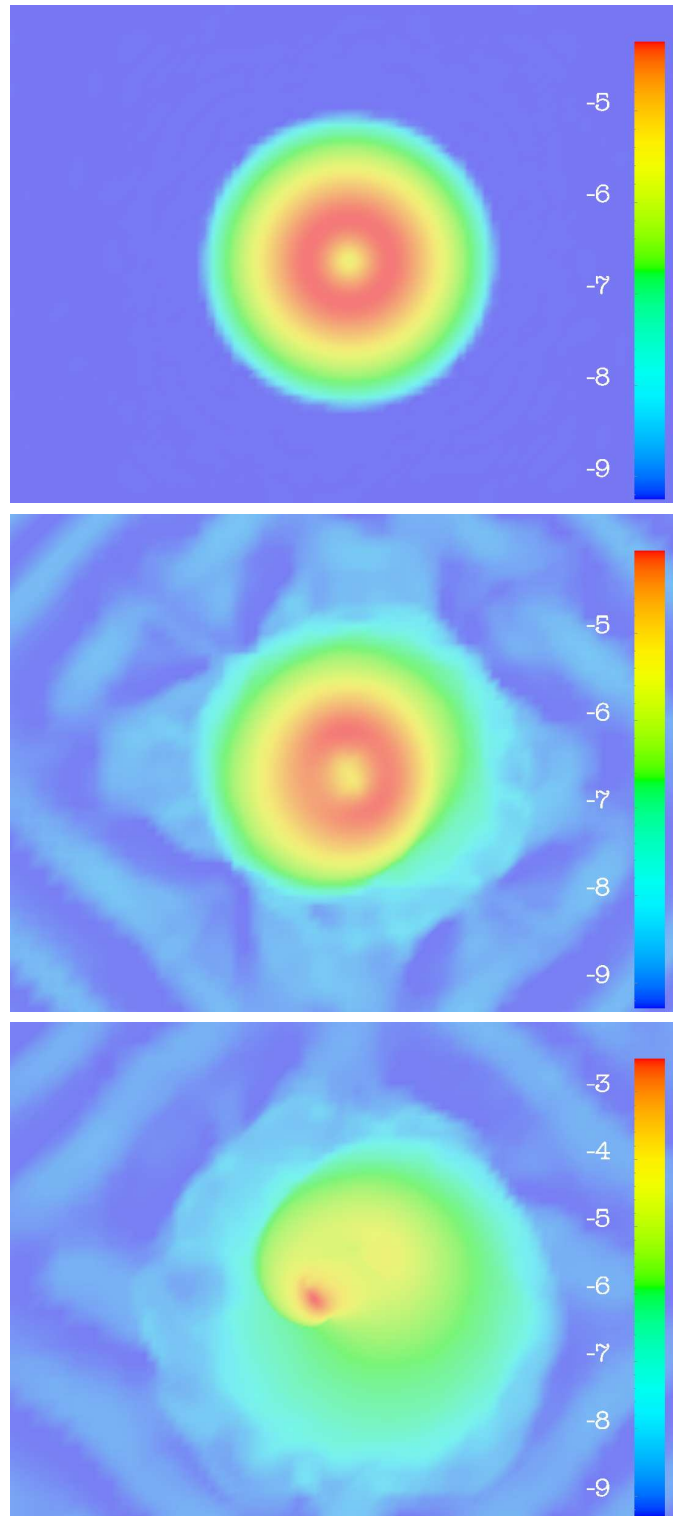


Figure 5.18.: Development of the fragmentation instability in the reference polytrope. Each plot shows the decadic logarithm of rest-mass density in the equatorial plane. The snapshots correspond to times $t/t_{dyn} = 0$ (top), 6.28 (middle) and 7.48 (bottom). The initial model, perturbed by eq. 5.6 with $\lambda_m = 1$ for $m = 1, \dots, 4$, develops a spiral arm instability and a collapsing fragment. Here, and in all evolution sequences which follow, the extent of the spatial coordinate domain plotted is the same in all snapshots.

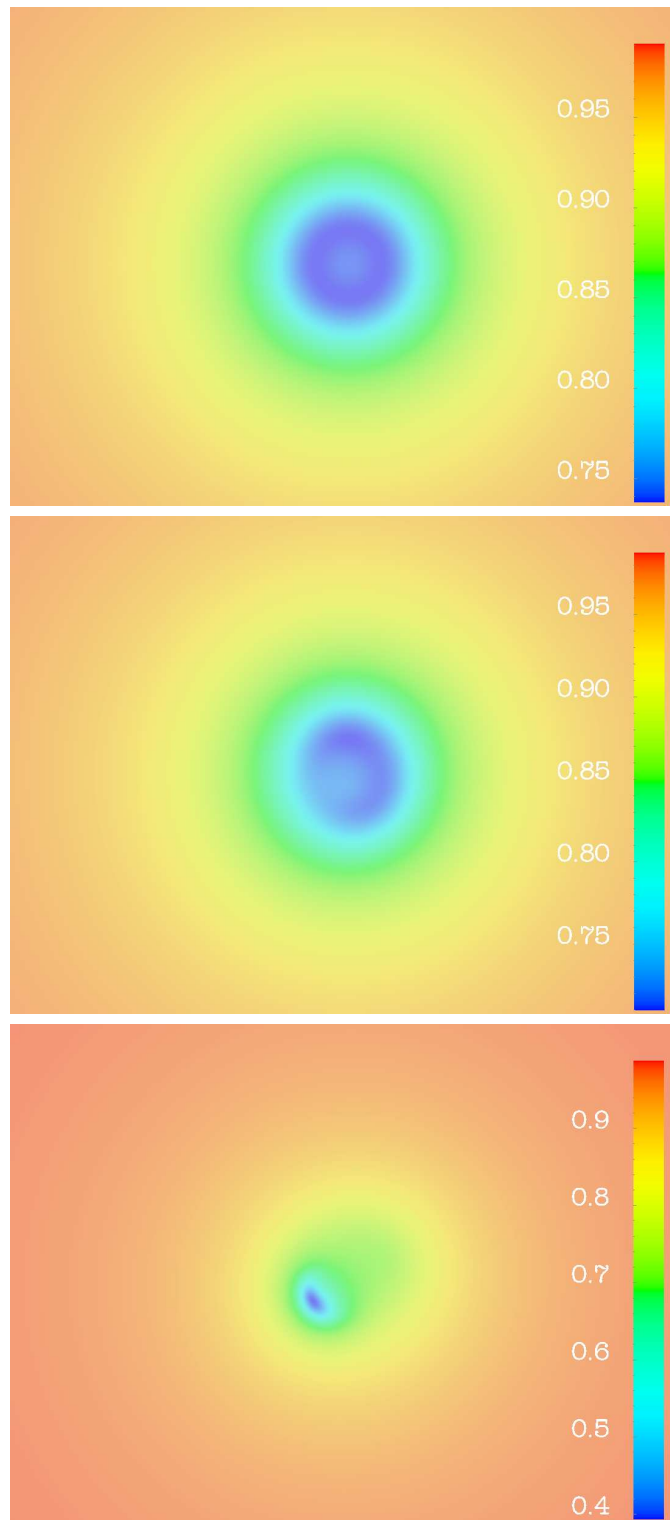


Figure 5.19.: As Fig. 5.18, but showing the lapse function. Note the collapse of the lapse at late times.

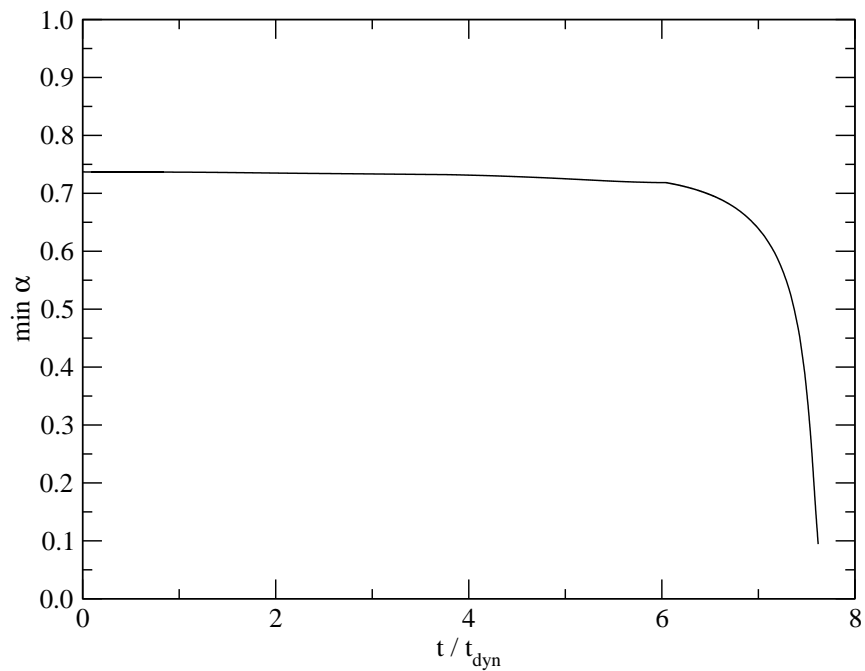


Figure 5.20.: Minimum of the lapse function α for the evolution shown in Fig. 5.19.

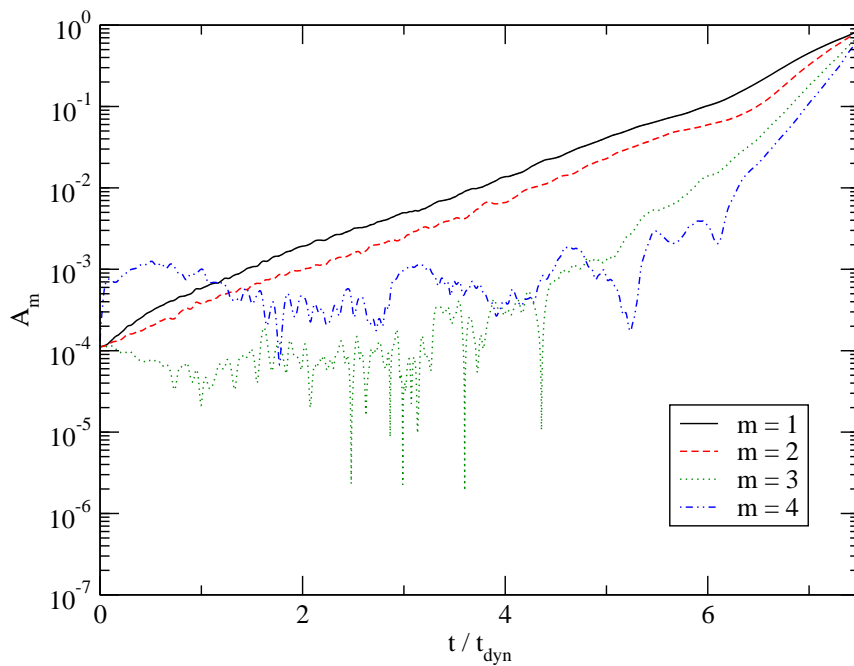


Figure 5.21.: Mode amplitudes versus time for the evolution shown in Fig. 5.18 at $r = 0.25R_e$, the radius of highest rest-mass density in the initial model. The amplitude A_m is the m -th harmonic Fourier projection of the density, normalized to the average value.

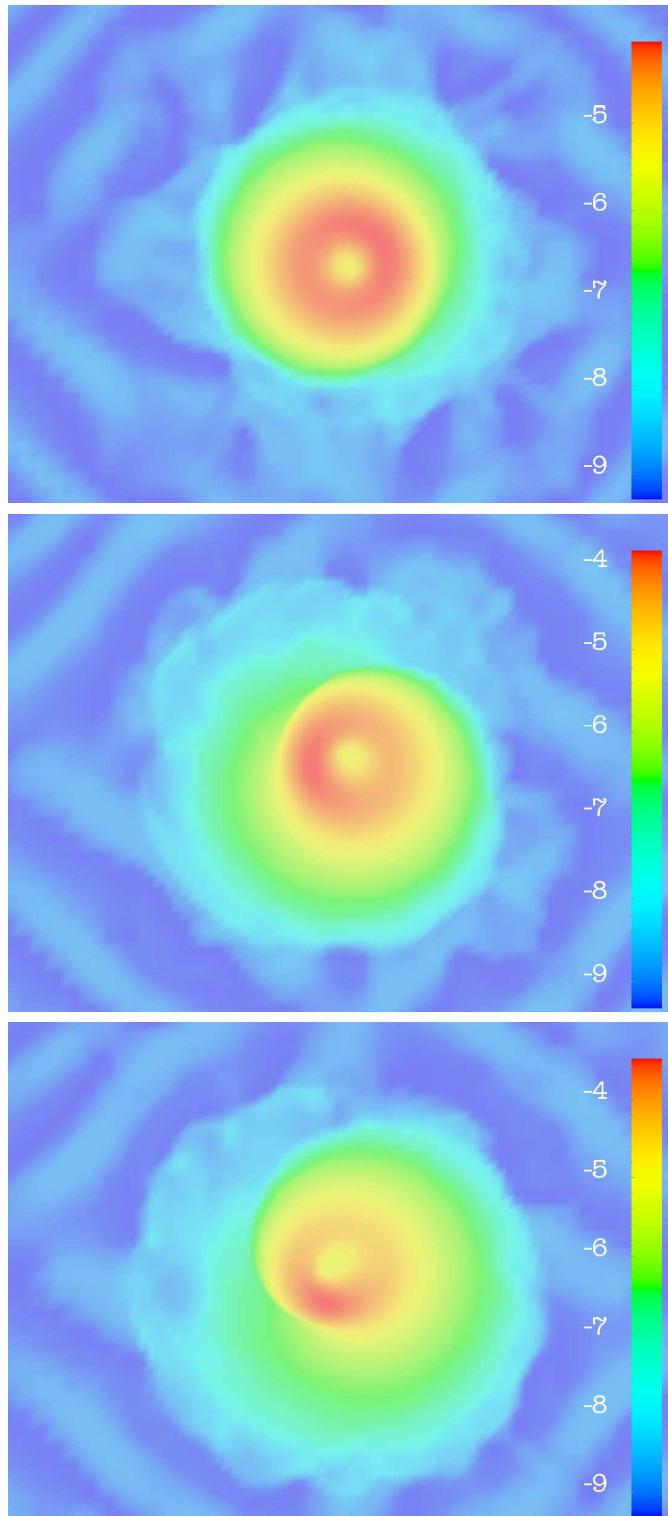


Figure 5.22.: Similar to Fig. 5.18, but now for a perturbation $\lambda_m = \delta_{m1}$. Shown is the decadic logarithm of the density in the equatorial plane. The snapshots correspond to times $t/t_{dyn} = 6.28$ (top), 7.11 (middle) and 7.48 (bottom). While the $m = 2$ mode is now suppressed, the qualitative evolution is similar to that displayed in Fig. 5.18.

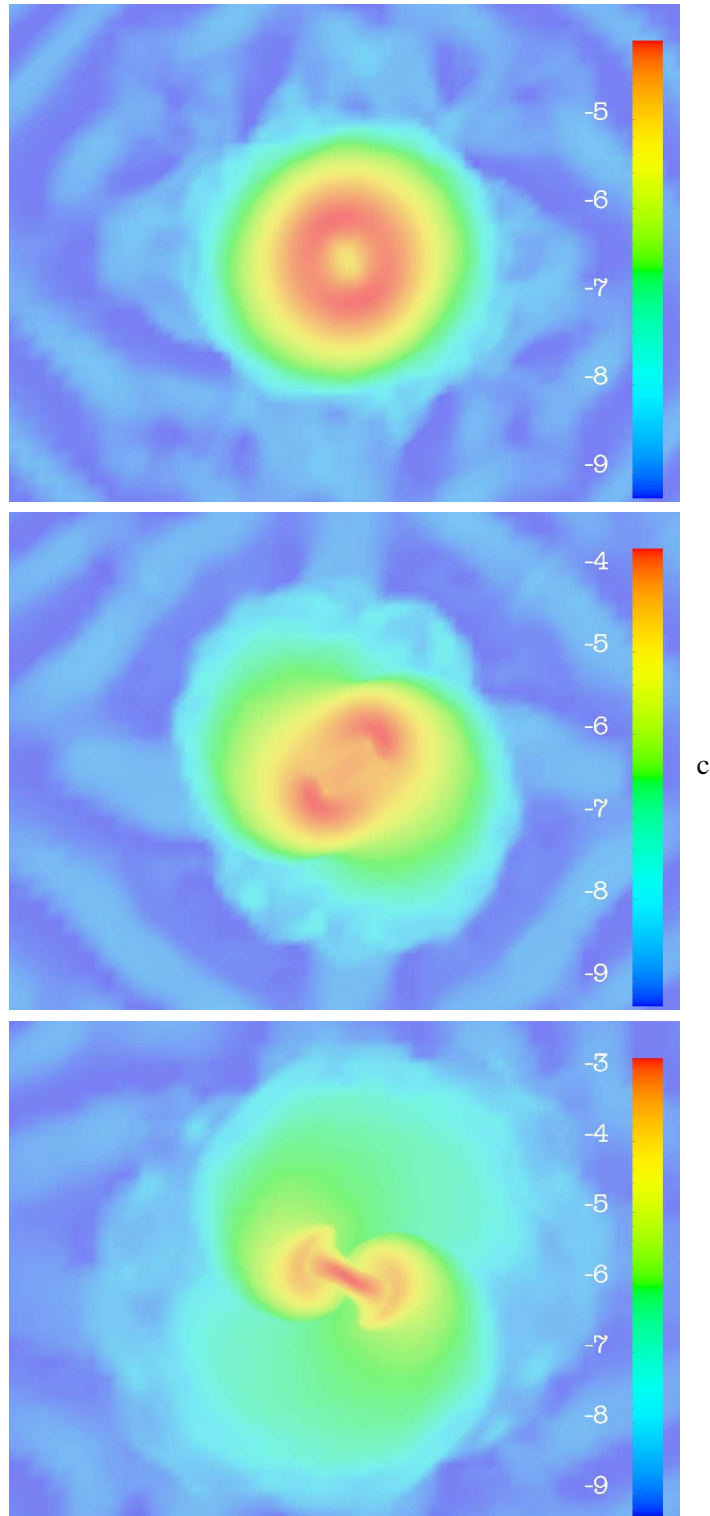


Figure 5.23.: Similar to Fig. 5.18, but for a perturbation $\lambda_m = \delta_{m2}$. Shown is the decadic logarithm of the density in the equatorial plane. The snapshots correspond to times $t/t_{dyn} = 6.28$ (top), 7.66 (middle) and 8.85 (bottom). Two fragments develop and encounter a runaway instability while orbiting each other.

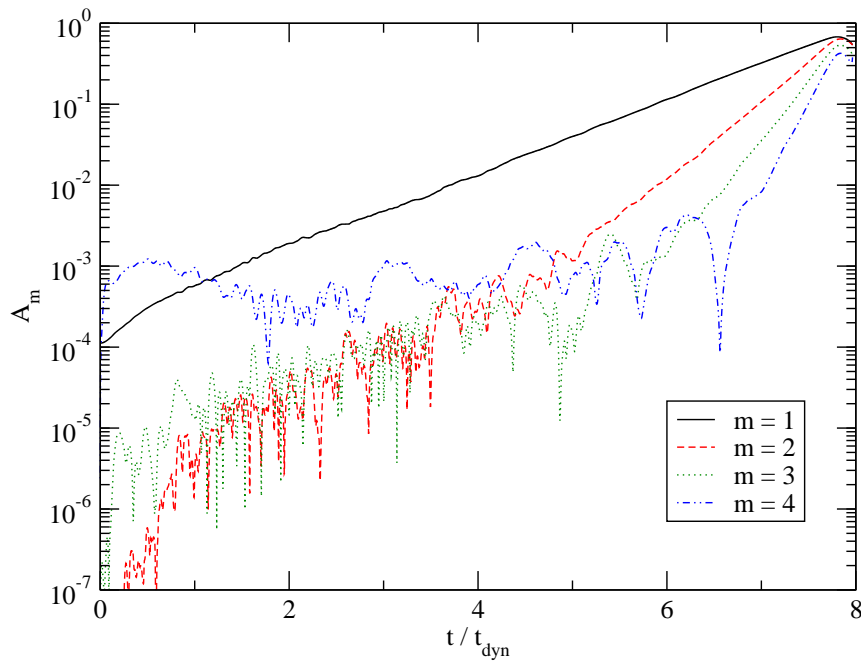


Figure 5.24.: Mode amplitudes versus time for the evolution shown in Fig. 5.22 at $r = 0.25R_e$, the radius of highest rest-mass density in the initial model.

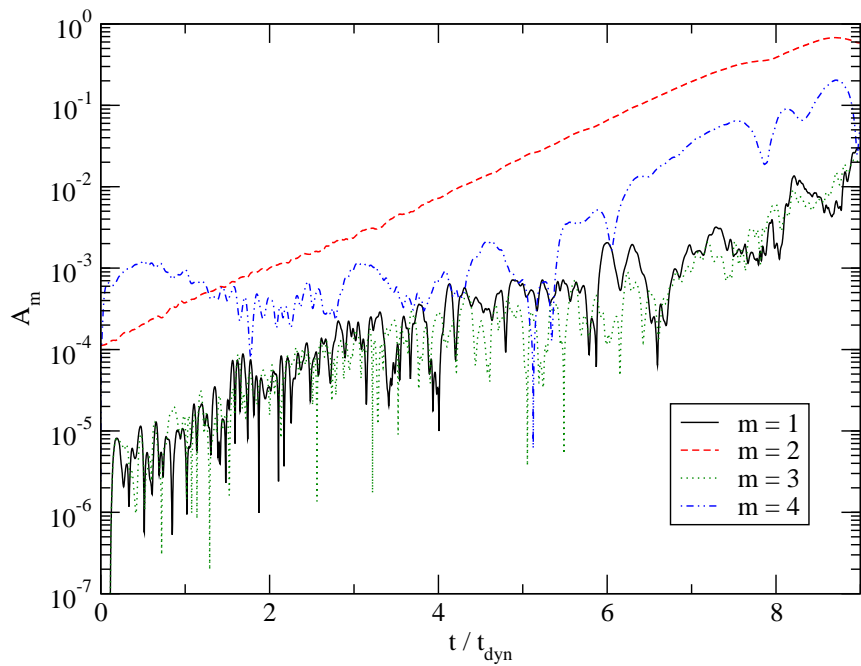


Figure 5.25.: Mode amplitudes versus time for the evolution shown in Fig. 5.23 at $r = 0.25R_e$, the radius of highest rest-mass density in the initial model.

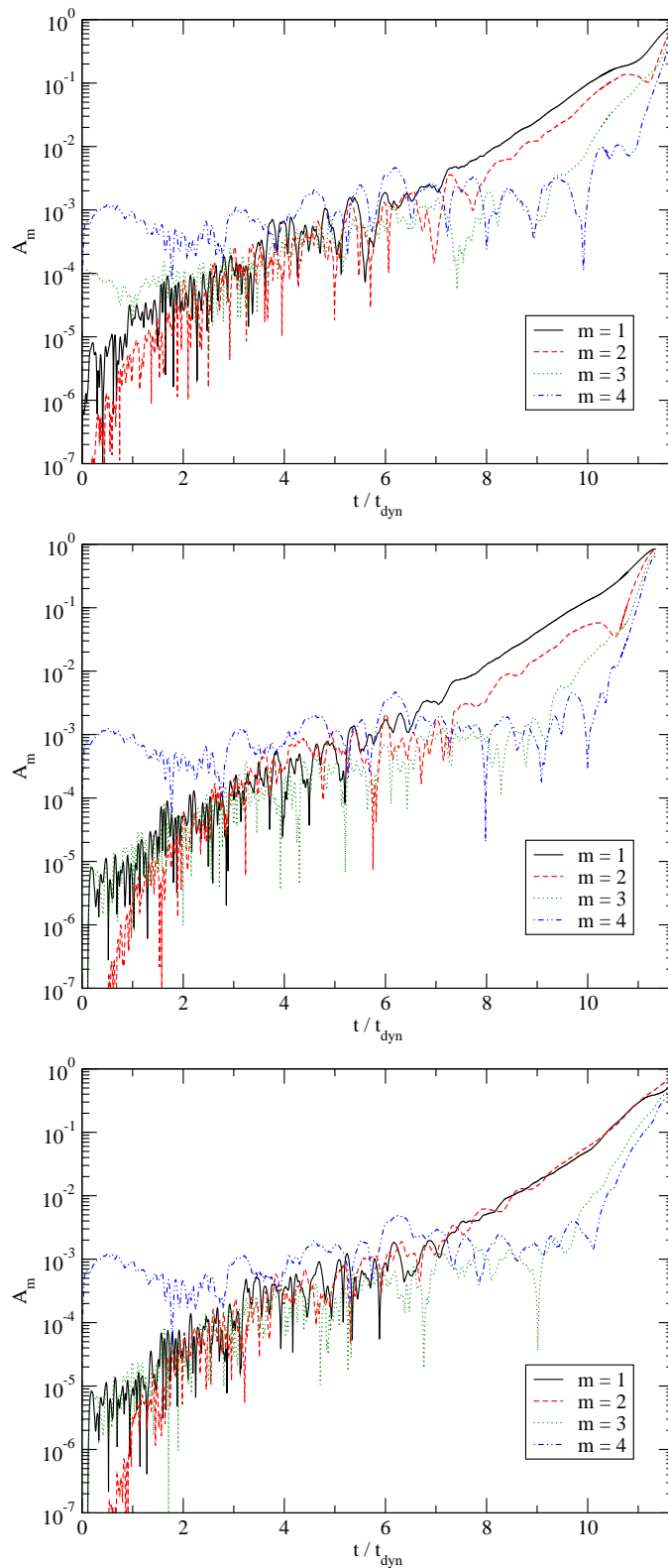


Figure 5.26.: Mode amplitudes versus time for the reference polytrope perturbed according to eqn. 5.6 and $\lambda_m = \delta_{m3}$ (top), $\lambda_m = \delta_{m4}$ (middle), and no explicit perturbation (bottom), extracted at $r = 0.25R_e$, the radius of highest rest-mass density in the initial model.

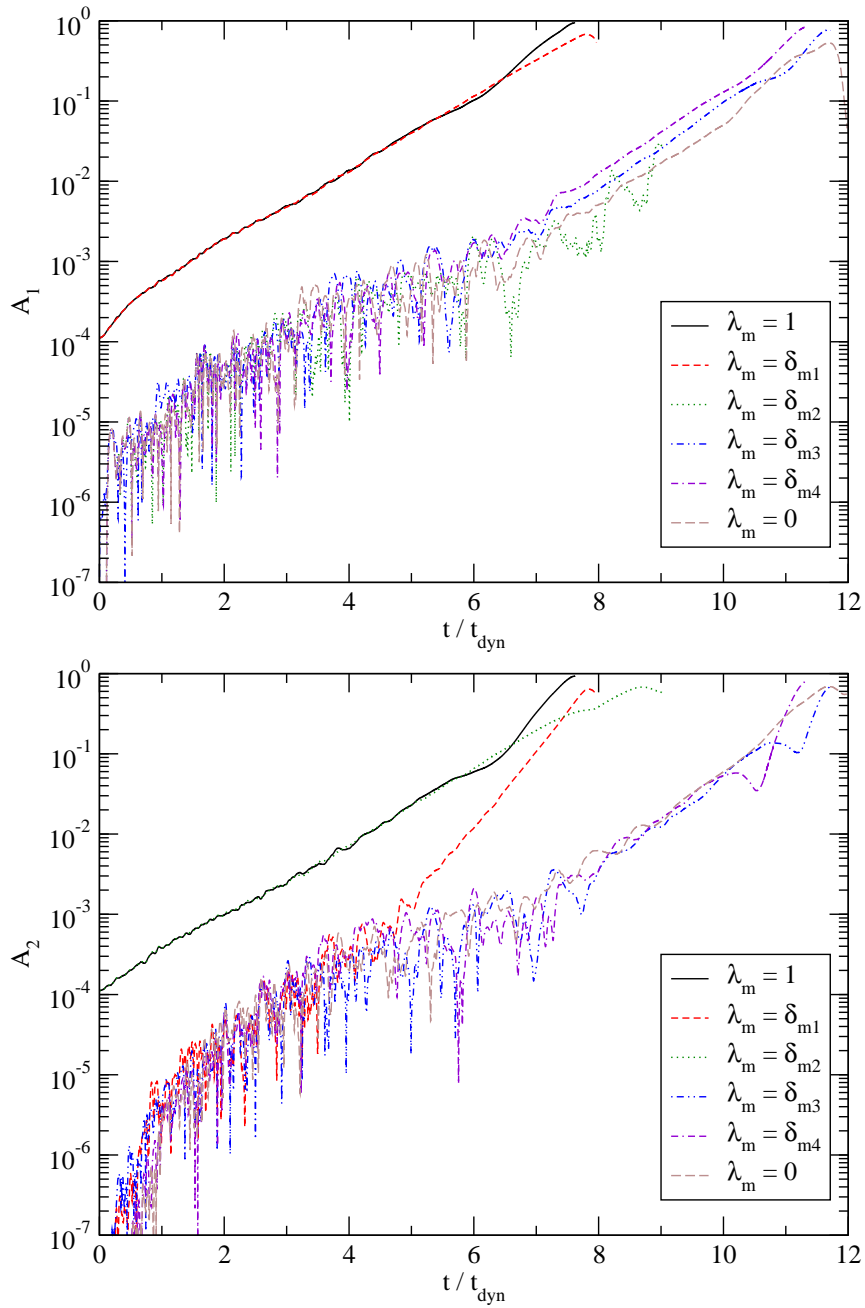


Figure 5.27.: Comparison of mode amplitude versus time for different initial perturbations. The upper panel shows the mode amplitude A_1 , and the lower one shows A_2 . Note that, in the case $\lambda_m = \delta_{m1}$, the $m = 2$ mode is dominated by non-linear effects from the fragmentation (cf. also Fig. 5.24).

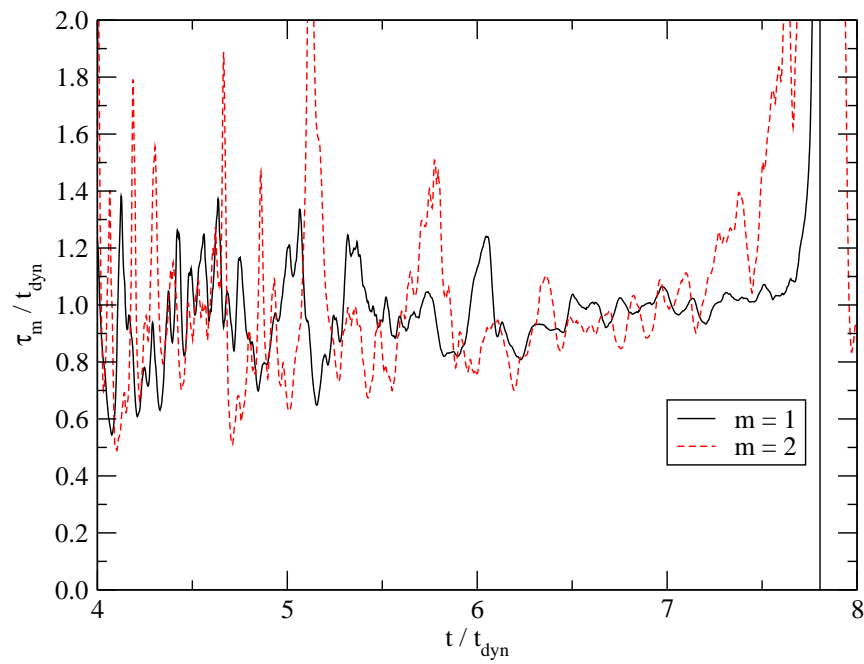


Figure 5.28.: Local growth time $\tau_m(t) := (d \ln A / dt)^{-1}$ for modes $m = 1$ and $m = 2$, both taken from simulations with the corresponding initial perturbation.

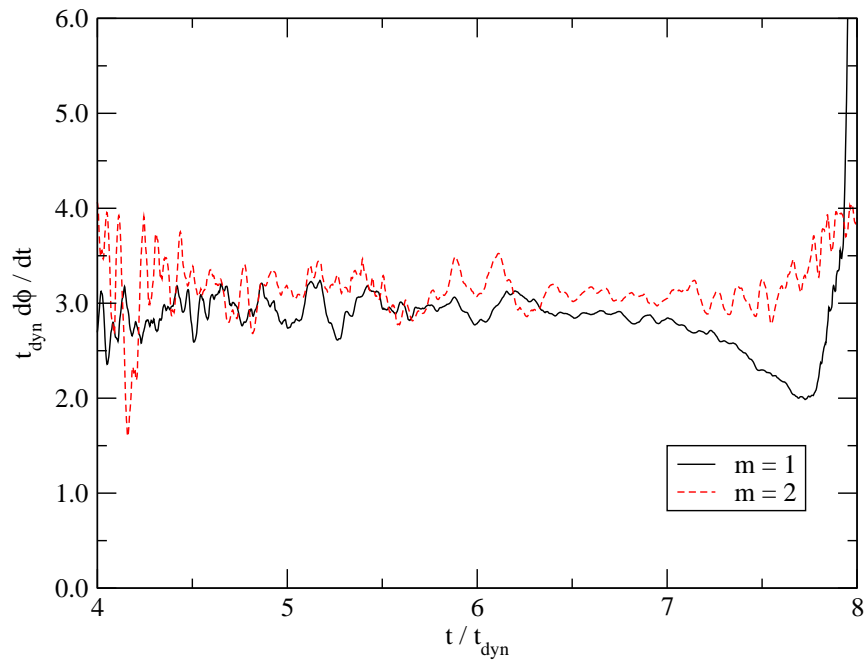


Figure 5.29.: Local frequency $t_{dyn} d\phi / dt$ for modes $m = 1$ and $m = 2$, both taken from simulations with the corresponding initial perturbation.

to select individual modes, and one simulation where no perturbation is applied. The mode amplitudes in these simulations are shown in Fig. 5.24 to 5.26, and the $m = 1$ and $m = 2$ modes are compared to the perturbation with $\lambda_m = 1$ in Fig. 5.27. As long as the mode development is not dominated by another mode which has an amplitude near unity, e.g. as in the case of the $m = 2$ mode in Fig. 5.24, the growth times are comparable for different perturbations.

The high-amplitude, strongly non-linear development at late times is sensitive to the perturbation function, as is visible from the evolutions shown in Fig. 5.22 and 5.23. In the case of the $m = 1$ perturbation, a single fragment develops and collapses in a similar manner to the case $\lambda_m = 1$. With an $m = 2$ perturbation, however, two orbiting fragments develop, contract, and subsequently encounter a runaway instability in the center (bottom panel in Fig. 5.23). Any perturbation with different values for λ_1 and λ_2 might produce a mixture of this spiral arm and binary-system fragmentation instability. One might argue that a fine-grained parameter space study in the space of λ_1 and λ_2 is necessary to obtain a more complete understanding of the remnants. However, the reference polytrope is already well inside the unstable region of the parameter space. We will see in Section 5.3.5 that, on a sequence of increasing $T/|W|$, the $m = 1$ mode dominates at first, and we in the next section it is shown that an apparent horizon is located around the fragment visible in the bottom panel of Fig. 5.22. Therefore, this process of fragmentation is also black-hole forming.⁶

To investigate the growth time τ of the modes, which, in the context of linear theory, is defined by the relation $A_m(t) = A_m(t = 0) \exp(t/\tau_m)$, we plot the function $\tau_m(t) := (d \ln A / dt)^{-1}$ in Fig. 5.28 for $m = 1$ and $m = 2$. As expected for a dynamical instability, the growth times are of the order of the dynamical timescale. Finally, in Fig. 5.29 the mode frequencies $\omega(t) = t_{dyn} d\phi/dt$ are plotted versus time. These, and the connected pattern speeds ω/m , will be important in the discussion of the corotation band in Section 5.3.1.4.

5.3.1.2. Black hole formation

Using the solution-based adaptive mesh refinement technique discussed in Section 3.4, the collapse of the fragment in the case $m = 1$ is followed further. This admits to look for apparent horizons on the grid. Due to technical difficulties, this was done in a number of post-processing steps based on three-dimensional output of the metric and extrinsic curvature.

The resulting horizon is displayed in Fig. 5.30: During the collapse of the fragment, a highly distorted apparent horizon has been located: its shape is close to ellipsoidal, with an axes ratio of $\approx 2 : 1.1 : 1$. The apparent horizon is covered by three refinement levels and 50 to 100 grid zones along each axis.

5.3.1.3. The global nature of the instability

While we will not focus on the global nature of the quasi-normal modes of general relativistic quasi-toroidal polytropes here, this section will give some indication about the structure of the instability. Consider Fig. 5.31 and 5.32, which display the equatorial distribution of the function $\log_{10}(|\rho(x, y, z, t) - \rho_0(x, y, z)| + \epsilon)$, where ρ_0 is the density function of the equilibrium polytrope and $\epsilon = 10^{-10}$. These logarithmic difference plots exhibit the node lines of the unstable mode in the equatorial plane, and show the spiral-arm structure of the $m = 1$ fragmentation instability in Fig. 5.31. We therefore expect that the $m = 1$ contribution is dominant throughout the star, although the phase angle varies with the radial coordinate. The $m = 2$ instability has a core region which encounters, at late time, injection of matter from two orbiting fragments, and two trailing “bar arms” in the low-density halo.

⁶The case $\lambda_m = \delta_{m2}$ also exhibits a ‘collapse of the lapse’ at late times, which suggests that in this case a black hole has formed, too. Unfortunately, it was not possible to locate an apparent horizon in this case due to numerical difficulties.

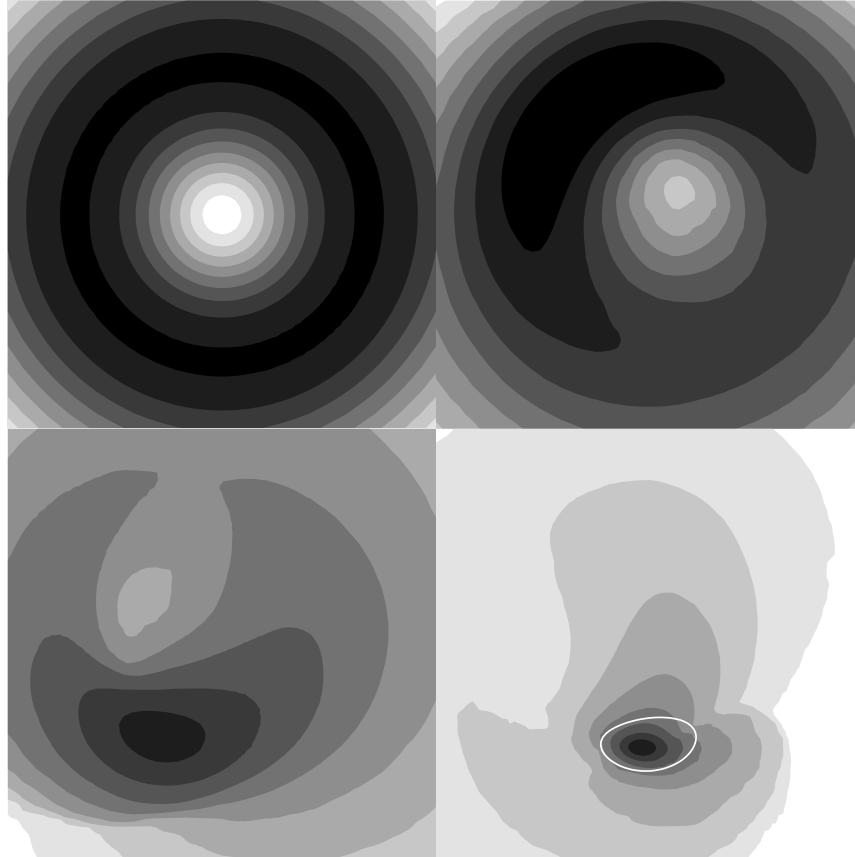


Figure 5.30.: Time evolution of the density in the equatorial plane of the reference polytrope using the perturbation parameters $\lambda_m = \delta_{1m}$. Shown are isocontours of the decadic logarithm of the rest-mass density. The four snapshots extend to $0.37 r_e$ and are taken at $t/t_D = 0$ (top left), 6.43 (top right), 7.14 (bottom left) and 7.45 (bottom right), respectively. They show the formation and collapse of the fragment produced by the $m = 1$ instability. The lower right panel contains an apparent horizon demarked by the thick white line. Note that the shades of grey used for illustration are adapted to the current maximal density at each time, and that darker shades denote higher densities.

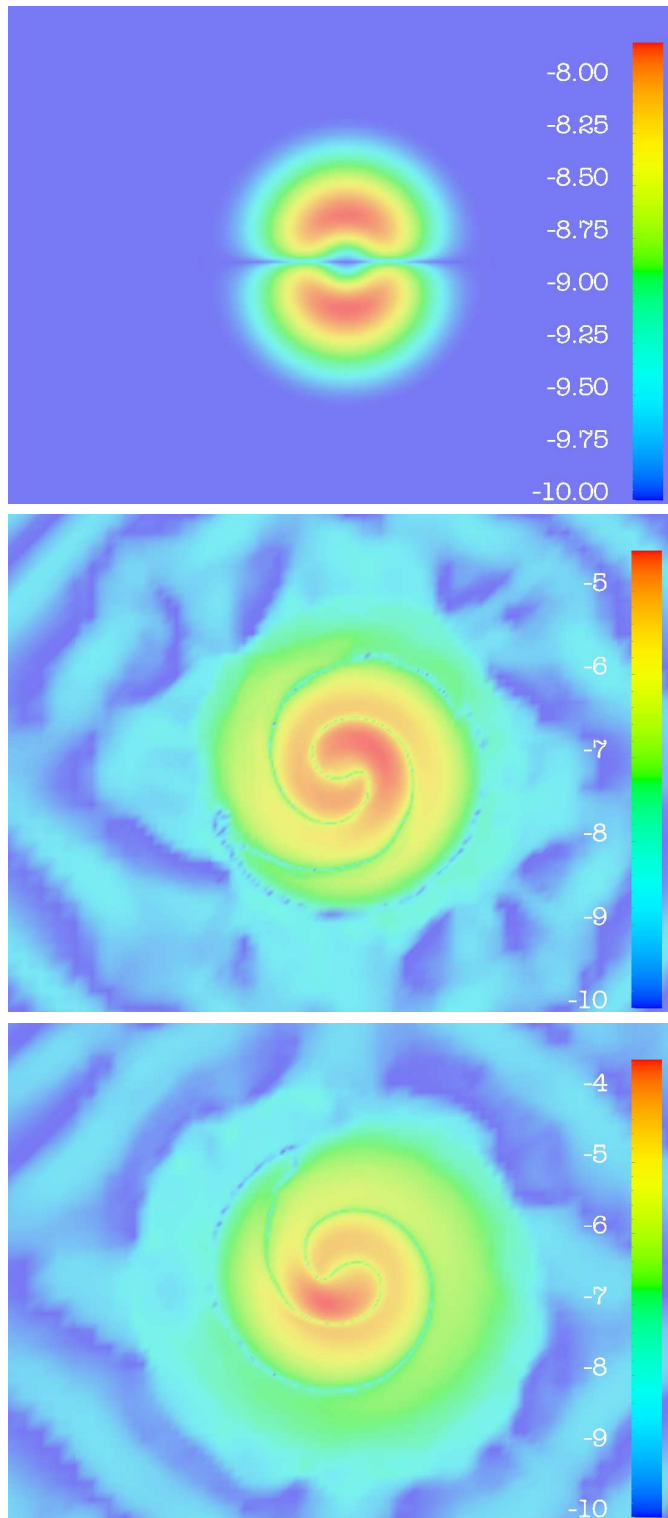


Figure 5.31.: Contour plot of the function $\log_{10}(|\rho(x, y, z, t) - \rho_0(x, y, z)| + \epsilon)$ in the equatorial plane, where ρ denotes the rest-mass density of the $m = 1$ evolution shown in Fig. 5.22, ρ_0 denotes the the density function of the equilibrium polytrope, and ϵ is a small number ($\epsilon = 10^{-10}$ in this plot).

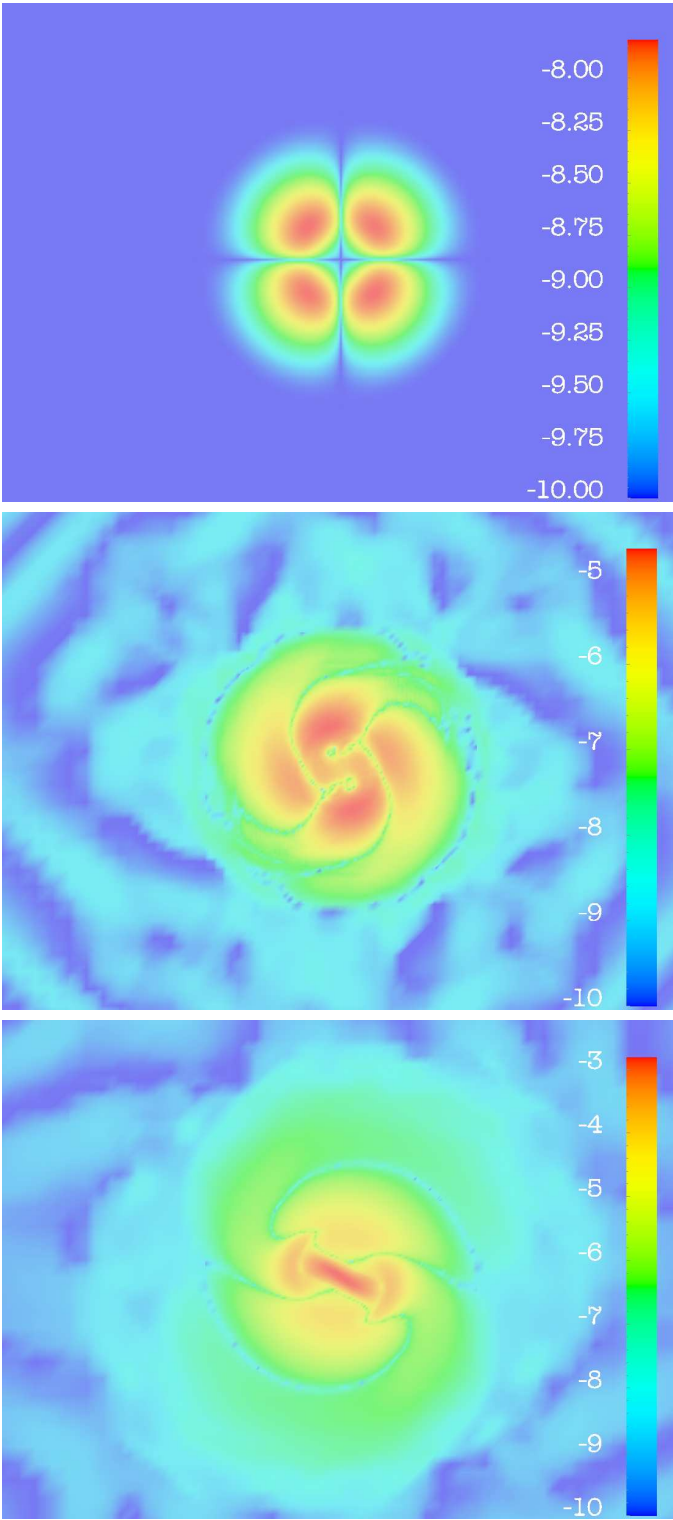


Figure 5.32.: Same as Fig. 5.31, but for the $m = 2$ evolution shown in Fig. 5.23.

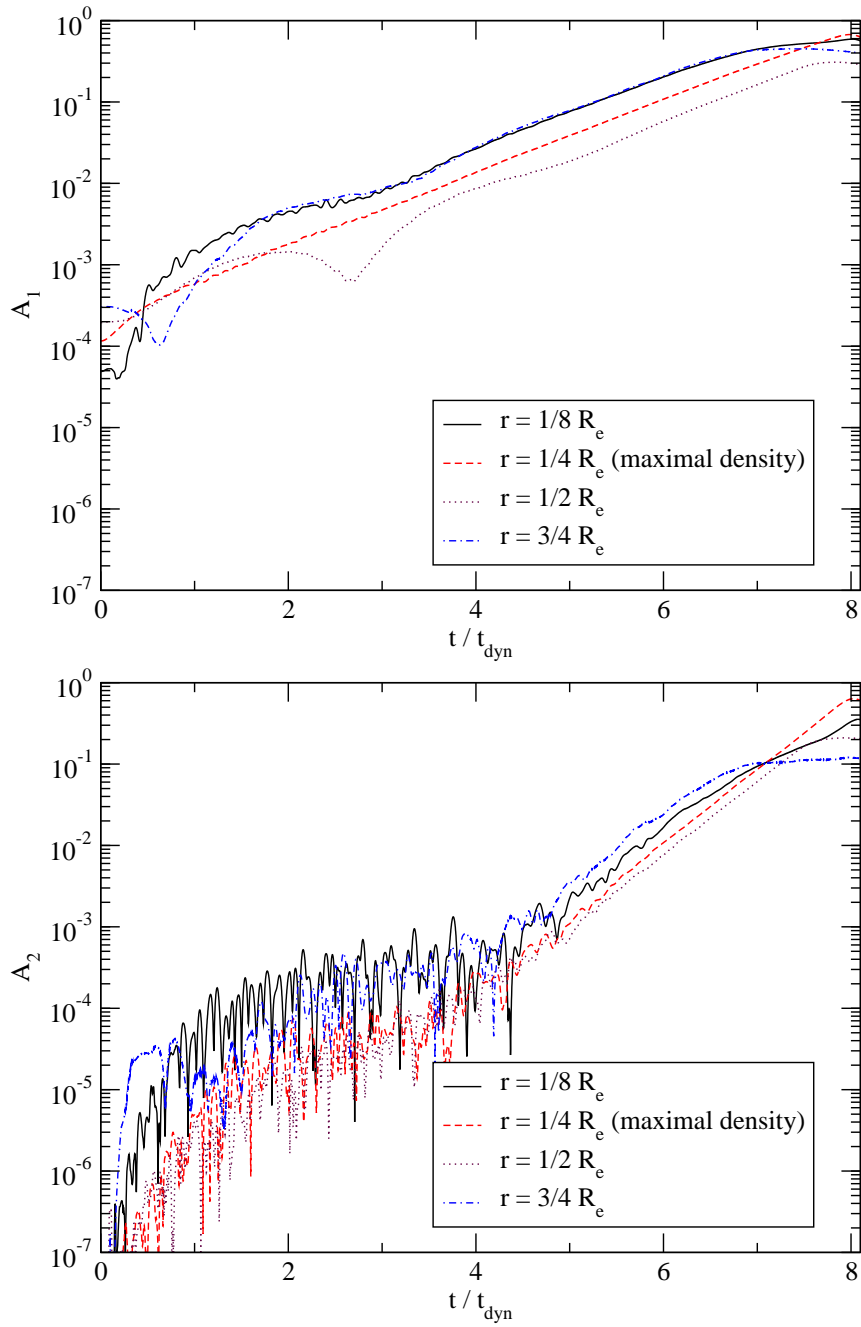


Figure 5.33.: Evolution of the mode amplitudes A_1 and A_2 in the reference polytrope perturbed by $\lambda_m = \delta_{m1}$, for different mode extraction radii. The radius of highest initial density is indicated.

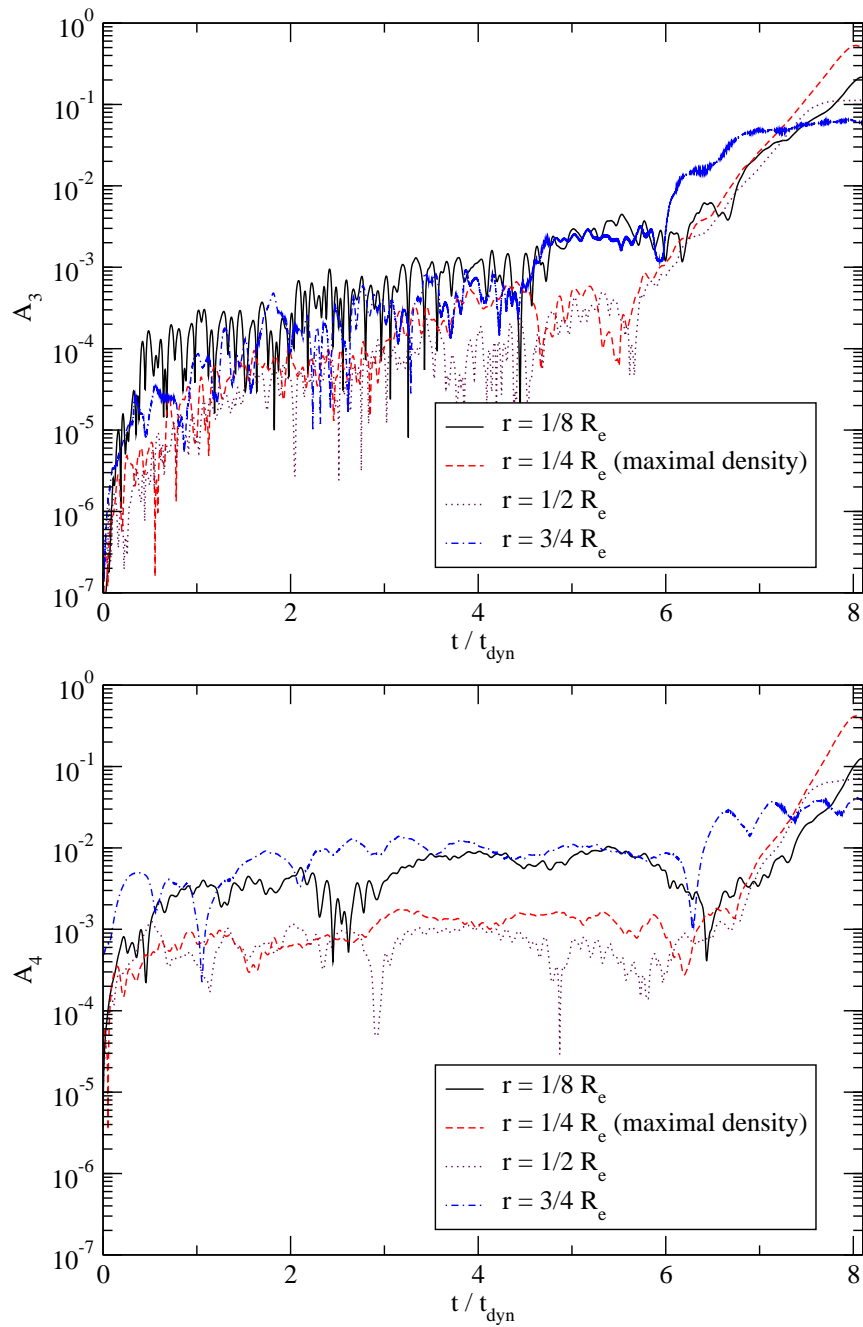


Figure 5.34.: Same as Fig. 5.33, but for the mode amplitudes A_3 and A_4 .

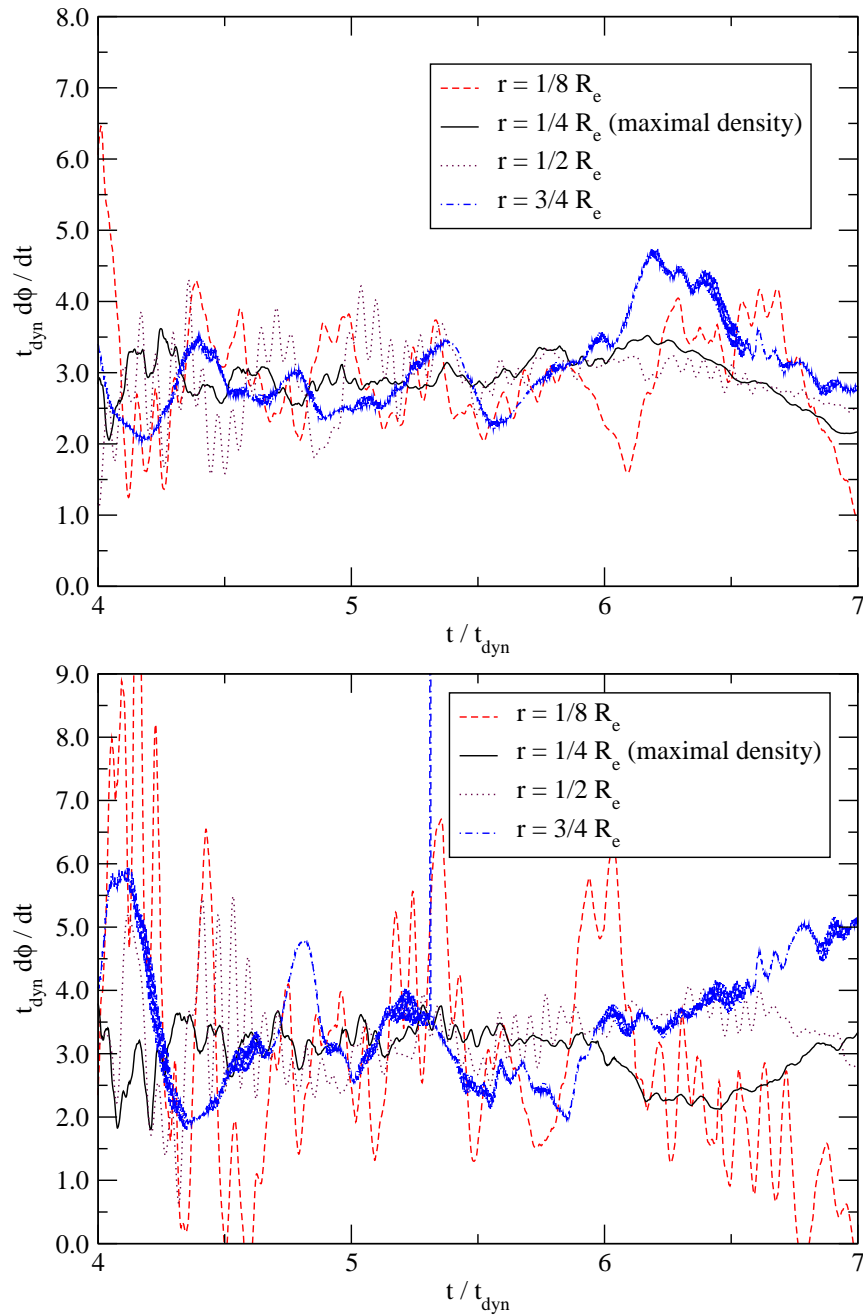


Figure 5.35.: Local mode frequency $t_{\text{dyn}} d\phi/dt$ for the modes $m = 1$ (top) and $m = 2$ (bottom) in the reference polytrope, extracted at different radii in the equatorial plane.

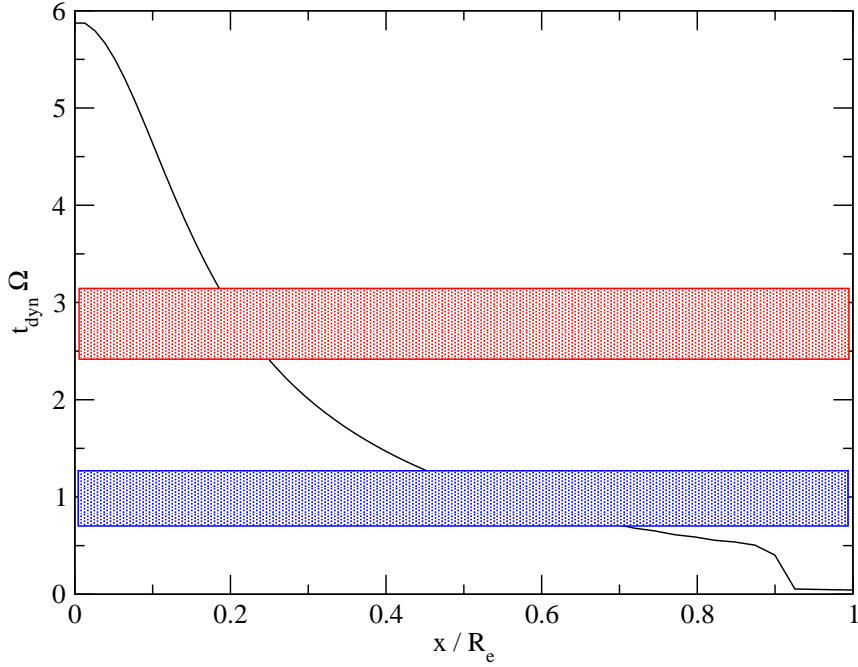


Figure 5.36.: Angular velocity of the reference polytrope over the x axis (black line), and approximate location (with error bar) of the pattern speed of the $m = 1$ mode (red rectangle), and the $m = 2$ mode (blue rectangle). Both modes are inside the corotation band.

The mode amplitudes at different extraction radii in the equatorial plane are shown, for a perturbation with $\lambda_m = \delta_{m1}$, in Fig. 5.33 and 5.34. The development of the unstable modes is not very sensitive to the extraction radius, at least as long as the amplitude of the dominant mode is not close to unity. Fig. 5.35 suggests that the local mode frequency does not depend strongly on the radius, at least within the considerable uncertainties of the plot.

5.3.1.4. The location of the unstable modes in the corotation band

To determine the location of the instability with respect to the corotation band (see introduction to this chapter), we define a coordinate angular velocity of the initial model by

$$\Omega(\varpi) \equiv \frac{\alpha v^\phi - \beta^\phi}{\varpi}. \quad (5.7)$$

This can be compared to the mode pattern speed $1/m d\phi/dt$, which we will assume to be valid for the whole star (cf. Fig. 5.35), to determine whether a certain mode has a corotation point. In Fig. 5.36, the angular velocity is plotted in addition to the numerical approximation of the location of the $m = 1$ and $m = 2$ pattern speeds. We find that both modes have corotation points: the $m = 1$ mode near the radius of highest density at $0.25 R_e$, and the $m = 2$ mode near $0.5 \dots 0.6 R_e$.

5.3.1.5. Grid resolution and convergence

For any parameter study with numerical methods, it is important to have an understanding of the amount of grid resolution needed to extract the physical features under consideration. A typical way to gauge this

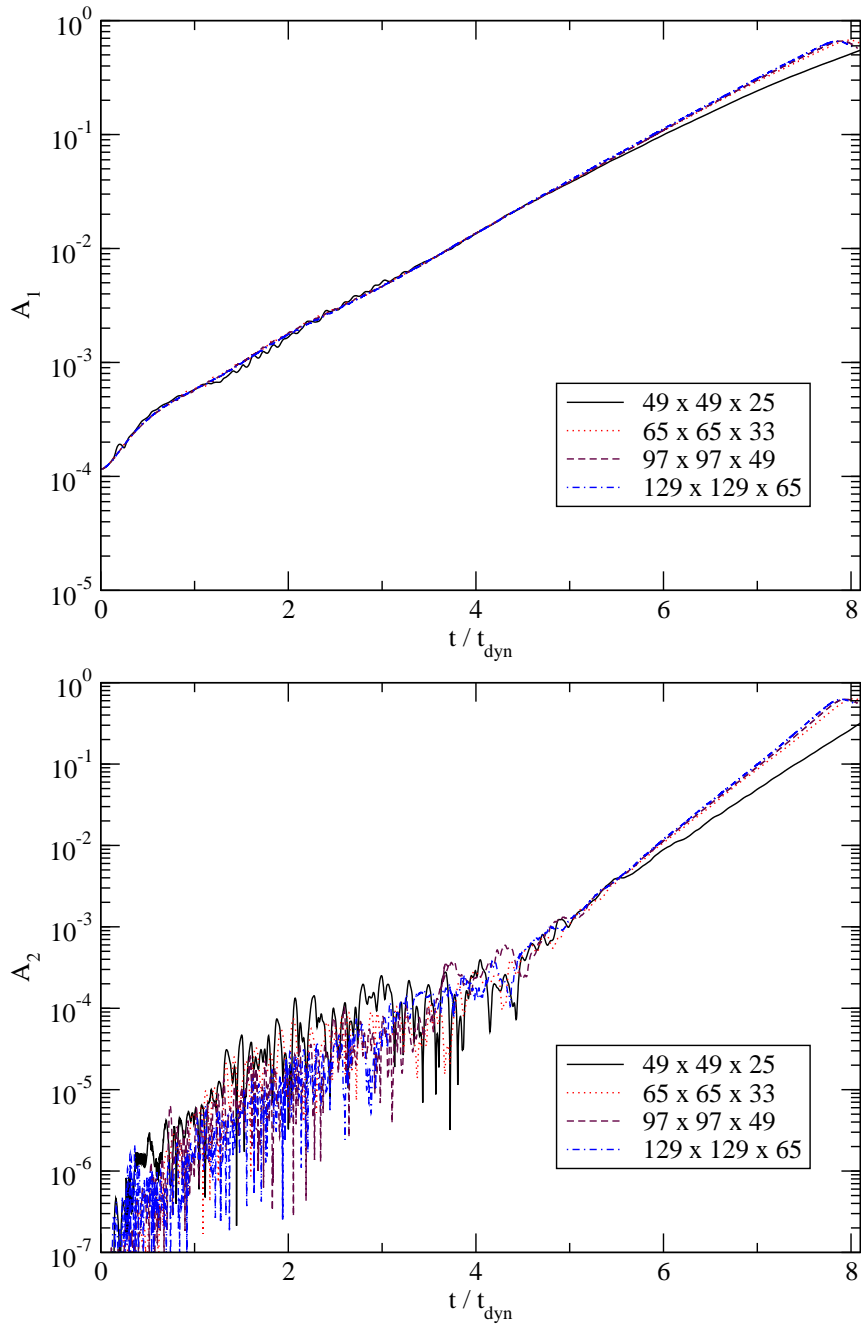


Figure 5.37.: Evolution of the mode amplitudes A_1 (top) and A_2 (bottom) for different grid resolutions. The resolutions in the legend refer to the four outermost grid patches; the innermost patch covering the high-density central toroidal region of the star has a resolution of $65 \times 65 \times 33$, $97 \times 97 \times 49$, $129 \times 129 \times 65$ or $193 \times 193 \times 97$, correspondingly.

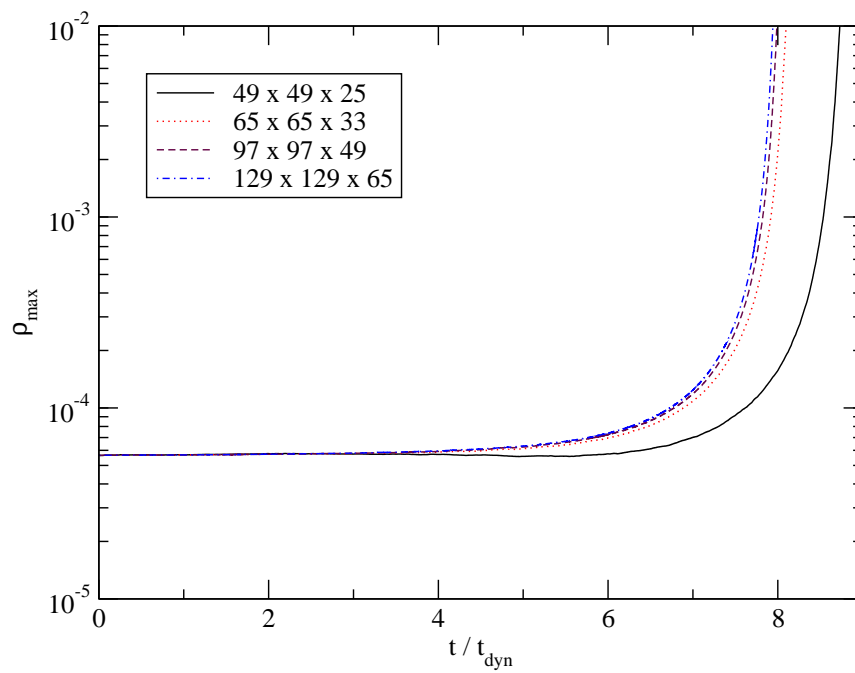


Figure 5.38.: Same as Fig. 5.37, but for the evolution of the maximal rest-mass density ρ_{\max} .

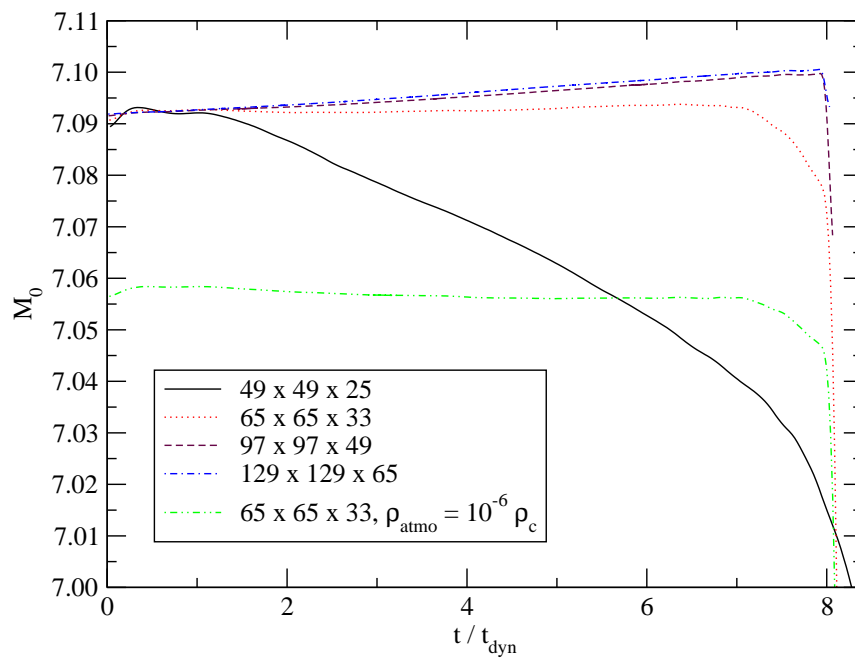


Figure 5.39.: Same as Fig. 5.37, but for the evolution of the total rest mass M_0 . The last graph is from a simulation with a less dense artificial atmosphere.

is to evolve a system with different resolutions and to compare the results. For the black-hole forming fragmentation instability shown in Section 5.3.1.1, it is expected that different phases of the evolution have substantially different resolution requirements. During the nearly exponential growth of the instability at low amplitudes (which we will call *linear regime*), the equilibrium structure of the star as a whole needs to be covered appropriately. The instability is, at first, a low-frequency effect on the star, and as such is not expected to dominate the resolution requirements. However, if the fragment evolves into a black hole (in the *non-linear regime*), it needs to be resolved with significantly more grid points.

As explained in Section 3.4, the star is covered by a grid with fixed mesh refinement. Typically, five grid patches are used, centered on each other, and with an increase of resolution by a factor 2 each. Only the central patch with highest resolution, which covers the region of highest density, is 0.75 times as extended as the second finest one to reduce artefacts from inter-patch boundaries. To test convergence, the reference model has been evolved with $49 \times 49 \times 25$, $65 \times 65 \times 33$, $97 \times 97 \times 49$ and $129 \times 129 \times 65$ zones per outer grid patch; the innermost patch covering the high-density toroidal region has $65 \times 65 \times 33$, $97 \times 97 \times 49$, $129 \times 129 \times 65$ or $193 \times 193 \times 97$ grid zones. Also, the initial data was calculated with a grid of 401×201 , 601×301 , 1201×601 and 2401×1201 .

The results from evolving the reference model with an $m = 1$ perturbation at different resolutions are shown in Fig. 5.1, 5.37, 5.38 and 5.39. The convergence of the Hamiltonian constraint has already been discussed in Section 5.2.1. The amplitude of the dominant $m = 1$ mode is virtually independent of resolution, while the $m = 2$ amplitude is slightly smaller at the lowest resolution. The evolution of the maximal rest-mass density (Fig. 5.38) exhibits a similar behaviour. Finally, the total rest mass of the system is conserved from within 1.4% (lowest resolution) to 0.1% (higher resolutions). The drift in the rest-mass can be explained by our use of an artificial atmosphere: The rest-mass density of the atmosphere is $10^{-5} \rho_c = 3.38 \cdot 10^{-11}$, which corresponds to an approximate total mass of $M_{0,atmo} \approx 4.7 \cdot 10^{-3}$ in a domain of coordinate volume 520^3 (not taking into account the volume form). This translates into a systematic shift in the total rest mass of the system as apparent when comparing to an evolution with a lower atmospheric density (bottom panel in Fig. 5.39), and a drift caused by the intrinsic atmospheric dynamics and the interaction with the outer boundary. Note that this is to be considered a (non-sharp) upper limit on the systematic errors induced by the atmosphere, because one could always extend the total computational domain arbitrarily without affecting the core region significantly.

Judging from the plots, we think that the lowest resolution considered here (which already covers the equatorial radius of the star with about 60 grid points when comparing to uniform grids) is sufficient to get qualitatively correct results. Quantitatively, the errors are in a range of a few percents. The next higher resolution of $65 \times 65 \times 33$ seems accurate to within about one percent. This resolution will therefore be used for the parameter study below. This is reasonable since the structure of the quasi-toroidal models has similar features, and therefore similar requirements concerning resolution. Nevertheless, selected models have been tested for convergence independently from the reference polytrope.

5.3.1.6. Influence of the artificial atmosphere

The standard artificial atmosphere we employ in our simulations has a density several orders of magnitude lower than the average density in the star, so we expect that it does not influence the dynamical properties of the star significantly. The atmospheric density is set in terms of the central density of the star: we have used a ratio of 10^{-5} in most simulations. To test the influence of this parameter, we have evolved the reference model also with a ten times lower atmospheric density (i.e. $10^{-6} \rho_c$), and with an $m = 1$ perturbation. The results are shown in Fig. 5.39 and 5.40. The latter shows that the dominant $m = 1$ mode is not influenced by the atmospheric setting, while the $m = 2$ amplitude shows dependence on the atmosphere setting only as long as its amplitude is on the level of the numerical noise.

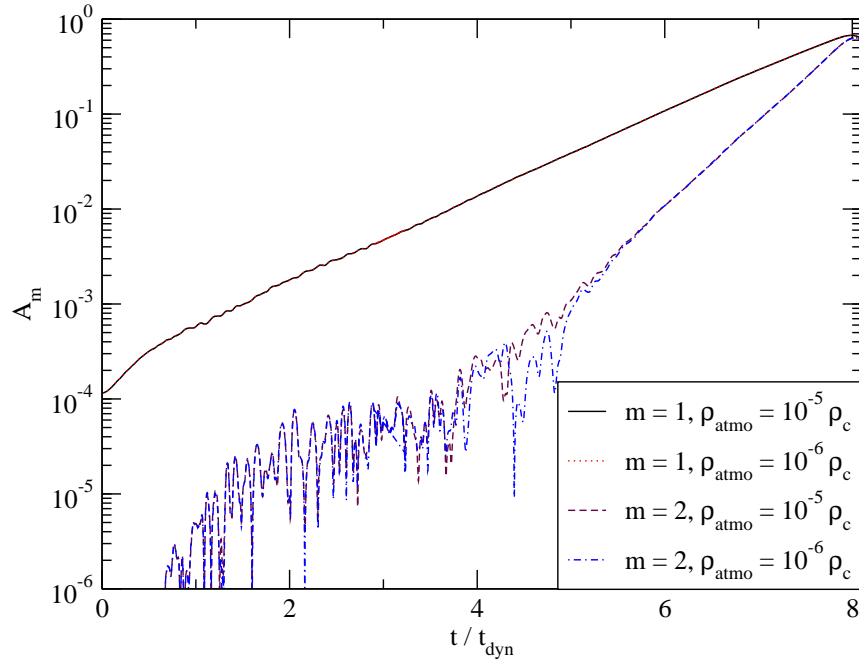


Figure 5.40.: Evolution of the mode amplitudes A_1 and A_2 in the reference polytrope, for artificial atmospheres of different density $\rho_{\text{atmo}}/\rho_c$.

5.3.1.7. Extraction of gravitational waves

Since the simulations are all fully relativistic, it is possible to extract gravitational radiation from the system. However, the simulations terminate shortly after black hole formation, which poses a dilemma: any detector used for wave extraction should be as far away from the source as possible, but at the same time, the domain of influence of the source is limited by the finite domain of integration. In no case were we able to extract signals from the black hole formation proper, but we could obtain partial signals from the process of fragmentation. The kind of signals one might expect would have two major frequency components: one lower-frequency component induced by the pattern motion of the instability, with an exponentially rising temporal amplitude before black-hole formation, and a higher-frequency one from oscillations of the fragment and the new-born black hole, which should have burst and ring-down characteristics. We are not able to discuss the higher-frequency component given the limitation of our simulations. However, we expect that we can predict the approximate frequency and an approximate lower limit on the amplitude of the lower-frequency component.

The *WaveExtract* module developed at the Albert Einstein Institute extracts the complex quantities $Q_{\ell m}^+$ and $Q_{\ell m}^-$ [148] at certain specified coordinate radii. Given these, the strains h_+ and h_\times can be obtained by evaluating eqn. 101 in [148]⁷. During the development of the instability, most bulk motion will be visible from an observer at the polar angular coordinate $\theta = 0$. In Fig. 5.41 and 5.42 we plot the strains h_+ and h_\times for a star of mass $10^6 M_\odot$ at a distance of 1 Gpc for different detector locations and resolutions. The signal has the expected form of an exponentially growing oscillation. Detectors closer to the stellar surface, at $r_e \approx 11M$ in the equatorial plane, exhibit a larger part of the whole signal, but at the expense of suffering

⁷Note that ref. [148] contains a small error in Appendix D: The correct explicit form of the quantity X^{22} is given by $X^{22} = ie^{i2\phi} \sqrt{15/8\pi} \sin 2\theta$, which guarantees that $X^{22}/\sin \theta$ is regular.

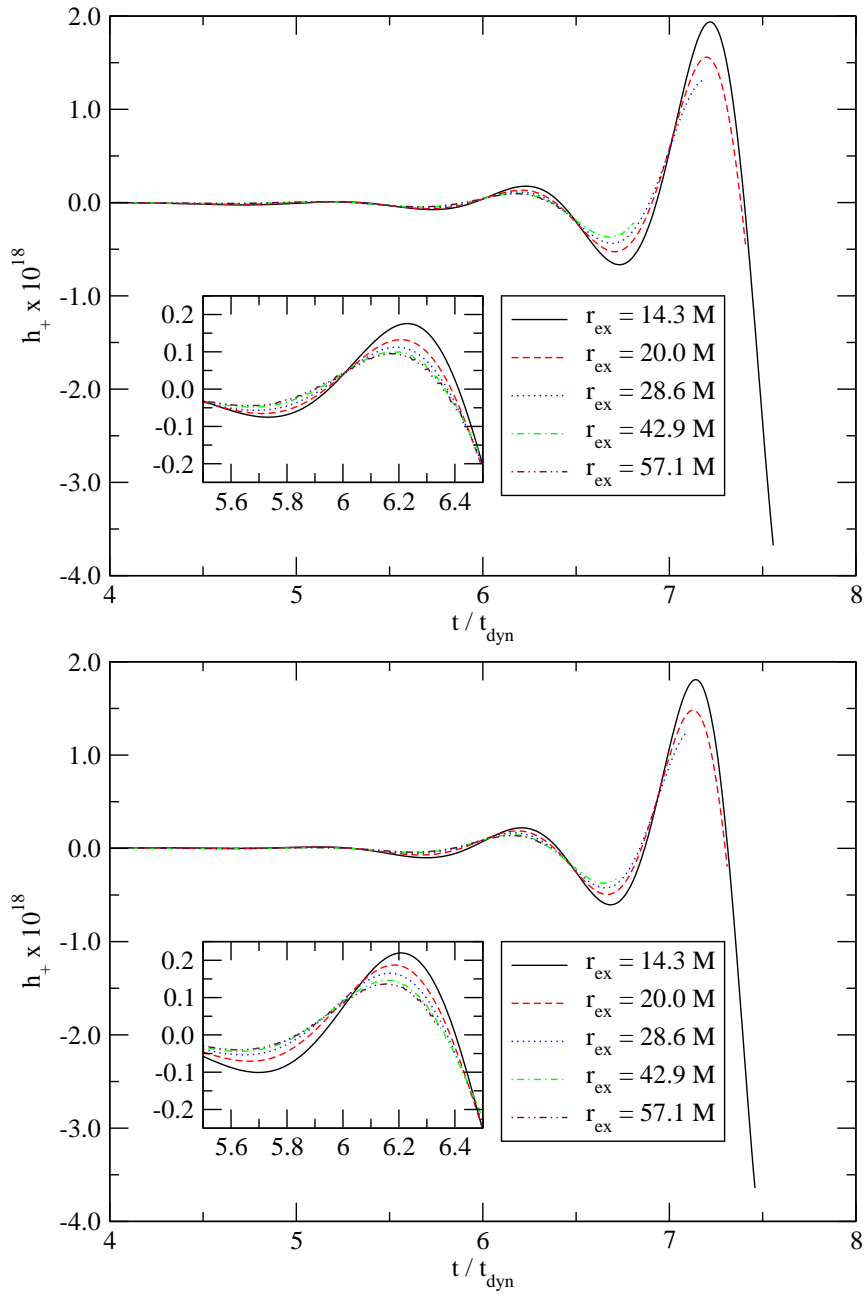


Figure 5.41.: The strain from gravitational radiation h_+ measured at different radial detector locations for a resolution of $65 \times 65 \times 33$ per patch (top) and $97 \times 97 \times 49$ per patch (bottom), emitted from the process depicted in Fig. 5.22. The amplitude is normalized to a star of $10^6 M_\odot$, and a distance of 1 Gpc.

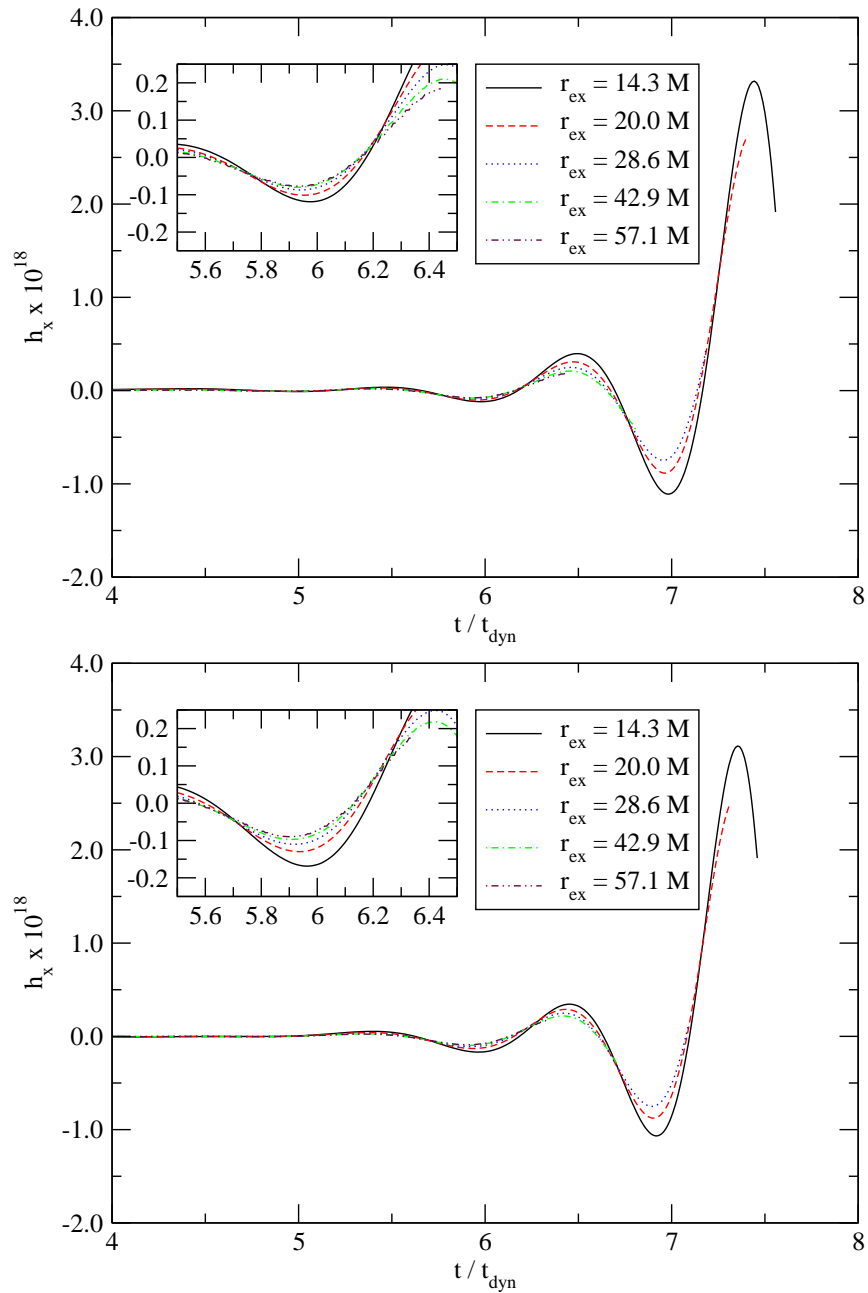


Figure 5.42.: Same as Fig. 5.41, but for the strain h_x .

from systematic errors due to the assumption of a Schwarzschild background. Judging from the insets, the detector at $r_{ex} = 14.3$ overestimates the signal amplitude by about a factor of two. The frequency is not very sensitive to the detector location. While we clearly cannot obtain the whole signal in this manner, we are, as already discussed, able to give a lower limit on the low-frequency part. The frequency of the signal is then

$$f_{GW} \approx 5.5 \left(\frac{10^6 M_\odot}{M} \right) \text{ mHz} \quad (5.8)$$

with a corresponding lower limit on the amplitude of about

$$h_{GW} \approx 10^{-18} \left(\frac{M}{10^6 M_\odot} \right) \left(\frac{1 \text{ Gpc}}{d} \right). \quad (5.9)$$

Given the aforementioned technical limitations, we will not study gravitational-wave signals in further detail, since a stable evolution of the final black hole would be necessary to obtain the most interesting part of the signal, and since we consider the comparison of partial signals to be of limited astrophysical value.

5.3.2. Evolution of the sequence of axes ratios

The R sequence has been described in Section 5.2.2.2. From Table 5.2, it is apparent that higher values of r_p/r_e are connected to lower $T/|W|$. In Maclaurin spheroids, this is related to a stabilization of the initial model. Consider Fig. 5.43: The growth time of the modes $m = 1$ and $m = 2$ increases with lower r_p/r_e , which indeed is a sign for approaching a limit of stability. The mode $m = 2$ even seems stable in the model $R0.34$.

5.3.3. Evolution of the sequence of stiffnesses

The change in the instability along the G sequence described in Section 5.2.2.3 is shown in Fig. 5.44. With increasing Γ , and $T/|W|$ decreasing from 0.227 to 0.159 (cf. Table 5.3), both the $m = 1$ and the $m = 2$ modes are stabilized. The member $G2.0$ with $\Gamma = 2$ is of special interest, since this choice is often used to obtain a simple polytropic equilibrium model of neutron stars. While it is known that strong differential rotation can induce bar-mode instabilities in neutron stars [63, 64], the particular model $G2.0$ does not seem to have enough rotational energy to exhibit a growth of the $m = 2$ mode.

5.3.4. Evolution of the sequence of compactnesses

The mode amplitudes A_1 and A_2 for different members of the C sequence (cf. Section 5.2.2.4 and Table 5.4) is shown in Fig. 5.45. The plot demonstrates that different choices of ρ_c do not have a significant effect on the growth time of the mode, which is in contrast to the effects of Γ and r_p/r_e discussed above. However, while the linear development of the mode is similar for different compactnesses, the non-linear behaviour is not. Consider Fig. 5.46: The reference polytrope $C1$ and the model $C2$, which is about half as compact, both show an unbounded growth in maximal density and a collapse of the lapse, indicating black hole formation. The models $C4$ and $C8$, however, appear to avoid black hole formation and re-expand after a state of maximum compression. Fig. 5.47 to 5.49 show these different evolutions in more detail: While the late-time evolution of $C2$ (Fig. 5.47) is quite similar to that of the reference model evolution (Fig. 5.18), the fragment in the less compact models $C4$ and $C8$ re-expands after the collapse. This is expected, since the Newtonian limit, for an equation of state $\Gamma = 4/3$, admits a stable equilibrium state of the fragment, if it has non-zero rotation. We conclude therefore that, even when the growth time of the

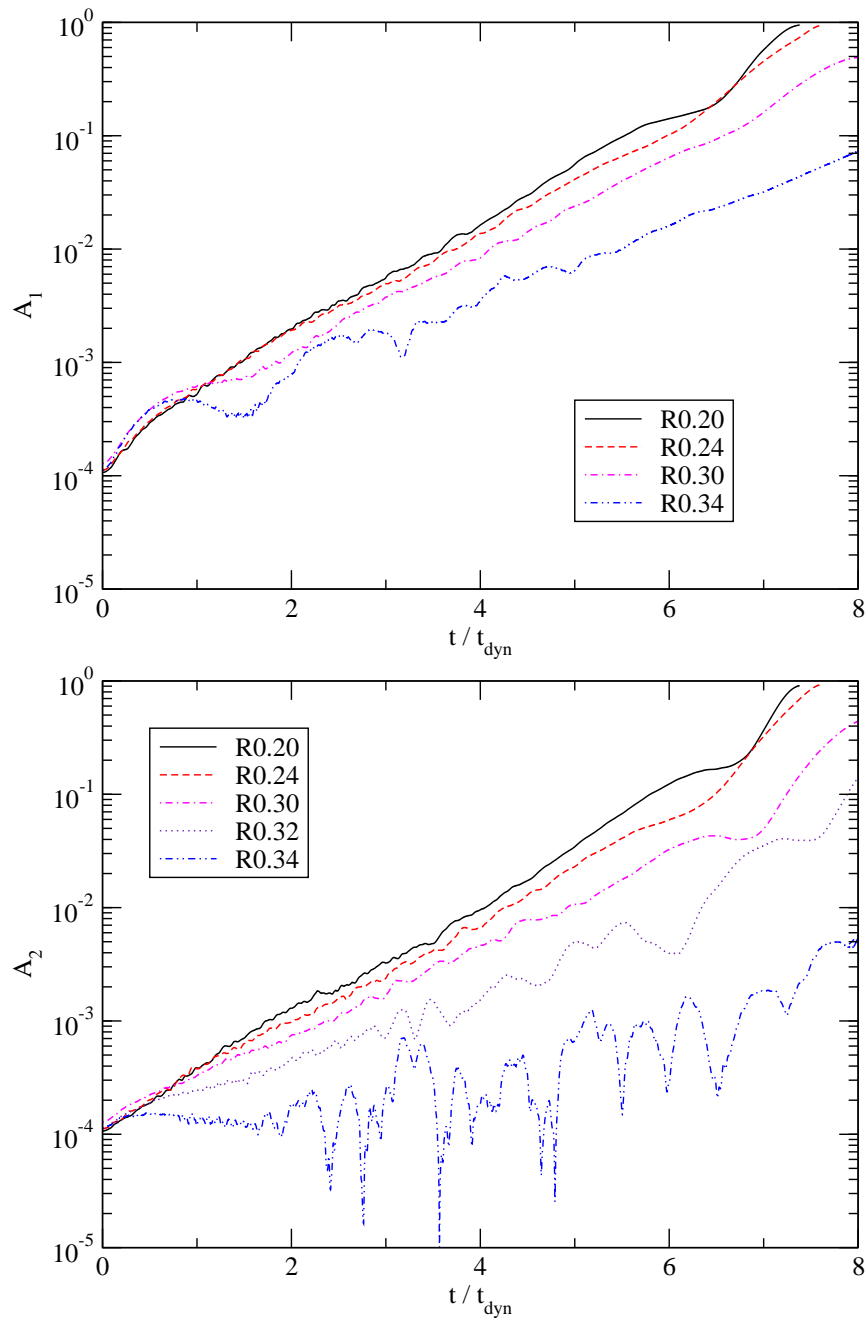


Figure 5.43.: Evolution of the mode amplitudes A_1 and A_2 for different members of the R sequence (cf. Table 5.2).

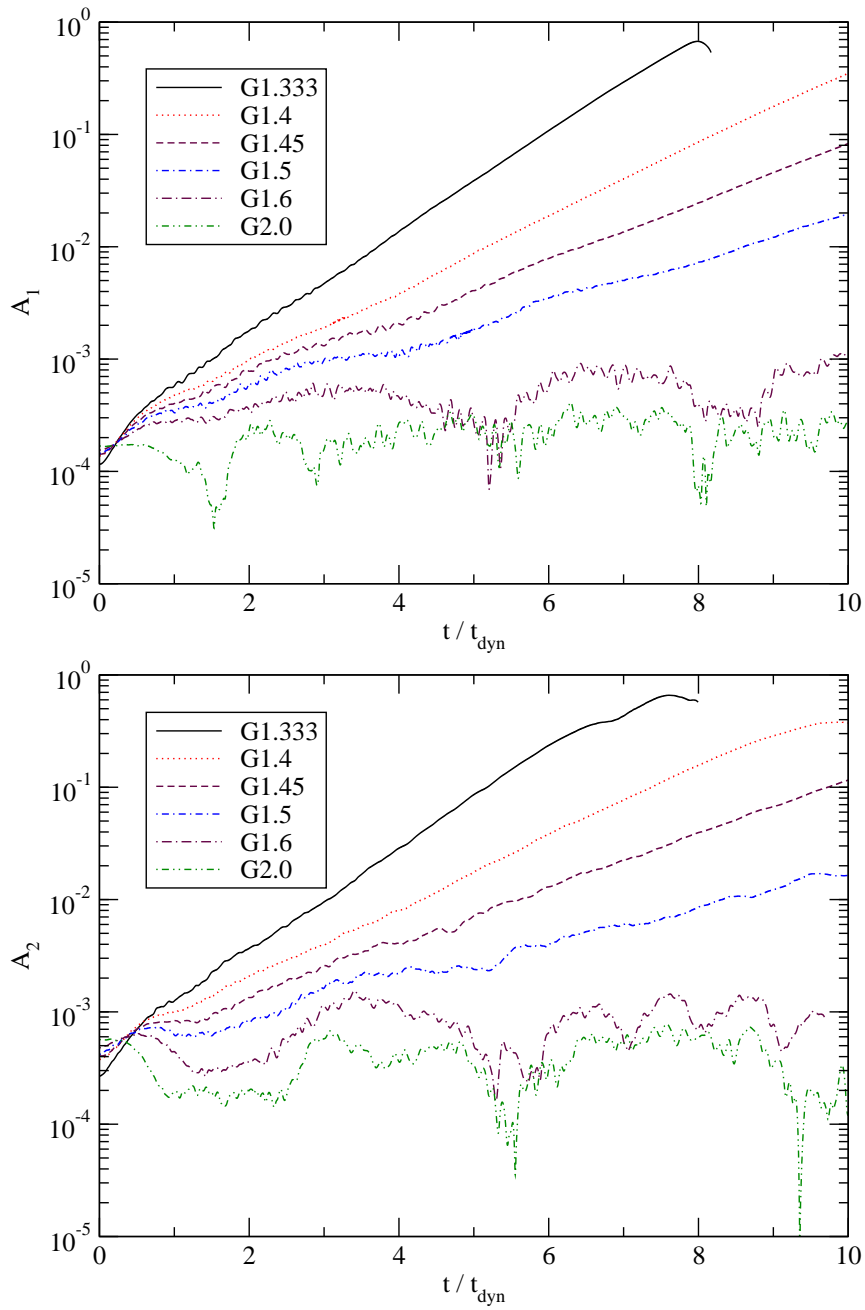


Figure 5.44.: Evolution of the mode amplitudes A_1 and A_2 for different members of the G sequence (cf. Table 5.3).

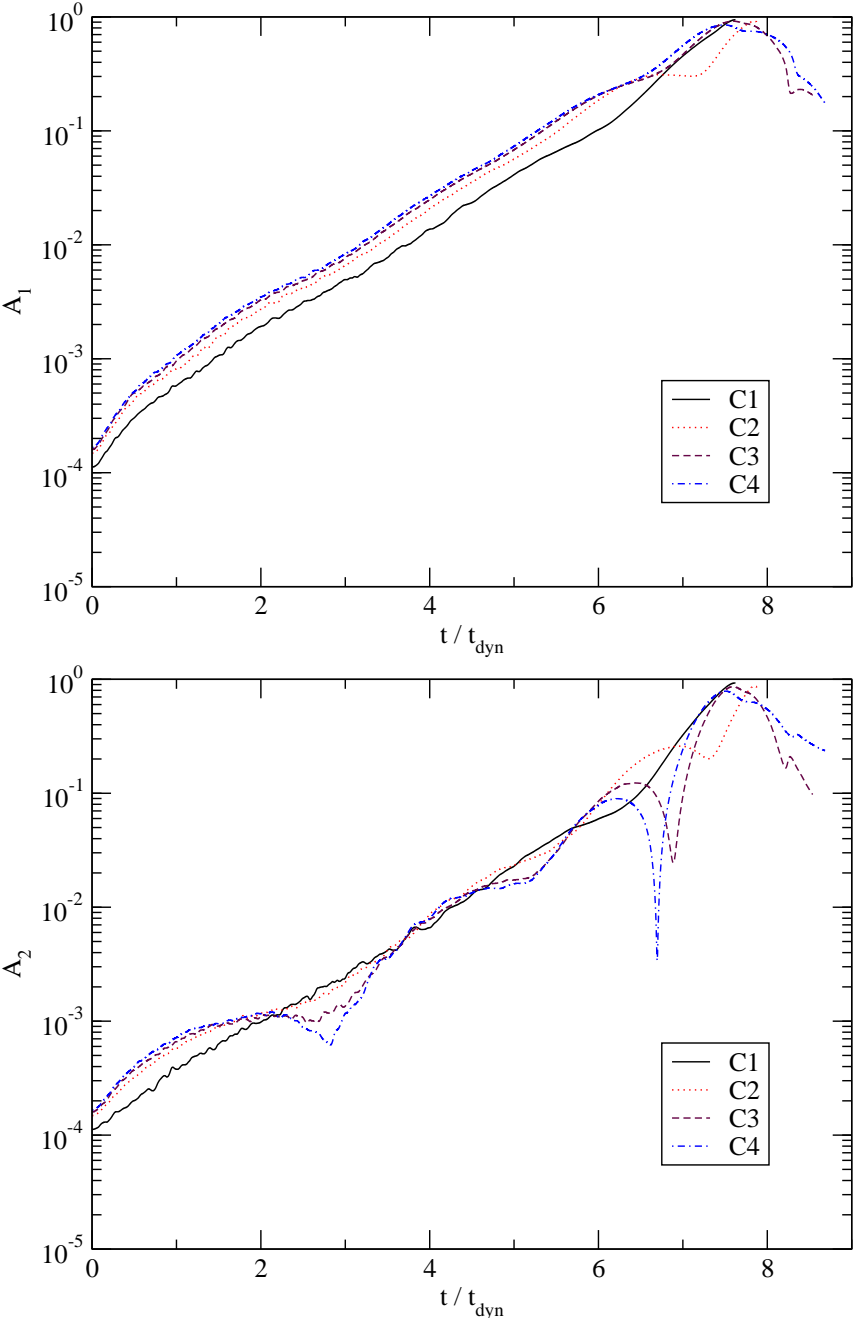


Figure 5.45.: Evolution of the mode amplitudes A_1 and A_2 for different members of the C sequence (cf. Table 5.4).

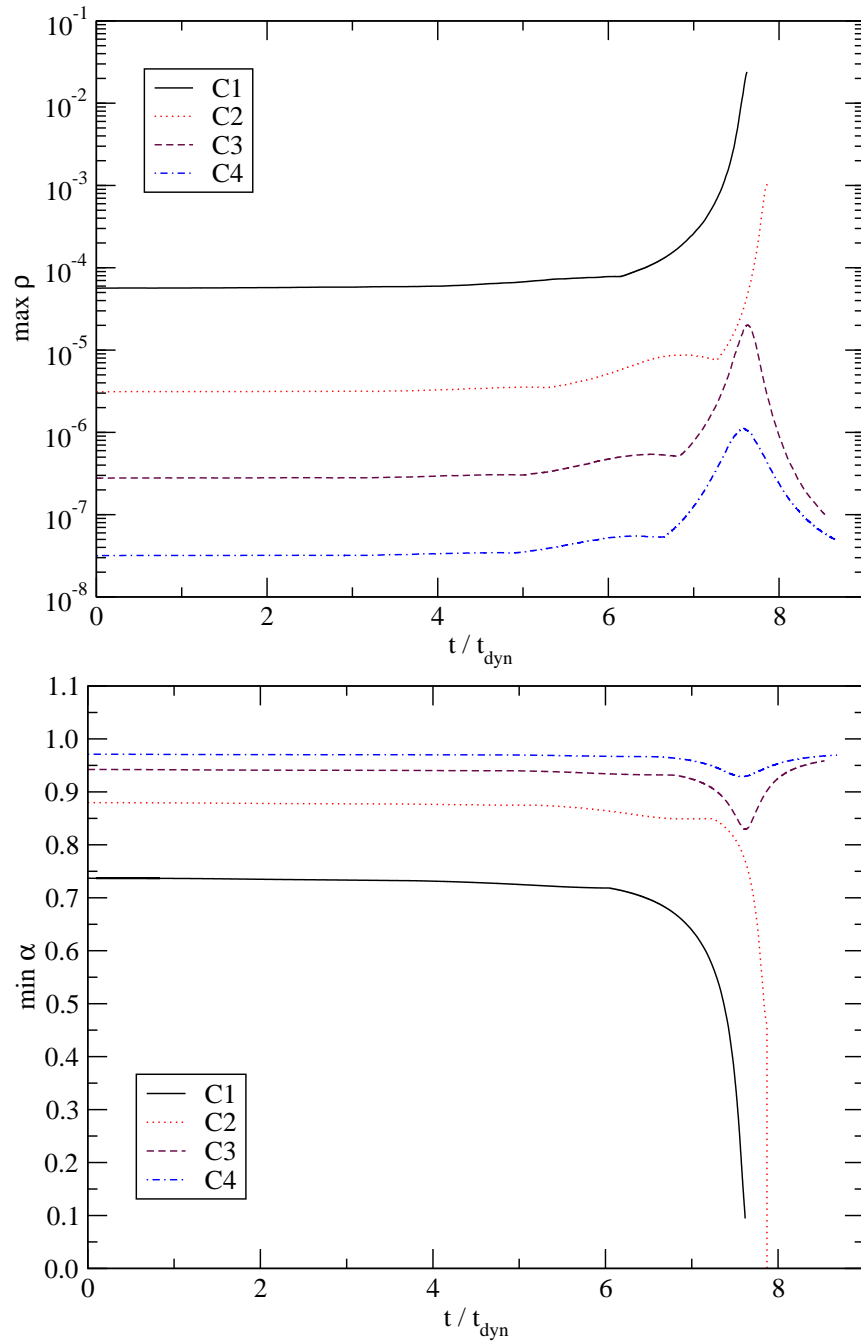


Figure 5.46.: Evolution of the maximum of the rest-mass density ρ and the minimum of the lapse function α for different members of the C sequence.

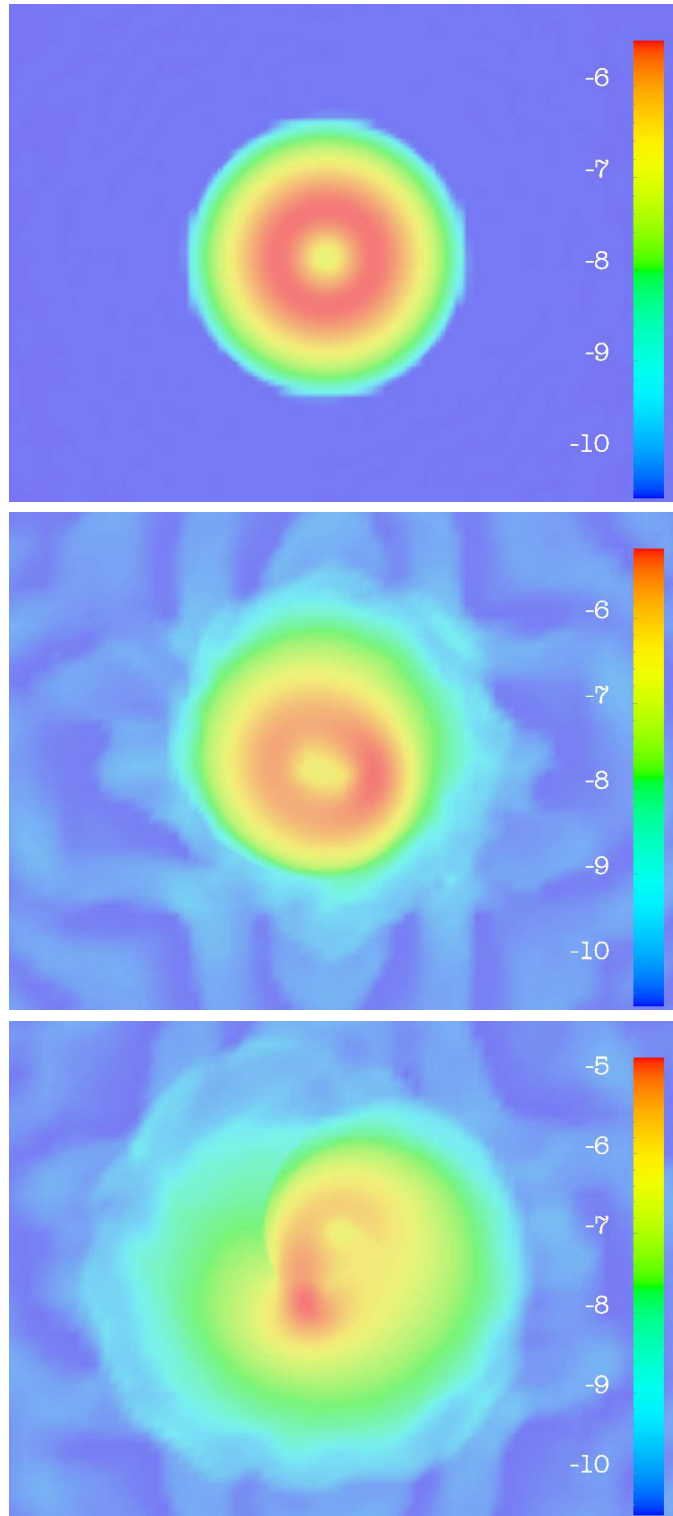


Figure 5.47.: Evolution of the density in the equatorial plane of the model C2. Shown is the decadic logarithm of the rest-mass density. The snapshots were taken at times $t/t_{dyn} = 0$ (top), 6.28 (middle) and 7.48 (bottom). Compare also to Fig. 5.18.

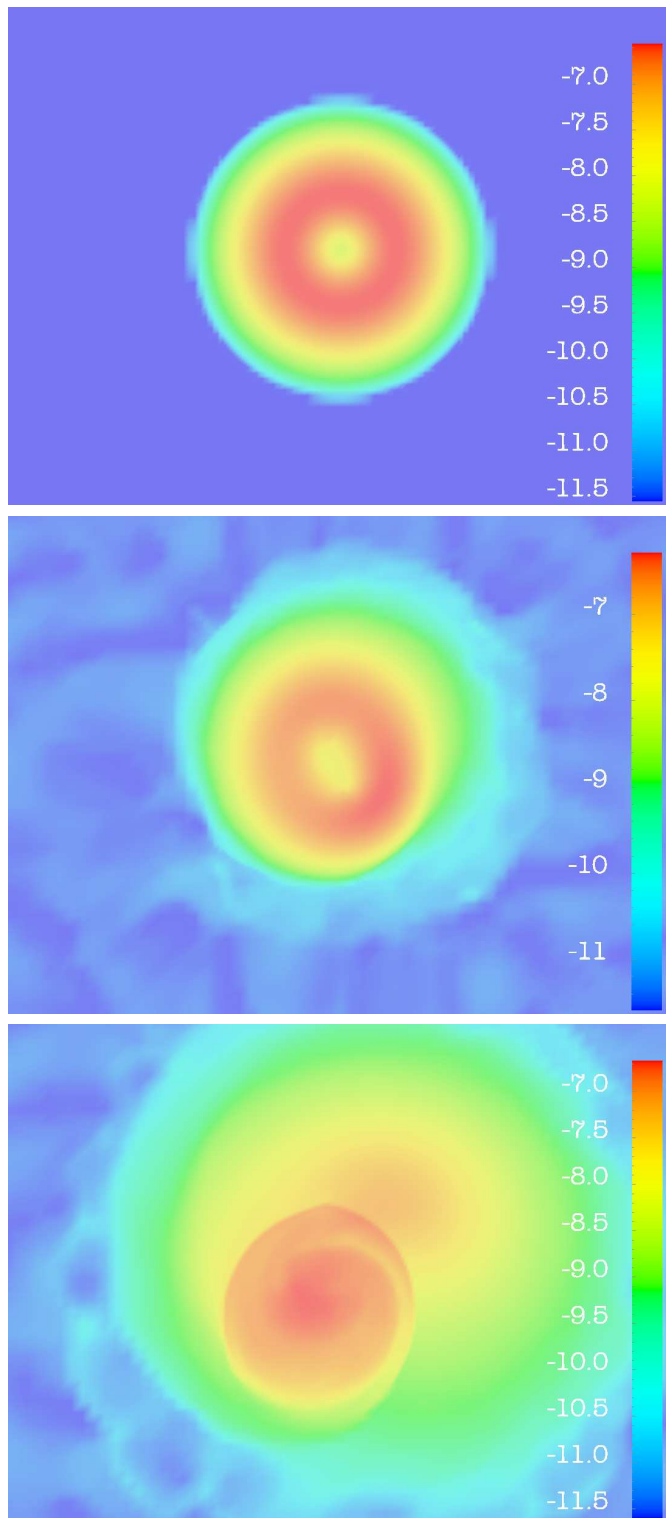


Figure 5.48.: Evolution of density in the equatorial plane of the model *C4*. Shown is the decadic logarithm of the rest-mass density. The snapshots were taken at times $t/t_{dyn} = 0$ (top), 6.28 (middle) and 8.28 (bottom). In contrast to the more compact models *C1* (Fig. 5.18) and *C2* (Fig. 5.47), the fragment re-expands after a maximal compression.

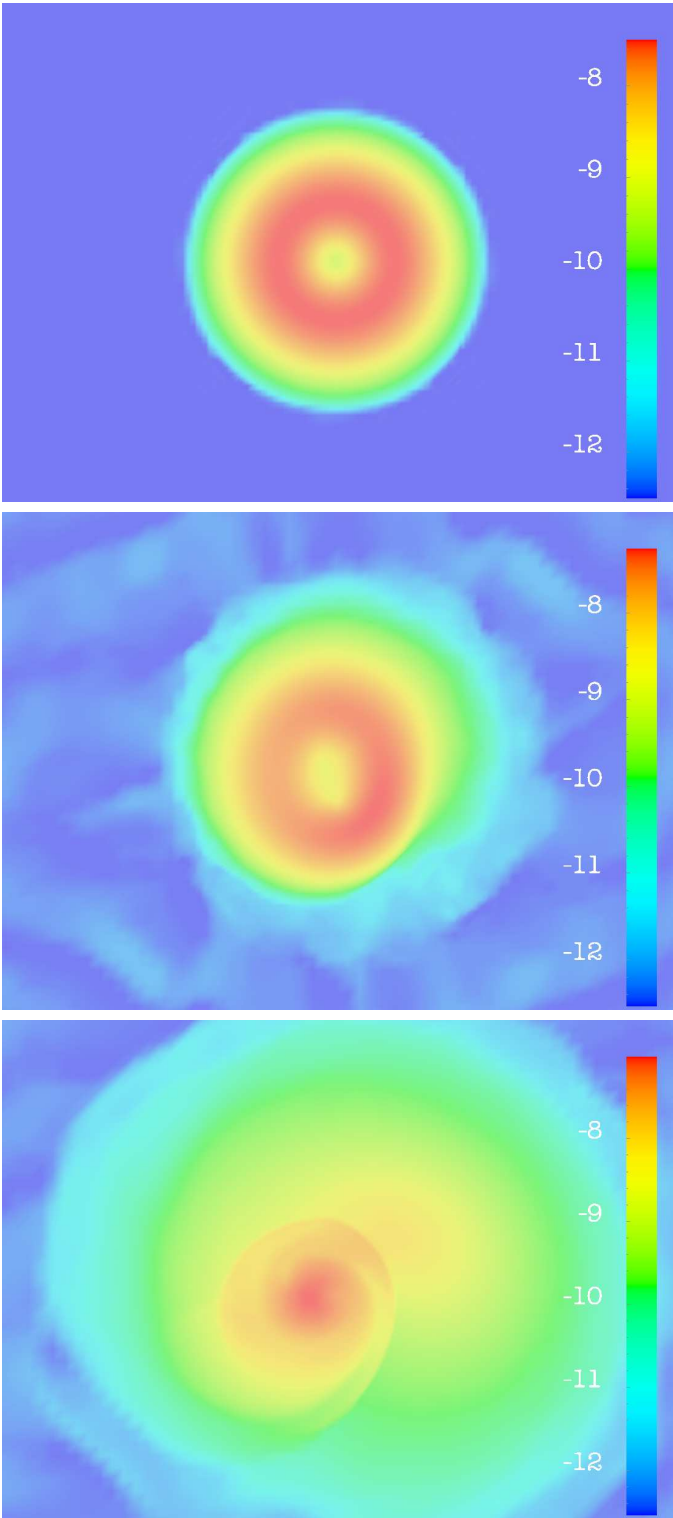


Figure 5.49.: Same as Fig. 5.48, but showing the evolution of the model C8.

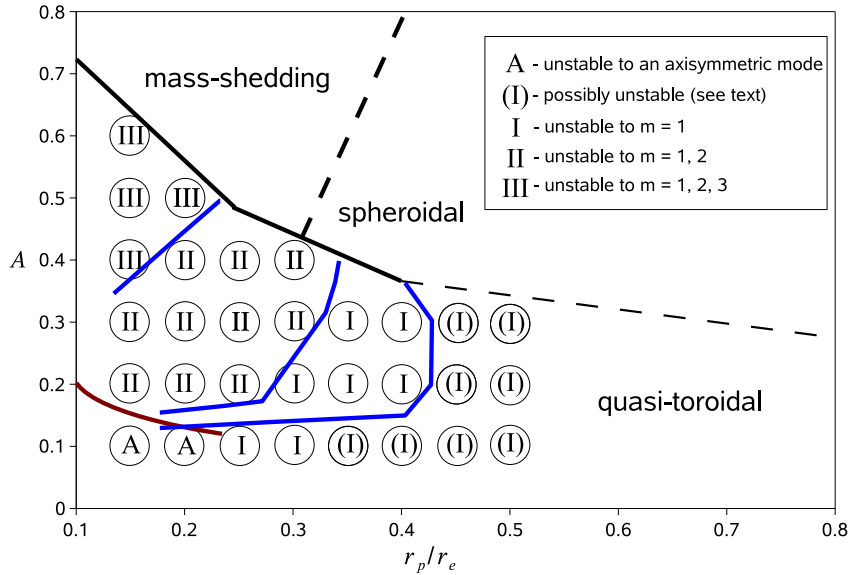


Figure 5.50.: Stability of quasi-toroidal models with $\rho_c = 10^{-7}$ (cf. Fig. 5.12). A Latin number denotes the highest azimuthal order of the unstable modes, i.e. ‘I’ for $m = 1$ unstable, ‘II’ for $m = 1, 2$ unstable, and ‘III’ for $m = 1, 2, 3$ unstable. Models denoted by ‘(I)’ are either long-term unstable with growth times $\tau \gg t_{dyn}$, or stable, and models denoted by ‘A’ exhibit an axisymmetric instability. The red line is the approximate location of the sequence $J/M^2 = 1$ (cf. Fig. 5.11), and the three blue lines are the approximate locations of sequences with $T/|W| = 0.14$ (right), $T/|W| = 0.18$ (middle) and $T/|W| = 0.26$ (left) (cf. Fig. 5.9).

instability is quite similar for stars of different compactness, the outcome of the fragmentation can differ drastically.⁸

5.3.5. Evolution of quasi-toroidal models of constant central rest-mass density

The structure of the parameter space plane $\Gamma = 4/3$ and $\rho_c = 10^{-7}$ has been discussed in Section 5.2.3. As already noted, the necessity of investigating only one plane is determined primarily by the computational cost of three-dimensional general relativistic hydrodynamical simulations. Also, the choice of the central density does not seem to affect the linear development of a non-axisymmetric unstable mode considerably, even for very compact quasi-toroidal polytropes (cf. Section 5.3.4), which is in contrast to axisymmetric modes. Finally, we note that the models with $\rho_c = 10^{-7}$ are already quite compact, with $R_e/M \approx 10 \dots 100$, and $r_p/M \approx 2 \dots 70$.

To investigate the stability of these models, members marked with a circle have been evolved in Fig. 5.12, imposing a perturbation of the form given by eqn. 5.6 with $\lambda_m = 1$, and with a resolution of $65 \times 65 \times 33$ grid points in the outer patches, and $97 \times 97 \times 49$ in the innermost patch. Selected models have been tested against individual $m = j$ perturbations with $\lambda_m = \delta_{mj}$, with different resolutions, and different densities of the artificial atmosphere, to test consistency and convergence. Also, central rest-mass densities different from 10^{-7} were investigated in a few models.

Fig. 5.50 gives an overview of the stability properties of the selected models. The Latin numbers ‘I’ to ‘III’ refer to the highest m with an unstable mode, i.e. in addition to the reference polytrope, which

⁸These results have been confirmed with lower and higher resolutions.

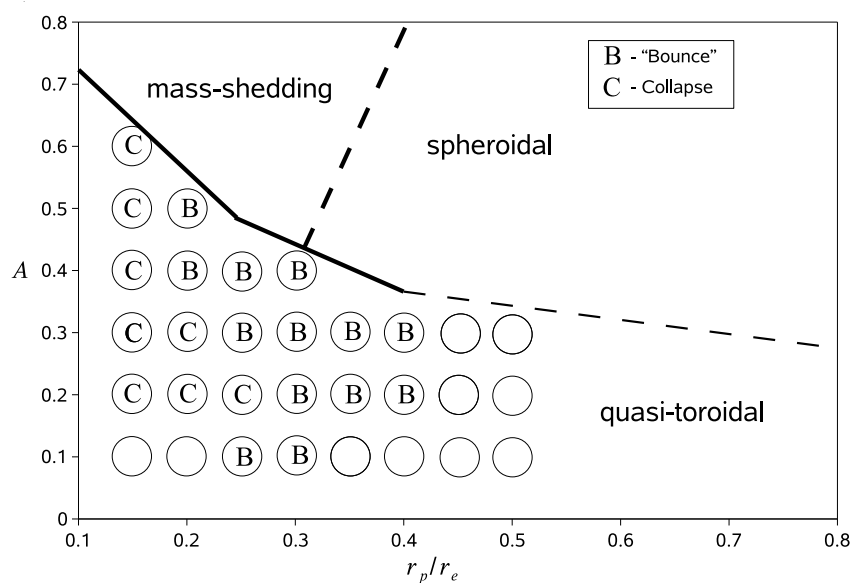


Figure 5.51.: Remnants of the models from Fig. 5.50, which are unstable with respect to non-axisymmetric modes. The non-linear behaviour has been analyzed by observing the evolution of the function $\min \alpha$ (see also Fig. 5.46). Models which show a minimum in this function are marked by ‘B’ for ‘bounce’, while models exhibiting an exponential collapse of the lapse are marked by ‘C’ for ‘collapse.’

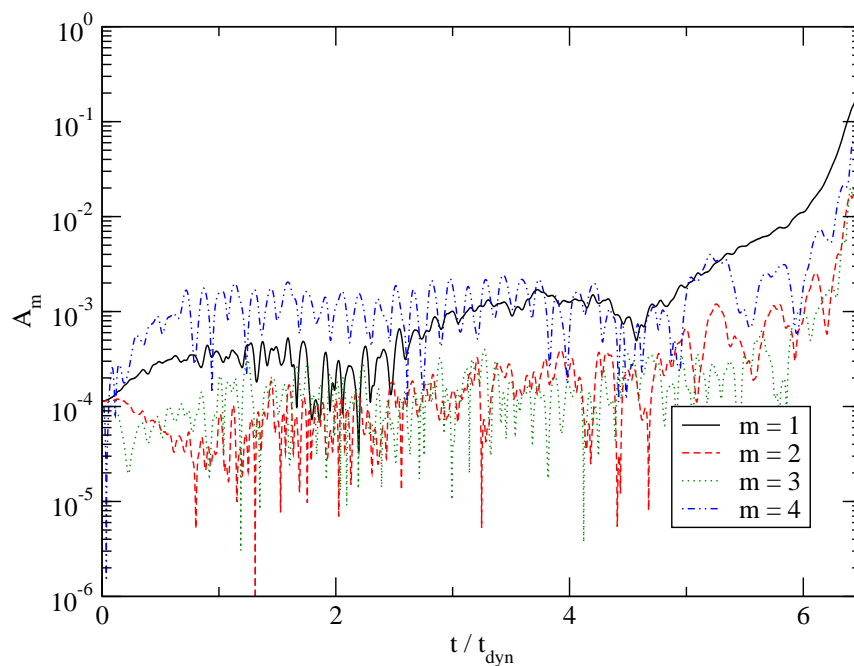


Figure 5.52.: Mode amplitudes in the model $A0.1R0.15$ (cf. Table 5.5), extracted at the radius of highest initial rest-mass density.

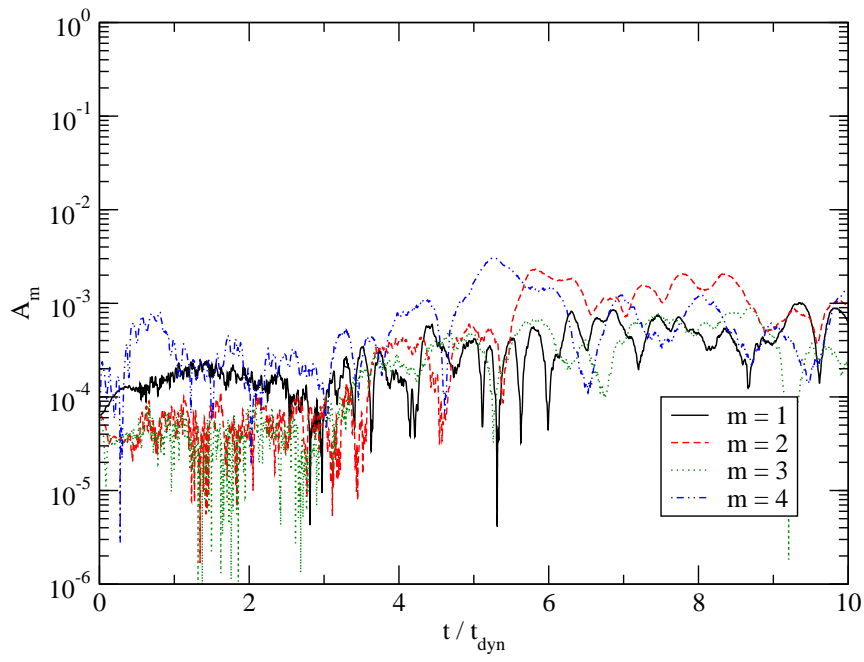


Figure 5.53.: Mode amplitudes in the model *A0.1R0.50* (cf. Table 5.5), extracted at the radius of highest initial rest-mass density.

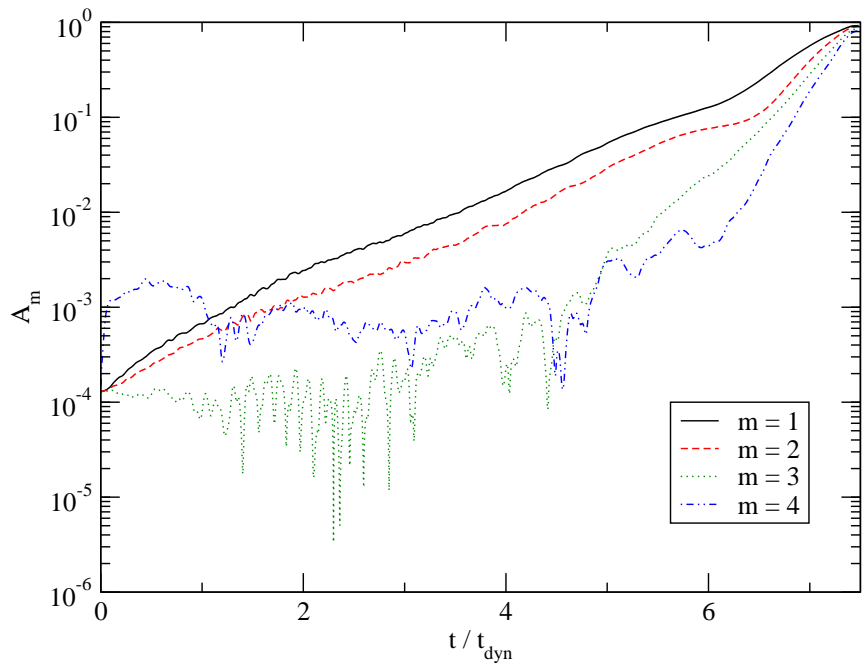


Figure 5.54.: Mode amplitudes in the model *A0.3R0.15* (cf. Table 5.5), extracted at the radius of highest initial rest-mass density.

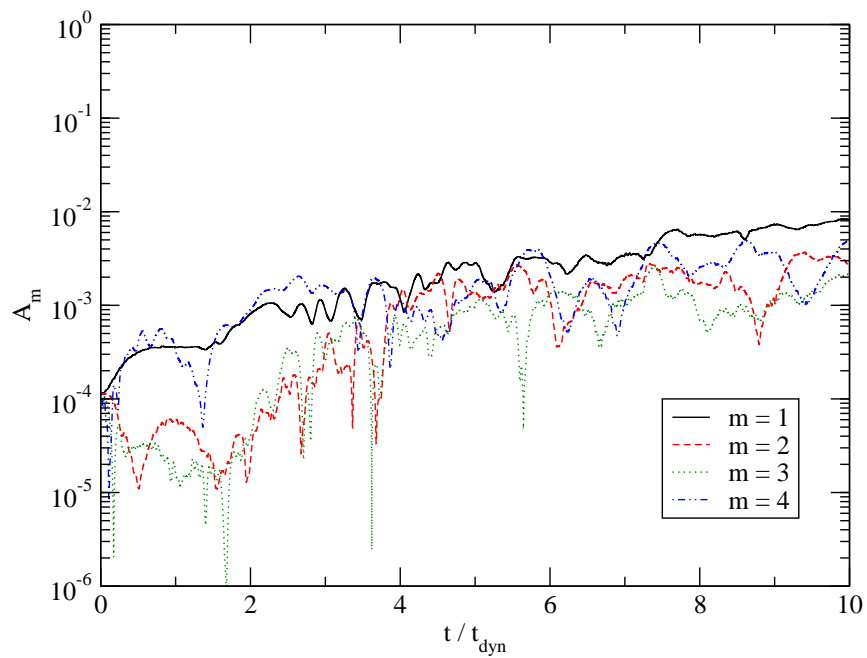


Figure 5.55.: Mode amplitudes in the model $A0.3R0.50$ (cf. Table 5.5), extracted at the radius of highest initial rest-mass density.

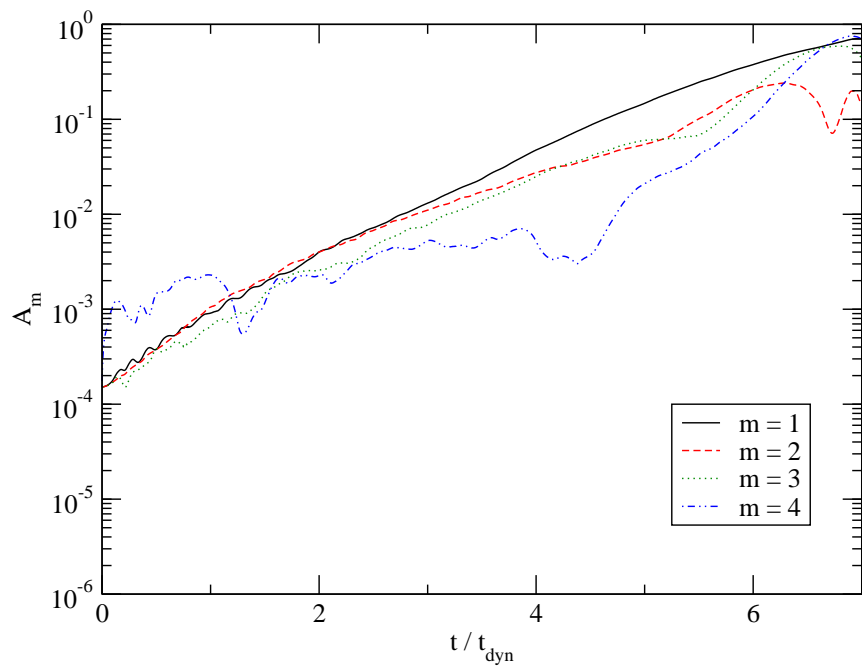


Figure 5.56.: Mode amplitudes in the model $A0.6R0.15$ (cf. Table 5.5), extracted at the radius of highest initial rest-mass density.

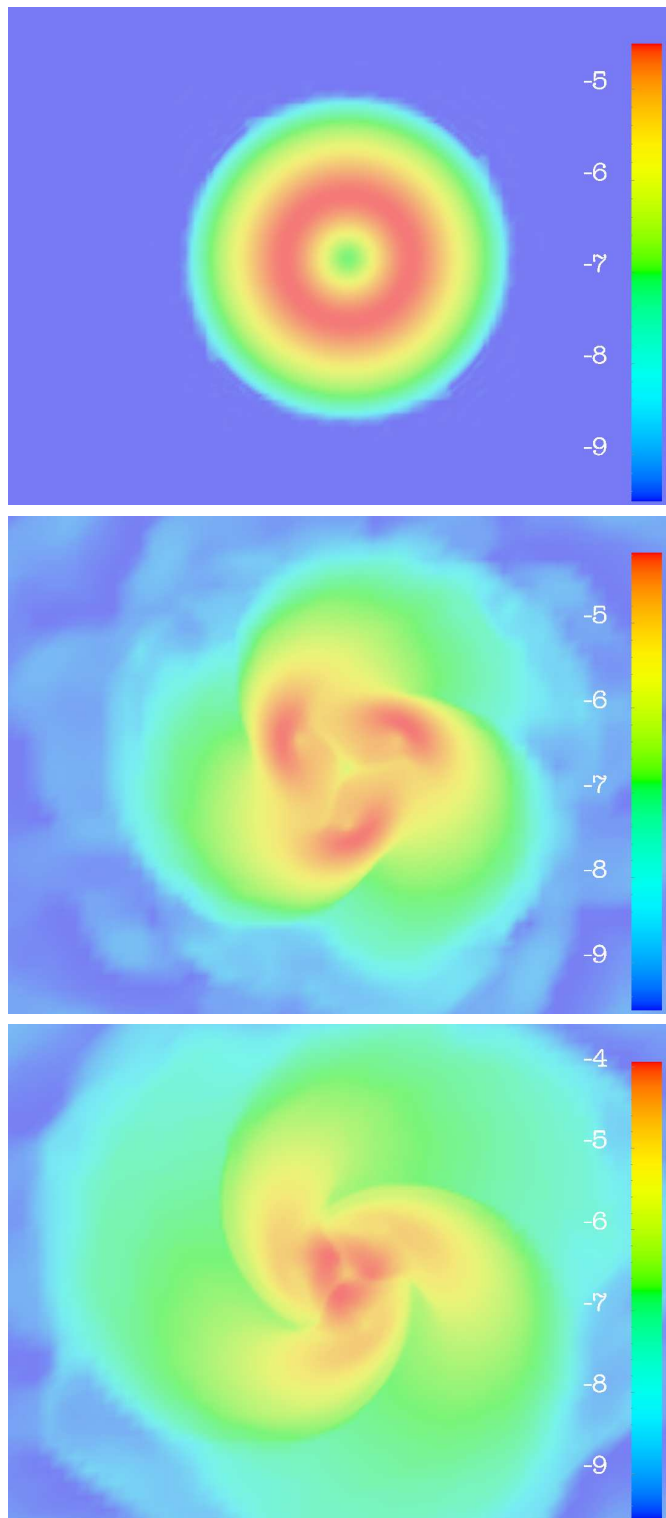


Figure 5.57.: Equatorial density evolution of the model *A0.6R0.15*, with an $m = 3$ perturbation. Shown is the decadic logarithm of the rest-mass density. The snapshots were taken at times $t/t_{dyn} = 0$ (top), 6.28 (middle) and 7.60 (bottom). Three fragments develop and subsequently encounter collapse similar to the two-fragment case (cf. Fig. 5.23). The evolution of the model perturbed with $m = 1$ and $m = 2$ is similar to the corresponding one in the reference polytrope.

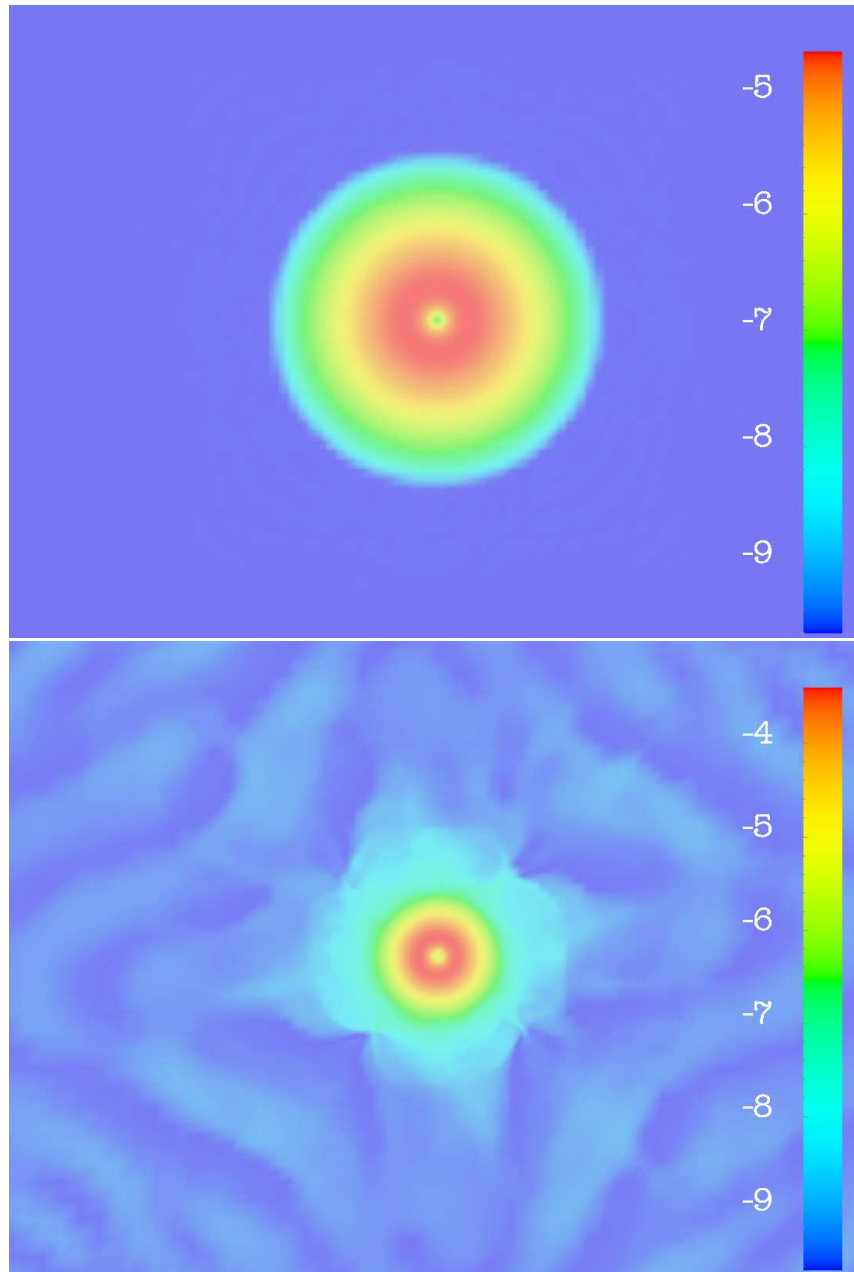


Figure 5.58.: Equatorial density evolution of the model *A0.1R0.15*. Shown is the decadic logarithm of the rest-mass density. The snapshots were taken at times $t/t_{dyn} = 0$ (top) and 6.28 (bottom). The model exhibits an axisymmetric instability.

belongs to the class “II”, we find models which are unstable to an $m = 3$ perturbation, and models which appear stable against $m = 2$ (within the restrictions illustrated in Section 5.3.7). The models denoted with an “A” have been found to be unstable to an axisymmetric mode, and collapse before any non-axisymmetric instability could develop. Finally, the models marked with “(I)” are either stable or long-term unstable with a growth time $\tau \gg t_{dyn}$. Each model has been evolved for up to $10 t_{dyn}$ to determine its stability. This limit is arbitrary, but imposed by the significant resource requirements of these simulations. If no mode amplitude exceeds the level of the $m = 4$ noise during this time, the model is marked with a “(I)”. This does not imply that the model is actually stable, and we will investigate a specific model denoted by “(I)” later. We will find it to be unstable to an $m = 1$ mode with slow growth (Section 5.3.7).

The additional lines in Fig. 5.50 are approximate isolines of the functions $T/|W|$ for the values 0.14, 0.18 and 0.26 (cf. also Fig. 5.9) and of the function J/M^2 for the value 1. As long as the models do not rotate too differentially, $T/|W|$ still seems to be a reasonable indicator of the non-axisymmetric stability of the polytropes, even though they are quasi-toroidal and relativistic.

The nature of the non-linear behaviour of models exhibiting a non-axisymmetric instability is indicated in Fig. 5.51. We primarily use the evolution of the minimum of the lapse function to classify the models, see also Fig. 5.46. Models denoted by “B” have a global minimum in the lapse, while models denoted by “C” do not. Given that the compactness of the models increases with smaller axes ratios in this plot (cf. Fig. 5.10), we expect that a black hole forms for each member of the “C” class. To determine this uniquely, each of these models should be tested using the adaptive mesh-refinement technique presented in [134], which is, however, beyond the scope of this study.

In Fig. 5.52 to 5.56, we have plotted the mode amplitudes A_m for selected models (cf. Table 5.5). The evolution of the model *A0.3R0.15* (Fig. 5.54) is quite similar to that of the reference polytrope. Model *A0.6R0.15* is further inside the unstable region, and exhibits also an $m = 3$ instability: the density evolution of this mode is plotted in Fig. 5.57. The models *A0.1R0.50* and *A0.3R0.50* are stable within the numerical restrictions mentioned above.

Only the model *A0.1R0.15* seems to have an unusual evolution of the mode amplitudes; this also applies to the model *A0.1R0.20*, which is not shown here. The density evolution of *A0.1R0.15* (Fig. 5.58) shows that the model has encountered an axisymmetric instability, before any non-axisymmetric modes can grow to an appreciable amplitude. We note that both models *A0.1R0.15* and *A0.1R0.20* have $J/M^2 < 1$, in contrast to most other models in the parameter space plane considered here; only the model *A0.1R0.25* has $J/M^2 = 0.961$. In Fig. 5.50, the isoline $J/M^2 = 1$ is marked. It approximately separates the region of axisymmetric from that of non-axisymmetric instability.

5.3.6. The location of the instability in the corotation band

Fig. 5.59 shows the location of the unstable modes in the corotation band, for three different models on the sequence $\Gamma = 4/3$, $\rho_c = 10^{-7}$, and $A = 0.3$. All modes are in corotation, but there is evidence that, for decreasing $T/|W|$, the corotation point moves toward the pole. This gives support to the arguments presented in [127], where the existence of low $T/|W|$ and spiral-arm instabilities in differentially rotation polytropes are connected to corotation⁹. Limitations of resources did not permit us to investigate the assumed boundary of the corotation region, where growth times of many t_{dyn} are expected, however, with the results of Sections 5.3.4 and 5.3.8, one can be optimistic that a purely Newtonian investigation might give results which are qualitatively similar to a relativistic study.

⁹There is evidence that, on a sequence of increasing rotation parameter, some modes in the discrete spectrum become unstable when entering the corotation band (which has a continuum spectrum), or might annihilate with other modes inside the band and become unstable. These are mechanism not present in uniformly rotating polytropes.

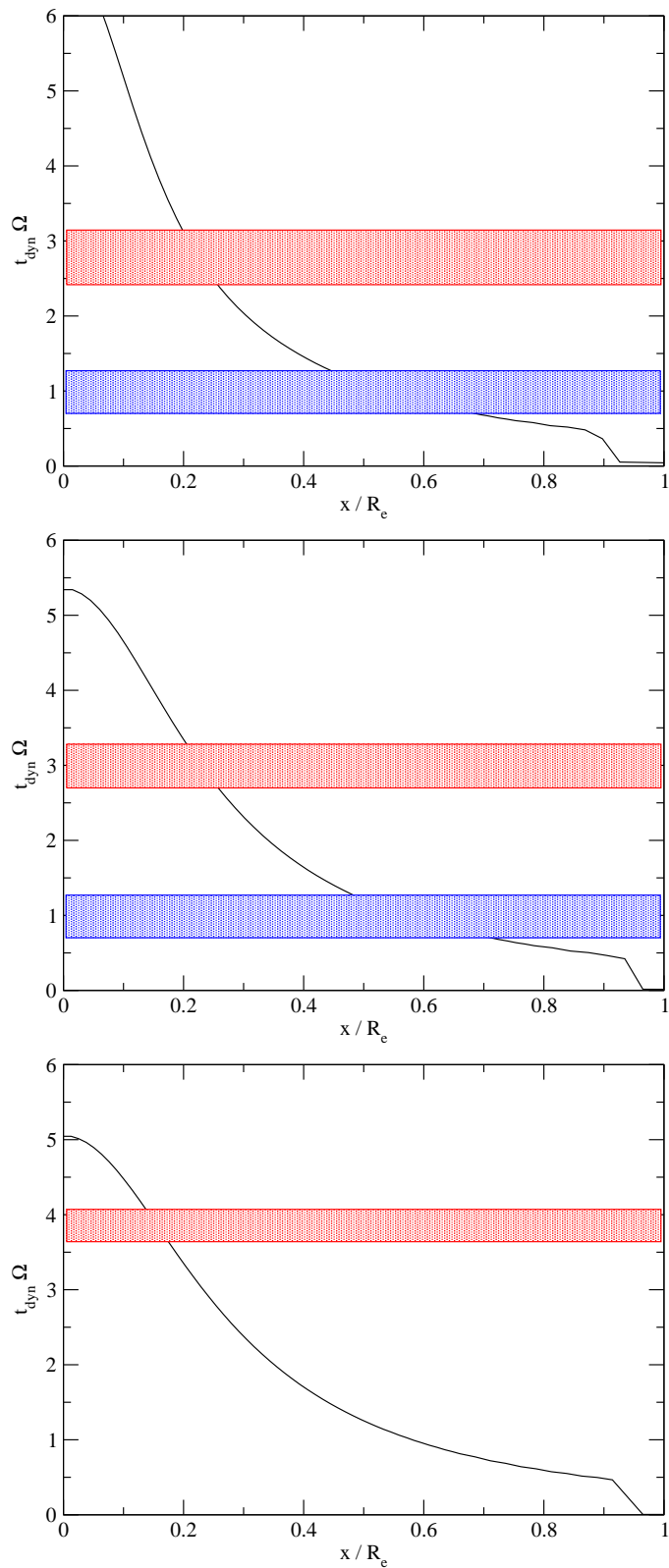


Figure 5.59.: Angular velocity of the polytropes $A0.3R0.15$ (top), $A0.3R0.30$ (middle) and $A0.3R0.40$ (bottom) over the x axis (black line), and approximate location of the pattern speed of the $m = 1$ mode (red rectangle) and the $m = 2$ mode (blue rectangle), cf. also Fig. 5.36.

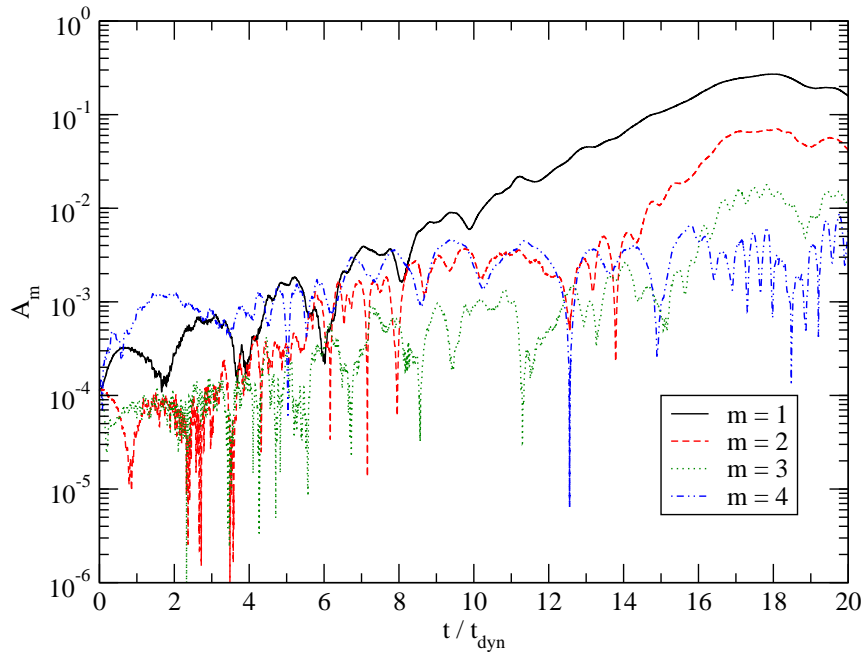


Figure 5.60.: Long-term evolution of the mode amplitudes for the model $A0.2R0.45$, which is unstable to an $m = 1$ perturbation. The mode, however, grows rather slowly over a time of $20 t_{dyn}$.

5.3.7. Evolution of a model with a slow growth of the $m = 1$ instability

As already discussed, the nature of the class “(I)” models in Fig. 5.50 could not be investigated in detail due to the high computational cost when evolving general relativistic, three-dimensional models. However, to illustrate the behaviour in one specific case, a long-term simulation of the model $A0.2R0.45$ has been performed (Fig. 5.60). A slowly growing $m = 1$ instability is apparent in the evolution, which saturates at high amplitudes only after $20 t_{dyn}$. While the $m = 1$ mode is clearly dominant, the $m = 2$ might be unstable as well. A detailed investigation of these sequences should be attempted in the limit of vanishing compactness, with a Newtonian model and preferably, with a cylindrical grid (see also the discussion in Section 5.4).

5.3.8. Evolution of a sequence of models with different compactness starting from the boundary between the regions “I” and “(I)”

In Section 5.3.4, we have already studied the influence of the compactness on the development of the instability in the reference polytrope. According to the results of Section 5.3.5, the reference model is located inside region “II” of the parameter space plane for $\rho_c = 3.38 \cdot 10^{-6}$. Thus, it is instructive to investigate the effect of compactness on a model’s evolution which is located close to the boundary between regions “I” and “(I)” in Fig. 5.50 (although this boundary is not sharply defined). A selected model, $A0.2R0.40$, has been extended to the L sequence of constant Γ , A , and $T/|W|$ (cf. Table 5.6). The influence of compactness on the $m = 1$ mode is illustrated in Fig. 5.61: The most compact models $L1$ and $L2$ show a growth of the non-axisymmetric mode already early on, but collapse due to an axisymmetric instability (both models have $J/M^2 < 1$). The growth rate of the non-axisymmetric instability is not very sensitive to the compactness, which confirms our findings for models of the C sequence. One can therefore

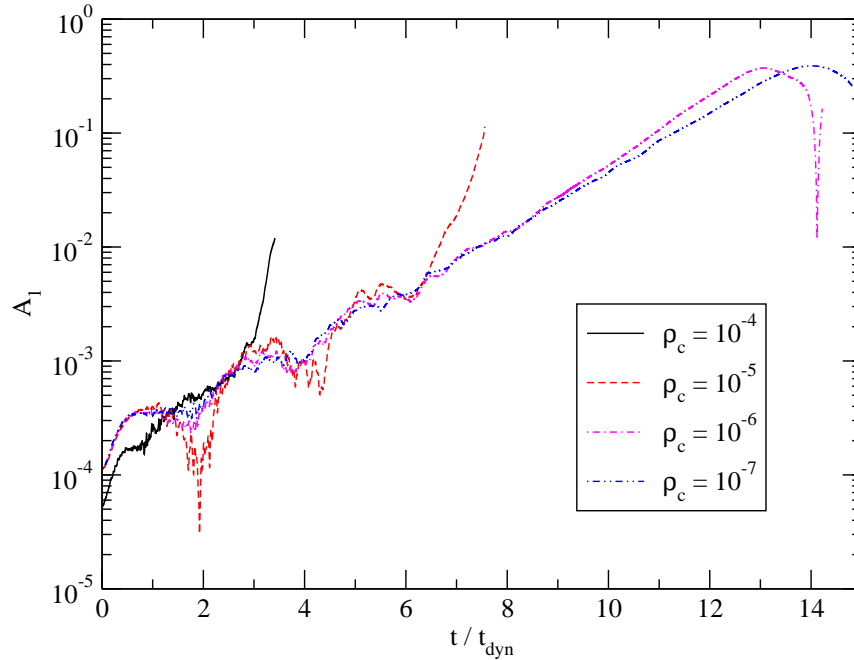


Figure 5.61.: Amplitude of the $m = 1$ mode for different models from a sequence with constant $T/|W|$ limiting in the model $A0.2R0.40$, which has $\rho_c = 10^{-7}$. Cf. also Table 5.6.

be quite optimistic that the *non-axisymmetric* stability properties of quasi-toroidal $N = 3$ polytropes are well-represented by Fig. 5.50, even for a different choice of central rest-mass density. The *axisymmetric* stability, and the question whether the collapse of the fragment will be halted or not, is sensitive to ρ_c .

5.4. Summary

In this chapter, we have investigated the non-axisymmetric instabilities, fragmentation and black hole formation in general-relativistic, quasi-toroidal polytropes. Our focus was to gain an understanding how various parameters determining the structure of the equilibrium polytrope affect the development of the instability, and the nature of its remnant. In addition, we have investigated the location of the unstable modes in the corotation band of the differentially rotating models.

All investigations have been performed using three-dimensional numerical simulations in general relativity, and assuming the stars to be self-gravitating perfect fluids with an adiabatic coefficient equal to the polytropic constant Γ . The equations of general relativistic hydrodynamics have been evolved using high-resolution shock-capturing methods, and the NOK-BSSN formalism has been used for the metric evolution. All grids use centered fixed mesh refinement, and impose an equatorial plane symmetry. The development of unstable modes has been followed by the use of a discrete Fourier transform of the rest-mass density computed at certain coordinate radii in the equatorial plane, with a preference on the radius of initial highest density.

The central results are represented in Fig. 5.30, 5.50, 5.51, and 5.59. For a plane of constant rest-mass density $\rho_c = 10^{-7}$ and $\Gamma = 4/3$, we have determined the region where quasi-toroidal models become dynamically unstable to non-axisymmetric fragmentation. From the structure of the space of initial models presented in Fig. 5.7 to 5.11, it appears that there is a rough relation between $T/|W|$ and the highest order

of unstable modes, at least as long as the degree of differential rotation is not too high. Since the numerical method is not well-suited to follow the development of instabilities with growth times much longer than a dynamical timescale, we could not determine the fate of models from class “(I)” with certainty. However, we have shown in one specific case that the model is actually unstable. In the same manner, a model from class “I” could be subject to a slowly growing mode with $m > 1$; however, in this case the $m = 1$ mode would clearly be dominant.

From the investigation of a sequence emanating from the model used in the publications [134], we have found that the central rest-mass density ρ_c , which controls the compactness of the polytrope, does not affect the development of the non-axisymmetric instability significantly. This is related to the fact that $T/|W|$ is insensitive to ρ_c . However, ρ_c determines the nature of the final remnant: While the model in [134] forms a black hole, two models having one fourth and one eighth as much compactness show a re-expansion of the fragment after maximal contraction.

The regions of models in the plane $\rho_c = 10^{-7}$ and $\Gamma = 4/3$ where such a re-expansion was observed is indicated in Fig. 5.51 by a “B”. If one accepts that the models *not* exhibiting this behaviour, marked with “C” in Fig. 5.51, are forming black holes in the same manner as shown in [134], then we can draw the following tentative picture of black hole formation by fragmentation of single stars.

The nature of the final system, either an almost unperturbed axisymmetric star, a single central black hole, single or multiple non-central black holes with a disk, or one or several expanding remnants without trapped surfaces, depends on the symmetry properties of the perturbation, and the location of the equilibrium star with respect to three types of surfaces in the space of parameters:

1. *Surfaces indicating the onset of the instability of a mode of a certain order m .* These surfaces might be close to isosurfaces of $T/|W|$ as indicated in Fig. 5.50, but the resource requirements of performing three-dimensional general relativistic simulations limit our ability to identify slowly growing modes. However, if only modes growing on the order of a dynamical timescale are considered, then $T/|W|$ might yield a reasonable indicator of the location of the limit surfaces. The compactness of the initial model seems to have no significant effect on the location of these surfaces, at least for $\Gamma = 4/3$. Thus, one may attempt to obtain a more precise location using a computationally less expensive Newtonian approach.
2. *Surfaces indicating the onset of an axisymmetric instability.* In our samples, all models with $J/M^2 < 1$ were unstable to quickly growing axisymmetric modes, and hence will likely evolve to central black holes. The surface $J/M^2 = 1$ can therefore be used as an approximate separator between axisymmetric collapse and stability (cf. [149] for a more detailed discussion of this point).
3. *Surfaces separating black-hole formation from re-expansion.* In Fig. 5.51, an approximate determination of such a surface has been attempted. In a first approach, and assuming that results for the stability of slowly and uniformly rotating relativistic polytropes [54, 55, 56] can be applied to the fragments, we expect a fragment with a higher compactness to be destabilized, and, given that the geometric development of the fragmentation process is similar for different choices of compactness of the equilibrium polytrope, that there is a close connection to isosurfaces of R_e/M . However, when comparing Fig. 5.10 and 5.51, the situation appears more complicated, and deserves further attention.

With respect to the question whether multiple black holes may form or not, two comments are in order: First, in the unstable systems of class “II” and “III”, all growth times of modes with different m are of comparable magnitude, i.e. the nature of the actual time development in a specific star will depend on the symmetry of the perturbation, as already mentioned. If the perturbation is random, it appears that one dominant fragment (the superposition of, say, $m = 1$ and $m = 2$) develops and collapses. Since our code

encounters numerical problems after black hole formation, we cannot determine the fate of the remaining disk of material in this interesting case. Second, even when two fragments are forming and collapsing, in all cases considered here a runaway instability develops and leads to a central collapse (Fig. 5.23). In this case, the gravitational wave signal is expected to resemble the ring-down phase of a highly deformed black hole.

Concerning the nature of the non-axisymmetric mode, we have collected evidence that, along a sequence with decreasing $T/|W|$, the corotation point moves towards the pole region of the polytrope. This gives support to the arguments by Watts et al. [127]. To also investigate the cases with large growth times, however, a Newtonian model, preferably with a cylindrical grid, would be of advantage to obtain more detailed results.

Possible future work on this problem can be roughly divided into three approaches. First, the nature of the low- $T/|W|$ and $m = 1$ instabilities in quasi-toroidal polytropes could be investigated in Newtonian gravity, or perhaps using some perturbative approximation of general relativity, to determine the location of the corresponding surfaces in parameter space, and to suggest regions where the quantity $T/|W|$ is still a good indicator for instability. Since the Newtonian polytropes can be considered to be limit points of relativistic sequences with vanishing compactness, the systematic effect of general relativity on their stability properties can be determined separately.

Second, the location of the surfaces separating black hole formation from “bounce” behaviour, and its relation to the initial compactness R_c/M , needs to be determined with more detail, specifically also its dependence on Γ . Could a newly formed, rapidly and differentially rotating neutron star fragment in this way? We have found no example of this kind here, but such a question deserves further attention.

Third, to connect more closely to certain astrophysical systems, a detailed model of the micro-physical processes, particle transport, and magnetic fields is necessary in many cases to obtain specific answers. The most important bulk property appears to be a change in Γ during evolution, since this would modify the non-linear evolution of the fragmentation significantly. In the specific case of core collapse, results in this context have been obtained already [139, 126].

6. Spherically symmetric dynamical black holes modeled with high-order summation-by-parts techniques

This chapter is based on a joint publication [150] with Peter Diener, Enrique Pazos and Manuel Tiglio. All simulations have been performed by the author. The numerical evolution code has been developed by the author, with the exception of the SBP operator implementation, which is by Peter Diener.

In this chapter, the discrete representation of the spherically symmetric Einstein-Klein-Gordon system is attempted with several modern tools in numerical relativity (see also Chapter 3).

1. *A first order hyperbolic formulation:* A first order system admits an easier discussion of the level of hyperbolicity, and therefore of the well-posedness of the initial-boundary-value problem. Also, one can easily guarantee that the system has only physical speeds of propagation (i.e. those which are inside or on the light cone), which is an important requirement for setting up excision surfaces. Here, the symmetric hyperbolic Einstein-Christoffel system is used (cf. Section 3.2.2).
2. *Multiple coordinate patches:* The coordinate domain is covered by one or several coordinate patches which do not intersect, with the intention to emulate the multi-patch setups to be applied to three-dimensional numerical relativity. Since any discrete function may be two-valued on an interface point, a stable technique to ensure consistency, penalty boundary conditions, is necessary.
3. *Excision:* The inner boundary is chosen in a way that it is always purely outflow for all modes. Since the modes are restricted to the light cone, and since the system is strongly hyperbolic, it is sufficient that the inner boundary is spacelike and ingoing.
4. *Constraint-preserving boundary conditions:* The outer boundary data is subjected to the requirement that it satisfies the constraint equations of the Einstein-Christoffel-Klein-Gordon system, which leaves only two modes of inflow: one mode associated with gauge, and one wave mode of the massless Klein-Gordon field.
5. *Cauchy-perturbative matching:* A simplified model of Cauchy-perturbative matching¹ is obtained by freezing the spacetime on the outermost patch, and using the Klein-Gordon field as a scalar analogue of gravitational radiation.
6. *Summation-by-parts operators:* To obtain a stable (in the linearized sense) discrete evolution system from the well-posed initial-boundary-value problem, finite difference and dissipation operators with the summation-by-parts property are used to evaluate derivatives. These operators also use one-sided stencils on the boundaries, and thus are ideal for excision and multiple coordinate patches.

¹The term *Cauchy-perturbative matching* refers to dividing the computational domain of a compact source into a central “Cauchy” part, which is evolved using the full set of equations, and an outer part which only evolves perturbations on a fixed background (often Schwarzschild). This procedure allows to propagate weak gravitational waves far from the source without the computational cost associated with the full evolution system.

7. *Penalty boundary operators*: Ensuring consistency and convergence with multiple patches while still maintaining the global stability requirements is possible with a penalty operator applied to the inter-patch boundaries. The free outer boundary is treated in the same manner by penalizing to analytically specified boundary data on the incoming modes.

6.1. Numerical setup

6.1.1. Cauchy–perturbative matching

Since there is no radiative degree of freedom in spherically symmetric spacetimes, we use the massless Klein-Gordon field as a scalar analogue of gravitational waves. To emulate the setup of three-dimensional Cauchy–perturbative matching as closely as possible, the scalar wave is evolved on a fixed Schwarzschild background in a “perturbative” patch defined for $r \geq r_m$, while the fully non-linear Einstein’s equations are evolved in the “Cauchy” patch, defined for $r \in [r_e, r_m]$, where r_e and r_m denotes the excision radius and the matching radius, respectively.

The fact that we are using constraint-preserving boundary conditions allows us to perform a clean matching. From the analytical point of view our matching works in the following way: As explained in Section 3.2.5, after the constraint projection procedure, only two free characteristic modes are entering the Cauchy computational domain (at $r = r_m$), denoted by u_3 and u_8 . Since in a very precise sense u_3 is a gauge mode, we are free to give boundary conditions to it in a very simple way: we just set it to its initial value. Regarding u_8 , we use the “perturbative” value of the same quantity coming from the perturbative domain as counterpart, and communicate these two modes (how this is done at the numerical level is explained below). Similarly, there is only one characteristic mode entering the perturbative domain, which is the linearized version of u_7 . We therefore communicate the non-linear and linear versions of that mode as well.

6.1.2. Numerical code

A one-dimensional code which supports constraint-preserving boundaries, multiple grid patches, and the use of the aforementioned high order summation-by-parts derivative and dissipation operators has been developed. In addition, the code is able to reproduce the (single grid and without Cauchy–perturbative matching) second-order methods of Ref. [151] for comparison. The time integration is performed by a 4th order Runge-Kutta method. The grid patches that we consider here are not intersecting, but touching. This implies, that each grid function is double valued at the patch interface coordinate since the SBP derivative operators are one-sided at the boundaries. To ensure consistency without compromising (linear) stability, we make use of a penalty method (cf. Section 3.3.5). Constraint-preserving boundary conditions require the calculation of derivatives of certain grid functions at the outer boundary, which we also obtain by using the summation-by-parts derivative operators. An illustration of the computational domain is provided in Figure 6.1.

In a black hole setting, the computational domain next to the excision boundary tends to quickly amplify high frequency noise, which is not represented accurately on the discrete grid. This is especially true for high order accurate derivative operators. Thus, high order accurate simulations of black holes need a certain amount of numerical dissipation to be stable. This dissipation is here provided by the SBP dissipation operators constructed in Ref. [152] (cf. Section 3.3.4). The free parameters of these operators, e.g. the strength of numerical dissipation, are found by numerical experiment.

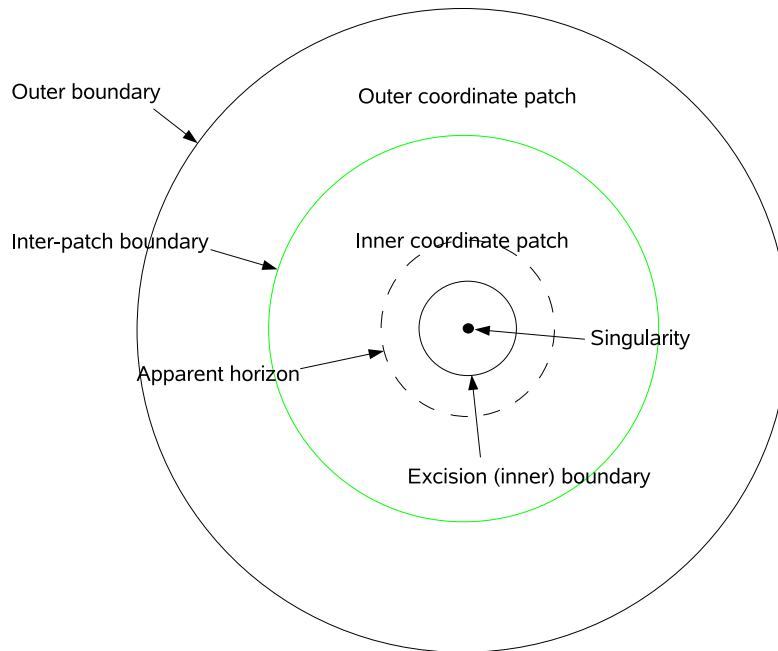


Figure 6.1.: Illustration of the computational setup used in this chapter. The solution is assumed to be spherically symmetric. The singularity at coordinate $r = 0$ is avoided by introducing the excision boundary, which must remain inside the apparent horizon to ensure that all modes are *outflow* there, i.e. no boundary data is necessary at the inner boundary. The division into several coordinate patches is optional, and it is indicated in the text whether one or two patches are used.

6.2. Results

The numerical experiments presented in this section are set up to systematically test the performance of the new techniques in several situations of increasing difficulty. We start with a series of tests evolving a Schwarzschild black hole in Painlevé-Gullstrand coordinates with either a single patch or two patches matched via the penalty method, and compare the performance of all SBP operators with the second-order finite-differencing method presented in [151]. Next, to test more dynamical situations, a gauge or scalar field signal is injected in a constraint-preserving manner through the outer boundary and accreted onto the black hole. A robust stability test is then performed with noise on the incoming gauge mode u_3 , and, with Cauchy-perturbative matching, on the scalar field mode u_8 . Finally, a series of high-precision tests involving all techniques are presented, in which a black hole accretes a scalar field injected through the outer boundary of the perturbative patch. These simulations also include a test of the long-term stability and accuracy after accretion and ring-down.

6.2.1. Schwarzschild black hole in Painlevé-Gullstrand coordinates

In our first series of tests, a Schwarzschild black hole is evolved with high-order accurate SBP operators, constraint-preserving boundary conditions and excision. Cauchy-perturbative matching is not used in these tests. To fix the coordinate system, we make use of the horizon-penetrating Painlevé-Gullstrand coordinates [29, 30], and we fix the coordinate functions $\tilde{\alpha}$ and β of Section 3.2.2 to their exact values.

For all tests, the inner boundary is located well inside the event horizon (more precisely, it is located at $r_e = 1M$), which implies that all modes are outflow due to the facts that the vector ∂_t is spacelike, and that the light cone is contained in the section of tangent space exterior to the boundary. Therefore, no boundary conditions may be applied at the excision boundary. The exact boundary location is not crucial as long as it is inside the apparent horizon, but this choice facilitates comparison with [151]. Also, in dynamical situations, the apparent horizon location may move significantly on the coordinate grid, and to ensure that ∂_t is spacelike at the inner boundary some penetration into the black hole is of advantage. To match the setup of [151], we set the outer boundary to $r = 10M$. To ensure well-posedness of the continuum problem, boundary conditions should be applied to the incoming modes u_1, u_2, u_3, u_4 , and u_8 . However, three of these modes, namely u_1, u_2 , and u_4 , can be fixed by the use of constraint-preserving boundary conditions, which leaves the freely specifiable gauge mode u_3 and the scalar field mode u_8 . Since in these initial tests we are only interested in obtaining a stationary black hole solution, the initial scalar field is set to zero, and the (scalar field) characteristic mode u_8 is penalized to zero as well. The incoming gauge mode u_3 is penalized to the exact solution.

An error function δM can be defined by use of the Misner-Sharp mass function [11]

$$M(r) := \frac{rg_T}{2} \left[1 + \frac{r^2}{g_T} \left(K_T^2 - \frac{f_{rT}^2}{g_{rr}} \right) \right], \quad (6.1)$$

where all field quantities have been introduced in Section 3.2.2. If the black hole mass is denoted by M , $\delta M(r) = (M(r) - M)/M$. Since the same error measure and continuum system is used in [151], we can compare the different discrete approaches directly.

6.2.1.1. One grid patch

The computational domain $r \in [1, 10]$ is represented by one coordinate patch, which is exactly the same setup as in ref. [151]. In Fig. 6.2 we compare, for coarse ($\Delta r = M/8$) and high resolutions ($\Delta r = M/64$), the performance of the methods used in ref. [151], namely second order spatial derivatives with fourth order Kreiss-Oliger dissipation (which is set to zero near the boundaries) and a third order extrapolation

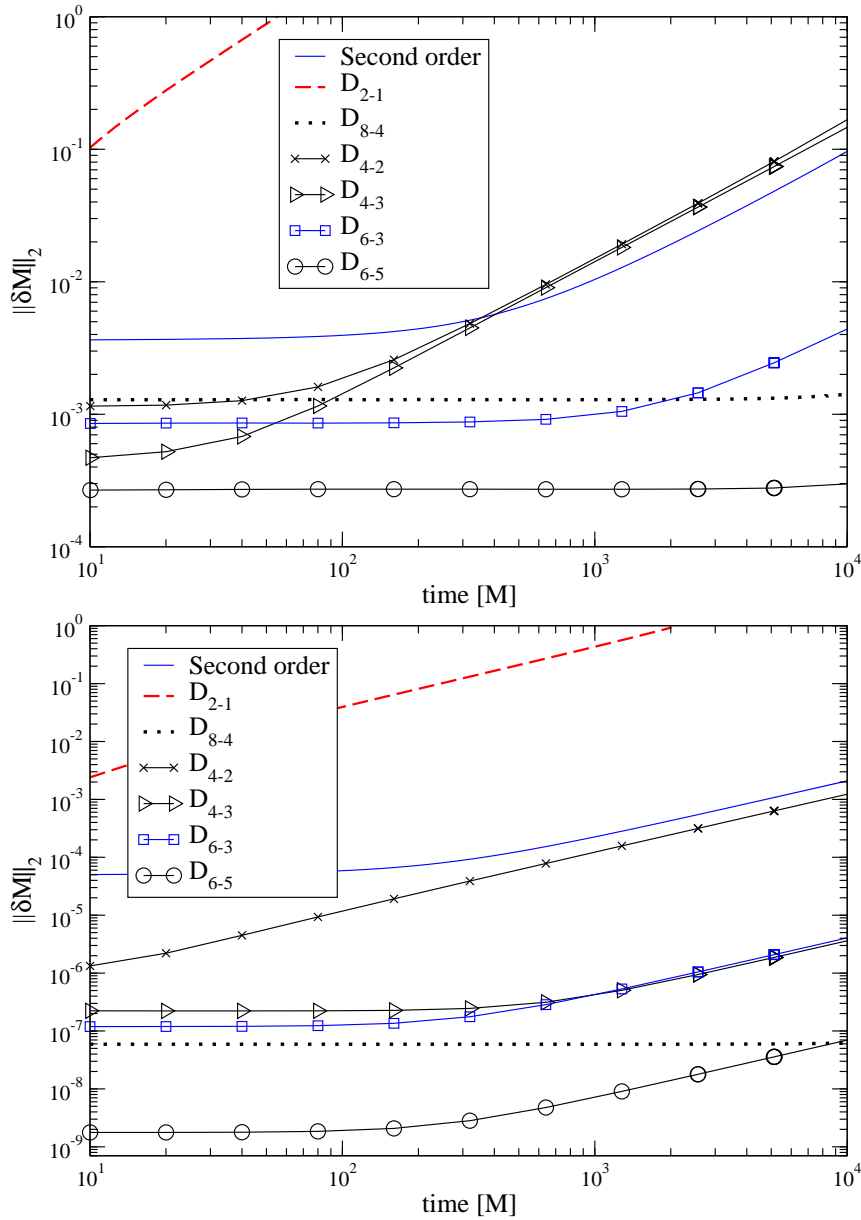


Figure 6.2.: Time evolution of the relative error in the Misner-Sharp mass function (eqn. 6.1) when evolving a Schwarzschild black hole in Painlevé-Gullstrand coordinates with one grid patch, for different discrete methods. Two resolutions are displayed, corresponding to $\Delta r = M/8$ (upper panel) and $\Delta r = M/64$ (lower panel). The result from the method presented in ref. [151] is denoted by ‘second order’, while new results are marked by the SBP derivative and dissipation operators used. The high-order operators D_{6-5} and D_{8-4} display superior performance already at the lowest resolution.

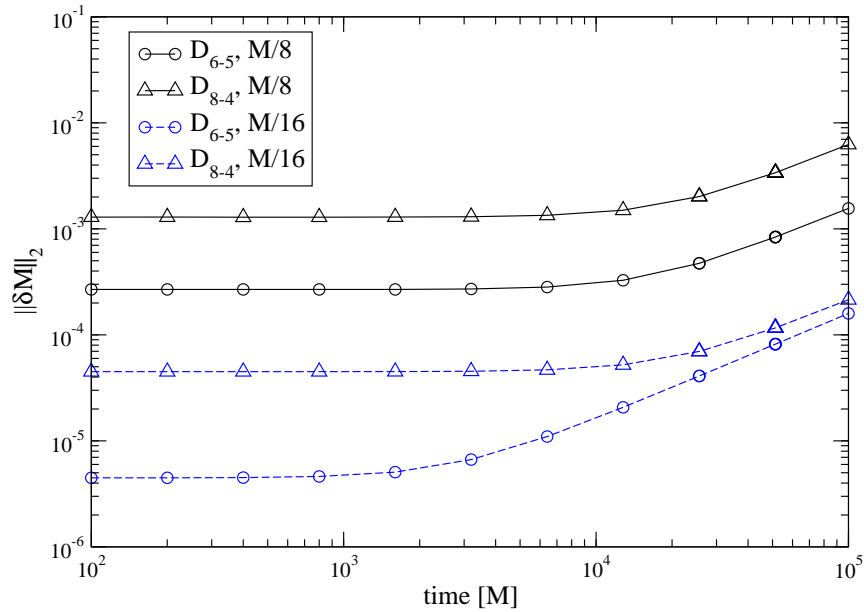


Figure 6.3.: Same as Fig. 6.2, but showing the evolution of a Schwarzschild black hole for $100,000M$. Even with low resolutions of $\Delta r = M/8$ and $M/16$, the operators D_{6-5} and D_{8-4} are able to evolve the black hole in a stable manner for a significant time.

at the boundaries, with the SBP derivative and dissipation operators D_{2-1} , D_{4-2} , D_{4-3} , D_{6-3} , D_{6-5} and D_{8-4} (see Section 3.3.4). The figure shows the evolution of the L_2 norm of the Misner-Sharp mass error over an evolution time of $10,000M$. In all cases displayed there is a linear growth in the error after some time. This is an artefact of the discrete representation of the constraint-preserving boundary conditions.

As soon as the error gets close to 1, the code encounters an instability, which, in this case, is associated with a migration of the excision boundary to the outside of the black hole, and consequently ill-posedness of the continuum problem. While this migration could be theoretically avoided by choosing horizon-fixing dynamical coordinate conditions, a solution with this magnitude of error is, in any case, not of practical use.

In the present numerical code, the SBP operators are also used as one-sided derivatives for determining the constraint-preserving boundary conditions, which suggests that the operator D_{2-1} , which is only first order at the boundaries, will yield less accurate outer boundary conditions than the third order method in [151]. Fig. 6.2 clearly demonstrates this fact. However, the operators D_{6-3} , D_{6-5} and D_{8-4} are significantly more accurate than the results presented in ref. [151], and already so at the coarsest resolution. Furthermore, at $\Delta r = M/64$ the SBP operator D_{6-5} induces a solution error of less than 10^{-7} (that is, four orders of magnitude smaller than the corresponding errors when using the second order method of [151] with the same resolution) within $10,000M$, which appears sufficiently accurate for many practical purposes.

The long-term evolution of a Schwarzschild black hole with the operators D_{6-5} and D_{8-4} is displayed in Fig. 6.3. The linear growth of errors dominates the solution at late times, but since this error significantly decreases with resolution, long evolution times can be obtained even for moderate radial grid spacings. This is naturally an interesting feature for simulations with three-dimensional spatial grids, where computational resources are still a viable concern.

6.2.1.2. Two grid patches

As discussed in the introduction, the use of multiple coordinate patches has advantages when modeling black holes. To implement a stable interface boundary condition, the penalty method is used to ensure linear stability. Here we first investigate the performance of the SBP operators coupled to an inter-patch penalty boundary method by evolving a black hole spacetime covered by two non-intersecting spherical shells, the first one from $r = 1M$ to $r = 5.5M$, and the second one from $r = 5.5M$ to $r = 10M$.

The free parameter of the penalty boundary condition δ introduced in section 3.3.5 is set to the value 0, which makes the inter-patch boundary dissipative. Only the operators D_{6-5} and D_{8-4} are used for comparison to the results from the previous section.

In Fig. 6.4 the performance of the multi-patch system is compared to the uni-patch results from the previous section. As expected, the use of one-sided derivatives at the inter-patch boundary reduces the total level of accuracy, but only by a very small amount; furthermore, the system is still stable and convergent. The time of the onset of the linear growth observed in all evolutions varies between the grid setups and choices of discrete operator. Fig. 6.5 shows the 3-metric component $g_{rr}(r)$ at the times $t = 0$ and $t = 10,000M$. The region around the inter-patch interface at $r = 5.5M$ is shown in the inset, which demonstrates that the penalty method introduces no strong visible artifacts in this part of the solution. This observation also holds for the other solution functions.

6.2.2. Gauge wave on a Schwarzschild background

The next series of tests focuses on a dynamical situation, namely the evolution of a Schwarzschild black hole in non-stationary coordinates. For this purpose, the initial data is set to a Schwarzschild black hole in Painlevé-Gullstrand coordinates as in section (6.2.1), as is the lapse and shift function at all times, but the incoming gauge mode u_3 at the outer boundary is set to a Gaussian pulse of the form

$$u_3(t) = u_3^{PG}(1 + Ae^{-(t-t_0)^2/\tilde{\sigma}^2}). \quad (6.2)$$

Here, u_3^{PG} is determined by the exact solution. As in ref. [151], we impose a strong pulse with $A = 1$, $t_0 = 5M$ and $\tilde{\sigma} = 2M$. Since the solution is not adapted to the asymptotically timelike Killing field, the SBP operators and multi-patch techniques can be tested on a solution with wave propagation without compromising the use of the error measure $\|\delta M\|_2$ (this is not the case when injecting a Klein-Gordon pulse). To facilitate comparison with ref. [151], the outer boundary is located at $r = 30M$ in these tests.

Fig. 6.6 shows results from the gauge pulse problem on a single grid patch and two grid patches, here with an inter-patch boundary at $r = 15.5M$. While in the stationary case the inter-patch boundary method only had to deal with small numerically introduced differences between the values of the geometrical quantities at the interface, the non-stationary case introduces a large pulse traveling over the boundary, and is thus a much more severe test for accuracy and stability of the penalty method. The solution error is dominated by the ability of the discrete method to represent the propagation and accretion of the gauge pulse, and by possible artefacts introduced by the inter-patch boundary.

Judging from Fig. 6.6, the high-order operators are stable and significantly more accurate than a second order method also in a dynamical situation, and even when using multiple matched domains.

6.2.3. Accretion of a scalar field pulse

Since the outer boundary has two free incoming modes, it is possible to inject a scalar field pulse in a way similar to the gauge pulse of section (6.2.2). In contrast to the gauge pulse, however, this system will result in an increase of mass of the black hole, which also implies that the Misner-Sharp mass cannot be used as a measure of the errors anymore. A possible choice for a scalar field source with compact

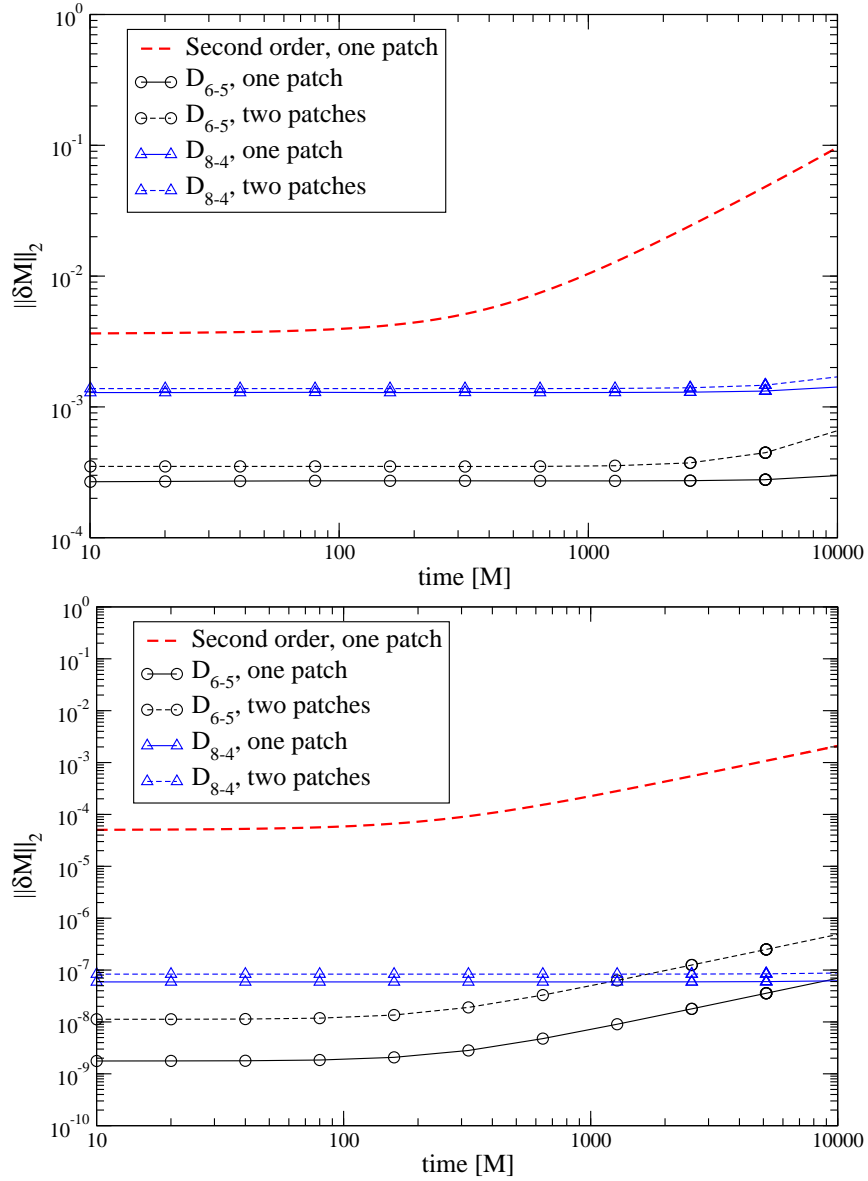


Figure 6.4.: Comparison of uni-patch and multi-patch evolutions of a Schwarzschild black hole in Painlevé-Gullstrand coordinates. The graphs denoted by “one patch” and “second order” are those from Fig. 6.2, while the corresponding graphs for “two patches” cover the computational domain with two non-intersecting spherical shells, the first one extending from $r = 1M$ to $r = 5.5M$, and the second one extending from $r = 5.5M$ to $r = 10M$. The one-sided derivatives at the interface boundary introduce a very small loss of accuracy. In the upper and lower panel the resolution is $\Delta r = M/8$ and $M/64$, respectively. For the late time behaviour of D_{6-5} and D_{8-4} see also Fig. 6.3.

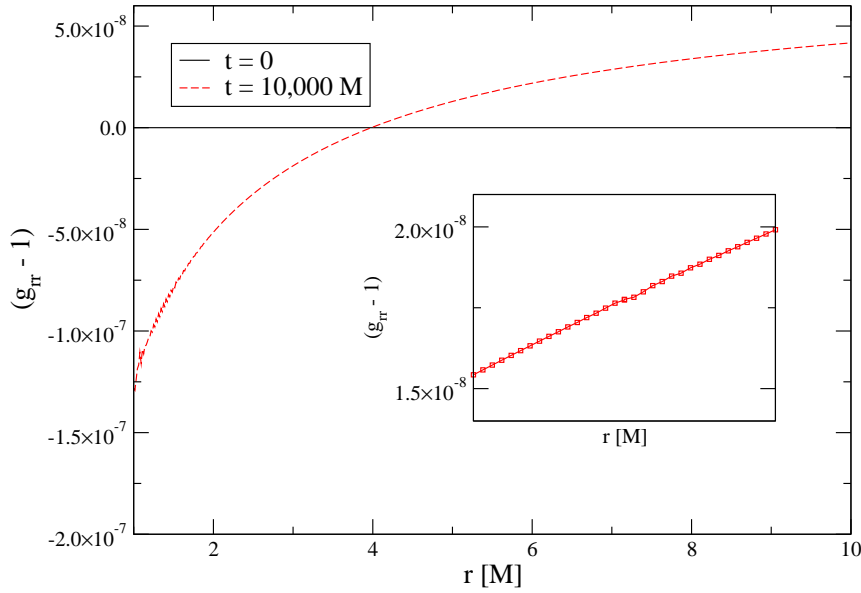


Figure 6.5.: Evolution of the metric function g_{rr} for a black hole in Painlevé-Gullstrand coordinates, obtained with a resolution of $\Delta r = M/64$, two grid patches with an interface at $r = 5.5M$, and using the SBP operator D_{6-5} . The two graphs show the metric function at $t = 0$ (where $g_{rr}(r) = 1$) and at $t = 10,000M$. The inset shows the region around the interface between the grid patches.

support is

$$u_8(t) = \begin{cases} 0 & t < t_I \\ \frac{A}{t_F^8} (t - t_I)^4 (t - t_F)^4 \sin\left(\frac{\pi t}{t_F}\right) & t \in [t_I, t_F] \\ 0 & t > t_F \end{cases}$$

Here, u_8 is the incoming scalar field mode.

To facilitate comparisons with ref. [151] we use an amplitude $A = 7.2$, and $t_I = 0M$, $t_F = 10M$, and set the computational domain to be $r \in [1, 50]M$.

For resolutions $\Delta r = M/20$ and $\Delta r = M/40$, the time evolution of the apparent horizon is shown in Fig. 6.7. The scalar pulse leads to a significant increase of the black hole mass by a factor of ≈ 2.7 after the pulse is inside the black hole. Larger amplitudes are not obtainable with the simple gauge prescription used here, but a gauge condition which fixes the coordinate location of the horizon could improve on this result. As a replacement for the Misner-Sharp error measure, we plot the L_2 norm of the Hamiltonian constraint versus time in Fig. 6.8. It is apparent that the high-order operators are again stable and more accurate than the second order operator. The graphs indicate a growth of the constraint near $t = 200M$, but a long-term evolution with $\Delta r = M/20$ (Fig. 6.9) demonstrates that the system settles down after the accretion phase.

6.2.4. Robust stability test with gauge noise

The term *robust stability test* [153, 154] typically refers to the discrete stability of a numerical system in response to random perturbations. In this case, we will use the same system as in section (6.2.1.2), but impose random noise on the incoming gauge mode u_3 with a certain amplitude. To test the discrete stability of the evolution system, we chose a large range of amplitudes from 10^{-4} to 0.3. Random perturbations

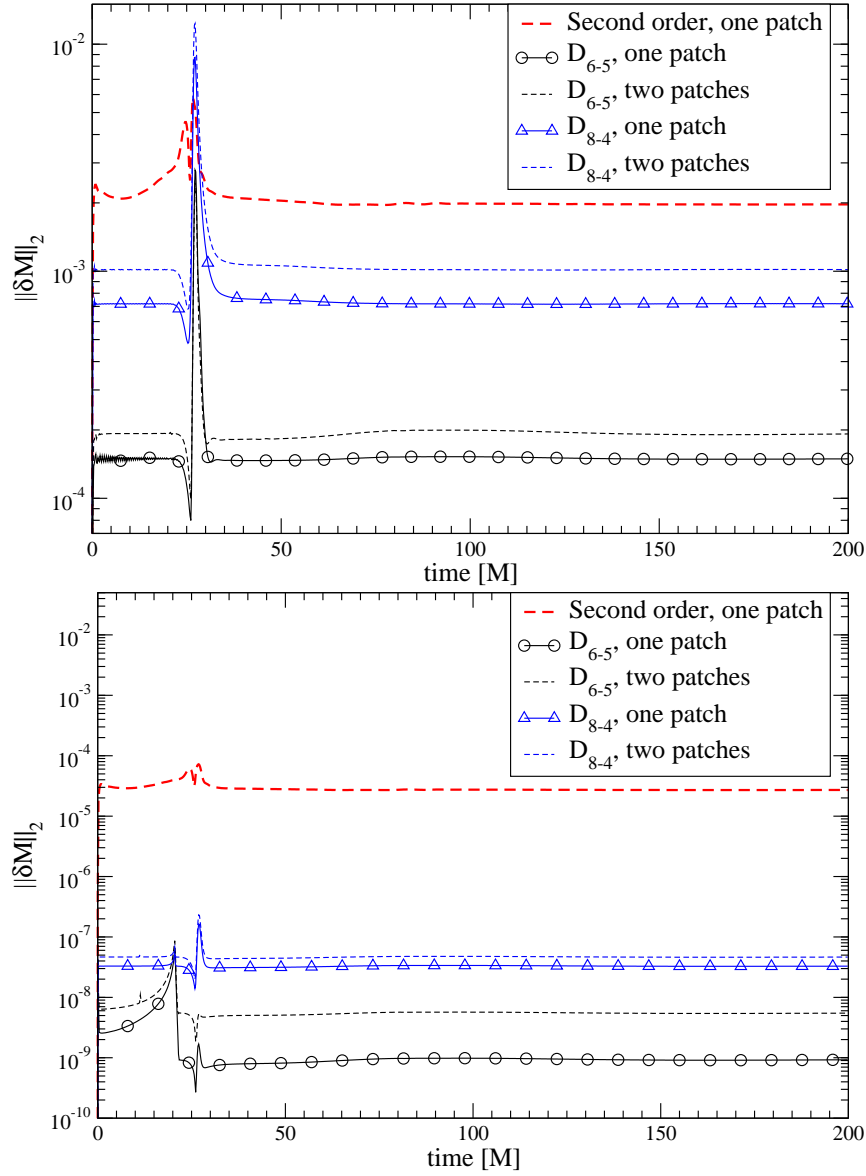


Figure 6.6.: Comparison of uni-patch and multi-patch evolutions of a gauge wave traveling on a Schwarzschild background. The graphs denoted by “second order” are obtained with the methods in ref. [151], while the corresponding graphs for “one patch” and “two patches” cover the computational domain with either one or two non-intersecting spherical shells, the first one extending from $r = 1M$ to $r = 15.5M$, and the second one extending from $r = 15.5M$ to $r = 30M$. The one-sided derivatives at the interface boundary introduce a small loss of accuracy, but the system is still stable. The upper and lower panels correspond to $\Delta r = M/8$ and $M/64$, respectively. The feature around $t = 25M$ is related to the most dynamical phase of the accretion process.

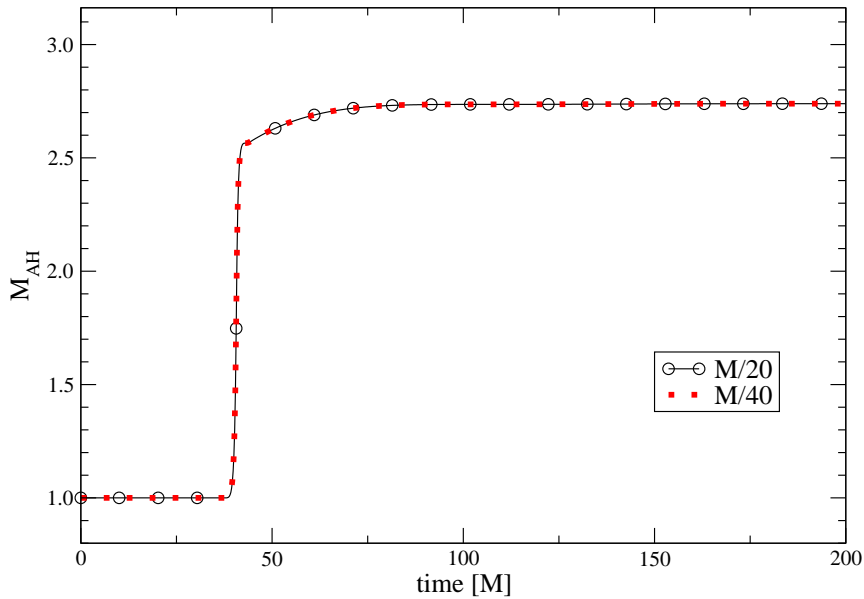


Figure 6.7.: Evolution of the apparent horizon mass for the accretion of a strong scalar pulse to a Schwarzschild black hole. Shown are plots for two resolutions, $\Delta r = M/20$ and $\Delta r = M/40$, using the SBP operator D_{6-5} . The large scalar field amplitude leads to a significant increase in the black hole mass.

of the latter amplitude are significant for a non-linear system².

For this multi-patch test, results in the mass error for a resolution of $\Delta r = M/8$ are shown in Fig. 6.10. It is apparent that strong random noise induces a stronger growth in the solution error. However, this growth is still linear. As in all black hole evolutions in section (6.2.1), the system encounters a numerical instability when the solution error approaches unity. This, however, is not a consequence of the random noise, but of the inner boundary becoming partially inflow due to a coordinate motion of the apparent horizon. Also, with increasing resolution, the growth rate of the error does not increase (Fig. 6.11)³. We conclude that this high-order evolution system is discretely stable against strong random perturbations.

6.2.5. Cauchy–perturbative matching: robust stability test with scalar field noise

We now test the stability of the system with Cauchy–perturbative matching against random perturbations in the scalar field. To this end, the computational domain is again subdivided as in section (6.2.4), but the outer patch evolves the scalar field on a fixed Painlevé–Gullstrand background. The inter-patch boundary is thus matching the Cauchy patch to a perturbative one, and we test the stability of the system against random perturbations by imposing random noise on the incoming scalar field mode on the outer boundary of the perturbative patch.

Since the mass error is not available for a system accreting a scalar field, the L_2 norm of the Hamiltonian constraint is used again in Fig. 6.12. No exponential growth can be observed in the Hamiltonian constraint violation. The same is true when increasing the resolutions (Fig. 6.13), which also deserves

²Beyond this amplitude the inner boundary tends to become timelike, which requires additional boundary data. More sophisticated gauge or inner boundary condition could alleviate this, but since we are interested here in a proof of principle, a simple system is preferred.

³Note that a discrete system with random noise is not convergent, since the amount of energy on the grid diverges with increasing resolution.

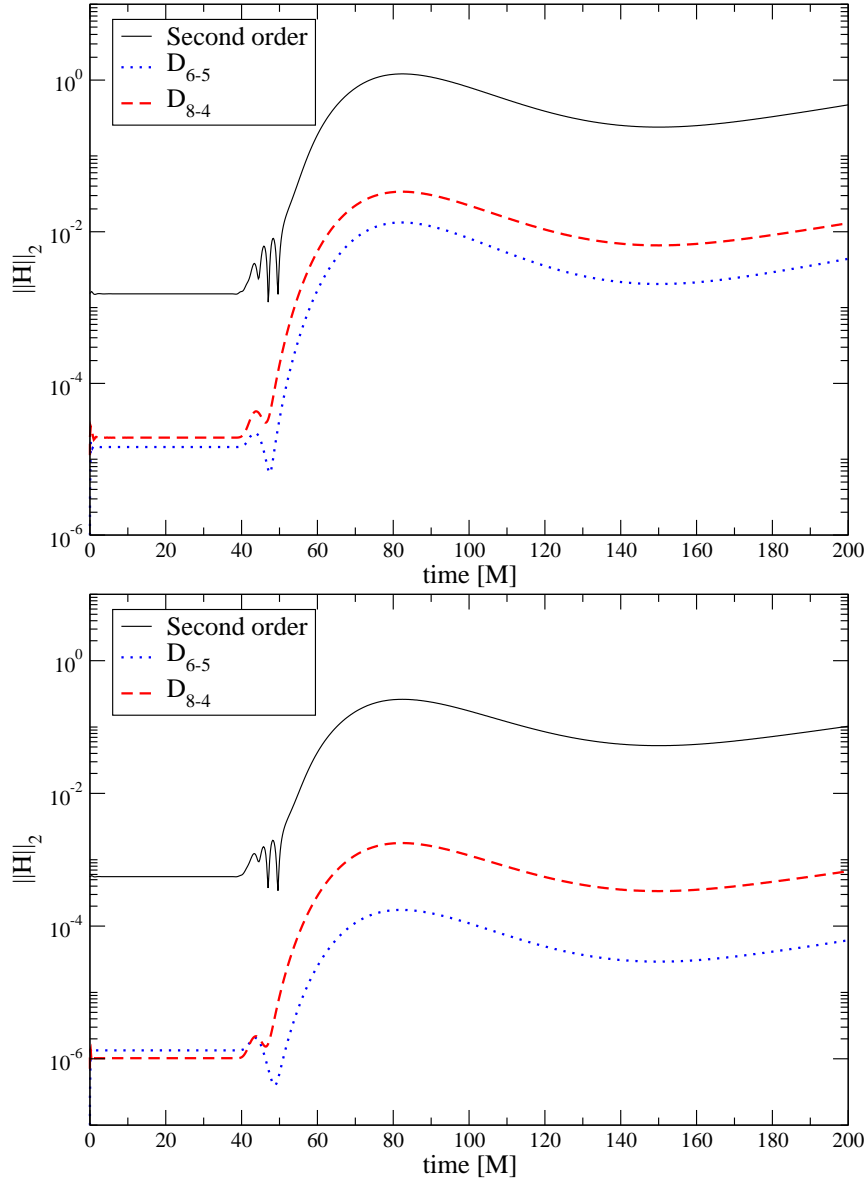


Figure 6.8.: L_2 norm of the Hamiltonian constraint versus time for the accretion of a strong scalar field pulse to a Schwarzschild black hole, with resolutions $\Delta r = M/20, M/40$ (upper and lower panels, respectively). The graph denoted by “second order” is obtained with the method presented in [151], and the D_{6-5} and D_{8-4} are obtained using the corresponding SBP operators. The feature around $t = 50M$ is again related to the most dynamical phase of accretion.

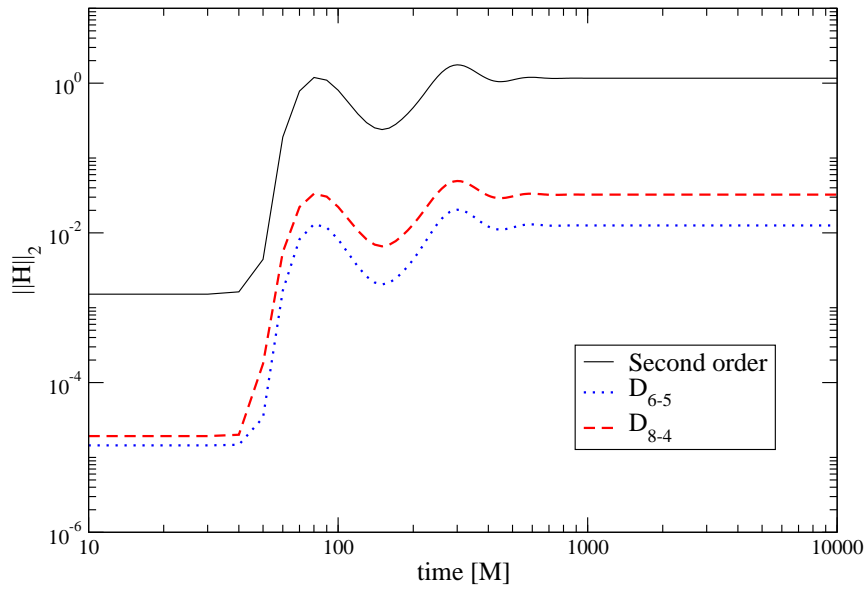


Figure 6.9.: Same as Fig. 6.8, covering the evolution up to 10,000 M with $\Delta r = M/20$ to demonstrate the long-term behaviour after accretion of the pulse.

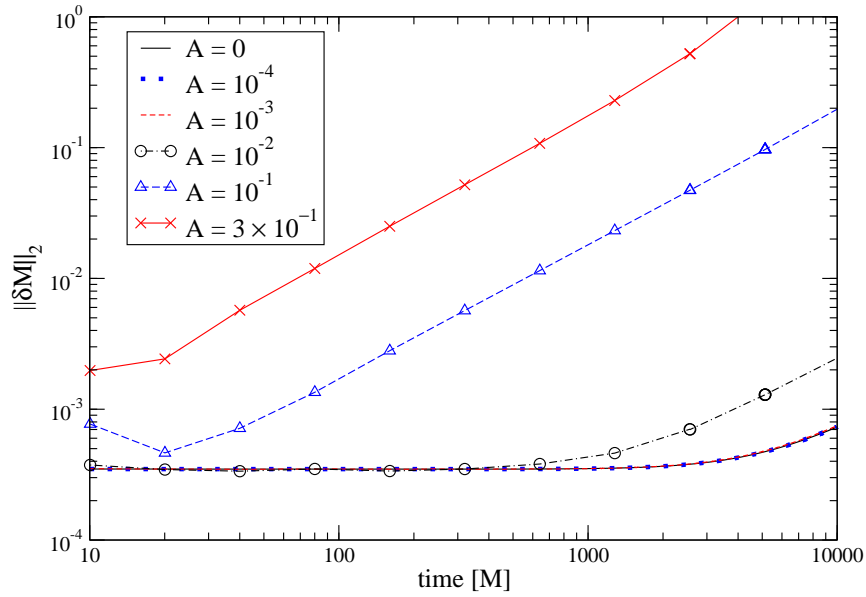


Figure 6.10.: Results of a robust stability test for different random noise amplitudes. The system is a Schwarzschild black hole in Painlevé-Gullstrand coordinates, and the computational domain $r \in [1, 10] M$ is covered by two patches joined at $r = 5.5M$, and a resolution of $M/8$. Random noise is superimposed on the ingoing gauge mode u_3 , with an amplitude denoted by A . The graphs show the mass error with time for different random noise amplitudes, obtained with the SBP operator D_{6-5} .

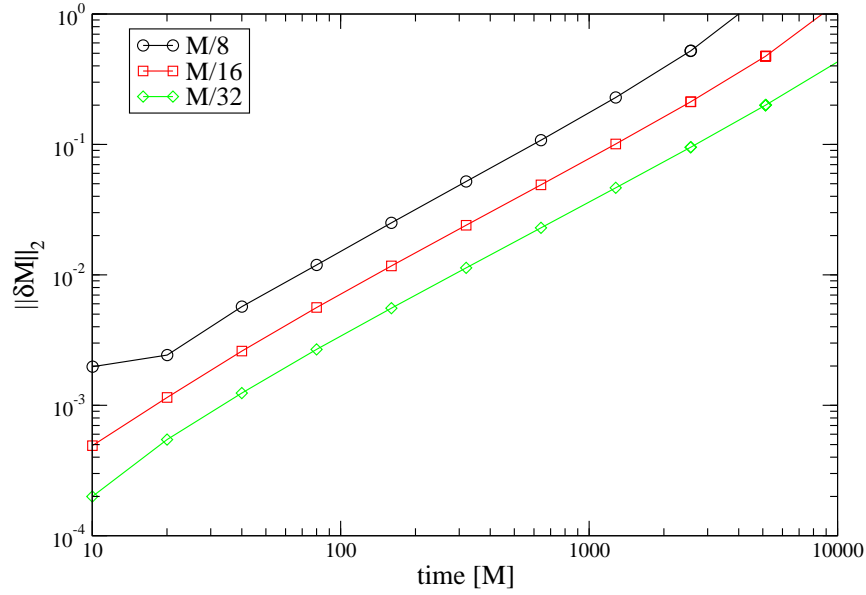


Figure 6.11.: Same as Fig. 6.10, but for the highest random noise amplitude (0.3) and different resolutions.

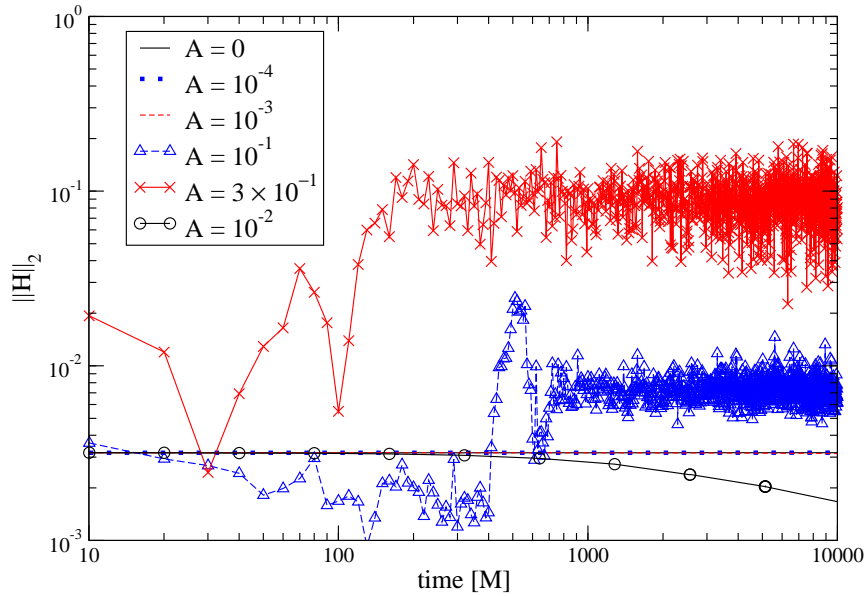


Figure 6.12.: Robust stability test with Cauchy–perturbative matching. The system is a dynamically evolved Schwarzschild black hole in Painlevé–Gullstrand coordinates matched to a perturbative patch at $r = 5.5M$. Random noise is imposed via the incoming scalar field mode at the outer boundary. Plotted is the L_2 norm of the Hamiltonian constraint versus time for different noise amplitudes. All evolutions are done with a resolution of $\Delta r = M/8$, and the SBP operator D_{6-5} .

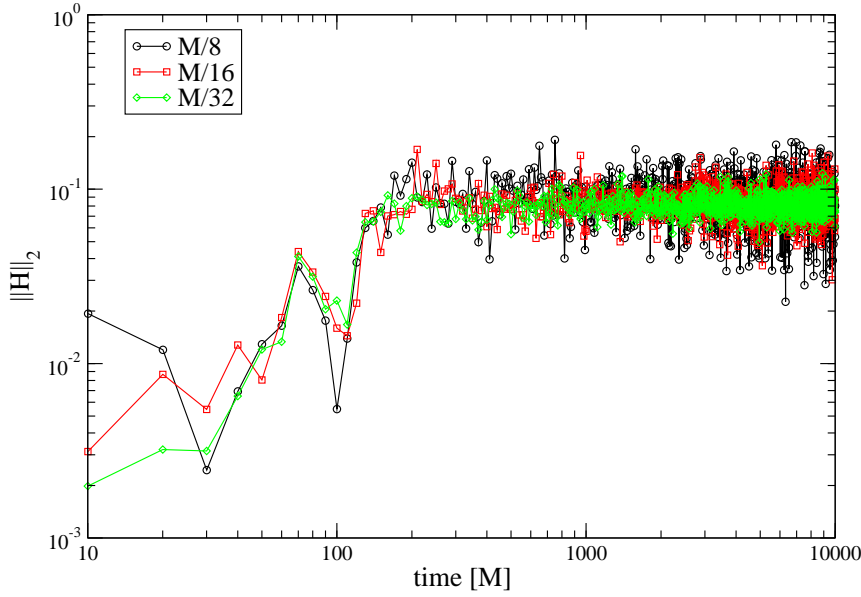


Figure 6.13.: Same as Fig. 6.12, but for the highest random noise amplitude and different resolutions.

some additional comments: The robust stability test does not lead to a converging sequence of solutions, if the random noise amplitude is not diminished with resolution. However, the purpose of these tests is to excite any unstable high frequency modes present in the numerical system. The absence of any mode growing with increasing resolution shows that the system with a Cauchy–perturbative matching interface is stable even against strong random noise injected into the system. This is a promising result for any effort to do three-dimensional matching between Cauchy modules and perturbative ones using multiple patches and high-order summation-by-parts operators.

6.2.6. Cauchy–perturbative matching: Accretion of a “gravitational wave” and long-term evolution

Finally, using the massless Klein-Gordon field as a scalar analogue of gravitational waves in spherical symmetry, we model the accretion of a gravitational wave packet across a Cauchy–perturbative matching boundary. This test is an extension of the single-patch scalar field accretion of section (6.2.3), and makes use of all ingredients presented above for a stable and accurate evolution of black holes with Cauchy–perturbative matching.

Since Cauchy–perturbative matching assumes the gravitational wave to be a small perturbation of a fixed background in the wave zone, the amplitude of the wave packet that we inject through the outermost boundary is chosen to be $A = 0.01$. Similarly to section 6.2.3, we describe the wave packet by the function

$$u_8(t) = \begin{cases} 0 & t < t_I \\ \frac{A}{t_F^8} (t - t_I)^4 (t - t_F)^4 \sin\left(\frac{\pi t}{nt_F}\right) & t \in [t_I, t_F] \\ 0 & t > t_F \end{cases}$$

where the number of half waves in the pulse is set to $n = 100$. We inject the packet from $t_I = 0$ to $t_F = 100M$. Fig. 6.14 displays the evolution of the grid function Φ , and specifically the behaviour of the function around the Cauchy–perturbative matching interface, which is located at $r = 25.5M$. The

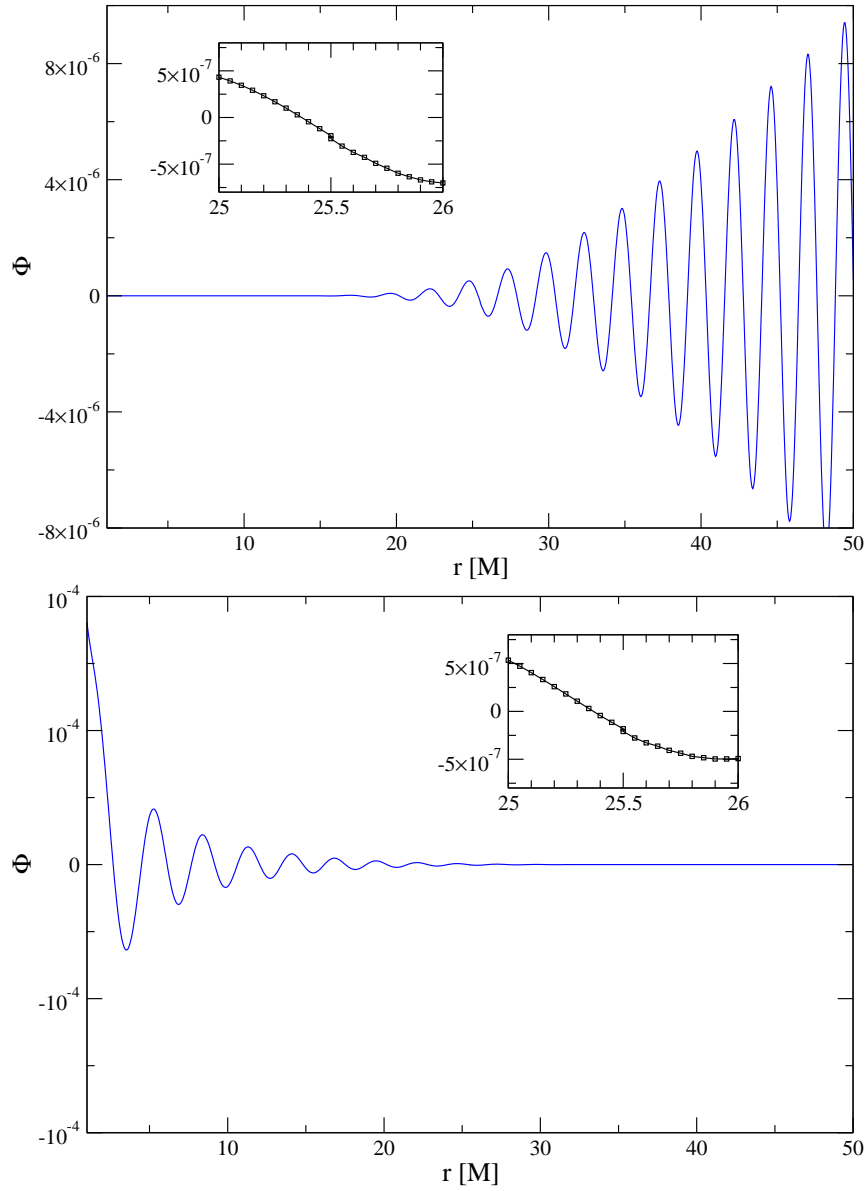


Figure 6.14.: Accretion of a scalar wave packet across a Cauchy–perturbative matching interface, as a scalar analog for gravitational wave accretion in three-dimensional simulations. The packet consists of 50 waves injected from $t = 0$ to $t = 100M$, as described in the text. Here, the grid function Φ is plotted over the radial coordinate at $t = 30M$ (top) and $110M$ (bottom), for the resolution $\Delta r = M/20$ and the SBP operator D_{6-5} . The inset shows the behaviour of the grid function around the matching interface, which is at $r = 25.5M$. Note that even though the grid function is in principle two-valued on the interface, the penalties in conjunction with high-order operators only lead to a very small mismatch.

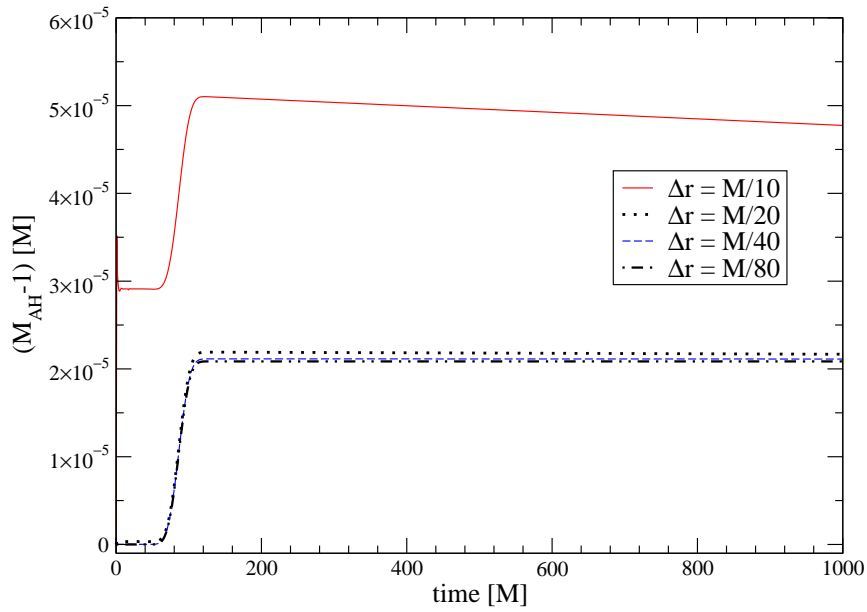


Figure 6.15.: Accretion of a scalar wave packet across a Cauchy–perturbative matching interface. This plot shows the apparent horizon mass versus time for evolutions with different resolutions and the SBP operator D_{6-5} .

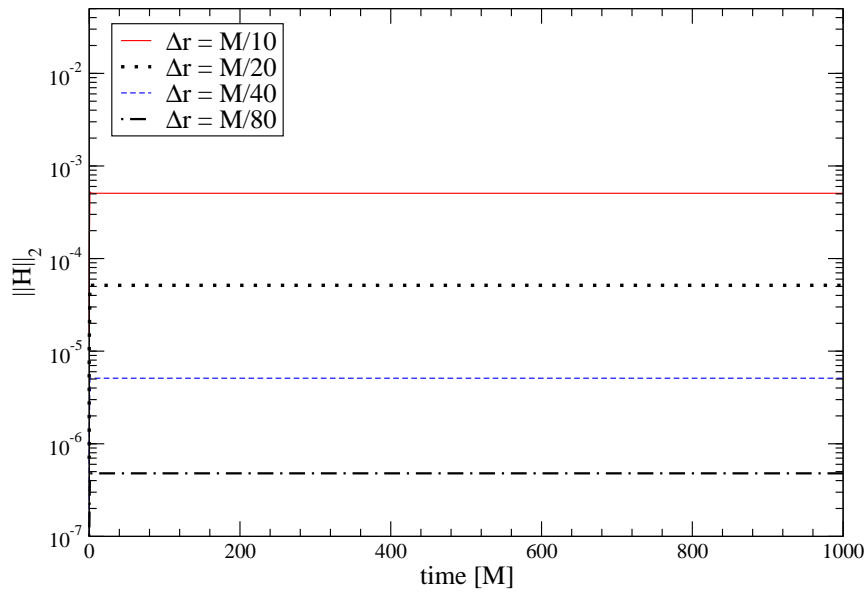


Figure 6.16.: Accretion of a scalar wave packet across a Cauchy–perturbative matching interface. This plot shows the L_2 norm of the Hamiltonian constraint for different resolutions, using the SBP operator D_{6-5} . Please note, for comparison with Fig. 6.9, that the amplitude of the Klein-Gordon signal is smaller compared to section (6.2.3).

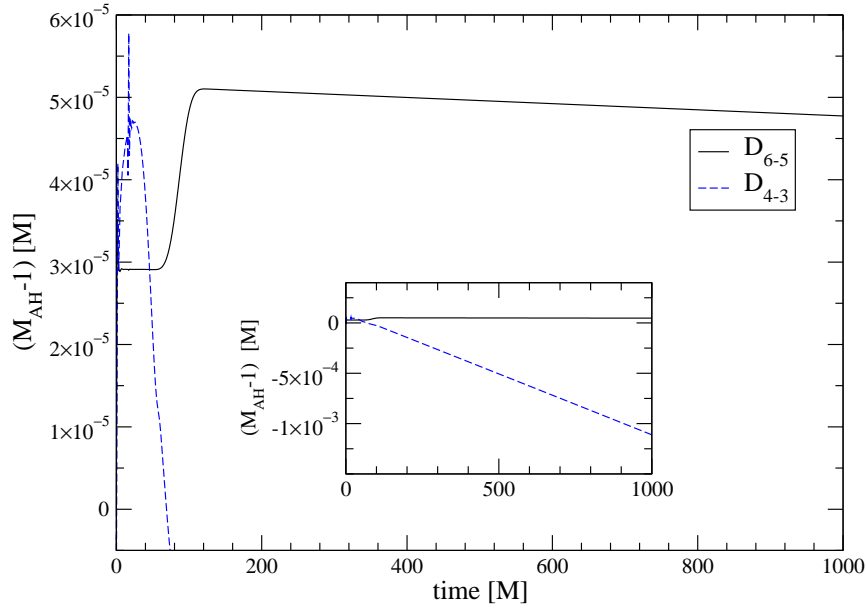


Figure 6.17.: Accretion of a scalar wave packet across a Cauchy-perturbative matching interface. To demonstrate the advantage of using high-order methods, $(M_{AH} - 1)$ is shown for evolutions obtained with the SBP operators D_{4-3} and D_{6-5} , at a resolution of $\Delta r = M/10$. The loss of mass after accretion of the wave packet with compact support in $t \in [0, 100]M$ is a numerical artefact, which converges away with resolution. The inset shows that the evolution obtained with the operator D_{4-3} is not unstable, but only considerably less accurate.

corresponding increase in apparent horizon mass is shown in Fig. 6.15. The evolution of the Hamiltonian constraint violation using the SBP operator D_{6-5} and different resolutions is shown in Fig. 6.16. It is apparent that the discrete system is not only stable and accurate, but also the amount of non-linear constraint violations introduced at the continuum by the Cauchy-perturbative matching are very small, in Fig. 6.16 they must actually be smaller than 10^{-6} .

The advantage of using high-order methods is made evident in Fig. 6.17 to 6.20. In these plots, the performance of the SBP operator D_{6-5} , which is sixth order in the interior and fifth order at the boundaries, is compared to that of the operator D_{4-3} , which is fourth order in the interior and third order at the boundaries, for different choices of resolution. Although both operators show convergence, for a mass increase of about 10^{-5} , the operator D_{4-3} is unable to reproduce the correct behaviour with reasonable grid resolutions. We consider this specifically important for three-dimensional simulations, where the necessary resources scale with n^4 , if n denotes the number of grid points in each direction. Thus, for all simulations requiring a certain amount of precision, high-order operators are an essential requirement.

The long-term evolution of a Schwarzschild black hole accreting a wave packet over a Cauchy-perturbative matching interface and settling down to equilibrium is shown in Fig. 6.21. The black hole is evolved for 1,000,000 M with the lowest resolution $\Delta r = M/10$ and the SBP operator D_{6-5} . While an evolution of this length might appear to be of only technical interest, we note that modeling phenomena like hypernovae and collapsars in general relativity will require the stable evolution of a black hole for at least several seconds, which is the lower end of time scales associated with the collapsar model of gamma-ray burst engines [155]. For a stellar mass black hole, $M = M_{\odot} \approx 5\mu s$, that is $1s \approx 200,000M_{\odot}$.

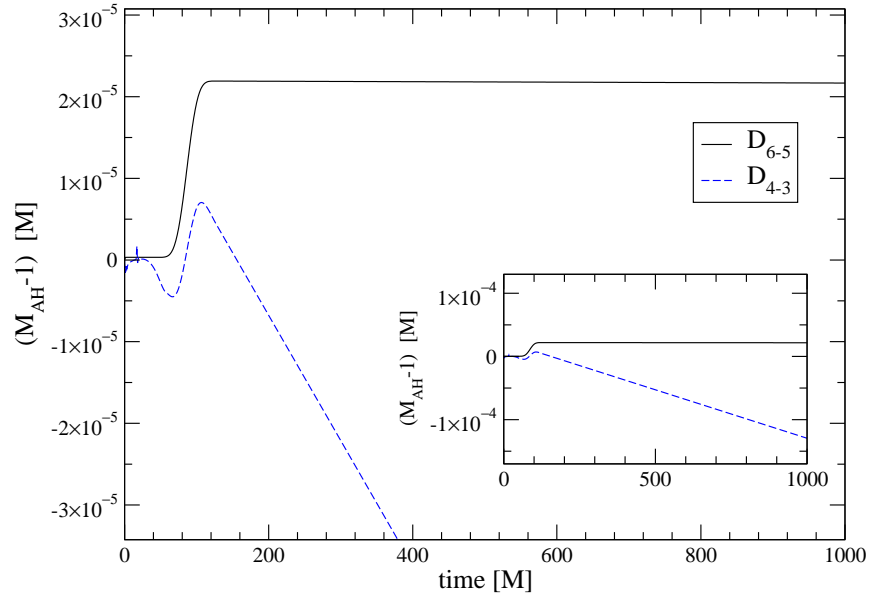


Figure 6.18.: Same as Fig. 6.17, but for a resolution of $\Delta r = M/20$.

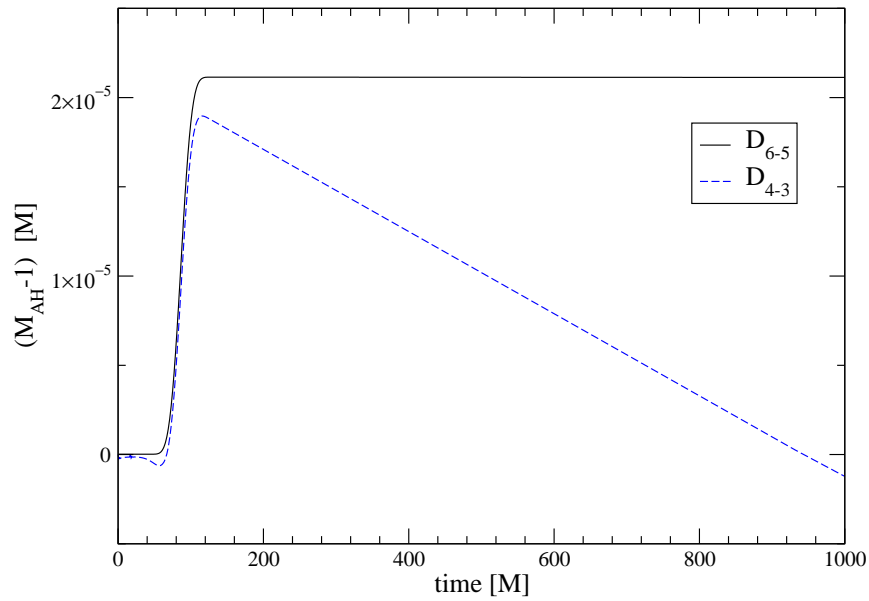


Figure 6.19.: Same as Fig. 6.17, but for a resolution of $\Delta r = M/40$.

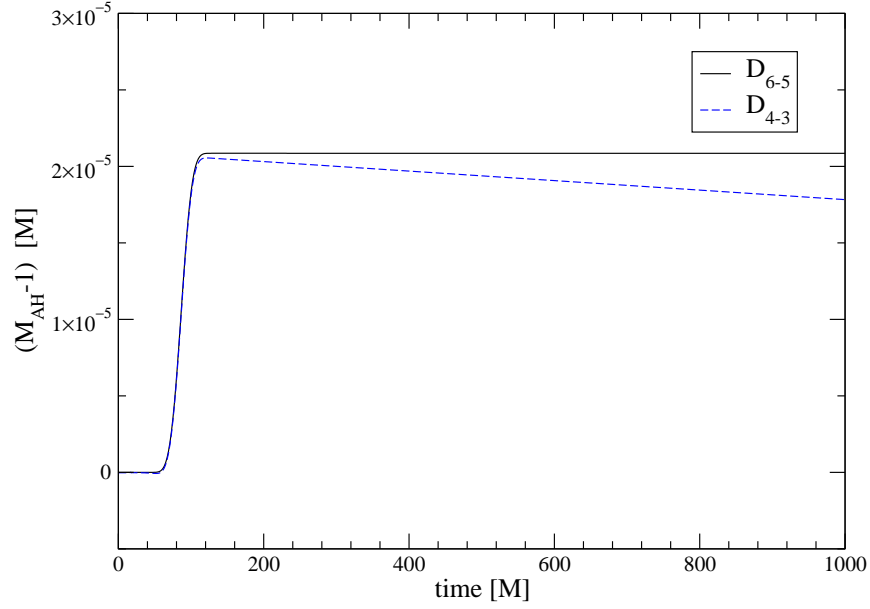


Figure 6.20.: Same as Fig. 6.17, but for a resolution of $\Delta r = M/80$.

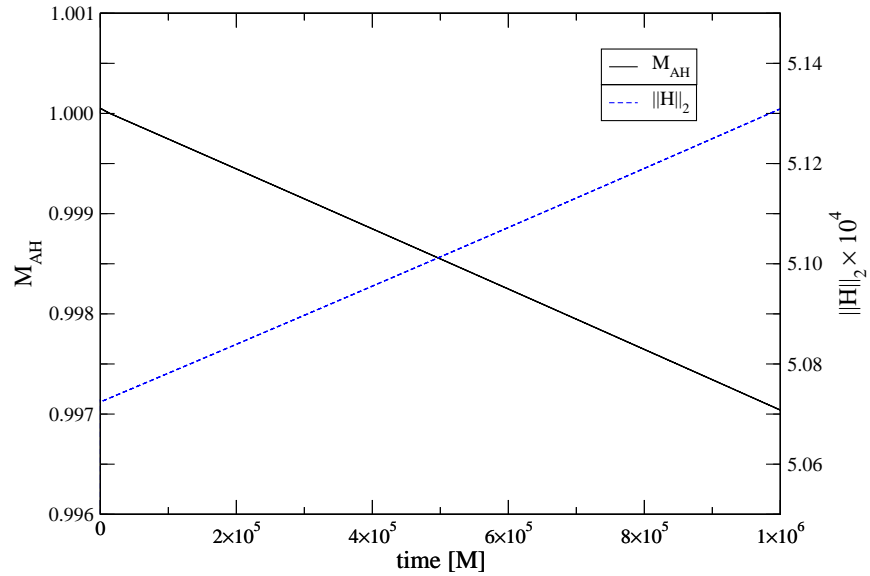


Figure 6.21.: Long-term stable evolution of a Schwarzschild black hole after accretion of a scalar wave packet with Cauchy–perturbative matching. The SBP operator D_{6-5} is used with a grid resolution of $\Delta r = M/10$. Plotted are the apparent horizon mass and the Hamiltonian constraint versus time. The apparent horizon mass indicates that the discrete evolution introduces a relative error of about 0.3% after 1,000,000 M .

6.3. Summary

To obtain long-term evolutions of compact astrophysical systems in three spatial dimensions, advanced numerical techniques are preferable in that they may improve stability and accuracy of the associated discrete model system. While high accuracy enables efficient use of the available computational resources, well-posedness of the continuum model and numerical stability are requirements which can not be met by increasing computational power. A number of techniques has been suggested to address these issues [156]: Multiple coordinate patches, typically adapted to approximate symmetries of certain solution domains, combined with high-order operators are expected to increase the accuracy of any model of a stellar system. Cauchy–perturbative matching provides an efficient way to accurately model the propagation of gravitational waves to a distant observer, and to yield physical boundary conditions on incoming modes of the Cauchy evolution. Constraint-preserving boundary conditions isolate the incoming modes on the constraint hypersurface, and, finally, for evolving black holes, an excision boundary is desirable to concentrate on the behaviour of the external spacetime. Only recently the consideration of the well-posedness of the differential system and the application of theorems on discrete stability of the numerical system have provided hints as how to address the outstanding issues. In this paper, we have applied all these techniques to a model system: a spherically symmetric black hole coupled to a massless Klein-Gordon field.

We find that the use of a first-order hyperbolic formulation of Einstein’s field equations, combined with high-order derivative and dissipation operators with the summation-by-parts property, penalized inter-patch boundary conditions and constraint-preserving outer boundary conditions leads to a stable and accurate discrete model. Specifically, isolated Schwarzschild black holes in coordinates adapted to the Killing fields, and in coordinates on which a gauge wave is imposed, and Schwarzschild black holes accreting scalar wave pulses were taken as typical model systems involving excision. The results show that the introduction of several coordinate patches and of a Cauchy–perturbative matching interface does not introduce significant artefacts or instabilities. Rather, the high-order methods allow the accurate long-term evolution of accreting black holes with excision and Cauchy–perturbative matching in reasonable resolutions. As an example, we have presented the evolution of such a system with the high-order SBP operator D_{6-5} , which, at a resolution of $\Delta x = M/10$, introduced an error of only 0.3% after an evolution time of 1,000,000 M .

Most systems of interest in general relativistic astrophysics will necessarily require the use of three-dimensional codes. Results from a one-dimensional study are useful in that (i) experience can be gained in a clean but non-trivial physical system, (ii) they can be easily reproduced without the need for implementation of three-dimensional codes with multiple coordinate patches and (iii) isolation of sources of difficulty in the three-dimensional setting can be obtained more easily. With the promising results from this study, we will, as a next step, apply these techniques to a three-dimensional general relativistic setting.

7. Summary

This thesis is concerned with two related subjects: the formation of black holes from quasi-toroidal, general relativistic polytropes ($P = K\rho^\Gamma$), and the performance of recently developed techniques in numerical relativity for long-term stable evolution of black holes.

The main conclusions are at the end of Chapters 5 and 6; therefore, only a short summary will be attempted here. The technical abilities of general-relativistic hydrodynamics codes like the combination Cactus/Whisky/Carpet is nowadays advanced enough to construct relativistic polytropes with strong differential rotation, and follow the subsequent development of a non-axisymmetric instability up to fragmentation and black hole formation. The dynamics of these systems as such is already an interesting area of research, since the stability properties of general relativistic stellar models are quite difficult to analyze perturbatively (or with numerical simulations), and therefore only very recently the necessary tools have become available.

It was found that many of the quasi-toroidal stars investigated here are unstable to non-axisymmetric perturbations, and that the development of the instability leads to a fragmentation process where one or several fragments are collapsing. In one model, the tentative evidence for black hole formation, namely the “collapse of the lapse”, has been shown explicitly to be connected with the formation of an apparent horizon centered on the fragment.

A parameter-space study has demonstrated that, if the degree of differential rotation is not too high, the parameter $T/|W|$ (relating the rotational kinetic to the gravitational binding energy) commonly used to compare the location of polytropes on some sequence with the Maclaurin sequence, still approximately admits to identify the degree of instability, i.e. the order of the highest unstable modes, at least to some extent. As in similar Newtonian studies, however, some significant differences could be observed: (i) The development of the $m = 2$ *bar-mode* instability well-known from Maclaurin spheroids occurs at much lower values of $T/|W|$, (ii) the systems admit the development of *spiral-arm* $m = 1$ instabilities, possibly connected with the existence of a continuous spectrum (the *corotation band*) of modes corotating with the star at some radius.

The formation of black holes can occur either by destabilizing modes in a fragment, or by unstable modes of an orbiting system of fragments; both scenarios have been observed, although it should be noted again that only the properties of the lapse function were used to identify forming singularities in these cases, and assuming that the weak cosmic censorship conjecture holds. The equatorial compactness of the polytrope can give partial evidence for the subsequent evolution, in the sense that, on a sequence of decreasing compactness, no black hole will form beyond some limit surface in parameter space. This behaviour is well known from the perturbative theory of slowly and uniformly rotating polytropes.

While the dynamical properties of non-axisymmetric instabilities in general-relativistic polytropes are an active field of research, there is another question which deserves attention: the gravitational wave signals emitted by these processes. And, unfortunately, concerning this issue the tools applied by the author fall short due to numerical instabilities related to black hole evolutions. This is especially important when evolving soft polytropes, since their extended core-halo structure requires to extract gravitational waves from the grid at large coordinate radii, resulting in the prediction of only the early, low-frequency components of the signal.

Since the stable evolution of black holes with matter is the central technical problem not only in these simulations, but also in simulations of binary black hole mergers, there have been many efforts to gain a

better understanding how to discretize these systems. One of these efforts involves multiple coordinate patches, a well-posed and constraint-preserving form of the continuum problem, and discrete operators satisfying certain notions of discrete stability. While the performance of these new operators has been tested already extensively with the classical scalar wave equation, with waves on a fixed Kerr spacetime background, and with linear gauge waves, no experience had been obtained how they would perform in the evolution of dynamical black holes, which has been well-known to pose serious problems to finite-differencing approaches, specifically when (typically less stable) high-order polynomials approximants are considered.

The results obtained in this thesis are very promising: With the spherically symmetric Einstein-Christoffel system coupled to a massless Klein-Gordon field, a black hole accreting a scalar wave packet, and the subsequent ring-down, can be followed stably and accurately for a coordinate time of 1,000,000 times the mass of the black hole. If the same kind of success can be repeated in the three-dimensional case, a neutron star collapse, or the more demanding fragmentation collapse, could be followed with significantly improved stability *and* accuracy.

Bibliography

- [1] URL <http://www.cactuscode.org>.
- [2] S. Chandrasekhar, *Ellipsoidal Figures of Equilibrium* (Yale University Press, New Haven, USA, 1969), revised edition 1987.
- [3] S. W. Hawking and G. F. R. Ellis, *The large scale structure of spacetime* (Cambridge University Press, Cambridge, England, 1973), ISBN 0-521-09906-4.
- [4] M. Alcubierre and B. Brügmann, Phys. Rev. D **63**, 104006 (2001), [gr-qc/0008067](#).
- [5] S. Frittelli and R. Gómez, J. Math. Phys. **41**, 5535 (2000), [gr-qc/0006082](#).
- [6] L. E. Kidder, M. A. Scheel, S. A. Teukolsky, E. D. Carlson, and G. B. Cook, Phys. Rev. D **62**, 084032 (2000), [gr-qc/0005056](#).
- [7] G. Calabrese, L. Lehner, O. Reula, O. Sarbach, and M. Tiglio, Class. Quantum Grav. **21**, 5735 (2004), [gr-qc/0308007](#).
- [8] K. Thorne, Rev. Mod. Phys. **52**, 299 (1980).
- [9] G. Calabrese, J. Pullin, O. Reula, O. Sarbach, and M. Tiglio, Communications in Mathematical Physics **240**, 377 (2003), [gr-qc/0209017](#).
- [10] L. Lehner, O. Reula, and M. Tiglio, Class. Quantum Grav. **22** (2005), [gr-qc/0507004](#).
- [11] C. W. Misner, K. S. Thorne, and J. A. Wheeler, *Gravitation* (W. H. Freeman, San Francisco, 1973).
- [12] R. M. Wald, *General relativity* (The University of Chicago Press, Chicago, 1984), ISBN 0-226-87032-4 (hardcover), 0-226-87033-2 (paperback).
- [13] R. Arnowitt, S. Deser, and C. W. Misner, in *Gravitation: An introduction to current research*, edited by L. Witten (John Wiley, New York, 1962), pp. 227–265, [gr-qc/0405109](#).
- [14] S. L. Shapiro (2005), [gr-qc/0509094](#).
- [15] T. W. Baumgarte and S. L. Shapiro, Phys. Rev. D **59**, 024007 (1999), [gr-qc/9810065](#).
- [16] T. Nakamura, K. Oohara, and Y. Kojima, Prog. Theor. Phys. Suppl. **90**, 1 (1987).
- [17] M. Shibata and T. Nakamura, Phys. Rev. D **52**, 5428 (1995).
- [18] A. Anderson and J. W. York, Phy. Rev. Lett. **82**, 4384 (1999), [gr-qc/9901021](#).
- [19] W. G. Unruh (1984).
- [20] J. Thornburg, Class. Quantum Grav. **4**, 1119 (1987), URL <http://stacks.iop.org/0264-9381/4/1119>.

- [21] C. Bona and J. Massó, Phys. Rev. Lett. **68**, 1097 (1992).
- [22] G. Calabrese, L. Lehner, and M. Tiglio, Phys. Rev. D **65**, 104031 (2002), gr-qc/0111003.
- [23] F. Banyuls, J. A. Font, J. M. Ibáñez, J. M. Martí, and J. A. Miralles, Astrophys. J. **476**, 221 (1997).
- [24] H.-O. Kreiss and J. Lorenz, *Initial-Boundary Value Problems and the Navier-Stokes Equations* (Academic Press, New York, 1989).
- [25] J. M. Martí and E. Müller, Living Rev. Relativity (1999), astro-ph/9906333.
- [26] J. A. Font, Living Rev. Rel. **2000-2** (2000).
- [27] O. Sarbach and M. Tiglio, Journal of Hyperbolic Differential Equations **2**, 839 (2005), gr-qc/0412115.
- [28] P. Painlevé, C. R. Acad. Sci. **173**, 677 (1921).
- [29] A. Gullstrand, Ark. Mat. Astron. Fys. **16**, 1 (1922).
- [30] K. Martel and E. Poisson, Am. J. Phys. **69**, 476 (2001), gr-qc/0001069.
- [31] B. Gustafsson, H.-O. Kreiss, and J. Olinger, *Time dependent problems and difference methods* (Wiley, New York, 1995).
- [32] URL <http://www.carpetcode.org>.
- [33] URL <http://relativity.phys.lsu.edu/postdocs/matt/taka.php>.
- [34] URL <http://www.aei.mpg.de/~hawke/Whisky.html>.
- [35] G. Allen, T. Dramlitsch, I. Foster, N. Karonis, M. Ripeanu, E. Seidel, and B. Toonen, in *Proceedings of Supercomputing 2001, Denver, USA* (2001), http://www.cactuscode.org/Papers/GordonBell_2001.ps.gz.
- [36] M. Alcubierre, B. Brügmann, D. Pollney, E. Seidel, and R. Takahashi, Phys. Rev. D **64**, 061501(R) (2001), gr-qc/0104020.
- [37] M. Alcubierre, B. Brügmann, P. Diener, M. Koppitz, D. Pollney, E. Seidel, and R. Takahashi, Phys. Rev. D **67**, 084023 (2003), gr-qc/0206072.
- [38] M. Alcubierre, W. Benger, B. Brügmann, G. Lanfermann, L. Neger, E. Seidel, and R. Takahashi, Phys. Rev. Lett. **87**, 271103 (2001), gr-qc/0012079.
- [39] L. Baiotti, I. Hawke, P. J. Montero, F. Löffler, L. Rezzolla, N. Stergioulas, J. A. Font, and E. Seidel, Phys. Rev. D **71**, 024035 (2005), gr-qc/0403029.
- [40] M. J. Berger and J. Olinger, J. Comput. Phys. **53**, 484 (1984).
- [41] E. Schnetter, S. H. Hawley, and I. Hawke, Class. Quantum Grav. **21**, 1465 (2004), gr-qc/0310042.
- [42] J. Thornburg, Class. Quantum Grav. **21**, 743 (2004), gr-qc/0306056.
- [43] I. Booth, L. Brits, J. A. Gonzalez, and C. Van Den Broeck, Class. Quant. Grav. **23**, 413 (2006), gr-qc/0506119.

-
- [44] P. Diener, *Class. Quantum Grav.* **20**, 4901 (2003), gr-qc/0305039, URL <http://stacks.iop.org/0264-9381/20/4901>.
- [45] N. Stergioulas and J. L. Friedman, *Astrophys. J.* **444**, 306 (1995).
- [46] N. Stergioulas, *Living Rev. Rel.* **1**, 1998 (1998).
- [47] H. Komatsu, Y. Eriguchi, and I. Hachisu, *Mon. Not. R. Astron. Soc.* **237**, 355 (1989).
- [48] G. B. Cook, S. L. Shapiro, and S. A. Teukolsky, *Astrophys. J.* **398**, 203 (1992).
- [49] L. Baiotti, I. Hawke, L. Rezzolla, and E. Schnetter, *Phys. Rev. Lett.* **94**, 131101 (2005), gr-qc/0503016.
- [50] L. Baiotti, I. Hawke, P. Montero, and L. Rezzolla, in *Computational Astrophysics in Italy: Methods and Tools*, edited by R. Capuzzo-Dolcetta (Mem. Soc. Astron. It. Suppl., Trieste, 2003), vol. 1, p. 327.
- [51] J. E. Tohline and I. Hachisu, *Astrophys. J.* **361**, 394 (1990).
- [52] M. Alcubierre et al. (2004), gr-qc/0411137.
- [53] M. Shibata and Y.-I. Sekiguchi, *Phys. Rev. D* **68**, 104020 (2003).
- [54] B. R. Durney and I. W. Roxburgh, *Royal Society of London Proceedings Series A* **296**, 189 (1967).
- [55] S. Chandrasekhar and N. R. Lebovitz, *Astrophys. J.* **152**, 267 (1968).
- [56] J. B. Hartle, K. S. Thorne, and S. M. Chitre, *Astrophys. J.* **176**, 177 (1972).
- [57] S. L. Shapiro and S. A. Teukolsky, *Black Holes, White Dwarfs, and Neutron Stars* (John Wiley & Sons, New York, 1983).
- [58] W. A. Fowler, *Reviews of Modern Physics* **36**, 545 (1964).
- [59] S. Chandrasekhar, *Phys. Rev. Lett.* **12**, 114 (1964).
- [60] S. Chandrasekhar, *Astrophys. J.* **140**, 417 (1964).
- [61] J. L. Friedman, J. R. Ipser, and R. D. Sorkin, *Astrophys. J.* **325**, 722 (1988).
- [62] M. Saijo, *Astrophys. J.* **615**, 866 (2004).
- [63] M. Shibata, T. W. Baumgarte, and S. L. Shapiro, *Astrophys. J.* **542**, 453 (2000), astro-ph/0005378.
- [64] M. Saijo, M. Shibata, T. W. Baumgarte, and S. L. Shapiro, *Astrophys. J.* **548**, 919 (2001), astro-ph/0010201.
- [65] T. G. Cowling, *Mon. Not. R. Astr. Soc.* **101**, 367 (1941).
- [66] C. Bona, J. Massó, E. Seidel, and J. Stela, *Phys. Rev. Lett.* **75**, 600 (1995).
- [67] S. W. Hawking, in *Black Holes*, edited by C. DeWitt and B. S. DeWitt (Gordon and Breach, New York, 1973), pp. 1–55.

- [68] S. Hod and T. Piran, *Phys. Rev. Lett.* **81**, 1554 (1998).
- [69] A. Ori, *Phys. Rev. Lett.* **67**, 789 (1991).
- [70] S. A. Hayward, *Phys. Rev. D* **49**, 6467 (1994), gr-qc/9306006, URL <http://link.aps.org/abstract/PRD/v49/p6467>.
- [71] A. Ashtekar, C. Beetle, and S. Fairhurst, *Class. Quantum Grav.* **16**, L1 (1999), gr-qc/9812065.
- [72] A. Ashtekar and B. Krishnan, *Living Rev. Rel.* **7**, 10 (2004), gr-qc/0407042.
- [73] I. Booth, L. Brits, J. A. Gonzalez, and C. V. D. Broeck, *Class. Quant. Grav.* **23**, 413 (2006), gr-qc/0506119.
- [74] A. M. Abrahams, L. Rezzolla, M. E. Rupright, A. Anderson, P. Anninos, T. W. Baumgarte, N. T. Bishop, S. R. Brandt, J. C. Browne, K. Camarda, et al., *Phys. Rev. Lett.* **80**, 1812 (1998), gr-qc/9709082.
- [75] L. Rezzolla, A. M. Abrahams, R. A. Matzner, M. E. Rupright, and S. L. Shapiro, *Phys. Rev. D* **59**, 064001 (1999), gr-qc/9807047.
- [76] M. E. Rupright, A. M. Abrahams, and L. Rezzolla, *Phys. Rev. D* **58**, 044005 (1998).
- [77] R. Gómez, L. Lehner, R. Marsa, J. Winicour, A. M. Abrahams, A. Anderson, P. Anninos, T. W. Baumgarte, N. T. Bishop, S. R. Brandt, et al., *Phys. Rev. Lett.* **80**, 3915 (1998), gr-qc/9801069.
- [78] J. Winicour, *Living Rev. Rel.* (submitted) (2005), gr-qc/0508097.
- [79] N. T. Bishop, R. Gómez, L. Lehner, and J. Winicour, *Phys. Rev. D* **54**, 6153 (1996).
- [80] R. Gómez, R. L. Marsa, and J. Winicour, *Phys. Rev. D* **56**, 6310 (1997), gr-qc/9708002.
- [81] M. D. Duez, S. L. Shapiro, and H.-J. Yo, *Phys. Rev. D* **69**, 104016 (2004), gr-qc/0401076.
- [82] I. Hawke, F. Löffler, and A. Nerozzi, *Phys. Rev. D* **71**, 104006 (2005), gr-qc/0501054.
- [83] M. M. May and R. H. White, *Phys. Rev.* **141**, 1232 (1966).
- [84] M. Saijo, T. W. Baumgarte, S. L. Shapiro, and M. Shibata, *Astrophys. J.* **569**, 349 (2002).
- [85] P. Goldreich and S. V. Weber, *Astrophys. J.* **238**, 991 (1980).
- [86] T. Zwerger and E. Müller, *Astron. Astrophys.* **320**, 209 (1997).
- [87] H. Dimmelmeier, J. A. Font, and E. Müller, *Astrophys. J. Lett.* **560**, L163 (2001).
- [88] H. Dimmelmeier, J. A. Font, and E. Müller, *Astron. Astrophys.* **388**, 917 (2002).
- [89] H. Dimmelmeier, J. A. Font, and E. Müller, *Astron. Astrophys.* **393**, 523 (2002).
- [90] H.-T. Janka, T. Zwerger, and R. Moenchmeyer, *Astron. Astrophys.* **268**, 360 (1993).
- [91] J.-L. Tassoul, *Theory of Rotating Stars* (Princeton University Press, 1978), ISBN 0-691-08211-1.
- [92] K. S. Thorne, *Reviews of Modern Astronomy* **10**, 1 (1997).
- [93] J. L. Houser, J. M. Centrella, and S. C. Smith, *Phys. Rev. Lett.* **72**, 1314 (1994), gr-qc/9409057.

- [94] J. R. Oppenheimer and H. Snyder, *Phys. Rev. D* **56**, 455 (1939).
- [95] S. L. Shapiro and S. A. Teukolsky, *Astrophysical Journal Letters* **234**, L177 (1979).
- [96] S. L. Shapiro and S. A. Teukolsky, *Astrophysical Journal* **235**, 199 (1980).
- [97] T. Nakamura, K. Maeda, S. Miyama, and M. Sasaki, *Progress of Theoretical Physics* **63**, 1229 (1980).
- [98] T. Nakamura, *Prog. Theor. Phys.* **65**, 1876 (1981).
- [99] T. Nakamura, *Prog. Theor. Phys.* **66**, 2038 (1981).
- [100] T. Nakamura, *Prog. Theor. Phys.* **70**, 1144 (1983).
- [101] R. F. Stark and T. Piran, *Phys. Rev. Lett.* **55**, 891 (1985).
- [102] M. Shibata, *Prog. Theor. Phys.* **104**, 325 (2000).
- [103] M. Shibata, T. W. Baumgarte, and S. L. Shapiro, *Phys. Rev. D* **61**, 044012 (2000), [gr-qc/9911308](#).
- [104] M. Shibata and S. L. Shapiro, *Astrophys. J. Lett.* **572**, L39 (2002).
- [105] J. A. Font, T. Goodale, S. Iyer, M. Miller, L. Rezzolla, E. Seidel, N. Stergioulas, W.-M. Suen, and M. Tobias, *Phys. Rev. D* **65**, 084024 (2002).
- [106] M. Shibata, *Phys. Rev. D* **67**, 024033 (2003), [gr-qc/0301103](#).
- [107] M. D. Duez, P. Marronetti, S. L. Shapiro, and T.-m. W. Baumgarte, *Phys. Rev. D* **67**, 024004 (2003), [gr-qc/0209102](#).
- [108] S. A. Hughes, C. R. Keeton, II, P. Walker, K. T. Walsh, S. L. Shapiro, and S. A. Teukolsky, *Phys. Rev. D* **49**, 4004 (1994), URL <http://link.aps.org/abstract/PRD/v49/p4004>.
- [109] A. M. Abrahams, G. B. Cook, S. L. Shapiro, and S. A. Teukolsky, *Phys. Rev. D* **49**, 5153 (1994).
- [110] D. M. Christodoulou, D. Kazanas, I. Shlosman, and J. E. Tohline, *Astrophys. J.* **446**, 472 (1995).
- [111] J. E. Tohline, R. H. Durisen, and M. McCollough, *Astrophys. J.* **298**, 220 (1985).
- [112] R. H. Durisen, R. A. Gingold, J. E. Tohline, and A. P. Boss, *Astrophys. J.* **305**, 281 (1986).
- [113] I. A. Bonnell and M. R. Bate, *Mon. Not. Roy. Astr. Soc.* **271**, 999 (1994).
- [114] A. Loeb and F. A. Rasio, *Astrophys. J.* **432**, 52 (1994).
- [115] I. A. Bonnell and J. E. Pringle, *Mon. Not. Roy. Astr. Soc.* **273**, L12 (1995).
- [116] B. K. Pickett, R. H. Durisen, and G. A. Davis, *Astrophys. J.* **458**, 714 (1996).
- [117] J. L. Houser and J. M. Centrella, *Phys. Rev. D* **54**, 7278 (1996).
- [118] M. Rampp, E. Mueller, and M. Ruffert, *Astron. Astrophys.* **332**, 969 (1998).
- [119] J. D. Brown, *Phys. Rev. D* **62**, 084024 (2000).
- [120] J. N. Imamura and R. H. Durisen, *Astrophys. J.* **549**, 1062 (2001).

- [121] J. M. Centrella, K. C. B. New, L. L. Lowe, and J. D. Brown, *Astrophys. J.* **550**, L193 (2001), astro-ph/0010574.
- [122] M. Colpi and I. Wasserman, *Astrophys. J.* **581**, 1271 (2002).
- [123] M. B. Davies, A. King, S. Rosswog, and G. Wynn, *Astrophys. J. Lett.* **579**, L63 (2002).
- [124] J. N. Imamura, B. K. Pickett, and R. H. Durisen, *Astrophys. J.* **587**, 341 (2003).
- [125] R. Banerjee, R. E. Pudritz, and L. Holmes, *Mon. Not. Roy. Astr. Soc.* **355**, 248 (2004).
- [126] C. D. Ott, S. Ou, J. E. Tohline, and A. Burrows, *Astrophys. J.* **625**, L119 (2005), astro-ph/0503187.
- [127] A. L. Watts, N. Andersson, and D. I. Jones, *Astrophys. J.* **618**, L37 (2005), astro-ph/0309554.
- [128] A. L. Watts, N. Andersson, H. Beyer, and B. F. Schutz, *Mon. Not. Roy. Astron. Soc.* **342**, 1156 (2003), astro-ph/0210122.
- [129] A. L. Watts, N. Andersson, and R. L. Williams, *Mon. Not. Roy. Astron. Soc.* **350**, 927 (2004), astro-ph/0311320.
- [130] J. C. B. Papaloizou and J. E. Pringle, *Mon. Not. R. Astron. Soc.* **208**, 721 (1984).
- [131] J. C. B. Papaloizou and J. E. Pringle, *Mon. Not. R. Astron. Soc.* **213**, 799 (1985).
- [132] E. Balbinski, *Mon. Not. Roy. Astr. Soc.* **216**, 897 (1985).
- [133] M. Saijo and S. Yoshida (2005), astro-ph/0505543.
- [134] B. Zink, N. Stergioulas, I. Hawke, C. D. Ott, E. Schnetter, and E. Müller, *Phys. Rev. Letters* **96**, 161101 (2006), gr-qc/0501080.
- [135] G. M. Fuller, S. E. Woosley, and T. A. Weaver, *Astrophys. J.* **307**, 675 (1986).
- [136] K. C. B. New and J. M. Centrella, in *AIP Conf. Proc. 575: Astrophysical Sources for Ground-Based Gravitational Wave Detectors* (2001), p. 221.
- [137] K. C. B. New and S. L. Shapiro, *Astrophys. J.* **548**, 439 (2001), astro-ph/0010172.
- [138] P. Bodenheimer and J. P. Ostriker, *Astrophys. J.* **180**, 159 (1973).
- [139] M. Shibata and Y.-i. Sekiguchi, *Phys. Rev. D* **71**, 024014 (2005), astro-ph/0412243.
- [140] M. Saijo, *Phys. Rev. D* **71**, 104038 (2005), astro-ph/0505423.
- [141] T. W. Baumgarte and S. L. Shapiro (2002), astro-ph/0211339.
- [142] M. D. Duez, Y. T. Liu, S. L. Shapiro, M. Shibata, and B. C. Stephens (2005), astro-ph/0510653.
- [143] M. Shibata, S. Karino, and Y. Eriguchi, *Mon. Not. Roy. Astron. Soc.* **334**, L27 (2002), gr-qc/0206002.
- [144] M. Shibata, S. Karino, and Y. Eriguchi, *Mon. Not. Roy. Astron. Soc.* **343**, 619 (2003), astro-ph/0304298.

-
- [145] N. Stergioulas, Ph.D. thesis, University of Wisconsin-Milwaukee, Milwaukee, Wisconsin (1996).
- [146] H. Komatsu, Y. Eriguchi, and I. Hachisu, *Mon. Not. R. Astron. Soc.* **239**, 153 (1989).
- [147] B. F. Schutz and E. Verdaguer, *MNRAS* **202**, 881 (1983).
- [148] A. Nagar and L. Rezzolla, *Classical and Quantum Gravity* **22**, R167 (2005), URL <http://stacks.iop.org/0264-9381/22/R167>.
- [149] Y.-i. Sekiguchi and M. Shibata, *Phys. Rev. D* **70**, 084005 (2004), [gr-qc/0403036](#).
- [150] B. Zink, P. Diener, E. Pazos, and M. Tiglio, *Phys. Rev. D* **73**, 084011 (2006), [gr-qc/0511163](#).
- [151] G. Calabrese, L. Lehner, and M. Tiglio, *Phys. Rev. D* **65**, 104031 (2002), [gr-qc/0111003](#).
- [152] P. Diener, E. N. Dorband, E. Schnetter, and M. Tiglio (2005), [gr-qc/0512001](#).
- [153] B. Szilágyi, R. Gómez, N. T. Bishop, and J. Winicour, *Phys. Rev. D* **62**, 104006 (2000), [gr-qc/9912030](#).
- [154] M. Alcubierre et al., *Class. Quant. Grav.* **21**, 589 (2004), [gr-qc/0305023](#).
- [155] A. I. MacFadyen, S. E. Woosley, and A. Heger, *Astrophys. J.* **550**, 410 (2001).
- [156] L. Lehner, O. Reula, and M. Tiglio (2005), [gr-qc/0507004](#).

Acknowledgements

Mein ausdrücklicher Dank geht zunächst an meinen Betreuer Ewald Müller, der mir mit Rat und Tat immer dann beigestanden hat, wenn es notwendig war, und in anderen Fällen mir die selbstverantwortliche Entscheidung über meine Forschungsaktivitäten ermöglicht hat. Viel Unterstützung habe ich auch von der Max-Planck-Gesellschaft und vom Sonderforschungsbereich/Transregio 7 “Gravitationswellenastronomie” der Deutschen Forschungsgemeinschaft erfahren, insbesondere zur Finanzierung von wichtigen Reisevorhaben.

Sieben Monate meiner Doktorandenzeit habe ich auf Einladung des Center for Computation and Technology in Louisiana an modernen Methoden der Numerical Relativity gearbeitet, und ich möchte mich herzlich bei Edward Seidel und Manuel Tiglio am CCT und beim Direktorium des Max-Planck-Instituts für Astrophysik für diese Möglichkeit bedanken.

Viele Kollegen haben mich während meines Promotionsvorhabens unterstützt, und es wäre sicher unangemessen, wenige zu nennen und andere auszulassen. Für meine Publikationen danke ich vor allem der Geduld meiner Koautoren Peter Diener, Ian Hawke, Ewald Müller, Christian Ott, Enrique Pazos, Erik Schnetter, Nikolaos Stergioulas und Manuel Tiglio.

Eine ganz persönliche Danksagung geht an meine Familie, die mir auf meinem langen Weg (oft tatkräftig) geholfen hat, und natürlich an meine Michi.

Publications

- B. Zink, N. Stergioulas, I. Hawke, C. D. Ott, E. Schnetter and E. Müller: *Non-axisymmetric stability and fragmentation of general relativistic quasi-toroidal stars*, in preparation.
- B. Zink, E. Pazos, P. Diener and M. Tiglio: *Cauchy-perturbative matching revisited: tests in spherical symmetry*, gr-qc/0511163, PRD, in press.
- B. Zink, N. Stergioulas, I. Hawke, C. D. Ott, E. Schnetter and E. Müller: *Formation of supermassive black holes through fragmentation of toroidal supermassive stars*, gr-qc/0501080, PRL, in press.
- B. Zink, C. D. Ott, I. Hawke, E. Schnetter and E. Müller: *Collapse and fragmentation of uniformly and differentially rotating $N = 3$ polytropes*, poster presentation at the 17th International Conference on General Relativity and Gravitation (GR17), 2004.
- B. Zink, M. Camenzind and I. Appenzeller: *General relativistic volume ray-tracing in application to a Kerr geometry*, Diplomarbeit at the Landessternwarte Königstuhl, University of Heidelberg, 2002.

Curriculum Vitae

Personal data

Name: Burkhard Sebastian Zink

Address: Max-Planck-Institut für Astrophysik, Karl-Schwarzschild-Straße 1, 85741 Garching

Date of birth: Dec 2, 1975 in Wolfsburg, Germany

Citizenship: German

Education

08/2005		Visitor at the Facultad de Matemática, Astronomía y Física of the University of Cordoba, Argentina, under the supervision of Prof. Oscar Reula
02/2005	- 08/2005	Visitor at the Center for Computation and Technology at Louisiana State University, under the supervision of Prof. Manuel Tiglio
09/2003		Advanced School and Conference on Sources of Gravitational Waves, Trieste
03/2003	- 03/2006	PhD student at the Max-Planck-Institut für Astrophysik, Garching, under the supervision of Dr. Ewald Müller
10/2002		Diplom degree in physics
10/2001	- 10/2002	Diplom thesis at the theoretical division of the State Observatory Königstuhl in Heidelberg, under the supervision of Prof. Max Camenzind
07/1998		Vordiplom degree in physics
07/1998		Vordiplom degree in mathematics
09/1996	- 10/2002	Study of physics at the University Ruperto Carola in Heidelberg
1995	- 1996	Military service
1995		Abitur degree at the Theodor-Heuss-Gymnasium in Wolfsburg
1982	- 1995	School education

Professional Societies

Member of the American Physical Society, TG Gravitation

Member of the Deutsche Physikalische Gesellschaft

Member of the International Society on General Relativity and Gravitation